Raman Spectroscopy Study on the Phase Transformation of Solids in Washing Powder Preparation Processes

by

Boyang Zou

A Dissertation Submitted in Accordance with the Requirements for the

Degree of

DOCTOR OF PHILOSOPHY

(Chemical Engineering)

UNIVERSITY OF LEEDS
Institute of Particle Science & Engineering
School of Chemical and Process Engineering
January 2017

The candidate confirms that the work submitted is his/her own and that appropriate credit has been given where reference has been made to the work of others.

This copy has been supplied on the understanding that it is copyright material and that no quotation from the thesis may be published without proper acknowledgement.

Acknowledgements

Abstract

Sodium sulphate and sodium carbonate are essential inorganic raw materials for the dry laundry industry. The composition of the final slurry mixture possesses a high process dependency, which has significant impact on the properties of the final granule product, such as particle size distribution, porosity, stability and liquid loading capacity. To obtain and design desirable properties requires a good understanding of the dissolution and crystallisation behaviour of both raw materials and their double salt Burkeite $(Na_4(CO_3)_{0.61}(SO_4)_{1.39})$.

To perform this study, first, inorganic slurry calibration models were developed by applying an in-situ Raman spectroscopy technique that contributes in real-time monitoring of composition alteration of a multi-component system over a dissolution and crystallisation process. Based on the calibration model, a new methodology was developed for fast determining a detailed isothermal ternary phase diagram of the Na_2CO_3-H_2O-Na_2SO_4 system. For Burkeite kinetic study, the detected metastable zone limits with respect to the phase equilibrium were correlated to the increased rate of supersaturation during dissolution of the Na_2SO_4. This novel strategy could be applied to other systems, offering a fundamental base for modelling nucleation rate and size control for industrial processing of co-crystals/double salts.

The impact of processing conditions on the sodium salt mixture demonstrates that increasing the system pH induces fast crystallisation and precipitates small crystals with larger inter- and intra-porosities. However, the addition of high pH sodium silicate solution in the system decreases the solubility of raw material and leads to less Burkeite formation, which was caused by the common ion effect and polymerisation of sodium silicates.

Overall, this research developed a feasible in-process monitoring method, which can simultaneously detect and analyse any composition and phase changes of the individual substance in a multi-component detergent slurry system. With the aid of this method, researchers were able to discover the fundamental cause of product failure, thereby sufficiently targeting, investigating and solving the problem, eventually achieving the desirable product by optimising the production procedure.

Table of Contents

List of Tables

List of Figures

List of Symbols

a   dimensionless thermodynamic parameter

α activity

α_c solute activity

$\alpha_\pm$ average ionic activity of the solute

a & a' anions

A   effective surface contact area between solid particles and the solution (m^2)

A the Debye-Hückel constant

A_ϕ osmotic coefficient constant

B   dimensionless thermodynamic parameter

c   electrolyte molar concentration (mol/L) or speed of the light (m/s)

c & c' cations

$c_+^{\nu_a}$ & $c_-^{\nu_b}$ ionic concentration of each ion (mol/L)

ΔC_{max} maximum allowance of supersaturation $(C - C_e)$ (m^{-3})

C_n time dependent stationary concentration of n sized clusters (m^{-3})

C_s concentration of the nucleation sites on which clusters of the new phase can precipitate (m^{-3})

d$_0$ diameter of the molecule (m)

d   the dimensionality of crystallites growth

d the distance between neighbouring planes of atoms $(nm\ or\ Å)$

D   diffusion coefficient (m^2/s)

$f_{e,s}$ molecule attachment per growth site $(\Delta\mu = 0)$

F   degree of freedom

ΔG change in Gibbs free energy (KJ/mol)

ΔG_v	free energy changes per unit volume (KJ/mol)
h	static layer of the liquid or Planck's constant
ΔH_f	molal enthalpy of the melt (fusion) of the solute (KJ/mol)
i^*	number of molecules in the critical nucleus
I	ionic strength (mol/m^3)
J	nucleation rate (m^{-3}s^{-1})
k	Boltzmann constant (1.3805*10^{-23} J/K)
k_j	nucleation rate constant (m^{-3}s^{-1})
k_n	nucleus shape factor
k_v	crystallites growth shape factor (m^{3-d})
K_{sp_a}	activity solubility product (for high solubility electrolytes)
K_{sp}	solubility product
K_{sp_c}	concentration solubility product (for sparingly electrolytes)
m	molality (mol/kg)
m	positive crystallites growth exponents
m_i	molal concentration of the ion i (mol/kg)
m_0	the order of nucleation
M	molar weight of solid in the solution (g/mol)
n	number of moles of water in the hydration form
N$_{det}$	detectable number of nuclei
ρ	density of the solid (kg/m^{-3})
P	total phases in a system
q	cooling rate ($\frac{dT}{dt}$) (K/s)
r	particles with the radius (m)
r*	critical nucleus size (m)
γ	interfacial tension or surface energy (J/m^2)

γ_{eff}	nucleus effective interfacial tension (J/m^2)
γ_c	activity coefficient
R	gas constant 8.314 (($J/mol \cdot K$)
s^*	equilibrium solubility (mol/L)
s_r	solubility of particles with the radius r (mol/L)
ΔS_f	molal entropy of fusion (($KJ/mol \cdot K$)
S	supersaturation ratio
τ	induction time (s)
T	temperature of the solution (K)
T_f	melting temperature of the solute (K)
T_e	equilibrium temperature (K)
T_c	detectable crystallisation temperature (K)
ΔT_c	critical under cooling (K)
ΔT_{max}	temperature difference between solution saturation and nucleation points (K)
u_c	critical under cooling
μ	chemical potential (J/mol)
$\Delta\mu$	chemical potential between the solute molecules in the solution and in the crystals (J/mol)
μ_-	chemical potentials of positive ions (J/mol)
μ_+	chemical potentials of positive ions (J/mol)
μ_c^θ	standard chemical potential (J/mol)
v	frequency of the light (Hz)
v_+	moles of positive ions
v_-	moles of negative ions
v_a & v_b	stoichiometric coefficient of ion A and B
V	molar volume (m^3)

w	wavenumber
x	mole fraction of the solute in the solution
x & y	stoichiometric constants
z	Zeldovich factor
z_+ or z_M	charge of the positive ions
z_- or z_X	charge of the negative ions
z_i	valence of the ion i
z_a^+ & z_b^-	valence of ion A and B
λ	molecular latent heat of crystallisation or wavelength (J)
Γ	gamma function
θ	is the angle of the incident ray and the surface

Chapter 1 **Introduction**

1.1 Addressing the Research Problem

Sodium carbonate and sodium sulphate are two common inorganic salts with high application values, such as they are widely applied in the dry laundry industry (1-3). Crystallisation from solutions of these two salts can result in anhydrous or a variety of hydrate forms of the raw materials or crystalline double salts Burkeite ($\sim Na_2CO_3 \cdot 2Na_2SO_4$) and sodium sulphate dicarbonate ($\sim 2Na_2CO_3 \cdot Na_2SO_4$). Therefore, the composition and properties of the final product from the sodium salt-based slurry system are highly dependent on raw material composition and experimental conditions, and are difficult to control. Furthermore, the presence of other chemicals, such as sodium silicate and surfactant phase, and their behaviour in the detergent system also have a great impact on the finishing product (such as reducing the solubility of the final product or causing more residue). An on-line measurement technique (Raman spectroscopy) was applied in this study, which will help to fundamentally understand the dissolution and crystallisation process of the multi-component slurry system.

1.2 Research Background

There has been literature published on sodium salt systems since the 1930's which is due to its strong presence in industrial processes. Formerly, mainly sodium salts existed in the pulp paper industry where the kraft cooking "black liquors" are slurries with around 60-85% of sodium salts. Energies and cooking chemicals are produced and recovered through evaporating and burning the black liquor. However, a severe scaling issue appeared which causes pipe clogging and subsequently reduces the efficiency of the recovery process. Later, it was discovered that one of the double salts, Burkeite, which formed from the existing sodium salts, was the key factor causing this issue (4).

However, in recent decades, sodium salts have been extensively applied as the environmentally friendly alternative to phosphates in the detergent industries, where the double salt Burkeite is critical to the performance of the

final product, due to its physical properties. Burkeite stability is much better than both mother salts, such as no hydrates form, which is favourable for storage purposes. Burkeite crystals normally grow into an agglomerated block-like shape (5). In 1995 Meenan et al. (2) applied additives (i.e. ionic polymers) into the system, which modified the crystal morphology of burkeite to dendritic aggregates. Therefore, significantly increasing the inter- and intra-porosity of the particles, further enhanced the performance of up-taking other chemicals in the detergent, such as surfactants and perfumes.

Crystallisation of solutions with different ratios of Na_2CO_3 and Na_2SO_4 has been studied at laboratory scale (6-9). Many analytical techniques have successfully demonstrated important applications in monitoring the crystal formation and investigation of the composition of final solid products, such as Focused Beam Reflectance Measurement (FBRM), Differential Scanning Calorimetry (DSC) and X-ray Diffraction (XRD).

Solubility studies into the Na_2CO_3-Na_2SO_4-H_2O ternary system by Harvie *et al.* have demonstrated the limited crystallisation of Burkeite at 25°C through semi-empirical modelling (10). One method of applying this solubility data to the solid-liquid composition of the Na_2CO_3-Na_2SO_4-H_2O slurry is to create a ternary phase diagram which displays the phase of each component as a function of concentration. Green *et al.* incrementally added Na_2CO_3 and Na_2SO_4 to various concentrations of aqueous solutions at 100°C to comprehend the ternary phase diagram (8). In his work, in order to achieve the solution equilibrium, each experiment took more than 20 hours to ensure equilibrium was reached. Then after filtration, the filtrate and wet residue were studied using the chemical analysis method. According to this method, to carry out a complete phase diagram was very time-consuming.

The in-situ Raman technique has drawn wide interest in recent research, such as monitoring polymorphic phase transformation (11) and real-time quantitative analysis (12).

In the present study, the in-situ Raman technique is applied for on-line monitoring the composition variation in multi-component slurry systems with the advantage that no sample preparation is required for these measurements, less interference of aqueous media and real-time data output. In Raman

spectroscopy, a single material may exhibit multiple infra-red absorptions; each of which can potentially scatter into several Raman peaks (13). Here, one of the chemometric modelling methods, Partial Least Squares (PLS), was introduced to obtain phase specific concentrations directly from the Raman scattered peak intensities. This predictive model is suitable to apply when multiple factors contribute to the response of a variable, yet all such factors are co-linear in relation to this variable.(14, 15) Despite this large number of factors, the response from the Raman detector is linear with respect to the concentration of the object studied (16), thus making PLS an ideal modelling technique for this application. For verifying the accuracy of the predicted result, the XRD technique was also applied comparatively to analyse the composition of dried powder samples.

1.3 Scope and Structure of the Research

The research question underlying this thesis is as follows:

For a slurry system with multiple components of alliterating composition, whether it is feasible to simultaneously quantitatively analyse the dissolution and crystallisation process?

The question was addressed through the following steps:

1. Examine the feasibility of the selected technique (Raman spectroscopy) on the current research system (Na_2CO_3-solution-Na_2SO_4).
2. Establish the calibration model for Na_2CO_3 and Na_2SO_4 slurry system. Define a methodology to validate the reliability of the accomplished models.
3. Develop a novel methodology to determine an isothermal ternary phase diagram for the Na_2CO_3-water-Na_2SO_4, which helps in estimating the composition of slurry mixtures according to the initial material input.
4. Investigate the feasibility of applying the calibration model and the newly developed KBHR method on conducting the kinetic studies of Burkeite.
5. Apply the calibration model to the real process to investigate the impact of process operation, condition and the intervention of other chemicals on Na_2CO_3 and Na_2SO_3 slurry systems.

6. Establish another phase diagram with other chemicals involved, such as Na_2CO_3-sodium silicate -Na_2SO_4.

With all the questions answered, the fundamental reaction mechanism will be understood, which can significantly contribute to the process optimisation in the scale-up step, additionally improving the performance of the final washing powder. Furthermore, the method of in-situ monitoring the composition/phase alteration of a multi-component system by applying a quantitative calibration model can also be implemented to other complex systems in a wide spectrum.

A general description of the thesis is illustrated schematically in Figure 1.1: Schematic describing the main information of each chapter in this thesis..

Chapter 1 Introduction

A general background to the research project as well as the scope of this study

Chapter 2 Literature Review

❑ Crystallisation fundamental theories:
- Solubility and solubility products
- Phase equilibrium and phase diagrams
- Crystallisation
❑ Sodium silicate (de-)polymerisation
❑ Primary analytical techniques

Chapter 3 Materials and Methods

❑ Materials used in this study
❑ Experimental methodologies
❑ Main analytical techniques

Chapter 4 Raman Calibration Model Establishment, Verification and Application

Chapter 5 Ternary Phase Diagram Determination for Na_2CO_3-H_2O-Na_2SO_4

❑ Phase diagram determination
❑ Kinetics of Burkeite ($\sim Na_2CO_3 \cdot 2Na_2SO_4$) crystallisation

Chapter 6 Impact of Solution Condition on the Phase Transition of a Sodium Salt Slurry System

❑ Water content and pH effects
❑ Sodium silicate influence
❑ Sodium salt impact on sodium silicate
❑ Other factors impact on sodium silicate

Chapter 7 Conclusions and Future Work

Figure 1.1: Schematic describing the main information of each chapter in this thesis.

Reference List

1. Atkinson, C., Heybourne, M.J., Iley, W.J., Knight, P.C., Russell, P.J., Taylor, T. and Jones, D.P. *Process for preparing needle-shaped crystal growth modified burkeite detergent additive*. Google Patents. 1990. Available from: https://www.google.be/patents/US4900466

2. Meenan, P., Roberts, K., Yuregir, K. and Knight, P. The influence of batch processing on the particulate properties of burkeite (Na2CO3 (Na2SO4) 2). *Journal of materials science.* 1995, **30**(12), pp.3115-3122.

3. Shi, B., Frederick, W.J. and Rousseau, R.W. Effects of calcium and other ionic impurities on the primary nucleation of burkeite. *Industrial & Engineering Chemistry Research.* 2003, **42**(12), pp.2861-2869.

4. Grace, T.M. Solubility limits in black liquors. 1975.

5. Evans, E.H. and Knight, P.C. *Process for the preparation of a granular detergent composition*. Google Patents. 1989.

6. Caspari, W.A. The system sodium carbonate–sodium sulphate–water. *Journal of the Chemical Society, Transactions.* 1924, **125**, pp.2381-2387.

7. Shi, B. and Rousseau, R.W. Structure of burkeite and a new crystalline species obtained from solutions of sodium carbonate and sodium sulfate. *The Journal of Physical Chemistry B.* 2003, **107**(29), pp.6932-6937.

8. Green, S.J. and Frattali, F.J. The System Sodium Carbonate-Sodium Sulfate-Sodium Hydroxide-Water at 100° 1. *Journal of the American Chemical Society.* 1946, **68**(9), pp.1789-1794.

9. Bialik, M.A., Sedin, P., Theliander, H., Verrill, C.L. and DeMartini, N.A. Model for Solubility and Solid Phase Composition in High-Temperature Na 2 Co 3-Na 2 So 4 Solutions. In: *The 2006 Annual Meeting*, 2006.

10. Harvie, C.E., Møller, N. and Weare, J.H. The prediction of mineral solubilities in natural waters: The Na-K-Mg-Ca-H-Cl-SO4-OH-HCO3-CO3-CO2-H2O system to high ionic strengths at 25 C. *Geochimica et Cosmochimica Acta.* 1984, **48**(4), pp.723-751.

11. Wang, F., Wachter, J.A., Antosz, F.J. and Berglund, K.A. An investigation of solvent-mediated polymorphic transformation of progesterone using in situ Raman spectroscopy. *Organic Process Research & Development.* 2000, **4**(5), pp.391-395.

12. Ono, T., Ter Horst, J. and Jansens, P. Quantitative measurement of the polymorphic transformation of L-glutamic acid using in-situ Raman spectroscopy. *Crystal Growth & Design.* 2004, **4**(3), pp.465-469.

13. Larkin, P. *Infrared and Raman Spectroscopy: Principles and Spectral Interpretation.* Amsterdam (NL): Elsevier 2011.

14. Martens, H. and Næs, T. *Multivariate Calibration.* Guildford (UK): John Wiley & Sons, 1991.

15. Sivakesava, S., Irudayaraj, J. and Demirci, A. Monitoring a bioprocess for ethanol production using FT-MIR and FT-Raman spectroscopy. *Journal of Industrial Microbiology and Biotechnology.* 2001, **26**(4), pp.185-190.

16. Smith, E. and Dent, G. *Modern Raman spectroscopy: a practical approach.* Wiley. com, 2005.

Chapter 2 Fundamental Theories of Crystallisation and the Chemistry of Sodium Silicate Systems

This study focuses on developing a novel method by selectively using cutting edge analytical techniques, which will provide an access to detect the internal changes of a complex mixture system (both qualitatively and quantitatively) through in-situ monitoring of the operating process.

The fundamental knowledge is reviewed and catalogued into six sections in this chapter. Figure 2.1 illustrates how this knowledge has been applied to the current study.
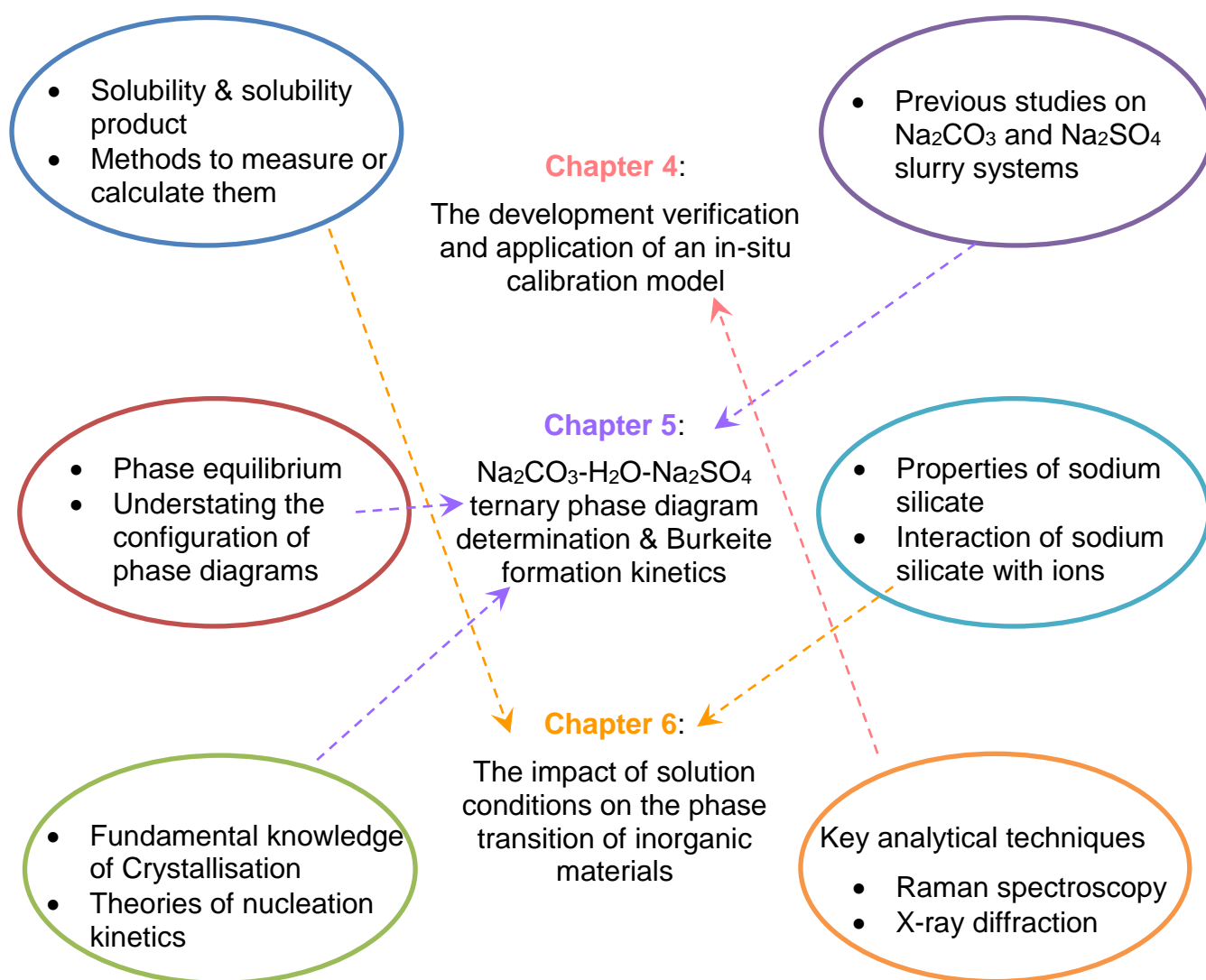
Figure 2.1: Knowledge is reviewed which contributes to the current research

2.1 Solubility and Solubility Products

2.1.1 Solvent Selection

Water has been selected as the prevalent solvent in the industrial process for crystallisation of inorganics from solution. It is a green resource, has low capital costs and is readily available. The predominant reason is that a great number of chemicals possess relatively high solubility in water solutions. However, multiple components (i.e. surfactant and organic phases) can be added to the solution according to different process requirements, which will alternatively change the solvent properties, therefore further impact on the dissolution and crystallisation process of the desired products. For instance, a common method to decrease the solubility of an inorganic material in the solution is by adding water soluble organic liquid(s) in the system, which is also known as the salting-out process (1).

There are some principles that need to be considered when selecting or creating solvents for a crystallisation study. Firstly, the study materials are better if they are readily dissoluble in the solvent. Also, they should easily precipitate out when there is a change in the operating conditions, such as temperature, temperature changing gradient, mixing rotation speed, etc. Secondly, chemical similarity between the solvent and solute has to be taken into account. Great similarity may cause huge energetic or economical costs, a certain level of environmental concern or significant difficulty in the crystallisation process. In addition, it is well known that the crystal habit can also change according to different solvents (1).

Generally, there are some common ways of triggering crystallisation, such as solvent evaporation, cooling or heating and seeding crystallisation. The first two methods are closely related to solvent properties. For instance, an evaporation crystallisation, the power of solvent is the key feature which needs to be considered, which expresses the capability of how much solute can be completely dissolved in a fixed amount of solvent under a constant temperature. For example, at 25°C, water is a more powerful solvent for Na_2SO_4 (13.9g/100g) (2) than toluene (0.052g/100g)(3), however, at temperatures under 25°C toluene is a better solvent for benzoic acid to

dissolve (10.6g/100g) in comparison to water (0.34g/100g) (4). In cooling(/heating) crystallisation, the temperature coefficient is an essential aspect; for example in water solutions below 33°C, Na_2SO_4 has a good solubility gradient (see Figure 2.2), cooling the solution down from 33°C to 25°C will crystallise around 11.32 in weight percentage (wt%) of Na_2SO_4 out as solid. Above 33°C Na_2SO_4 displays inverse solubility behaviour in the aqueous solution, crystallisation will occur by heating up the solution. However, this time the temperature coefficient is not as great as the previous discussion, there will be only 0.72 wt% of Na_2SO_4 crystals achieved (5). Both these two factors (solvent property and temperature coefficient) have to be considered in a crystallisation process. (1) The former one has an impact on the size of the reactor, and they will both determine the yield of crystals.
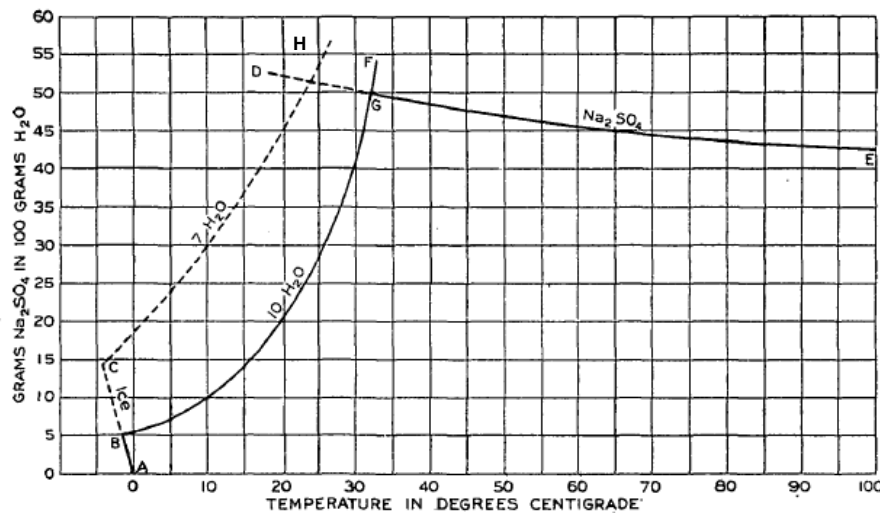
**Figure 2.2: Solubility of sodium sulphate in water
(after Wells, Roger C, 1923) (6)**

2.1.2 Solubility

An ideal solution is a solution where the interaction among solute-solute, solute-solvent and solvent-solvent molecules are identical. The enthalpy of mixing is zero. If a solute and solvent formed an ideal solution, the solubility of the solute should be able to predict from the Van't Hoff equation, as shown in Equation 2.1:

$$\ln x = \frac{\Delta H_f}{R}\left[\frac{1}{T_f} - \frac{1}{T}\right] \tag{Eq. 2.1}$$

where x is the mole fraction of the solute in the solution, ΔH_f (J/mol) is the molal enthalpy of the melt (fusion) of the solute, R is the gas constant 8.314 (J/mol·K), T (K) is the temperature of the solution, T_f (K) is the melting temperature of the solute (1).

As ΔS_f is the molal entropy of fusion and it equals $\frac{\Delta H_f}{T_f}$, therefore Equation 2.1 can be converted into:

$$\ln x = -\frac{\Delta H_f}{RT} + \frac{\Delta S_f}{R} \tag{Eq. 2.2}$$

For the ideal solution system, according to Equation 2.2 the slope of $\ln x$ against 1/T should be a linear line. However, for a non-ideal solution system the change of enthalpy and entropy of mixing must be taken in to account. Therefore, Equation 2.2 will be re-written as Equation 2.3 and subscripts diss. illustrate dissolution. The alternative way to apply Equation 2.3 is to use the experimental solubility data of a single solute in the solution to plot the relation of $\ln x \ vs \ T^{-1}$, then the achieved intercept and slope will be the value of enthalpy and entropy of the dissolution at saturation point.

$$\ln x = -\frac{\Delta H_{diss}}{RT} + \frac{\Delta S_{diss}}{R} \tag{Eq. 2.3}$$

2.1.3 Prediction of Solubility

The temperature determined Gibbs free energies of solids and the activity coefficient for electrolytes of a solution phase are the two key parameters in solubility prediction.

2.1.3.1 Gibbs Free Energy

Gibbs free energy (G) is a thermodynamic figure that can be applied to ascertain whether a reaction is spontaneous or not. The change in Gibbs free energy (ΔG) of the system is equal to the change in enthalpy minus the change in the product of the temperature times the change of entropy, see Equation 2.4. If a system is thermodynamically equilibrium, then ΔG should be equal to zero. For a reaction A+B↔C, $\Delta G < 0$ indicates the reaction will spontaneously occur to the right under constant temperature and pressure, in the contrast if, $\Delta G > 0$ then the reaction will spontaneously proceed towards the left.

$$\Delta G = \Delta H - \Delta TS \qquad \text{(Eq. 2.4)}$$

For an isothermal system the equation can be written into Equation 2.5.

$$\Delta G = \Delta H - T\Delta S \qquad \text{(Eq. 2.5)}$$

Alternatively, the overall Gibbs free energy can be expressed regarding the activity (α) of one of the components.

$$\Delta G = RT \ln \alpha \qquad \text{(Eq. 2.6)}$$

2.1.3.2 Activity and Ionic Strength

The colligative properties of solutions relies on the impact of solute concentration on the activity of the solvent. The chemical potential, μ, of an electrolyte in a solution in which the electrolyte concentration is greater than 10^{-3} molar can be expressed as:

$$\mu = \mu_c^\theta + RT \ln \alpha_c \qquad \text{(Eq. 2.7)}$$

where c is the electrolyte molar concentration (mol/L), μ_c^θ is the standard chemical potential (J/mol) (on a molar basis, exhibiting infinitely dilute solution behaviour.) and α_c is the solute activity (on a molar basis). The activity is expressed as a function of solute molality (m) Equation 2.8 which is defined as the number of moles of the solute per kilogram of solvent (7), the factor γ_c is known as the activity coefficient. If $\gamma_c \approx 1$ indicates the system is close to ideal solution (1).

$$\alpha_c = m * \gamma_c \qquad \text{(Eq. 2.8)}$$

If one mole of an electrolyte completely dissolved in water, the ionization process will produce v_+ moles of positive ions possessing a charge of z_+ and v_- moles of negative ions possess a charge of z_-. For example, Na$_2$CO$_3$ $v_+=$ 2 with $z_+=$ +1 and $v_-=$ 1 with $z_-=$ -2. Therefore the chemical potential (μ) factor can be expressed as (8):

$$\mu = v\mu_\pm = v_+\mu_+ + v_-\mu_- \qquad \text{(Eq. 2.9)}$$

where v is the overall number of free ions in the aqueous solution, μ_- and μ_+ are the chemical potentials of negative and positive ions respectively. So Equation 2.7 becomes:

$$\mu = v(\mu_\pm^\theta + RT \ln \alpha_\pm) \qquad \text{(Eq. 2.10)}$$

$\alpha_\pm$ indicates the average ionic activity of the solute, which possesses the relation with the activity α as:

$$\alpha = \alpha_\pm^v = \alpha_+^{v_+} * \alpha_-^{v_-} \qquad \text{(Eq. 2.11)}$$

So, substituting Equation 2.8 into the equation above will achieve the expression:

$$\alpha = \gamma_\pm^v m_\pm^v = \gamma_+^{v_+} * \gamma_-^{v_-} * m_+^{v_+} * m_-^{v_-} \qquad \text{(Eq. 2.12)}$$

Ultimately, the equation for chemical potential developed to:

$$\mu = \mu_\pm^\theta + vRT \ln \gamma_\pm m_\pm \qquad \text{(Eq. 2.13)}$$

In the electrolyte solution, the activity coefficients are essentially impacted by electrical interactions Equation 2.14. The interaction among electrolytes has a significant influence on the properties of the solution, such as dissociation or the solubility of other components. One of the important features of an electrolyte solution is the ionic strength (I).

$$\log \gamma_\pm = -A|z_+z_-|I^{1/2} \qquad \text{(Eq. 2.14)}$$

where,

$$I = \frac{1}{2}\sum z_i^2 m_i \qquad\qquad \text{(Eq. 2.15)}$$

z_i is the valence of the ion i and m_i is its molal concentration. (1, 8).

Understanding the concept of thermodynamic parameters is a fundamental step to interpretation of the Pitzer formalism (see section 2.1.5), which is the essential theory that applied for determining the solubility product of Burkeite in this study.

2.1.4 Solubility Product

2.1.4.1 Single and Multi-Electrolyte Solutions

The dissociation equation of the sparingly electrolytes in an aqueous solution is regularly demonstrated as:

$$A_{v_a}B_{v_b} \rightleftharpoons v_a A^{z_a+} + v_b B^{z_b-} \qquad\qquad \text{(Eq. 2.16)}$$

Where v_a and v_b are the stoichiometric coefficients, z_a^+ and z_b^- are the valencies of ion A and B separately. The solubility of these kinds of electrolytes always express with regard to the concentration solubility product, Ksp_c, which is a constant value (1).

$$K_{sp\_c} = c_+^{v_a} \cdot c_-^{v_b} \qquad\qquad \text{(Eq. 2.17)}$$

where $c_+^{v_a}$ and $c_-^{v_b}$ are the ionic concentration of each ion with the unit mol per litre. When the dissociation reaches its equilibrium at a constant temperature, the solubility product and equilibrium solubility (s^*) of the electrolyte have a relation as displayed in Equation 2.18. Therefore, for 1:1, 1:2 and 1:3 electrolytes the equilibrium solubility can be achieved according to Equations 2.19- 2.21 (1).

$$s^* = (K_{sp\_c}/(v_a{}^{v_a}v_b{}^{v_b}))^{1/(v_a+v_b)} \qquad\qquad \text{(Eq. 2.18)}$$

$$s^* = (K_{sp\_c})^{1/2} \qquad\qquad \text{(Eq. 2.19)}$$

$$s^* = (K_{sp\_c}/4)^{1/3} \qquad\qquad \text{(Eq. 2.20)}$$

$$s^* = (K_{sp\_c}/27)^{1/4} \qquad\qquad \text{(Eq. 2.21)}$$

However, the above discussion and equations are only applicable for the case of materials possessing extremely low solubility (less than 10^{-3} mol/L), since at very low concentration the activity coefficients of the dissolved ions in the solution are at unity (the number 1) (9). For solutions with a solute concentration greater than 10^{-3} mol/L, it is more accurate to involve the parameter activity α. Under this circumstance, the activity solubility product (K_{sp_a}) should be applied for the equilibrium solubility studies (1, 7).

$$K_{sp\_a} = \alpha_+^{v_a} \cdot \alpha_-^{v_b} \qquad\qquad \text{(Eq. 2.22)}$$

Where $\alpha_+^{v_a}$ and $\alpha_-^{v_b}$ are the activities of ion A and B. As Equation 2.8 shows, the activity often expressed as the product of ionic activity coefficient γ times ion molality m, therefore 2.22 can be re-written as **(7)**

$$K_{sp\_a} = (\gamma_a m_a)^{v_a} \cdot (\gamma_b m_b)^{v_b} \qquad\qquad \text{(Eq. 2.23)}$$

For a single solute system, when the concentration is smaller than 10^{-3} mol/L, the value of concentration solubility product (K_{sp_c}) is almost equal to the activity solubility product (K_{sp_a}). For a multi-electrolyte system, the activity and activity coefficient of every single ion can also be greatly influenced by other surrounding ions. So, even though the electrolyte studied had low solubility, there may still exist a significant difference between K_{sp_a} and K_{sp_c} (1).

2.1.4.2 Double Salt Dissociation and Its Solubility Product

For other types of strong electrolytes, double salts, the expression of its dissociation equation also follows the rules which were mentioned in the previous section. The formula of double salt and its hydrated form are known as $x(A_{v_a}B_{v_b})\cdot y(D_{v_d}E_{v_e})$ and $x(A_{v_a}B_{v_b})\cdot y(D_{v_d}E_{v_e})\cdot nH_2O$, where x and y are the stoichiometric constants, n is the number of moles of water in the hydration form (9). The dissociation equation at equilibrium is:

$$x\left(A_{v_a}B_{v_b}\right)\cdot y\left(D_{v_d}E_{v_e}\right) \tag{Eq. 2.24}$$
$$\rightleftharpoons xv_a A^{z_a+} + xv_b B^{z_b-} + yv_d D^{z_d+} + yv_e E^{z_e-}$$
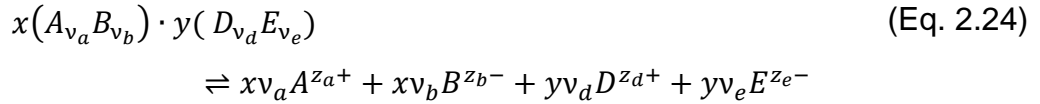
Here x and y represent the moles of the mother salts $A_{v_a}B_{v_b}$ and $D_{v_d}E_{v_e}$. So for a saturated solution the activity solubility product of the hydrated double salt is expressed as follows:

$$K_{sp\_\alpha} = (m_a)^{xv_a}(m_b)^{xv_b}(m_d)^{yv_d}(m_e)^{yv_e} \tag{Eq. 2.25}$$
$$* \left(\gamma_{A_{v_a}B_{v_b}}\right)^{x(v_a+v_b)} \left(\gamma_{D_{v_d}E_{v_e}}\right)^{y(v_d+v_e)} * (\alpha_w)^n$$

If the double salt is anhydrous, then the above equation does not involve the last term of $(\alpha_w)^n$. Gautier (2014) investigated the solubility product of hydromagnesite $Mg_5(CO_3)_4(OH)_2\cdot4H_2O$, the expression is given as below (10):

$$\tag{Eq. 2.26}$$
$$K_{sp\_a} = \alpha_{Mg^{2+}}^5 \cdot \alpha_{CO_3^{2-}}^4 \cdot \alpha_{OH^-}^2 \cdot \alpha_{H_2O}^4$$
$$= m_{Mg^{2+}}^5 \cdot m_{CO_3^{2-}}^4 \cdot m_{OH^-}^2 * \gamma_{Mg^{2+}}^5 \cdot \gamma_{CO_3^{2-}}^4 \cdot \gamma_{OH^-}^2 \cdot \alpha_{H_2O}^4$$

This theory will contribute to the later study of determining the solubility product of Burkeite ($Na_4(CO_3)_{0.61}(SO_4)_{1.39}$) in a complex slurry system.

2.1.5 Pitzer Theory

There are several thermodynamic approaches which have been utilised for solubility predictions for multi-electrolyte aqueous solutions. Most of these methods are constructed using the Debye-Hückel theory (11) and involve thermodynamic parameter production, such as activity coefficient γ, enthalpy H and entropies S of the solutions.

Normally, the activity coefficient was presented as a function of the ionic strength using the Debye-Hückel model for diluted solutions with low ionic strength (12). The Pitzer parameters are required for every single pair of ions (i.e. cation-cation, cation-anion and anion-anion) in the solution. All of the parameters are assumed to be independent of the ionic strength of the solution, however they all are temperature dependent (13). Pitzer's model has been recognised to be the comprehensive tool for achieving the activity coefficient of single or multi-component electrolyte solutions (14, 15). The model was derived based on the excess Gibbs free energy which is associated with the variation in osmotic pressure and the energy among the ions in the electrolyte solutions. The essential equations for achieving the thermodynamic parameters of an electrolyte solution were discussed by previous researchers for single electrolyte solutions and more complex multi-component systems (16) (17, 18) (19).

2.1.6 Particle Size Impact on Solubility

The relationship between particle size and solubility has been studied for more than a century. The decrease in the particle size of a solute will greatly increase its dissolution rate, due to the enlarged solid surface area in contact with the solution phase. The relationship was firstly revealed in the Noyes Whitney theory and modified by Nernst and Brunner (20) (21):

$$\frac{dm}{dt} = \frac{DA(s^* - s(r))}{h} \qquad \text{(Eq. 2.27)}$$

The term on the left of Equation 2.27 indicates the rate of the changing mass (m) over time t; on the right-hand side, D is the diffusion coefficient via a static layer (h) of the liquid, A is the effective surface contact area between solid particles and the solution, s(r) is the solubility of particles with the radius r, s^* standard solubility of the material.
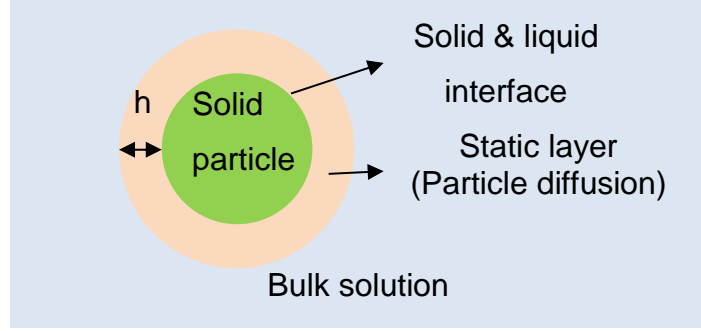
Figure 2.3: Noyes Whitney theory of particles diffusion in the solution

After that the Gibbs-Kelvin relationship was derived from theory and applied for vapour pressures in vapour-liquid systems in 1871 (1, 21). This model was then applied in crystallisation studies (i.e. Parfitt,1973 (22)).

$$\log \frac{P_r}{P_\infty} = \frac{2\gamma V}{rRT} \qquad \text{(Eq. 2.28)}$$

where V is the molar volume, R is the gas constant (8.314 J/(K·mol)), T is the absolute temperature.

Later on, Ostwald (23) applied to the solid-liquid systems and Equation 2.29 was given in the publication of Rawlins in 1977 (24):

$$\ln\left[\frac{s(r)}{s^*}\right] = \frac{2\gamma_i M}{v\rho rRT} \qquad \text{(Eq. 2.29)}$$

Here, M is the molar weight of the solid in the solution, γ_i is the interfacial tension of the solid in contact with the solution, v is the number of moles of the ions dissociated from 1 mole of the solid Equation 2.30, ρ is the density of the solid (1):

$$v = v_+ + v_- \text{ (for non} - \text{electrolyte } v = 1) \qquad \text{(Eq. 2.30)}$$

The kinetic study in section 5.3 was based on the importance of particle size influence on solubility determination and the dissolution process.

2.2 Phase Equilibrium and Phase Diagrams

2.2.1 The Phase Rule

A phase diagram would normally be required to understand the behaviour of a complex system over a wide range of pressures, concentrations and temperatures. This kind of diagram is generally represented in two or three dimensions, and indicates the equilibrium between different phases of a system.

The phase rule was developed in 1876 by J. Willard Gibbs **(25)**:

$$P + F = C + 2 \qquad\qquad\qquad \text{(Eq. 2.31)}$$

where P stands for total phases in a system, C is the minimum number of compounds required to express the composition of any phase, and F is the degree of freedom (26).

For instance, the Na_2CO_3 and water system, where 5 components may exist, i.e. $Na_2CO_3 \cdot H_2O$, $Na_2CO_3 \cdot 7H_2O$, $Na_2CO_3 \cdot 10H_2O$, Na_2CO_3 and H_2O. (27). But when applying the phase rule, there are only 2 components which will be taken into account, Na_2CO_3 and H_2O. The reason is that the composition of each phase can be expressed by the equation:

$$Na_2CO_3 + x\ H_2O = Na_2CO_3 \cdot xH_2O$$
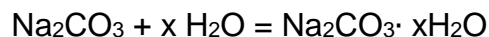
A phase must stay homogeneous in a system. Any mixture of gases will be counted as one phase. Any mixtures containing several entirely miscible solids or liquids are also regarded as one phase. However, for partially miscible or heterogeneous mixtures, it can be described as an n-phase system according to certain conditions.

Pressure, temperature and concentration are counted as the 3 basic variables for determining the number of degrees of freedom (F). If the changing of these variables is not going to alter the number or property of phases in an equilibrium system, then the freedom degree of this particular system is the number of these independent variables (25). For example, in a water vapour-

water-ice system, there are 3 phases in total (P=3), one component (C=1), so according to the phase rule, the degree of freedom F should be zero, which denotes without varying the number of phases, neither temperature nor pressure will be changed. This is called an invariant system. However, for the water and water vapour system, C=1, P=2 and F=1, which means one of the variables (i.e. temperature or pressure) may change without changing the nature of the phases. Such cases are known as uni-variant systems. By the same token, for the single phase water system, F=2, so both temperature and pressure can be changed independently without interfering with the number of phases, and this is called a bi-variant system (28).

2.2.2 One Component System

In a one component system only two variables can impact the equilibrium and these are pressure and temperature. A temperature-pressure equilibrium diagram is often chosen to describe this kind of system.

Figure 2.4 (left) shows the equilibria between the solid, liquid and solid phases of a single component. Curves AB and BC indicate the vapour pressure change as a function of the temperature for the solid and liquid phase, respectively. Line BD shows the influence of the pressure on the melting point of the solid. Some components possess more than one polymorph, such as in Figure 2.4 (right) the area ABEF and BCE illustrate the α solid exists as the stable form of polymorph 1 and 2, respectively. The curve AB and BC are the vapour pressure curves for these two solids individually and C is the melting point of polymorph 2. The dotted curve BE denotes the transformation temperature of the polymorphs changing with the pressure. The triple point E indicates an equilibrium state in between the two solid polymorphs and the liquid phase (26).

The dotted lines in Figure 2.4 stand for a metastable condition. For instance, BB' and BA' represent the metastable solid form of polymorph 1 and 2 separately. They are normally achieved in a rapid heating or cooling process. Similarly, CB' is the vapour pressure curve for the metastable liquid and B'E is the melting point line for the metastable polymorph 1. Therefore, B' is the metastable triple point where the liquid and vapour and solid 1 stay in equilibrium (26).

The transition between the polymorphs can be reversible and irreversible. Figure 2.4 (right) is the example of the former case. At Point B, these two crystals are co-existing and slow heating or cooling will lead a mutual transformation between them.
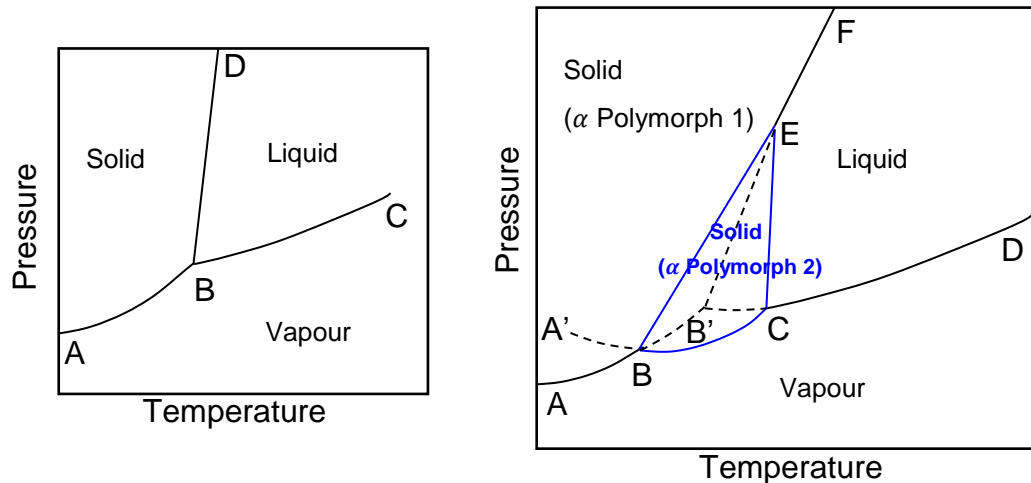
Figure 2.4: Phase diagram of a single component and its polymorph (reproduced from (26))

2.2.3 Binary System

In the two-component system there are three variables which can influence the equilibrium of the system, these are temperature, pressure and concentration. The phase diagram can be presented in 3D or 2D, however, the solid and liquid phase transition generally attract the attention, besides pressure only plays an inconsequential role in the solid-liquid system, therefore the phase diagram is normally expressed in a temperature-concentration scheme and the pressure will be considered to be atmospheric.
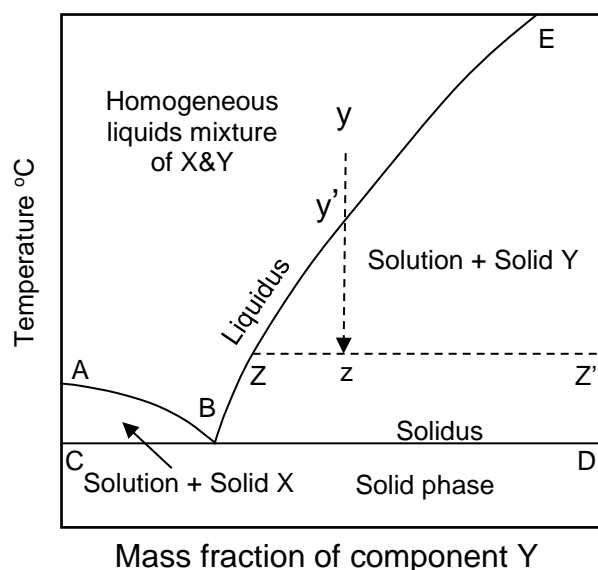
Figure 2.5: Phase diagram for a simple eutectic system, X&Y indicate two non-reacting components (reproduced from (26))

Figure 2.5 is the temperature-concentration phase diagram of two non-reacting components. The line CBD separates the phase diagram in two sections, below which line the mixture of X&Y are completely solid, above this temperature the solid mixture starts to melt. Point A and E are the melting or crystallizing point for X and Y, respectively. If a solution is cooled down from the y point, pure Y solid will begin to crystallise out when the temperature of the system reaches or goes below the liquidus curve BE. The over composition of the system remains the same, only the physical state of the system has been transformed. The ratio of the precipitated solid Y to the remaining solution follows the mixture rule, which is equivalent to the length ratio of zZ/zZ' (26).

2.2.3.1   New Compound Formation

In general, the solute and solvent or solvent and solvent will associate to generate new components, such as hydrates formed in an aqueous system or solvates in non-aqueous systems. Some of these new components will stay in a dynamic equilibrium in the solution that possesses the same composition, and others will disintegrate. These two cases are known to have congruent and incongruent dissolution points (26) (29).

Sodium carbonate water (Na_2CO_3-H_2O) and sodium sulphate water (Na_2SO_4-H_2O) systems contain both eutectic and incongruent points, but not congruent

points. They are both well-known to display inverted solubility behaviour after the incongruent points (see Figure 2.2 and Figure 2.6) However, when both sodium salts present in water with a certain molar ratio, a co-crystal would form in which case the congruent dissolution points can be found in the phase diagram, these will be discussed in full in the results section of this work.

In Figure 2.2, below 32.38°C the Na_2SO_4-H_2O system has two hydrate solids existing, which are the metastable form $Na_2SO_4 \cdot 7H_2O$ and the stable solid $Na_2SO_4 \cdot 10H_2O$. Points B and G are the eutectic points of the Ice-$Na_2SO_4 \cdot 10H_2O$-solution system and the Na_2SO_4-$Na_2SO_4 \cdot 10H_2O$-solution system separately. Point H is the incongruent dissolution point of the $Na_2SO_4 \cdot 7H_2O$. The curve CH represents anhydrous Na_2SO_4 crystals in the metastable equilibrium with the saturated solution. The area BCHG symbolises the single phase metastable solution of $Na_2SO_4 \cdot 7H_2O$. (1, 6, 26, 30, 31).
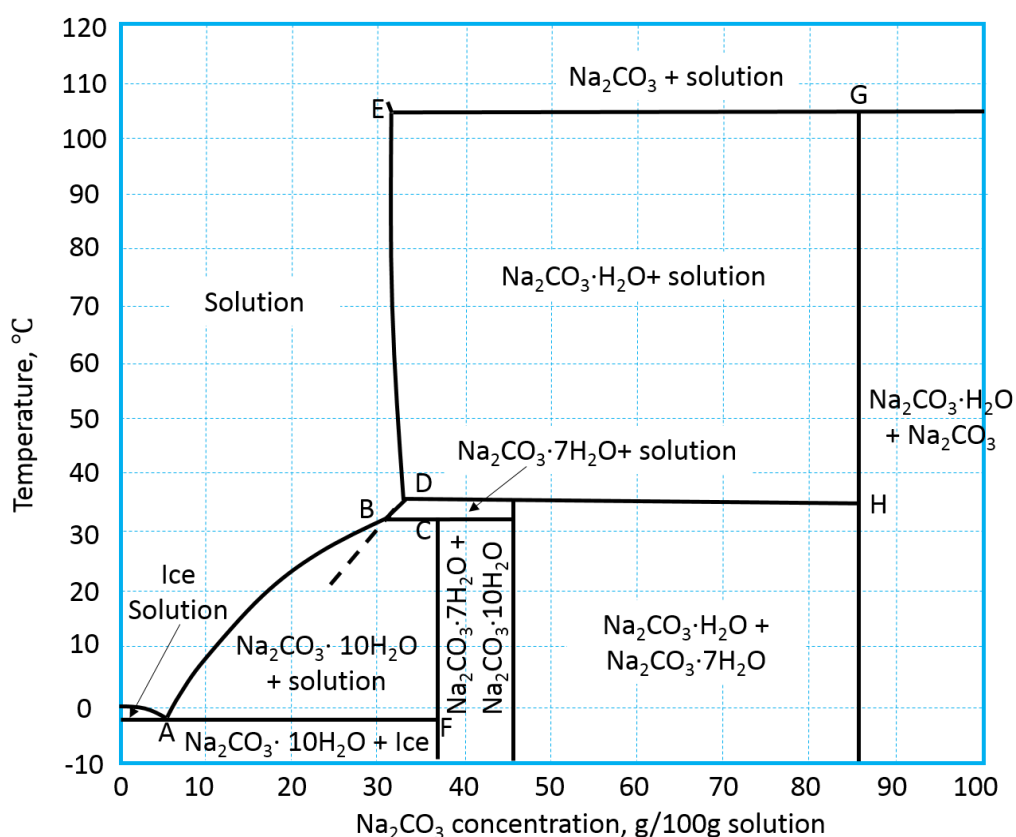
Figure 2.6: Temperature-concentration phase diagram of the Na_2CO_3-H_2O system (32-35)

Figure 2.6 indicates the phase behaviour of the Na_2CO_3-H_2O system in the range of -10 to 120°C. 0A is the freezing point curve, AB is the solubility curve of Na_2CO_3 decahydrate ($Na_2CO_3 \cdot 10H_2O$) solids. A is the eutectic point at which $Na_2CO_3 \cdot 10H_2O$ and ice would precipitate out as a solid mixture with a fixed composition. The CF line denotes the percentage of $Na_2CO_3 \cdot 10H_2O$ in mass. B, D and E are the incongruent dissolution points or the transition points, which represent the decomposition of a high degree of hydrated crystals to the lower degree of hydrates or even anhydrous solids. The monohydrate ($Na_2CO_3 \cdot H_2O$) is the most stable salt in the range between 35.4 and 107.3°C (26, 35).

2.2.3.2   Solid Solutions

When a temperature change apply to a homogeneous liquid phase, which contains two or more components, if no single component precipitates as a pure solid phase at any stage, then the deposited solid mixture would be known as a solid solution (26, 36).

Figure 2.7 gives two examples of the solid phase diagram of a binary system. In Figure 2.7a, point A and B represent the melting or dissolution points of two components, respectively. Any liquids or melts that are above the liquidus line are homogeneously mixed; any systems below the solidus line are fully solidified into one phase. The liquid and solid solution are equilibrium in the mixtures that are located in the closure AB area. For instance, A mixture X contains a liquid with the composition of L and a solid solution of composition S, moreover any points on the LS line possess the some composition of liquid and solid solution. Therefore, if a slow cooling process is applied to the liquid A, the first crystal would deposit with the solid composition of S, when the temperature reaches the L point. Along with the temperature decreasing in the future, more crystals would precipitate with the changing solid composition that follows SS'. Beyond point S' the entire system becomes solidified.

In Figure 2.7 b, there are 3 melting points, A, B and E. At point E, the solid solution precipitates with a certain composition, the crystals ideally should have the same structure with the identical composition; therefore E is not a eutectic point.
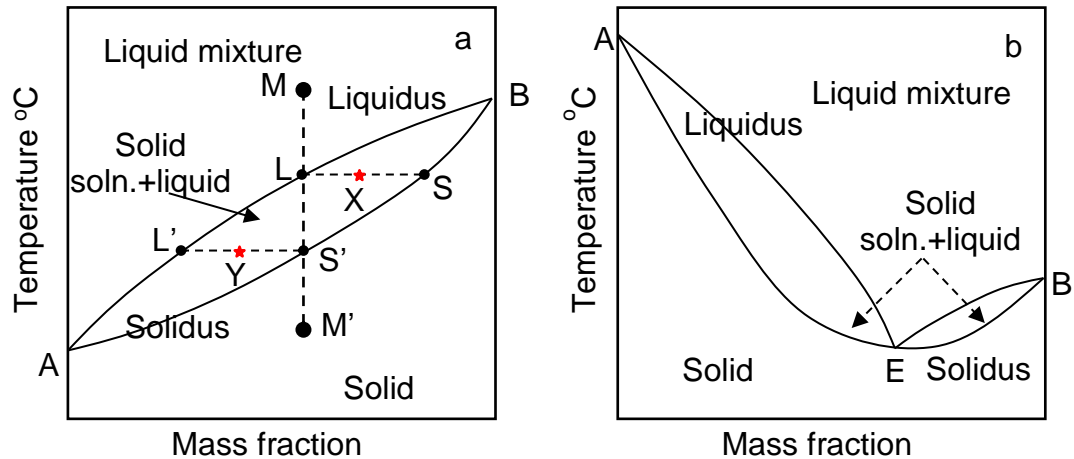
Figure 2.7: Solid solution phase diagrams of a binary system (reproduced from (26))

2.2.4 Equilibrium of a three-compound system

2.2.4.1 Eutectic Formation

A temperature-concentration space diagram can also be applied to represent the equilibrium relationships for a three compound system. Figure 2.8 shows a ternary system, A, B and C represents three compounds, respectively. Assume that there is no mutual interaction among these three materials, for the purpose of simplifying the explanation of understanding. Points A', B' and C' are the melting points of each pure component. The vertical edges represent temperature, and AB, BC and AC illustrate the concentration of each binary system.

Figure 2.8 (b) shows the projection of the curve FD, ED and DG in Figure 2.8 (a) on to the triangular base. Three apexes represent the pure components and the melting points of them, separately. Points F, E and G represent the eutectic points of three binaries, and point D stands for the eutectic point of the ternary system. Curve FD, ED and GD separate the diagram into three regions that represent the three liquid states, respectively. The temperature falls from either the apexes or sides of the triangle to point D, in addition some of the isothermal curves are showing on the diagram, therefore the composition of a ternary mixture can be speculated when the cooling process takes place.
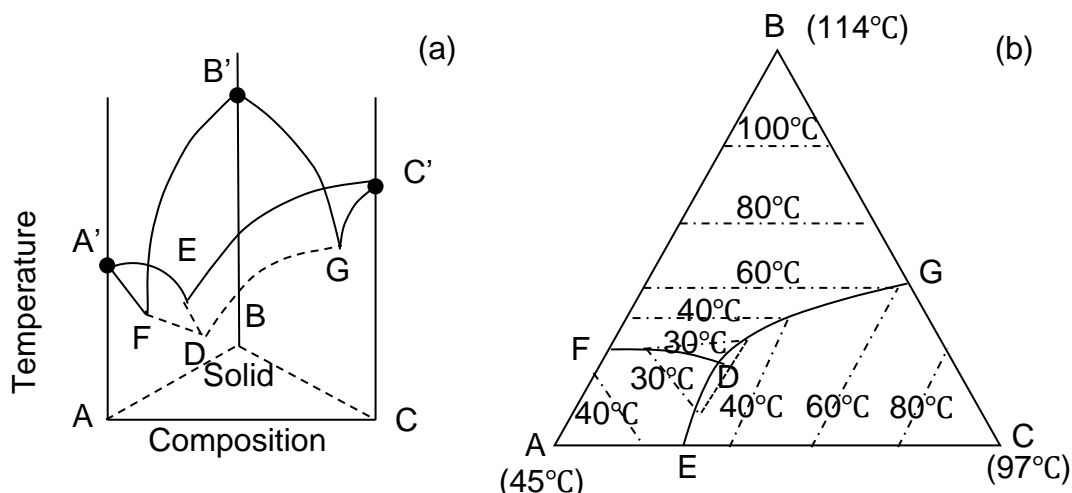
Figure 2.8: (a) temperature-concentration space diagram for a three-compound system; (b) projection on a triangular diagram (Reproduced from [5])

2.2.5 Two Salts and Water System

There are various kinds of phase behaviour which come across with respect to a mixture of water and two salts. For instance: no new substance formations, solvate formations, double salt formations or hydrated double salt formations. Consolidation of the knowledge on the configuration of phase diagrams will assist in determining the ternary phase diagram of Na_2CO_3 and Na_2SO_4 solution system, which is the essential step of this research.

2.2.5.1   No Substance Formations

The composition of this kind of mixture is very easy to analyse along with temperature variation, since neither the salt hydrate formations nor chemical reactions occur. The phase diagram (Figure 2.9) has some similarities with Figure 2.8 (b). C and E are the water solubility points of salts A and B at a constant temperature, correspondingly. So, curve CD and ED represent the composition of a saturated ternary mixture in equilibrium with salt A and B. Region H_2O-C-D-E is homogeneous solution under the saturated state. Point D is the eutectic point, at this point the solution is saturated regarding to both salts.
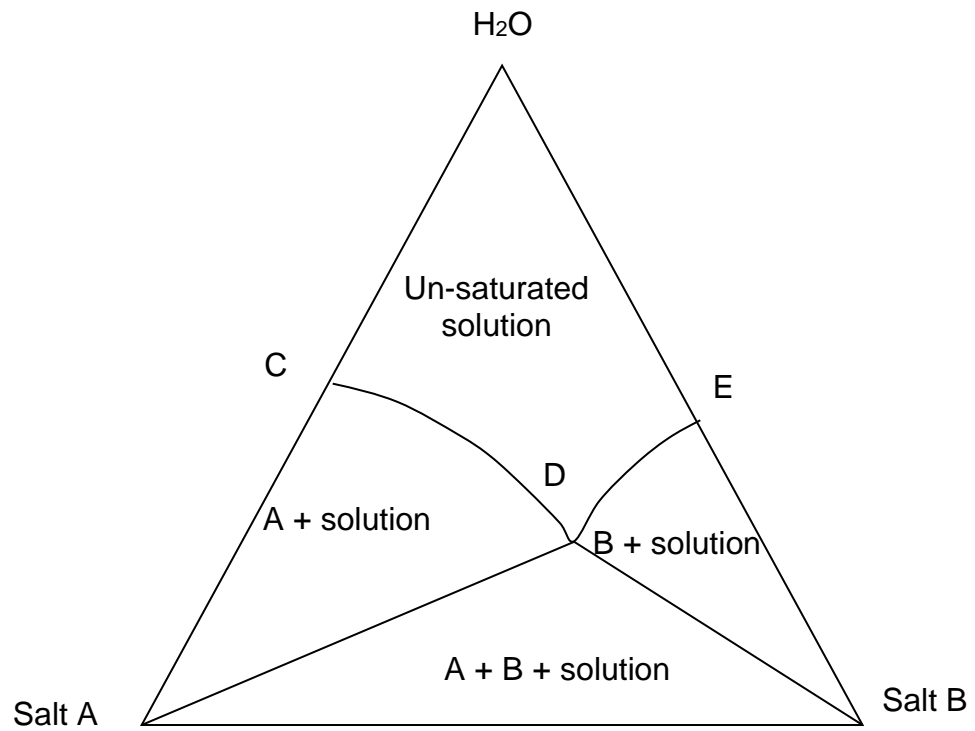
Figure 2.9: Phase diagram for the system A-B-H$_2$O at a certain temperature (reproduced from (26))

2.2.5.2 Solvate Formation

When solutes can generate new compounds with the solvent, the phase diagram, therefore, will be expressed in more regions. For example Figure 2.10 shows isothermal diagrams for the ternary aqueous system NaCl-Na$_2$SO$_4$-H$_2$O at two different temperatures, 17.5℃ and 25℃.
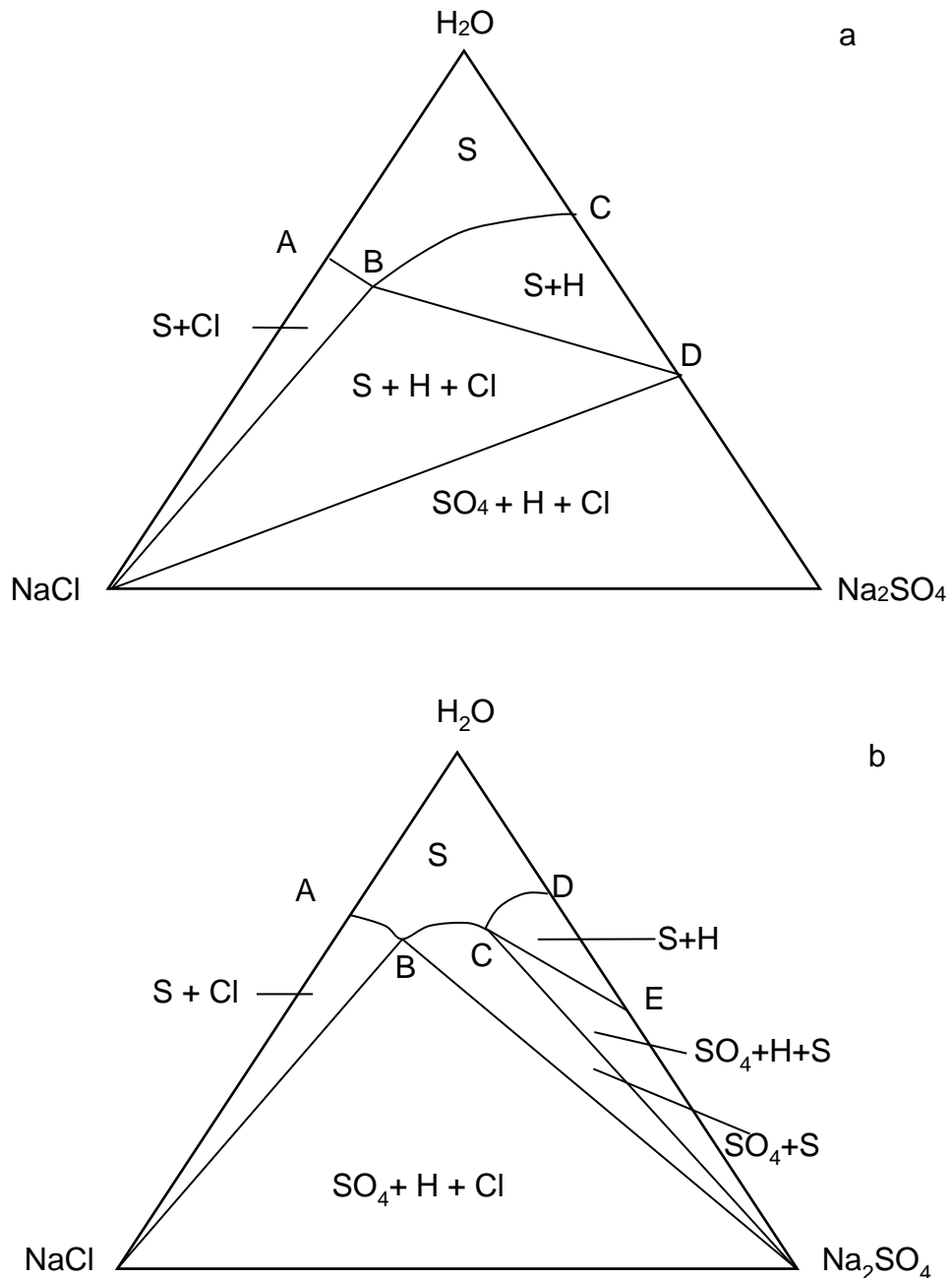
Figure 2.10: Isothermal phase diagram for the system of NaCl-Na$_2$SO$_4$-H$_2$O :(a) at 17.5℃; (b) at 25℃ (S means solution; H means hydrate Na$_2$SO$_4$·10H$_2$O; SO$_4$ and Cl indicate Na$_2$SO$_4$ and NaCl, respectively) (reproduced from (26))

Points A and C in graph (a) are the solubility of NaCl and Na_2SO_4 in water at 17.5℃. B is the eutectic point. AB and BC stand for the equilibrium states of NaCl and $Na_2SO_4 \cdot 10H_2O$ solid phase with respect to the solution. Point D gives the composition of $Na_2SO_4 \cdot 10H_2O$. The solution stays unsaturated in the region of A-B-C-H_2O.

A similar description can be applied to Figure 2.10 (b). Points A and D represent the solubility points of these two compounds under a temperature of 25℃ aqueous solution. E denotes the composition of hydrate in this case. Curves AB, BC and CD are equilibrium curves for component NaCl, Na_2SO_4 and $Na_2SO_4 \cdot 10H_2O$, individually. Point B is also the eutectic point, at which the solution is saturated regarding salt NaCl and Na_2SO_4. At point C, the only way can facilitate the excessed NaCl dissolving is to dehydrate $Na_2SO_4 \cdot 10H_2O$, then remove the precipitated Na_2SO_4 from the system. If NaCl kept being added this would cause the entire hydrate forms of Na_2SO_4 to withdraw from the system.

2.2.5.3   Double Salt Formation

In this case, the two dissolved components are going to associate in a fixed, or a range, of proportions to generate a new compound which is called double salt. Figure 2.11 denotes the phase diagram template for the system of aqueous solution with two soluble materials. Figure 2.11 (a), A and B are two soluble salts; D represents the composition of the double salt that formed from raw materials A and B. A system on the HE line behaves as a solution of a single salt in water. Once the composition of the system reaches E, then the mixture of raw material A and double salt D precipitates out in a fixed proportion that is equal to the lengths of DI/AI. Likewise, as soon as the system reaches point F, a mixture of B and D precipitates with a fixed proportion of DJ/JB. Curves CE and FG illustrate ternary solutions saturated with raw material A and B separately. E and F are the eutectic points. The curve EF is the equilibrium curve between saturated solutions and the double salt D, which means beyond this curve the double salt will be the only solid phase crystallised out. A different case is illustrated Figure 2.11 (b), the line HD crosses the saturation curve FG instead of EF that indicates the double salt is not a stable form in water. It will decompose and salt B will be precipitated.

(a)

(b)
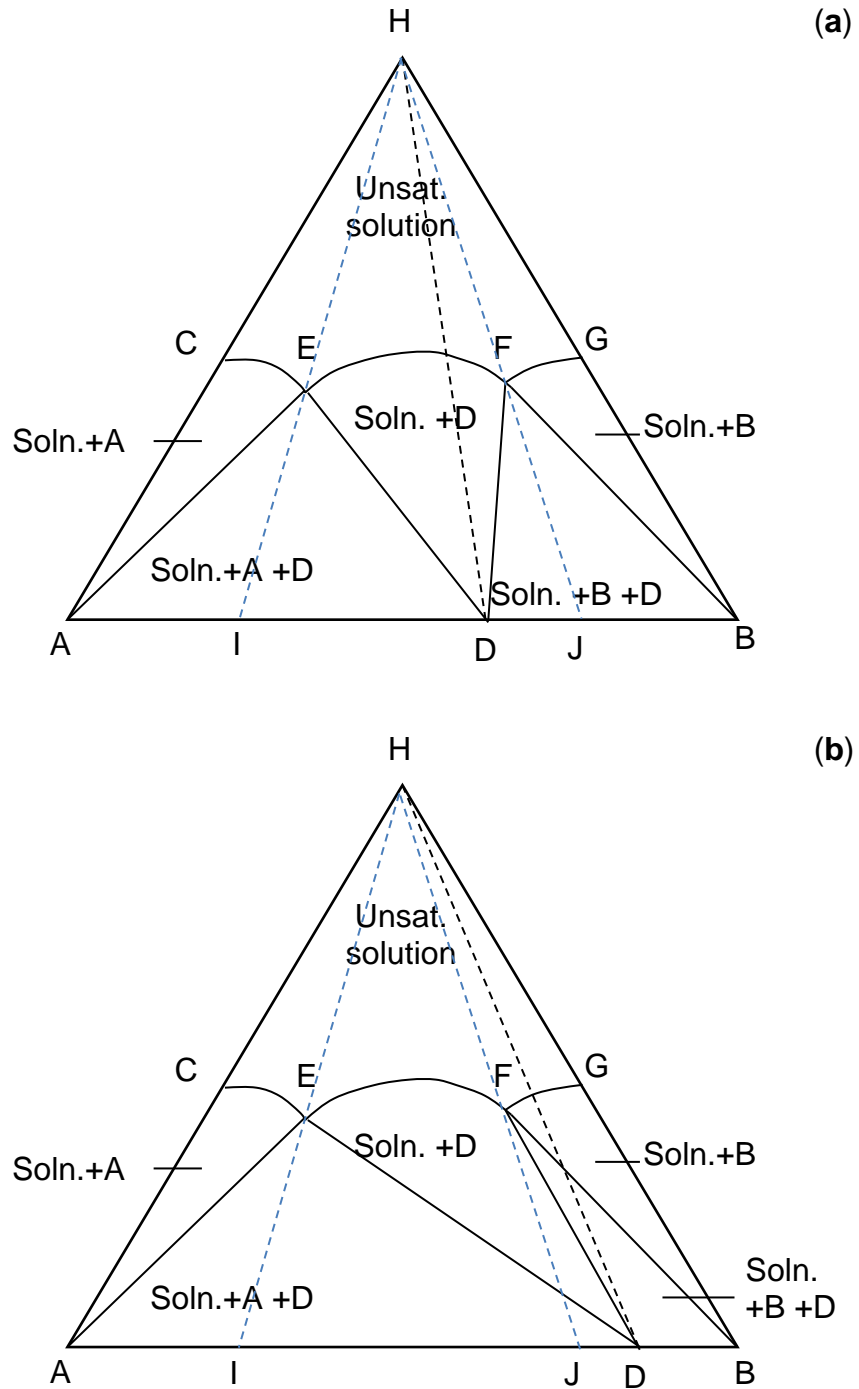
Figure 2.11: Phase diagram of double salt formation: (a) double salt stable in water; (b) double salt decomposed in water. (Unsat. = Unsaturated; Soln. = solution) (reproduced from [5])

Figure 2.12 was reproduced from the literature [8] and used as an example to illustrate the variation on the ternary phase diagram presentation of a system where new component(s) formed after mixing two raw materials. Curves BH, HD and DE separate the triangle mainly into four parts; the top region is the

unsaturated solution area. Curve BH and DE illustrate the equilibrium of solution with solid Na_2CO_3 and Na_2SO_4, respectively. While HD denotes the equilibrium state between solutions and newly formed double salt Burkeite. Normally, the composition of Burkeite is defined as 2 molars of Na_2SO_4 to 1 molar of Na_2CO_3. However, practically Burkeite can be formed in a range of molar ratios between Na_2SO_4 and Na_2CO_3. Stanley and Francis (1946) (37) indicated that the ratio should be around 1.4-2.2, but in 2003 Shi and Rousseau (38) clarified that 1-1.8 should be the ratio to form Burkeite. Due to the uncertain composition of Burkeite, therefore in Figure 2.11 there is a range (FG) to express the formation of the double salt.
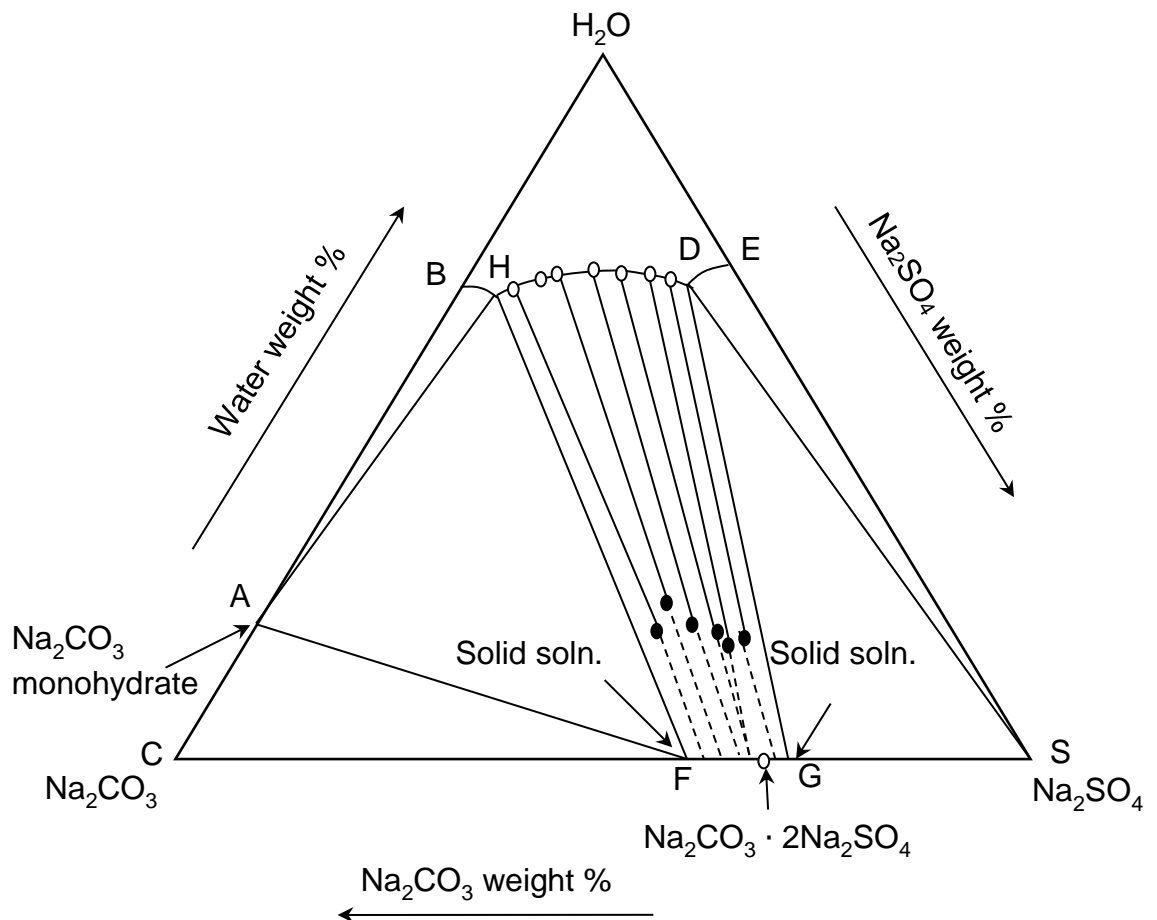
Figure 2.12: Phase diagram of Na2SO4-H2O-Na2CO3 system at 100°C; ○ , saturated solution; ● , wet residues [8].

2.2.5.4   Hydrated Double Salt

Figure 2.13 shows the phase diagram for a hydrated double salt formation in the water solution. However, this case will not be discussed in detail here due to the double salt Burkeite having no hydrate forms in this research. A more detailed explanation can be found in Mullins' crystallization book [5].
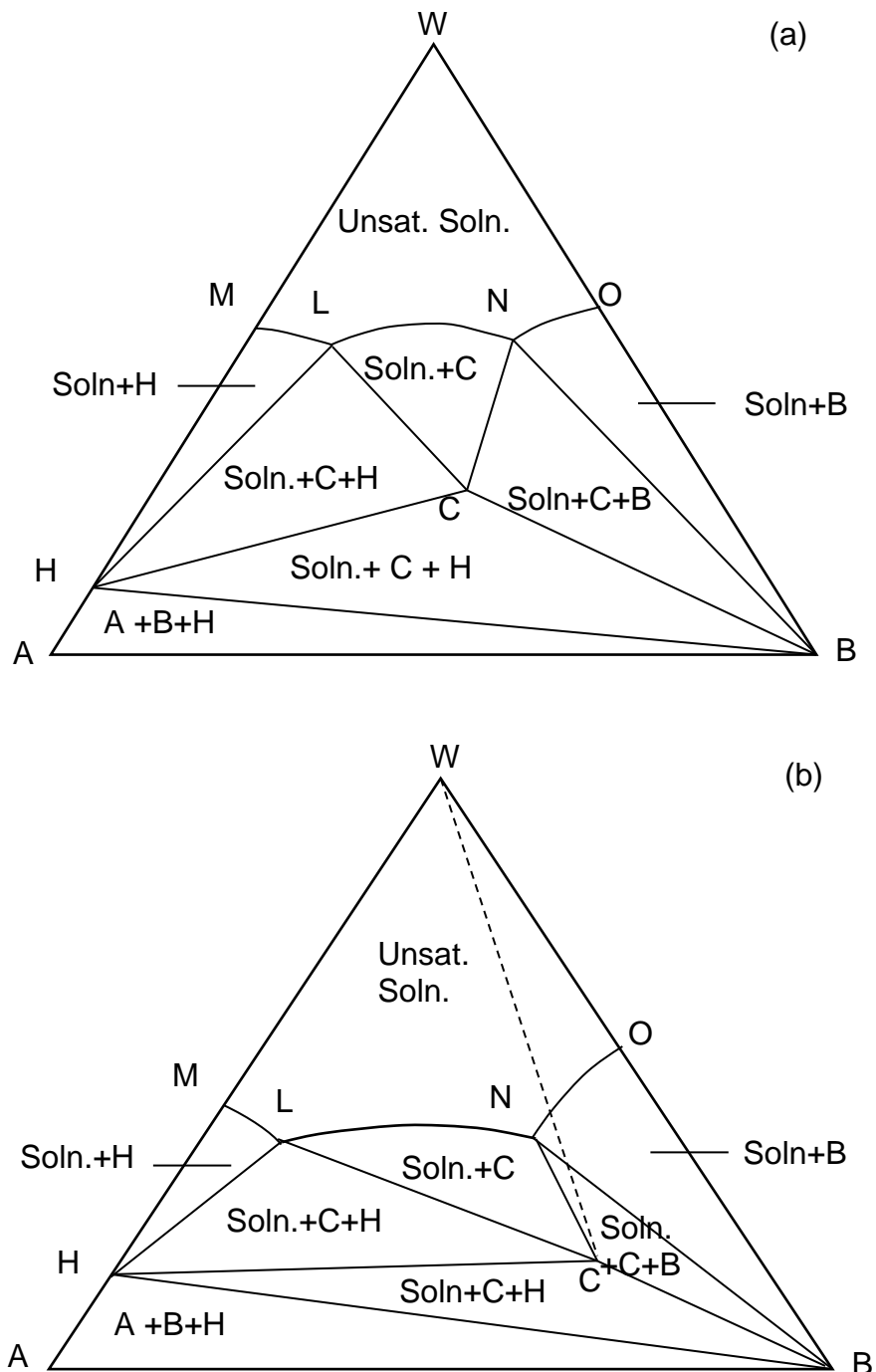
Figure 2.13: Phase diagrams of hydrated double salt formation: (stable in water), (b) decomposed by water (reproduced from [5])

2.3 Crystallisation

2.3.1 Solubility Metastable Zone Width (MSZW)

In most cases the solubility curve of a compound has the tendency that solubility increases with temperature, however it is also possible for a compound to have an inverse solubility, such as Na_2SO_4 and Na_2CO_3 that has been focused on in this study.Figure 2.14 illustrates the case of a system with the feature of an inverse solubility.

For an un-saturated solution, A (Figure 2.14) either increases the temperature or the concentration of solute(s), the system will move toward to the saturated states, where the points B & F are. With further increasing either or both of these two variables (temperature and concentration), the solution will enter into the metastable area and, eventually, a supersaturated state will be approached.   It is impossible for crystallisation to occur in unsaturated conditions, not to mention crystal growth. However, once the system has developed above the solubility limit and entered the metastable area (i.e. point C), then the crystallisation process can be induced by adding seeds into the solution. However, the spontaneous crystallisation still cannot happen in the metastable region. But, the process will start when the system reaches the metastable limit (i.e. point D). Beyond the metastable limit is identified as the precipitation area, where large amount of crystals will deposit from the solution rapidly (39).

MSWZ can be affected from several aspects, for instance (28) (40):

- Saturation temperature;
- The rate of achieving the supersaturation;
- Impurity type and concentration;
- Agitation speed, also the type of impeller;
- Solution thermal history;
- Size of crystallizer.
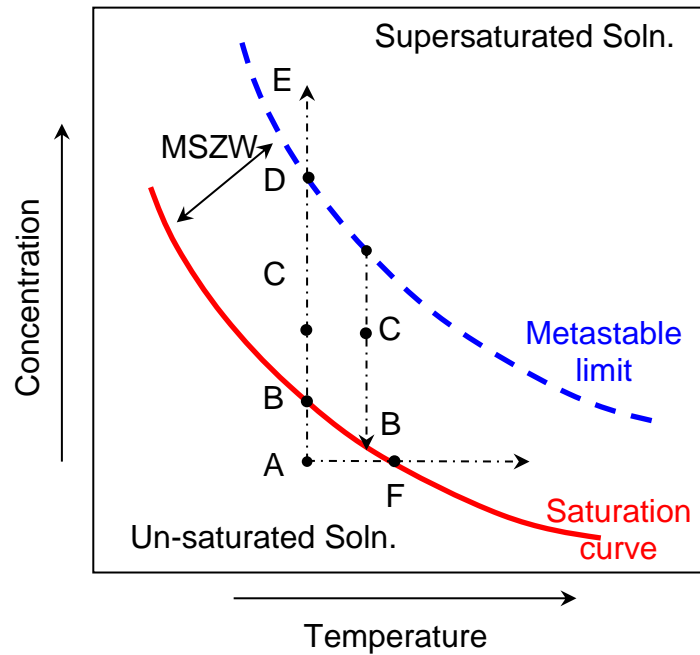
Figure 2.14: A solution system with inverse solubility [8]

The evaporation crystallisation method is utilized based on the theory of solution saturation and metastable limits. Solution evaporation results in an increased concentration, therefore pushing the system goes beyond the metastable limit to induce nucleation and crystallisation. In order to generate the favoured crystals, sometime manipulating the experimental conditions is necessary, such as altering the cooling or evaporation rate.

2.3.2 Nucleation

Nucleation theory is the first principle that has to be understood for any crystallisation process (41). It is a process of generating a small solid phase from the supersaturated uniform mother liquid phase, in our case the mother liquid is Na_2CO_3-Na_2SO_4 aqueous solution. During the process, bonds were generated between molecules. In other words, a nucleation can be seen as a bulk of molecules assembled by the weak intermolecular force and packed in the regular sequence to form small clusters. In order to nucleate, a supersaturated solution is required, and the size of clusters depends on the supersaturation degree (41). A supersaturated solution is like a metastable zone; nucleation does not always occur spontaneously within it. However, by continuously increasing the supersaturation level eventually the nucleation

event will happen spontaneously (42). It is vital to control the nucleation process so as to obtain the desirable crystal properties, for instance the amount of final crystals, their size distribution, crystal polymorphism and so on (43). A fast nucleation process causes the precipitation of many crystals with a narrow particle size distribution.

In general, certain experimental operations, for instance agitation, friction or high pressures, will trigger or accelerate the nucleation process. The mechanism of nucleation is normally expressed in two ways: progressive nucleation (PN) or instantaneous nucleation (IN). In the former case, new crystal nuclei are constantly generated in the presence of the already growing ones (44, 45). The nucleation event will last over a period of time, and it occurs simultaneously with the crystal growth, therefore the solution contains a poly-distribution in the particle size at any point. In the latter case, all nuclei precipitate simultaneously at the beginning of the crystallisation event and subsequently grow at the same rate and develop into same size of crystals. (44, 46) In general, this is followed by the heterogeneous mechanism which is preferred when nucleation active sites exist, such as impurities or foreign particles. A summarising scheme is illustrated in Figure 2.15.
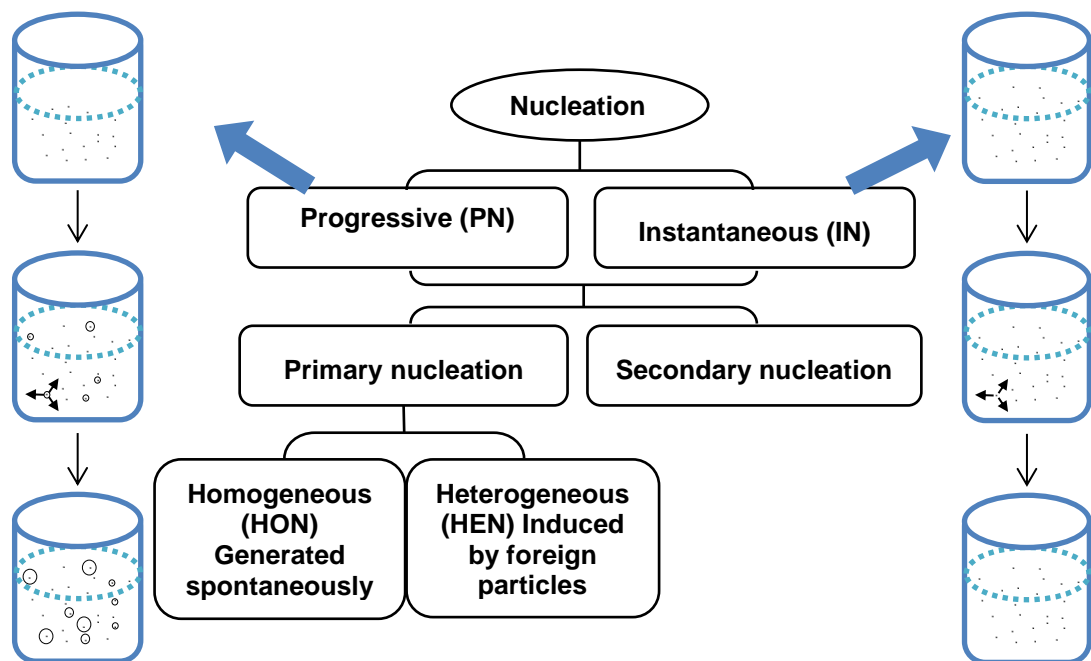
Figure 2.15: Classification of important nucleation mechanisms (47).

Primary nucleation can be obtained from systems without any initial crystalline content. Whereas, secondary nucleation can only occur from supersaturated solutions in which crystals have already existed (28). This type of nucleation normally takes place at a lower supersaturation compared with the primary nucleation, when the crystals of the solute have already existed in the solution, or they were added in to the system intentionally (28, 48). This phenomenon can be found in the continuous crystalliser.

There are several of reasons which may lead to secondary nucleation. For instance, seeding, small crystals are induced in the supersaturated solution (48). This method is commonly applied in the crystallisation process in industry for the purpose of controlling particle size and their distribution (28). Besides, some shapes of crystals are very fragile (i.e. thin needle shape crystals), therefore the broken pieces of crystals may perform like the seed/(secondary nuclei) and lower the interfacial tension to encourage nucleation to occur. Apart from the seeding mechanism, secondary nuclei can also be aroused by the shearing force between crystals and the flowing solution, or the contacts between the new crystals and their surroundings, such as the wall of the reactor, impeller or other crystals generated from nucleation (48).

The rate of a nucleation event depends upon many factors such as the degree of solution superstation, the concentration of crystals in the suspension (M_T) and the fluid dynamics between crystals and the solution. Therefore, Equation 2.32 was developed for predicting the secondary nucleation rate **(48)**.

$$B = k_b M_T^j N^k \Delta c^b$$ (Eq. 2.32)

where, B denotes the rate of the secondary nucleation;

k_b the value of a specified function of the reactor geometry, usually between 2 and 4;

N stands for either the measurement of the fluid mechanics' interactions, or the average power input into the reaction.

Δc illustrates the supersaturation.

Roger Davey and John Garside (2000) (48) concluded that the secondary nucleation rate is a product of three functions. Firstly, it presents the rate at which the energy is conveyed to crystals via a collision. Secondly, it indicates the number or the size distribution of fragments achieved in every unit of the conveyed energy. The last function is considered as a survival item, which describes the amount of the fragments that remain to turn into nuclei and grow to count a size distribution (48).

2.3.2.1 Homogeneous Nucleation

Crystallisation will occur when the surrounding environment changes, such as cooling (or heating), evaporation or adding another solvent to reduce the solubility of the solute in the supersaturated solution. Small particles will therefore appear and grow to macroscopic size due to local density changes (homogeneous nucleation) (49). This kind of nucleation occurs spontaneously without any interference from foreign particles, it does not however occur very often in practice due to the unavoidable impurities.

Because of the random movement of the particles in a supersaturated solution, particles will be bonded into various sized clusters, smaller ones normally will soon disintegrate and the larger ones will grow even larger to form an embryo (Ostwald ripening (50)). From this point onwards, particles begin to arrange in regular lattices, eventually organised into a new separated phase.

Thermodynamics of nucleation
To understand the thermodynamics of a nucleation event it is probably better to correlate the free energy changes with the nucleus formation (28, 51), here assuming that all nuclei are presenting in a spherical shape:

$$\Delta G = 4\pi r^2 \gamma + \frac{4}{3}\pi r^3 \Delta G_v \qquad \text{(Eq. 2.33)}$$

where, ΔG is the overall excess free energy between the solute in solid form and the solute in the solution. r represents the radius of the particle. γ is the interfacial tension or surface energy, which is located on the surface between the newly formed crystal and the supersaturated solution. ΔG_v is the free energy change per unit volume. The excess energy from the overall surface and volume of the particle attribute to the term $4\pi r^2 \gamma$ and $(4/3)\pi r^3 \Delta G_v$ respectively. The former term has a positive value and increases proportionally to r^2. The latter one is the negative term that decreases as a

function of r^3. Therefore, the total free energy ΔG must have a maximum value as indicated in Figure 2.16, where the critical nucleus size r* is defined, in the system if nuclei are smaller than r* they will dissolve back into the solution, on the other hand nuclei will keep growing to reduce the overall free energy in the system (28).
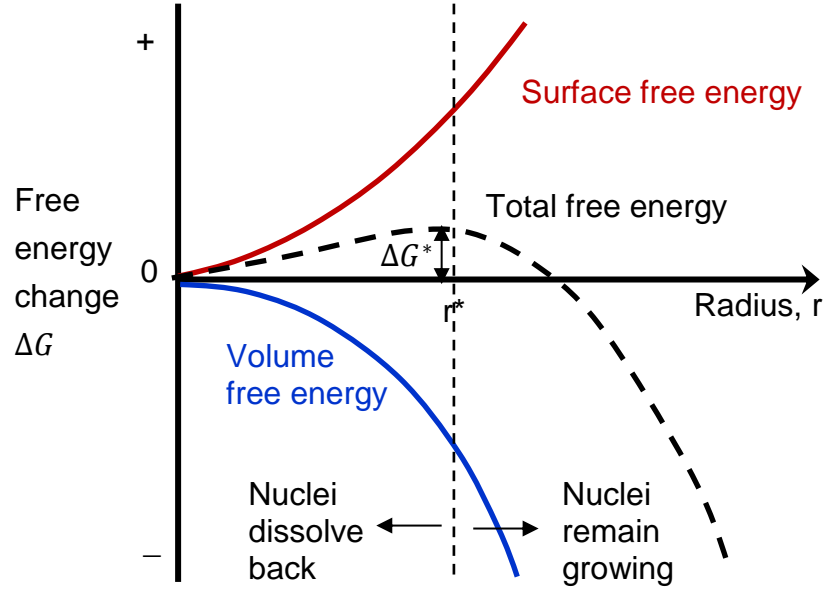
Figure 2.16: Free energy variation in a nucleation event (28).

An equation can be used to describe the critical nuclei size at the maximum free energy point by differentiating Equation 2.33, and defining the term on the left of the equation to zero, then it will obtain the relationship as in Equation 2.34 (28, 52).

$$\Delta G^* = \frac{16\pi\gamma^3}{3(\Delta G_v)^2} = \frac{4\pi\gamma r^{*2}}{3} \qquad \text{(Eq. 2.34)}$$

(28, 52)

If considering the relation between particle size and solubility in a solid-liquid system:

$$\ln\frac{s}{s^*} = \ln S = \frac{2\gamma v_0}{kTr} \qquad \text{(Eq. 2.35)}$$

(28, 47)

Then:

$$\Delta G^* = \frac{16\pi\gamma^3 v_0{}^2}{3(kT\ln S)^2} \qquad \text{(Eq. 2.36)}$$

(27)

where k is the Boltzmann constant ($1.3805*10^{-23}$ J/K) and v_0 is the molecular volume.

According to the Arrhenius reaction velocity equation and combining with Equation 2.36, the rate of nucleation J can be expressed as:

$$J = k_j exp\left(-\frac{\Delta G}{kT}\right) = k_j exp\left[-\frac{16\pi\gamma^3 v_0{}^2}{3(kT\ln S)^2}\right] = k_j\exp[\frac{-B}{(\ln S)^2}] \qquad \text{(Eq. 2.37)}$$

(28, 47)

here, k_j is an empirical parameter (47).

Kinetics of nucleation

According to the Szilard mechanism, the nucleation happens with regard to the dynamic process of a single molecule attaching and detaching from clusters with the size n, where n represents a cluster of n molecules (n=1,2,3…) (28, 53).

Therefore, the kinetics of nucleation can be considered as the attachment (f (n)(s^{-1})) and detachment (g(n)(s^{-1})) frequencies of the single molecule. The process can be expressed as nucleation rate J ($m^{-3}s^{-1}$), the difference in the frequency of transformation from a n* sized cluster to a n*+1 sized cluster, see Equation 2.38 (53).

$$J = f(n^*)C(n^*) - g(n^* + 1)C(n^* + 1) = zf^*C^* \qquad \text{(Eq. 2.38)}$$

where, $C(n)$ is the time dependent stationary concentration of n sized clusters; z is the Zeldovich factor (53).

2.3.2.2   Heterogeneous Nucleation

Heterogeneous nucleation, is another way to precipitate crystals, where impurities act as starting points for nucleation in the supersaturated solutions. Under such conditions the nucleation occurs relatively fast compared with spontaneous nucleation, and the rate of nucleation certainly determines both the amount and the particle size of the nuclei generated, as discussed above.

2.3.3 Approaches to Evaluate Nucleation Kinetics

The determination of MSZW of the material studied is the essential step for investigating crystallisation, through which some of the important parameters can be inferred, such as crystal size (and distribution) and crystal shape. Operational temperature, solution type, cooling or heat rate, impurity and mechanical variation all have impact on defining MSZW (54). It can be determined either by changing the system temperature or concentration; the former one is generally applied. In this case, the MSZW is expressed as the solution critical undercooling for crystallisation (ΔT_C), which is the difference between the solution equilibrium temperature (T_e) and the detectable crystallisation temperature (T_c) (51).

$$\Delta T_C = T_e - T_c \qquad \text{(Eq. 2.39)}$$

Isothermal (47) and polythermal (47, 51, 55) methods are the two common ways that have been used in nucleation studies, both applied the concept of metastablility. Other methods are all based on the concept of these two and were reviewed in detail by Diana M.C.C. (51).

The recently developed nucleation kinetics method KBHR has overcome this drawback. It is based on the Kolmogorov-Johnson-Mehl-Avrami (KJMA) theory, which derived the relation of ΔT_c and q at the beginning of the nucleation, considered the concept of the fraction of crystallised volume and the number of nucleated crystallites. In addition, it also helped to determine the mechanism of a nucleation event by differentiating between progressive nucleation (PN) and instantaneous nucleation (IN) (51). In Chapter 5, this KBHR method will be modified and applied to the kinetic study of Burkeite under the current experimental conditions.

2.3.4 Crystals and Crystallography

2.3.4.1   Basic Crystallography

The crystal lattice can be considered as being infinite in distance with a three dimensional order. A single crystal can then be considered as a crystalline solid possessing 3-D order developed from the microscopic proportionally to the macroscopic. A unit cell was defined as the primary unit of any crystal lattice, it repeats in three dimensions to create specific crystal structures. The

crystal lattice is normally expressed in three vectors a, b and c and three angels α, β and γ, the spatial structure that they form is displayed in Figure 2.17 (56).
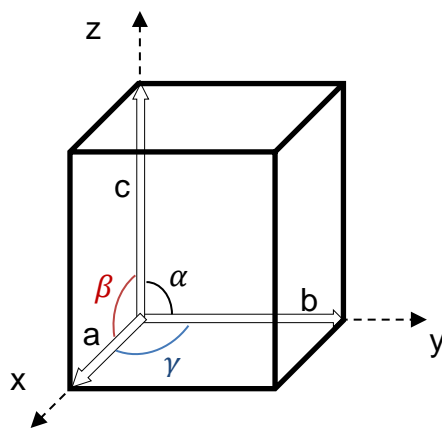
Figure 2.17: A crystal lattice

Crystals have anisotropic features, the growth and dissolution rate are face dependent due to each face containing different chemical groups. However, these properties can be changed by involving other molecules in the lattice. Crystals can exist in various forms such as cubic, octahedron and tetrahedron, which depended on the repeating lattice and symmetry factors (i.e. point, axis or plane).(57) In 1848, A. Bravais and M. L. Frankenheim (58) found that there are only 14 different lattice types and they named them Bravais lattices Figure 2.18 gives all the Bravais lattices classified into 7 groups.
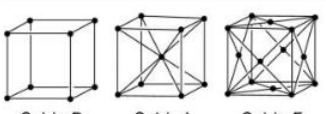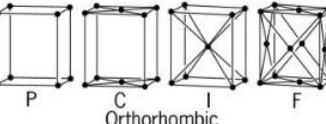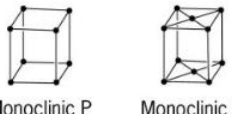
Bravais lattice cells	Axes and interaxial angles	Examples
Cubic P, Cubic I, Cubic F	Three axes at right angles; all equal: $a = b = c; \alpha = \beta = \gamma = 90°$	Copper (Cu), silver (Ag), sodium chloride (NaCl)
Tetragonal P, Tetragonal I	Three axes at right angles; two equal: $a = b \neq c; \alpha = \beta = \gamma = 90°$	White tin (Sn), rutile (TiO_2), β-spodumene ($LiAlSi_2O_6$)
Orthorhombic P, C, I, F	Three axes at right angles; all unequal: $a \neq b \neq c; \alpha = \beta = \gamma = 90°$	Gallium (Ga), perovskite ($CaTiO_3$)
Monoclinic P, Monoclinic C	Three axes, one pair not at right angles, of any lengths: $a \neq b \neq c; \alpha = \gamma = 90° \neq \beta$	Gypsum ($CaSO_4 \cdot 2H_2O$)
Triclinic P	Three axes not at right angles, of any lengths: $a \neq b \neq c; \alpha \neq \beta \neq \gamma \neq 90°$	Potassium chromate (K_2CrO_7)
Trigonal R (rhombohedral)	Rhombohedral: three axes equally inclined, not at right angles; all equal: $a = b = c; \alpha = \beta = \gamma \neq 90°$	Calcite ($CaCO_3$), arsenic (As), bismuth (Bi)
Trigonal and hexagonal C (or P)	Hexagonal: three equal axes coplanar at 120°, fourth axis at right angles to these: $a_1 = a_2 = a_3 \neq c;$ $\alpha = \beta = 90°, \gamma = 120°$	Zinc (Zn), cadmium (Cd), quartz (SiO_2) [P]

Figure 2.18: The fourteen Bravais lattices (P: Primitive; C: Side-centred; F: Face-centred; I: Body-centred) (58).

2.3.4.2   Miller Indices

Crystal faces and lattice planes can be expressed in terms of the intercepts on the axis (i.e. a, b and c) (see Figure 2.17). The former one is strongly related to the physical and chemical properties of the materials. The Lattice planes can be detected and determined by XRD analysis, which helps to reveal the crystal structures. In 1839, Miller (27) introduced a way of describing crystal faces by using indices h, k and l, which were expressed as:

$$h = \frac{a}{X}, k = \frac{b}{Y} \ and \ l = \frac{c}{Z} \qquad \text{(Eq. 2.40)}$$

An example is given in lattices Figure 2.19. The plane ABC crossed with the axis giving the intercepts of OA=a=1, OB=b=1 and OC=c=1, therefore plane

ABC is expressed as (1 1 1). Plane DEF, OD=2a, OE=3b and OF=3c so the indices of this face can be obtained as follows:

$$h = \frac{a}{2a} = \frac{1}{2}$$

$$k = \frac{b}{3b} = \frac{1}{3}$$

$$l = \frac{c}{3c} = \frac{1}{3}$$

Thus, $h : k : l = \frac{1}{2} : \frac{1}{3} : \frac{1}{3}$, because the index has to be written in integer, so this equation has to multiply a common number of 6 to give (3 2 2). If negative intercepts were achieved, then the expression should be in the form of $(\bar{h}\,\bar{k}\,\bar{l})$. Hence, plane DGF is indexed $(3\,\bar{3}\,2)$.
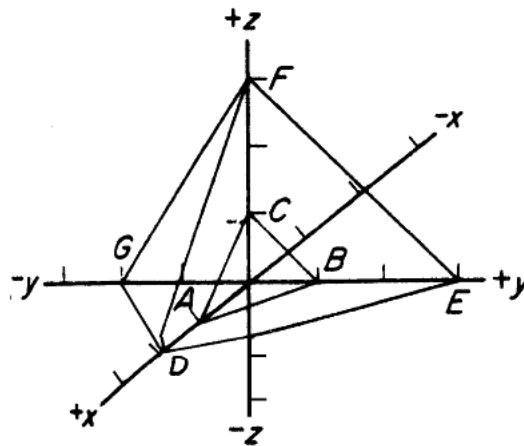
Figure 2.19: An example of determined planes on a crystallographic axis (28).

2.3.4.3 Crystal Morphology

The external shape of a crystal is often defined by its habit or morphology. It is an essential criterion in determining the desirable processes and products. It is normally to differentiate between the equilibrium and growth morphologies. In the previous case, the shape that a crystal possesses at its minimum surface free energy allows it to stay in equilibrium with the surroundings. In the latter case, the shape of the crystal changes along the growth which is driven by kinetics. The morphology of crystals can also be significantly

affected by the crystallisation environment, for instance solvent selection, supersaturation degree and impurity effect (48).

2.3.4.3.1 Sodium Sulphate and Its Polymorphs

There are at least 5 polymorphs of Na_2SO_4, and they convert to one or the other with the altering temperature (see Figure 2.20). Form V and III has been reported as the most stable and metastable phase at room temperature, respectively. (59, 60) The metastable form will slowly convert to the stable phase with the moisture content in the surroundings, however under dry conditions this phase transition process is rather slow (i.e. longer than one year). If precipitated Na_2SO_4 crystals from the aqueous solution are around 25°C, phase V would be the dominant one (60).

$$Na_2SO_4\ V \xrightleftharpoons[\sim180°C]{} IV \xrightleftharpoons[\sim200°C]{} III \xrightleftharpoons[\sim228°C]{} II \xrightleftharpoons[\sim235°C]{} I \xrightleftharpoons[883°C]{} Melt$$

245-253°C

244°C
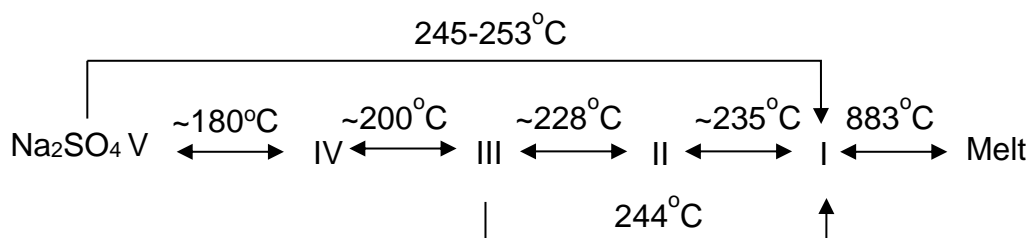
Figure 2.20: Polymorphic transformation of Na_2SO_4 anhydrous (31, 59-63).

The stable Na_2SO_4 phase V has an orthorhombic crystal structure with unit cell parameters a=5.858Å, b=12.299 Å c=9.814 Å, α=90° β=90° γ=90°, Z=8 (64). Groth (1908) discovered the growth patterns and discussed them in (65), (66), (67) and (42) (see Figure 2.21), furthermore in 1992 Meenan further proved that V is the dominant growth form (65).
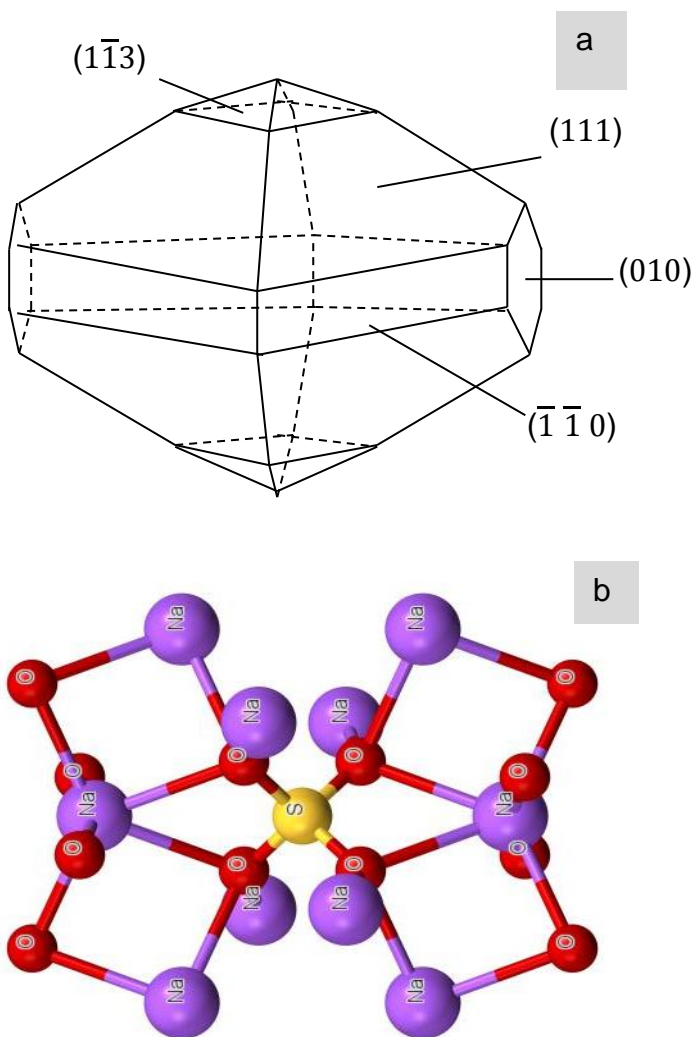
Figure 2.21: a: Morphology of Na₂SO₄ anhydrous [17]; b: Na₂SO₄ molecular modelling structure from ICSD database

Apart from the X-ray diffraction study, other analytical techniques were also applied in the phase transition study, such as Differential Scanning Calorimetry (DSC), Dilatometer, Infrared radiation (IR) and Raman spectroscopy (60, 61, 63, 64).

One of the Raman studies on the phase transition behaviour of Na_2SO_4 was carried out by Davies J. Eric D. in 1975 (63). Different pressures and heating-cooling cycles were applied, a reversible transition between polymorph III and I was observed. Additionally, a transformation process of the freshly made III to V and a controlled trial were recorded and compared through Raman measurement, see Figure 2.22. The controlled trail that was placed in dry air had no sign of the phase transformation even after 20 months of tracking observation.
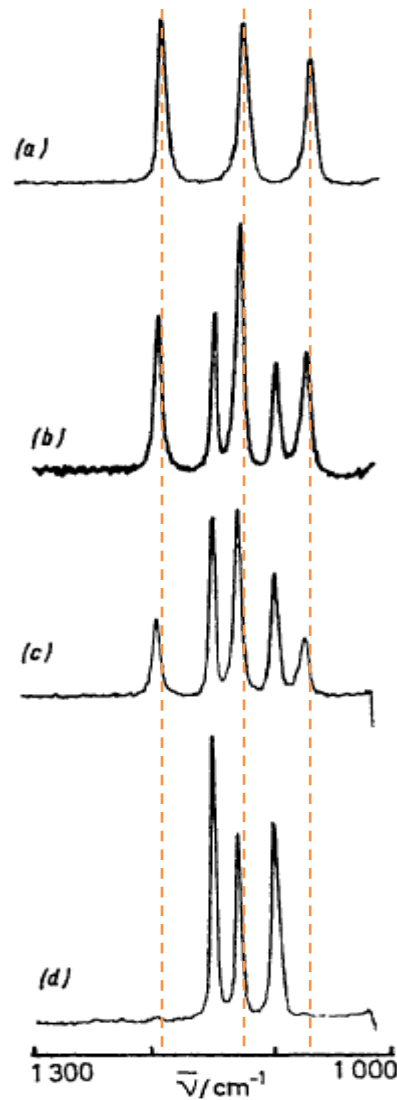
Figure 2.22: Raman spectra of Na₂SO₄ (III) transformation (sample was located in undried air environment: freshly prepared; 9 weeks after preparation; 19 weeks after preparation; 11 months phase transition completed after preparation (63).

2.3.4.3.2 Sodium Sulphate Hydrates Form

In a Na_2SO_4-H_2O system, according to Figure 2.2 below 32.4°C the decahydrate of Na_2SO_4 is the thermodynamically stable phase in contact with the saturated Na_2SO_4 solution. Under room temperature (~20°C) if the relative humidity dropped below 71%, then the decahydrate will rapidly dehydrate to the heptahydrate ($Na_2SO_4 \cdot 7H_2O$). This is a metastable phase therefore the dehydration process is totally reversible once the humidity rises back up. However, $Na_2SO_4 \cdot 7H_2O$ is also a stable phase relative to the surroundings that have no moisture content (68). The differentiation of these two hydrates on the Raman spectrum were compared and listed in Table 2.1, which can

help to detect if any phase changes or transformations happened to the Na_2SO_4 during the experiment or in the final product, which will potentially benefit the stability study of the product in divergent process stages if required.

Table 2.1: Raman wave numbers achieved from samples with the random orientation (v_1: symmetric stretch, v_2 & v_4: bending mode, v_3: anti-symmetric stretch) (59, 60, 69)

Assignment and free ion values (cm⁻¹)	Solution (cm⁻¹)	Mirabilite (Na₂SO₄·10H₂O) cm−1	Heptahydrate (Na₂SO₄·7H₂O) cm−1	Na₂SO₄ (V) cm⁻¹	Na₂SO₄ (III) cm⁻¹
SO_4 v_1 − 981	981.9	989.3	987.6	993.5	996.0
SO_4 v_2 −451	450.9	446.7	464.4	451.8	458.1
	-	457.9	482.7	466.6	468.0
SO_4 v_3 −1104	1115.2	1086.3	1106.6	1097.8	1076.2
	-	1108.4	1134.9	1102.1	-
	-	1118.9	-	1132.1	1130.9
	-	1128.9	-	1152.7	1198.9
SO_4 v_4 −613	617.0	615.9	592.5	620.5	615.9
	-	627.0	644.6	632.8	637.5
	-	-	-	647.2	(640)
H_2O v_2 − 1595	~1638	~1671	~1711	-	-
H_2O v_1 and v_3 3652 and 3756	3092, 3208,3257,3299 & 3448	~3092,3242. 3343.3381 & 3506	~3337, 3384, 3418, & 3466	-	-
Others	-	2162	2157 & 2181	-	-

2.3.4.3.3 Sodium Carbonate

According to the structure database the structure of Na_2CO_3 is temperature dependent. The hexagonal structure α can be achieved in the temperature range of 483-699°C, below this range monoclinic structure will predominate, such as the monoclinic β form (332-478°C). However, the incommensurate γ

and lock-in δ monoclinic structures will be obtained around room temperature and -163°C, respectively (70). Based onFigure 2.23, the amount of Na$^+$ that engaged in the second co-ordination sphere of the C atoms can increase from 3 up to 7 with the decreasing temperature. As the result of the varying Na$^+$ composition, the molecule distance of C-O and mobility of O will be altered, therefore leading to transformation in the crystal habit (70). The incommensurate structure is usually considered as a super space formalism in which the lattice repeats periodically in four and six dimensions. Brouns and his colleagues had already discussed this abnormal super-lattice arrangement in Na$_2$CO$_3$ in 1964. This super-lattice γ phase possesses a C2/m space group with the unit cell parameters being a=8.920Å, b=5.245 Å c=6.050 Å, β=101.35° Z=4 (66, 70-72).
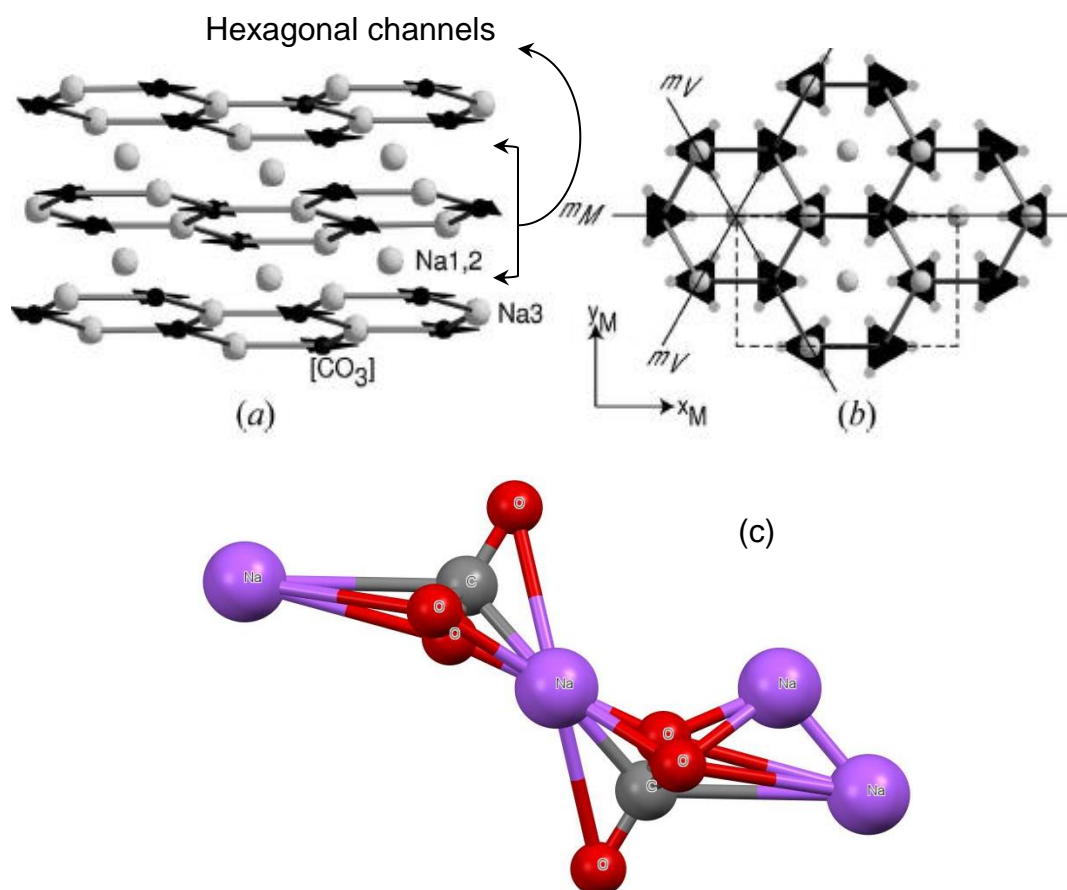
Figure 2.23: The crystal structure of Na$_2$CO$_3$: (a) perspective view, (b) the (001) plane projection (the three atomic planes of the (110)$_{hex}$ are equivalent in the hexagonal a phase and indicated as m$_M$ and m$_V$ corresponding to one mirror plane and two virtual mirror planes in the monoclinic configuration; the structure in the dotted box is a monoclinic unit cell) (70) and c: Na$_2$CO$_3$ molecular modelling structure from ICSD database.

2.3.4.3.4 Sodium Carbonate Hydrates

The common hydrated form of Na_2CO_3 are monohydrate ($Na_2CO_3 \cdot H_2O$), heptahydrate ($Na_2CO_3 \cdot 7H_2O$) and decahydrate ($Na_2CO_3 \cdot 10H_2O$). The morphology of each crystal was predicted by Meenan P, based on the Bravais/Friedel/Donnay/Harker (BFDH) laws. Besides, the crystal habits of $Na_2CO_3 \cdot H_2O$ and $Na_2CO_3 \cdot 10H_2O$ were discussed (56). The thermodynamic properties and phase transition of the hydrates were comprehensively investigated by Fredrik G. et al. in 1983 (73).

The sodium carbonate monohydrate is the most stable phase compared with its anhydrous form (under 35-100°C and 15-65wt% water content). Damir et al. (74) proposed there are two mechanisms for the unstable phase transfer towards to the stable ones. The first one is a solid-state transformation, in which case an internal crystal lattice reorganisation takes place. In the second case, the dissolution of the unstable phase and crystallisation of the new stable phase happen simultaneously. Based on these theories, Amjad A. et al. (35) discovered that the hydration process of Na_2CO_3 anhydrous to its monohydrate is a solution-mediated transformation (the latter mechanism) as opposed to the classical crystallisation phenomena, the measurement was done by applying the in-situ size analysis technique-FBRM (Focused laser Beam Reflectance Measurement).
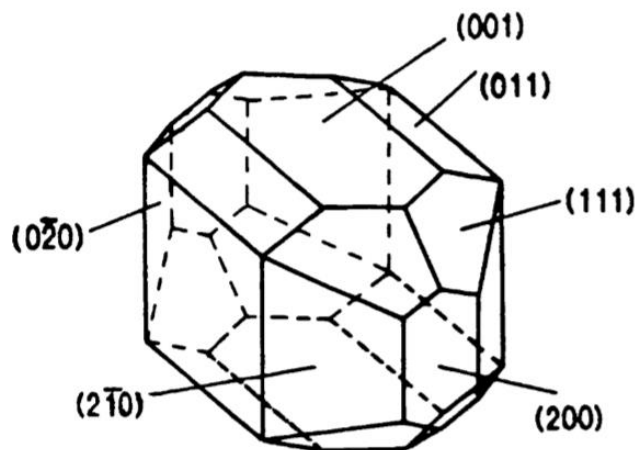
Figure 2.24: Predicted morphology of $Na_2CO_3 \cdot H_2O$ as the principle of BFDH rules (56).

2.3.4.3.5 Burkeite

Double salt Burkeite is widely used for industrial purposes, such as in the kraft pulp, paper and detergent industries (38, 75, 76). According to the early stage literature, it was collected from Searles Lake in California and applied into the potash industry and brines refinement (77) (78). Vergouwen (1979) (79) also indicated that Burkeite exists naturally, however it is always hard to do the quantitative test as it normally shows intergrowth with other minerals.

Giuseppetti's group (1988) (80) found that Burkeite ($Na_6(CO_3)_x(SO_4)_{(1-x)}$) crystals are orthorhombic with variable unit cell parameters α=5.17-5.19Å, b=9.21-9.25Å, c=7.06-7.09Å & Z=2 and the space group Pmnm. Later on Meenan predicted Burkeite morphology by using the BFDH method (Figure 2.25), which matches the observed micrograph orthorhombic structure perfectly well. The growth rate of a specific crystal plane can be measured using this method. In Figure 2.25 the dominant crystal plane is (010), which caused Burkeite crystals normally to appear the plate shape (81).
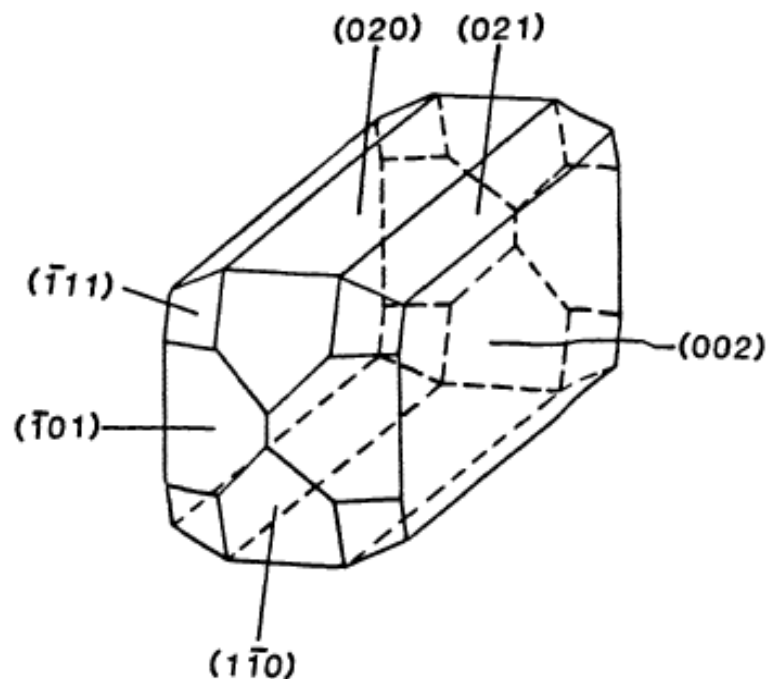
Figure 2.25: Predicted morphology of a Burkeite unit cell (56)

2.3.4.4 Effect of impurities on crystal growth

The existence of impurities can influence the nucleation significantly. In some cases, the impurity will slow down or even restrain the growth of the crystal entirely. On the contrary, in other cases impurities help to accelerate the growth (82, 83). Moreover, some impurities only impact on the growth rate of certain faces, therefore adjusting or altering the habit of crystals (28). The mechanism of all these influences is different, for instance impurities can either alter the solution properties or the concentration of equilibrium states. Apart from that, they can also affect the consolidation among particles through changing their way of absorption onto crystals - solution interface. Examples are given in Figure 2.26 which cites from the work of Davey and Mullin in 1974 (84).
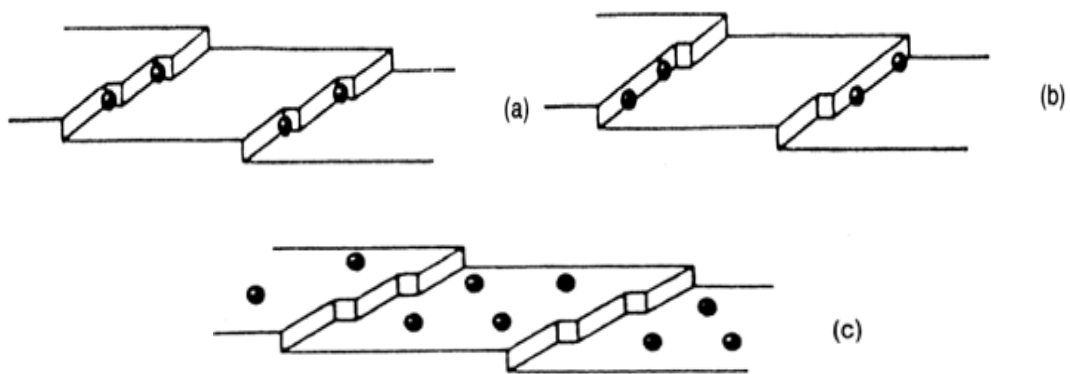
Figure 2.26: Sites for impurity adsorption on a growing crystal, based on the Kossel model: (a) kink; (b) step; (c) ledge (face) (84).

Shi (2003) (85) proved that quite an amount of ion impurities could affect the nucleation of the sodium double salt, Burkeite, by using the Focused Beam Reflectance Measurement (FBRM) method. The result illustrated that calcium ions inhibited both the nucleation and crystal growth, which results in large Burkeite crystals formation. They also clarified the inhibitions are attributed to two mechanisms, one of which is the substitution between the calcium ions and sodium ions which changed the electrical neutrality, therefore preventing the collision of like-charged embryos, decreased the possibility of big cluster formation and adequately generated nuclei. However, one calcium ion can also substitute two sodium ions, which leads to vacancies in the molecular structure, so that dislocations will occur in the crystal lattice (85, 86).

They also focused on other cations which have the similar ionic radius as calcium; most of them influenced in a similar way as calcium did on the burkeite nucleation. However, the existence of Nd ions (+3) inhibited the nucleation occurrence of Burkeite completely. Nevertheless, they could not find the same influence on the nucleation of neither sodium carbonate nor sodium sulphate while calcium ions were present in the solution. This phenomenon indicates that the impurity ions may locate in a special way during the substitution process (85).

2.4 Previous Arts on the Crystallisation of Na_2CO_3 & Na_2SO_4 system

In order to make a comprehensive overview of the research project, a literature review on the sodium carbonate and sodium sulphate aqueous system was carried out, for example the effects of additives, experimental methods and the analytical techniques were applied in previous research. Any incompatible theories or research gaps might be covered in this research project.

The Na_2CO_3 and Na_2SO_4 solution system and their associated double salts are well-known as their inverse solubility properties (solubility decreasing with the increased temperature). Bayuadri (87) summarized the work that was done by Shi (38, 85), Seidell and Linke (88) and Green (37), and established the solubility curve (see Figure 2.27) for the system of Na_2CO_3-Na_2SO_4-H_2O.
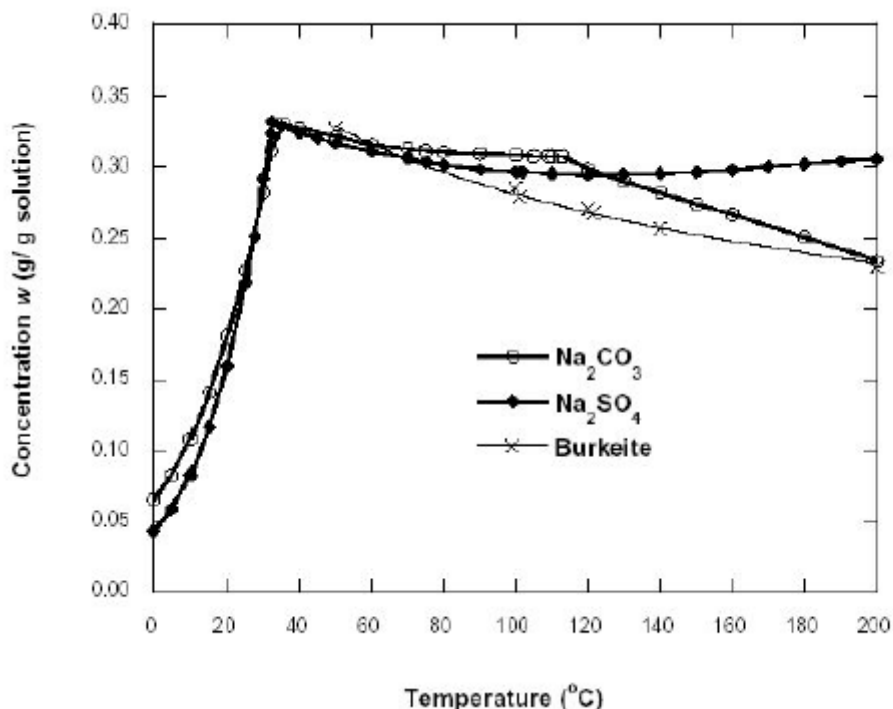
Figure 2.27: Solubilities of sodium carbonate, sodium sulphate and Burkeite in water [9].

Burkeite is one of the double salts that can be achieved from the Na_2CO_3 and Na_2SO_4 solution system. Burkeite crystals exist in the orthorhombic form. It does not crystallise in the regular proportion of carbonate to sulphate molar ratio, but undergoes a very large stoichiometric range as $CO_3:SO_4$ equal to $(1+x):(2-x)$. The value of x varies between -0.25 and 0.5 which was determined by Shi and Rousses (38).

Caspari (1924) (89) found that in a saturated sodium salt system by applying the evaporation crystallisation method, Burkeite can only be obtained when the temperature was above 26.1 ℃, the quantity increased with the temperature. Because burkeite can participate in a wide range of concentration ratios of sodium salts, therefore it was mostly the dominant product in the system. Caspari used the titration chemical analysis method to determine the amount of CO_3^{2-} and SO_4^{2-}, thereby further estimating the type of salt present. Eventually, a phase diagram of the Na_2CO_3 and Na_2SO_4 aqueous system was accomplished by Caspari, see Figure 2.28.

Both Makarov and Bleiden (1938) and Harvie's (1984) achievements illustrated rough agreement with Caspari's work. The previous research group found that the temperature for Burkeite formation was 25.5℃, and the latter

one achieved a significant yield in Burkeite around 25°C when the molar ratio was equivalent to 1:2 Na_2CO_3 to Na_2SO_4 (90, 91).
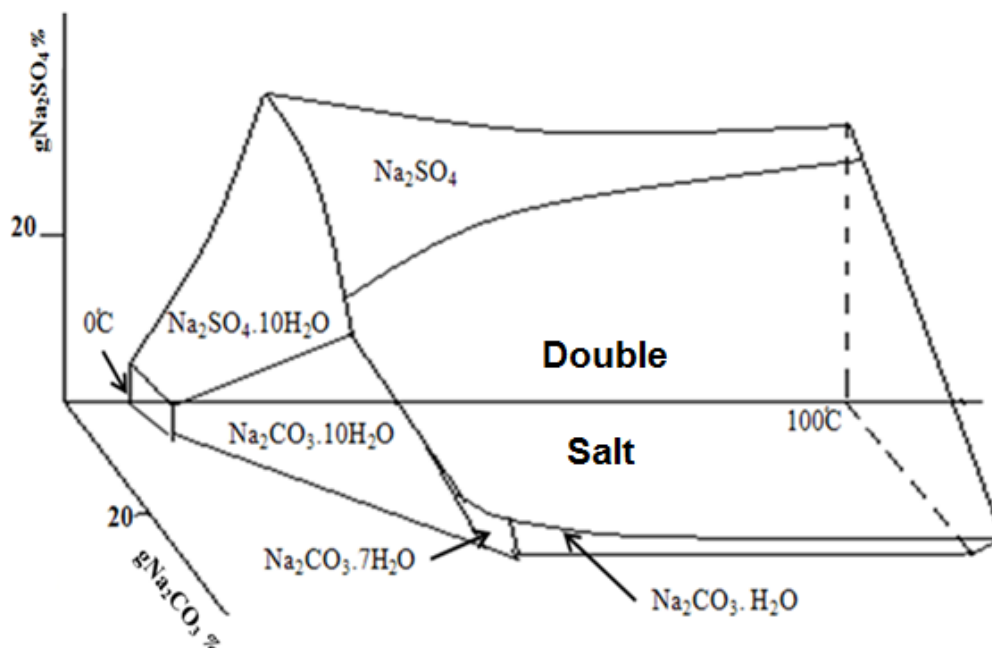
Figure 2.28: Phase diagram for Na_2CO_3 and Na_2SO_4 aqueous phase (89)

Initially, it was known that Burkeite only deposits from saturated solutions with the molar ratio of Na_2CO_3 to Na_2SO_4 is 1:2. However, later on, the ratio varied from different research projects, for instance Forshag (1935) gave the ratio 1:9; Schroeder et al., (1936)'s results were a range of 1:1-1:3 and Green and Frattali (1946) claimed that 1:1.4-1:2.2 was the variety. Giuseppetti et al., (1988) focused on the crystallisation Burkeite, they found out that at 30°C Burkeite formed as the dominant compound with a molar range of 1:1 to 1:3 (Na_2CO_3 : Na_2SO_4). But Meenan (1992) was not satisfied with this result; he said that at that ratio the dominant phase should be $Na_2SO_4 \cdot 10H_2O$ rather than Burkeite. Meenan's conclusion aligned with the diagram (Figure 2.28) that was given by Casparis. X-ray diffraction was used for phase identification in Meenan's work, however this method could not provide an accurate analysis for the quantitative measurements as the result of plate-like crystals leading to a crystallographic preferred orientation.

In 2003 Shi and Rousseau explained the reason for the inconsistent outcome between Meenan and Giuseppetti, which was probably due to the crystallising phase being a function of the degree of supersaturation (85). They noticed

that the varying temperature, the adding sequence and/or the ratio of materials had a significant influence on the precipitation of crystal species which varies from experiments. The achieved crystal species could be varying among carbonate, sulphate, dicarbonate and Burkeite. In Shi et al.'s results they suggested a wider ratio range for the Burkeite formation that is 1:5-12:1(C:S). The coulometric titration and capillary ion electrophoresis chemical analysis were applied in their research to determine the molar ratio between carbonate and sulphate ions exist in the crystal species.

Apart from the disagreement results, there were also some consistent outcomes between Giuseppetti and Shi and Rousseau, for example the Burkeite crystal structure, which was mentioned in section 2.3.4.3.5 of this report. Two super lattices 2X and 6X were categorised for Burkeite as the reason for the variable concentration of carbonate and sulphate in the solution. The stable 2X crystal structure would be achieved when the value of x in $Na_6(CO_3)_x(SO_4)_{(1-x)}$ smaller than 0.5, once this value was larger than 0.5 another stable structure-6X would be attained instead. Shi and Rousseau (2003) developed 4 groups of sub-cell models (Figure 2.29) according to the theory of Giuseppetti et al.
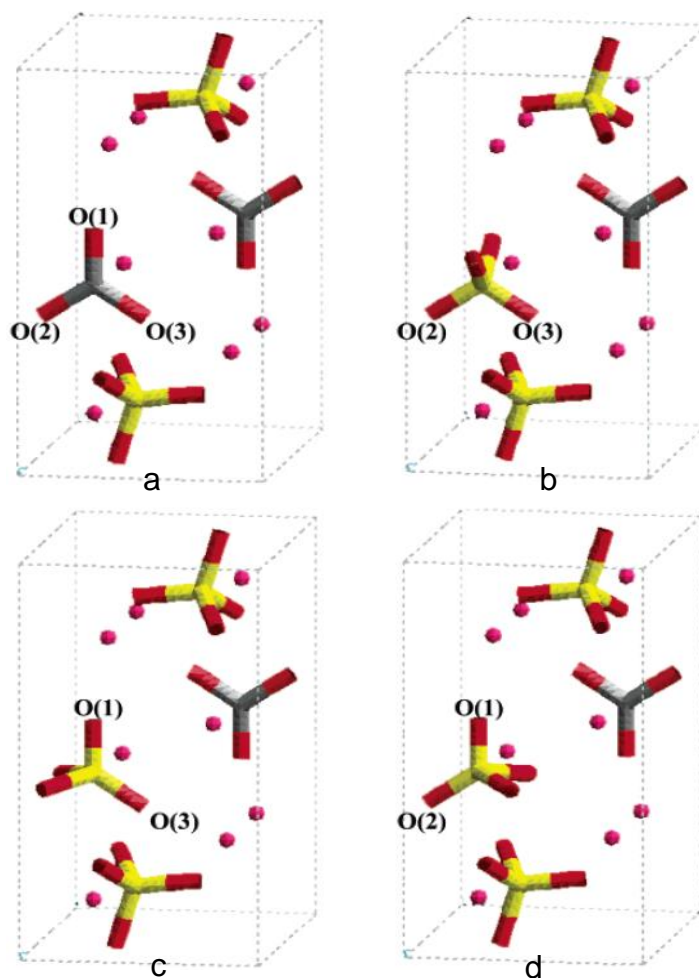
Figure 2.29: Showing four kinds of Burkeite sub-cells (a)CO_3^{2-} (grey) partially replaces SO_4^{2-} (yellow) in two anionic sites; (b,c,d) SO_4^{2-} in the middle anionic sites can stay in 3 different orientations (38).

In 2006, Bayuadri used the evaporation crystallisation method to study sodium carbonate and sodium sulphate systems. The result showed good agreement with Shi and his colleague's results. Besides that, the latter work denoted that the double salt crystals generated from this system were agglomerates (39). This phenomenon has already been mentioned by Matusevich and Shabaline in 1952. They explained that there is an inversely proportional relationship between the agglomeration of Burkeite crystals and the agitation intensity, solute concentration and average crystal size (92). Meenan further clarified that Burkeite performances as the agglomerate or nuclei combining with other surrounding crystals, could be another reason to explain the agglomeration phenomenon (76).

Meenan (1995) accomplished some experiments in order to investigate Burkeite properties in a mixed slurry system that contained sodium silicates and sodium polyserylate. Experiments were carried out at 85℃ by using a batch crystalliser mixing for 20 minutes. The samples produced underwent a spray drying process and were then analysed using the X-ray diffraction technique. The analytical results indicated that Burkeite is the only phase generated from the experiment, however, they could not determine the concentration of this phase. Then in the following year, Meenan attempted to take samples from the slurry system during the process of the experiment, washed them with n-hexane and then spray dried them. The results illustrated that firstly the formation of Burkeite was highly dependent on the addition of sodium carbonate; secondly the formation happened between 1 – 2 hours; thirdly the volume of pore increases with the decreasing drying rate. The micrographs showed that as the experiment continued the plate-like Burkeite crystals started to form outside of slurry particles. Then the porosity of Burkeite particles augmented until the end of Burkeite crystal formation (76).

As one of the objectives of the current research, a method of quantitatively determining the composition in the slurry will be developed that complements the downside of Meenan's work. Also, an inconsistency was found and will be discussed in this research.

2.5 (De-)polymerization of Sodium Silicate

Sodium silicate is another material that has been generally used in the dry laundry industry. The properties of soluble silicate is going to be reviewed as the fundamental knowledge for investigating the interaction between the inorganic phase and sodium silicate in the current research, such as the impact of sodium silicate on the dissolution and crystallisation process of sodium salt, and the influence of the sodium salt involved in the speciation/polymerisation of the soluble silicate system.

Soluble silicates are one of the oldest industrial materials with a wide range of applications, such as water treatment, oil recovery, detergent, adhesives, soap builders, metal cleaner, cements and binders of other materials (93-95). They are manufactured by fusing sand (SiO_2) with either sodium or potassium

carbonate (Na_2CO_3 or K_2CO_3) at around 1100-1300°C, then the resulting product is dissolved with high pressure steam to form a viscous liquid which is famously known as water-glass (96) (97). The most common sodium silicates ($Na(SiO_2)_nO)$) are water solutions with different ratios of sodium oxide (Na_2O) and silicon dioxide (SiO_2), the range of standard commercial liquid sodium silicates is in the weight ratio 1.6 to 3.3 of SiO_2 to Na_2O. The structure and species composition has been studied and explored by previous researchers with various chemical and analytical techniques, such as potentiometric titration, dye absorption, chemical derivatization, gas chromatography (GC), Fourier transform infrared (FTIR), Raman spectroscopy, and [29]Si nuclear magnetic resonance (^{29}Si NMR) (98-101). The chemical and physical properties of silicate solutions were reviewed (97, 102, 103). For Instance, Vail, J. et al. (97) demonstrated a ternary phase diagram of the Na_2O-SiO_2-H_2O system, Figure 2.30, which gives a general indication of the species composition in sodium silicates.
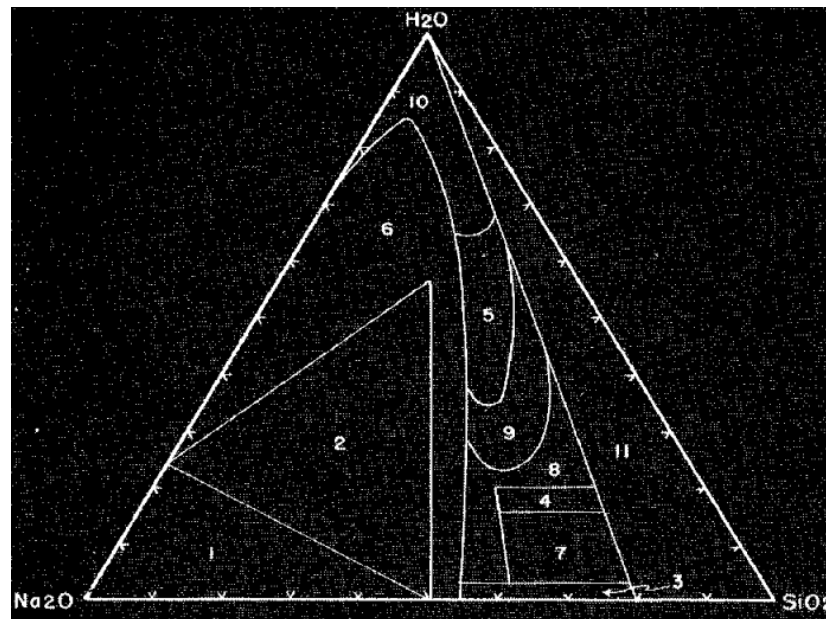
Figure 2.30: A ternary phase diagram of Na_2O-SiO_2-H_2O (Region 1 contain highly alkaline mixtures; 2 is the alkaline crystals area such as sodium meta-silicate and its hydrates; commercial glasses were made according to the area 3; 4 defines the region of hydrated amorphous powder which can be achieved by spray drying process; 5 represents the commercial sodium silicate solution field; 6 denotes the crystals and solution mixtures; 7 less profitable hydrated glasses; 8 semi- solid masses ; 9 highly viscous silicates solutions; 10 significant dilute solutions and 11 describes unstable gels and solutions *(97)*).

2.5.1 Speciation of Sodium Silicate Solutions
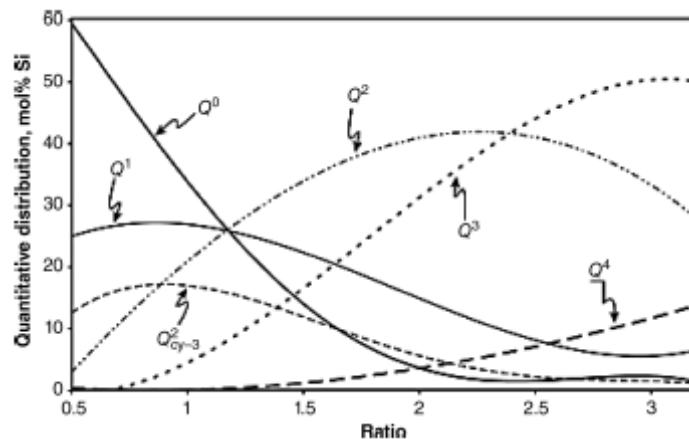
Figure 2.31: Distribution of the anion species in soluble silicate solutions (reproduced after James S *(94)*).

The composition of solutions varies according to the ratio between SiO_2 and Na_2O and also the concentration of the solution. As shown in Figure 2.31, the species include a different level of monomer, dimer, ring structure, chain structure and sheet structure which is considered as a high polymerization degree (i.e. Figure 2.32). The concept of naming Q^n for different silicate species was invented by Engelhardt's group in 1987 and adopted by researchers ever since. Here, Q stands for the 'Si' atom, and n equals 0-4 that indicates the number of 'Si' units attached together by the bridging oxygen to an individual silicon atom. In addition, due to the total oxygen being known, thereby the amount of non-bridging oxygen atoms can be simply quantified (104-106). Generally, Q^0 describes an ortho-silicate monomer that has a tetrahedral structure. Q^1, Q^2, Q^3 and Q^4 are denoted as the end groups, middle groups, branching groups and three dimensional cross-linked groups, individually. For instance, Q_2^1 is a dimer and Q_3^2 is a cyclic trimer (107).
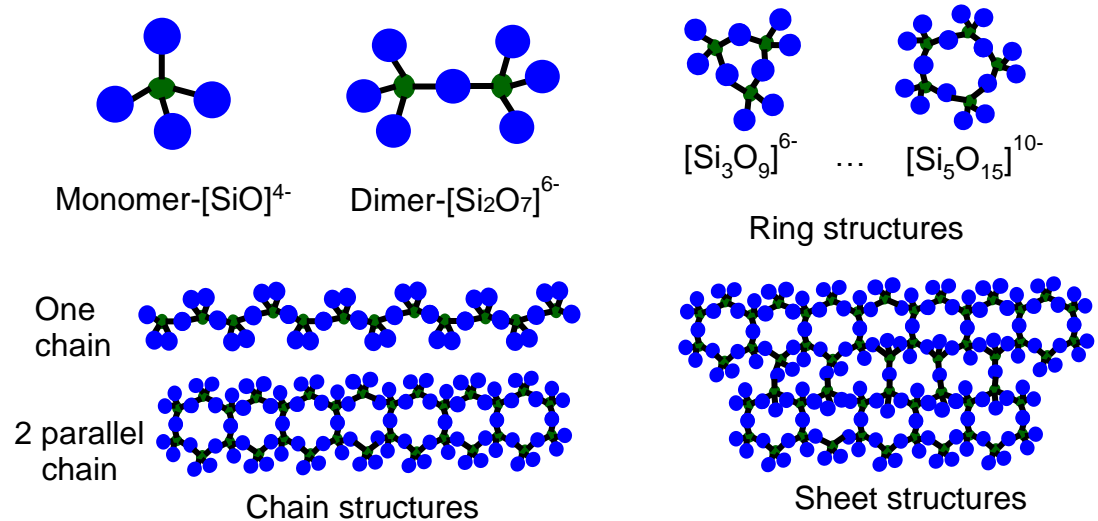
Figure 2.32: The structure of different species in silicate solutions

As mentioned above, the ratio of SiO_2 to alkali metal oxides has an impact on the speciation of silicate solution. The higher the ratio, the greater the polymerisation degree. In previous studies, the major forms are Q0 and Q^1 in the solutions with a ratio less than 0.5 (98). The predominant species in the solutions with the molar ratio less than or equal than 1.5 are linear (Q^1) and cyclic forms (Q^2) and the nuclearities ≤ 4. Increasing the ratio will cause polymerisation to occur, Q^3 units will become the dominant species with a mean nuclearities number of 6-8. In the case of SiO_2/M_2O equal to or greater than 3.5, Q^4 is the principal phase, keep increasing the ratio will trigger gelation of the solution i.e. pH around 10 (98, 108).

2.5.2 Dissolution of Silicates

The dissolution of soluble silicates is one of the essential and challenging procedures in industrial production. The dissolution rate can be influenced by many aspects, such as the ratio between SiO_2 and alkali metal oxide (M_2O), silicate solution concentration, impurities content, process conditions (i.e. temperature and pressure) and/or silicates particle size (94, 109). There are two steps involved in the dissolution process:

Ion exchange:

$$\equiv Si - ONa + H_2O \rightarrow \equiv Si - OH + Na^+ + OH^-$$
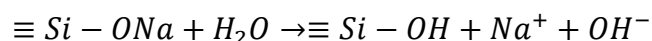
and the network disintegrate:

$$\equiv Si - O - Si \equiv +OH^- \rightarrow \equiv Si - O^- + HO - Si \equiv$$
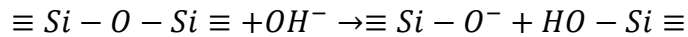
If there is not sufficient hydroxide ion hydrolysed from the ion exchange step, then the silica network will not breakdown extensively. Similarly, if excess Na^+ is presented or introduced to the solution, the overall dissolution rate will be decelerated by preventing SiO_2 groups decomposed by OH^-. The solubility of alkaline silicates declines with the atomic radius of alkali metal ions that possess higher charge densities, for instance $LiSiO_3 < NaSiO_3 < KSiO_3$ (94, 109-111). Besides, it also decreases dramatically with the existence of high valence ions, such as Mg^{2+}, Ca^{2+}, Al^{3+}, Fe^{3+} and so on, which are often referred to as the impurities in the solution (93, 94). Wu et al, in 1980 revealed the solubility of a silicate solution is highly associated with the fraction of available free silanol groups. Additionally, the composition of free silanols gorups varies linearly according to the existing impure metal ions (Figure 2.33). For example, when Al^{3+} ions are induced, it will substitute Si^{4+} from silica. Once the moles of Al_2O_3 are equivalent to the moles of Na_2O, the fraction of the free silanol group becomes 1, which denotes the overall sodium silicate system is fully associated or polymerised, there are no non-bridging oxygens (112).
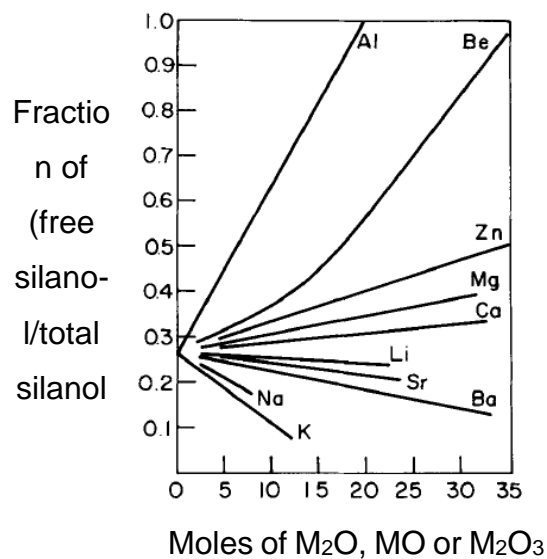
Figure 2.33: Fraction of free silanol in a 4 ratio of SiO₂/Na₂O solution as a function of present metal ions (reproduced after Scholze H.1959) (113)

2.5.3 Understanding of Silicate Solutions

Many techniques were applied to investigate the composition of silicate solutions with different ratios of SiO_2 to Na_2O as well as different concentrations from the very early stage. With the time and the evolution of analytical techniques more and more conclusions were drawn.

In 1928, Harman concluded from the measurement data of conductivity, activity, diffusion and equilibrium point that the colloidal silica present in sodium silicate solutions when the ratio of SiO_2 to Na_2O larger than 2. Additionally, the amount of colloid increases with both increasing SiO_2 to Na_2O ratio and silicate solution concentration (114, 115). The light-scattering technique was also applied around the same period of time by Ganguly and subsequently improved and developed by Nauman and Debye in 1949 (116, 117) They claimed that, in the non-metal contaminant systems, there should be no large colloidal particles in the stable silicate solutions. Aggregation of particles was observed in the solutions with high concentration and high ratio of SiO_2 to Na_2O (117). Later on, the gas chromatography (GC) and trimethylsilyation work verified the conclusions that were given by previous researchers. Moreover, the GC work also denoted the existence of various silicate species (i.e. Q1, Q2 and Q3) in both dilute and highly concentrated silicate solutions (118). Plus, the silicate anions present in a dynamic equilibrium mode in silicate solutions (119). Ray also discovered that the addition of alkali metal salts increases the polymerisation degree of silicate solutions and, on the contrary, adding alkali metal hydroxides would decrease their degree of polymerization (118).

With the development of analytical techniques, a lower amount of samples and their preparation were required. Especially a reduced amount of inaccurate measurement results are achieved with the arrival of in-situ techniques.

The Fourier Transform Infrared (FTIR) spectroscopy was applied to identify the species of silicate solutions (107, 120), however this technique is not applicable for quantitative studies. ^{29}Si NMR is the most popular technique for investigating silicate solutions (107, 108, 121). It provides the most

valuable information on a stable silicate solution, which makes the quantitative analysis feasible (104). When the pH of a silicate solution is greater than 10, then the kinetic for all the species to achieve dynamic equilibrium is really fast, however the process is easily altered by metal impurities and their own concentrations. Raman spectroscopy is a more efficient way to compare with the NMR technique. In the early stages, it was applied mainly on silicate glasses and melt studies. Then gradually moved on to silicate solution systems, which demonstrated that the polymeric anions even exist in dilute sodium silicate solutions that cross the range of SiO_2/Na_2O ratio from 0.33-3.3 (122). In recent years, researchers have been developing new Raman models for quantitative analysis of the species of silicate systems, meanwhile cross calibrating the spectral information with the results achieved from the sophisticated NMR technique (123-125).
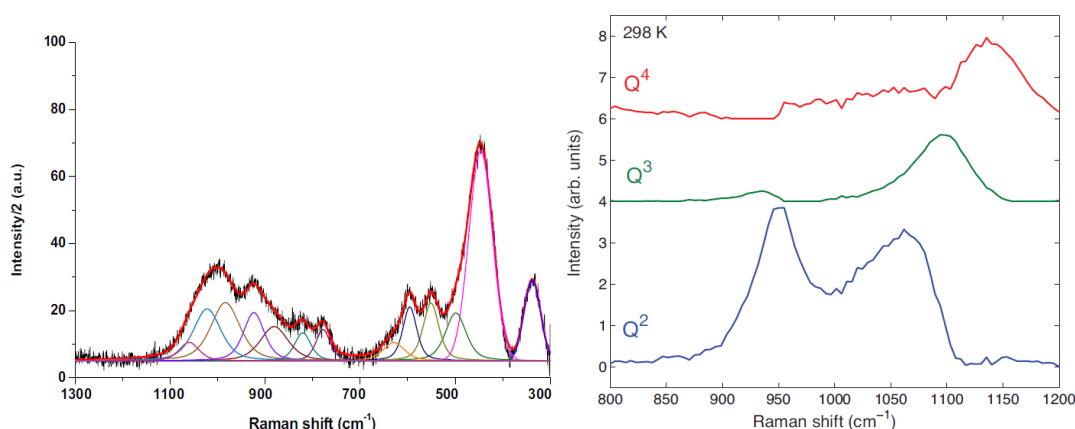
Figure 2.34: A deconvolution of Raman spectrum of 0.7 molar ratio of potassium silicate solution*(126)*; partial Raman spectra for the sodium silicate glasses at room temperature *(124)*.

Examples of the de-convoluted Raman spectra were published and shown in Figure 2.34. A summary of the speciation information is included in this study and listed in Table 6.6. There are some discrepancies in the speciation of the Raman vibrations assignment from different literature studies, such as Halasz I. (127, 128) who concluded that peak 606, 540 and 464cm^{-1} can be assigned as the deformation vibrations of 3 4 and 6 member rings, respectively. However, Vidal H. (126) believed that 600, 490 and 450cm^{-1} are corresponding 3, 4 and 5 member rings. The reason is probably due to the fact that they were focusing on different vibration modes. The speciation

information in Table 6.6 was concluded according to the sodium silicate solutions that were studied in this project.

2.5.4 Polymerisation and Depolymerisation of Silicates

The polymerisation and depolymerisation characteristics of the dilute silicate solutions at pH$\geq$10 are responsive to the changing conditions, for instance pH, temperature, presenting ions, ionic strength and dielectric constant. Above this pH value, the rate constant of the depolymerisation process becomes significant, whereas at lower pH conditions the acids lead polymerisation to occur (94).

All the polymer silicate species are under a dynamic equilibrium in a stable silicate solution (93), therefore even solutions having the same composition can reveal different physical and chemical properties. Katsanis, E.P. expounded that the precipitation limits of sodium silicate solutions enlarge as a function of its aging time (129, 130), also associated with the solution salinity and the percentage of existing metal ions (130). Generally, a concentrated silicate solution with a high viscosity undergoes a slow process to achieve the steady state (94).

2.5.5 The Impact of Metal Ions on Silicate Solutions

In a silicate solution, the activities of metal ions are responsive to the present silicate anion structures and the solution pH. The interactions between these metal ions and the anionic silicate species have further impact on the particle dispersion in the solution. Another result, concluded by Falcone James S., was consistent with Iler's observation that the absorption of multivalent metal ions occurs at the pH value approximately 1-2 units below the pH at which the metal hydroxide is precipitated (93, 131). Silicate anions are ready to interact with metal ions in a higher ratio solution, and the interaction gets more intense as the polymerisation degree increases. Large polymers contain more acidic Si-OH groups on the surface which attracts metal ions to create active bonding sites, thereby reducing the activates of the metal ions and the solution pH, in turn resulting in even larger silicate anions to incorporate more metal ions (93).

2.5.6 The Impact of Salt on Silicate Solutions

Salts impact on silicate polymerisation has also been investigated since half a century ago, as an extension to research on the cation induced polymerisation phenomenon. In 1953, Brady A.P. compared both cation ions (NH_4^+, Li^+, Na^+ & K^+) and anions (CO_3^{2-}, SO_4^{2-}, HCO_3^-, HPO_4^- and Cl^-) influence on a potassium silicate with the ratio 3.8. He claimed that the polymerisation occurred faster when sodium salts were present. The rate is approximately corresponding to the fourth power of the added salt concentration, and almost proportional to the inverse square root of the silicate composition. At electrochemically equivalent conditions, chloride ions lead to faster kinetics than sulphate ions. However, when both ions are at equal molalities, the conclusion would be drawn contrarily (132). The conclusion that sulphate ion has a minor effect on silicate polymerisation was also proved by Marshall and Warakomski (133). Nevertheless, they discovered the degree to which the given salt causes the polymerisation to increase with the amount of hydrated cations, and depended on the identity of the cation rather than that of the anions (133-135).

By comparing the actual mechanisms, acid induced polymerisation can be slowed down, stopped or even reversed by the addition of alkali (in enough amount). However, if the alkali solution contains a certain level of salt, then reversed polymerisation will soon re-polymerise again. Therefore, it is obvious that the bonds formed through these two kinds of polymerisation are different (132).

2.6 Primary Analytical Techniques

2.6.1 Raman

2.6.1.1   Understanding of Raman Spectroscope

Raman scattering and Infrared absorption are the two theories that have been applied for detecting the vibration in molecules. The information on chemical structure and physical forms is provided through these techniques. Therefore, the determination of substances and the quantity of a compound in a sample are able to work out according to the characteristic spectral pattern. There is

no physical limitation on detecting samples. For instance, samples can be in solid, liquid or gas state, or they can be tested in hot or cold conditions either as a thin layer or in bulk. Other advantages of Raman spectroscopy include: 1) minimum sample preparation and less amount of sample requirement; 2) great capability for on-line kinetics study in a controlled environment as the short spectra collection interval (i.e. several seconds); 3) relatively low photo energy (886-1653 mev) compared with XRD (124 ev-124 kev), so less chance of phase transition caused by equipment operation (136).

When lights hit on a subject, the photons can be absorbed, scattered, interact with the subject or just pass through it without any interaction. If the energy of the incident photons is between the ground state and the excited state of a molecule, photons can be absorbed and the molecule therefore encouraged to the higher energy level. The energy difference between the incident light and the radiated light is then expressed as the absorption spectroscopy. But it is also possible that protons scatter from the object without any absorption (136).

Scattering is a common technique that has been widely applied, for instance in particle size and shape measurements. While, the most prevalent scattering technique for molecule identification has to be Raman scattering (136). In this technique, the incident light interacts with molecules, alters the electron cloud outside of the nuclei in order to generate a "virtual state" (see Figure 2.35 (a)). Photons at this level are not stable; they will be radiated again in a very short period. Then, if the molecule returns back to its vibrational state that denotes there was no energy transition, so Rayleigh scattering occurs. In the case of stoke Raman scattering, the molecule returns to a higher state, the photon loses energy, hence have a longer wavelength than its original condition. The anti-stokes Raman scattering is the opposite case (137).
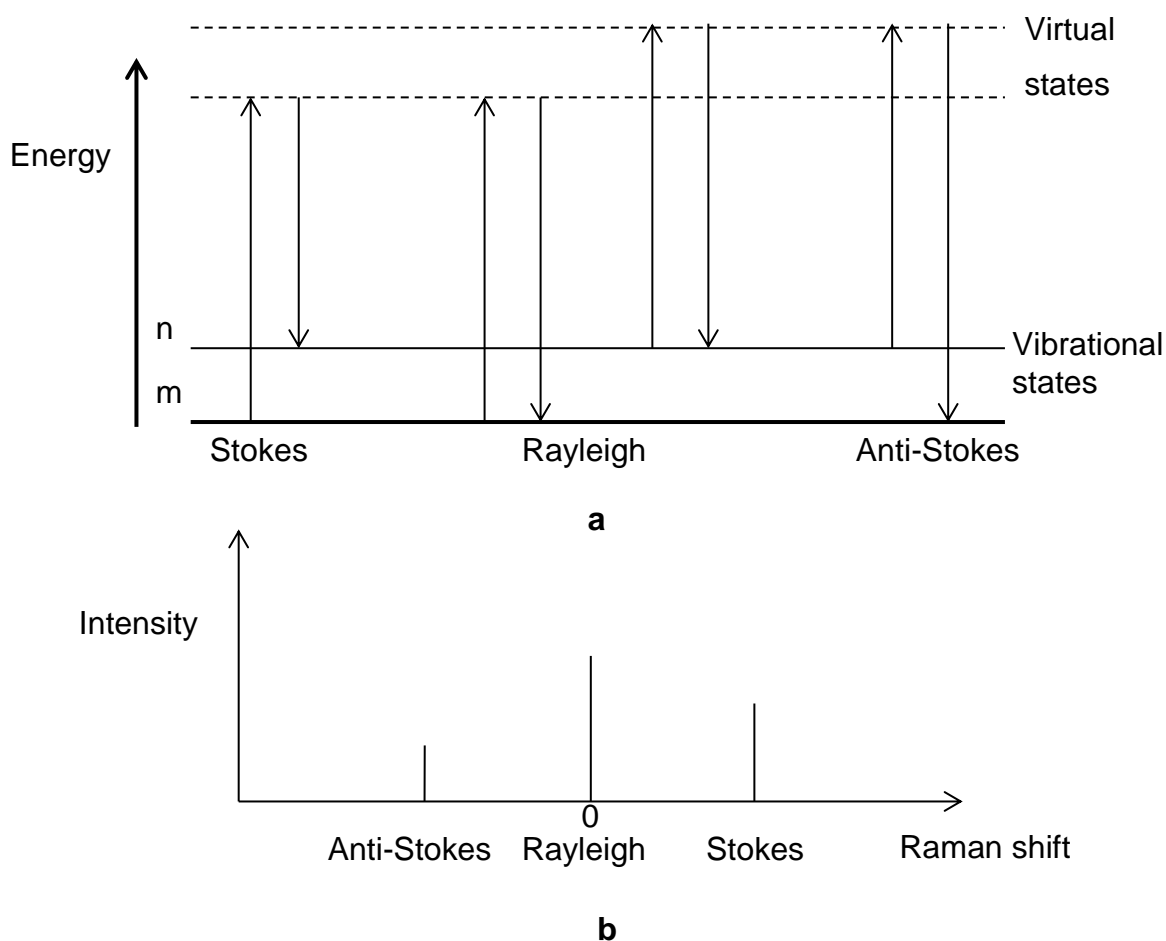
Figure 2.35: (a) Energy level diagram showing Rayleigh and Raman scattering for a certain wavelength (m is the lowest energy vibrational state). Both of the low energy (upward arrows) and the scattered energy (downward arrows) have higher energy compared with the vibration energy. (b) A Raman spectrum corresponding to (a) (136, 137).

Rayleigh scattering happens when there is only electron cloud distortion. It is an elastic scattering. However, if the nuclear motion is involved in the scattering process, an energy transfer will occur among incident photons, molecules and scattered photons. This time is an inelastic scattering and the energy difference between the incident photon and the scattered photon is one vibrational unit. This is called Raman scattering. The intensities of both Rayleigh scattered light and Raman scattered light are proportional to the number of molecules being irradiated (136).

Raman spectrum is a plot that shows the intensity of Raman scattering vs. wavelength (see Figure 2.35 (b)). The X axis is called Raman shift which is the difference between the excitation wavelength and Raman wavelength indicated in wavenumbers. The wavenumber indicates the number of waves every centimetre, it is the reciprocal of wavelength and the unit of wavelength is 'cm'. For instance, a near infrared laser beam has a wavelength of 785 nm (785×10^{-7}cm), a wavenumber 12738.85 of cm^{-1}. The wave number is a unit of energy (E), therefore the relationship can be expressed as:

$$E = hv = \frac{hc}{\lambda} = hcw$$
(Eq. 2.41)

where h: Planck's constant;

    v: the frequency of light (Hz);

    λ: the wavelength of light (cm);

    c: the speed of the light (m/s);

    w: the wavenumber of the light (cm^{-1}).

At thermal equilibrium the ratio of the molecules in one vibrational state to another can be explained by the Boltzmann distribution (137):

$$N_1/N_0 = \left(g_1/g_0\right)exp[-(\Delta E)/kT]$$
(Eq. 2.42)

where N_1/N_0 is the ratio of the number of molecules in a higher vibrational energy level to the lower one; g_1/g_0 describes the degeneracy of the higher vibrational level to the lower one; ΔE represents energy difference between the higher and lower level; k is the Boltzmann constant; T is temperature with unit K (137).

Therefore, the sample temperature can be calculated by comparing the difference in the intensity of the stokes and anti-stokes scattering according to Equation 2.42.

2.6.1.2   Raman peak intensity

The Raman scattering intensity corresponds to the amount of molecules being irradiated, which is the principle of quantitative analysis by applying Raman spectroscopy. Besides, the incident laser intensity or frequency also has an

impact on the Raman peak intensity. The equation for obtaining peak intensity was given by Pelletier (137).

2.6.1.3 Molecular vibrations

Molecules are considered atomic nuclei linked through chemical bonds. For the diatomic molecules, the vibrational frequency ω expresses as:

$$\omega = \frac{1}{2\pi c}\left(\frac{k}{\mu_r}\right)^{1/2}$$
(Eq. 2.43)

where k is known as the force constant and μ_r is the reduced mass of the atoms $(m_1 m_2/(m_1 + m_2)$.

The tenser the chemical bonds the larger k is, therefore the higher vibrational frequency will be obtained. For instance, the frequency of two carbon atoms is varying with the connection bond, where $C \equiv C > C = C > C - C$. Increasing the mass of one or both atoms will have the opposite impact on the frequency (136).

For a triatomic molecule three vibrational modes exist, which are bending, symmetrical and asymmetrical stretching, see the scheme in Figure 2.36. This figure also illustrates molecular rotations which generates Raman scattering.
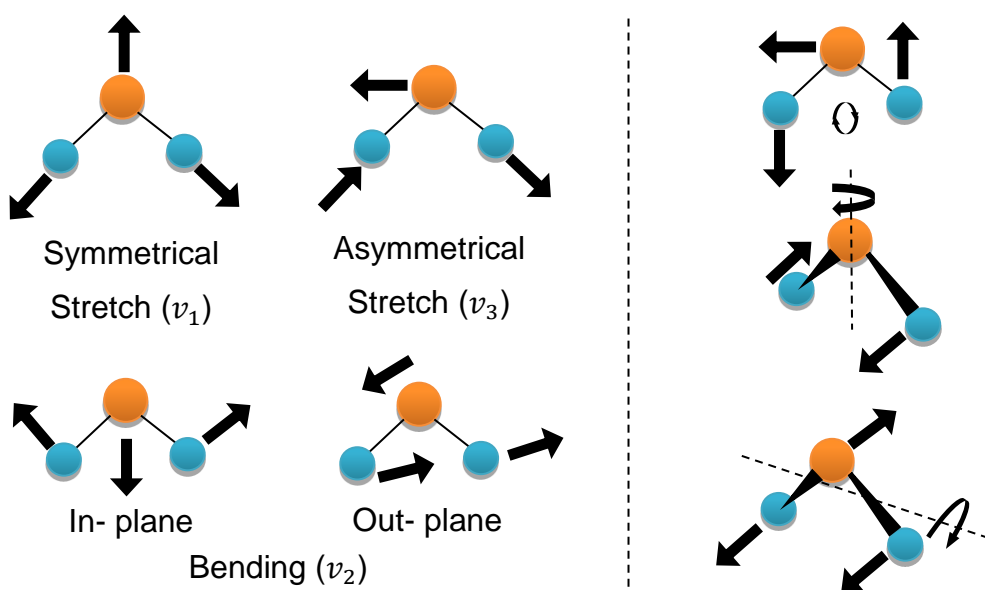
Figure 2.36: Molecular vibrations and rotations causing Raman scattering

There are 10 possible reasons that can cause alteration on the Raman spectra (i.e. peak intensity, width, depolarization ratio or the integrated area), which are (137):

1. Chemical equilibrium change (influence product and raw material composition, system pH, bond formation and decomposition, etc.);
2. Phase variation;
3. Density change;
4. Temperature change;
5. Pressure change;
6. Crystal lattice deformation;
7. Refractive index change;
8. Vibrational or rotational excited-level distribution alteration;
9. Vibrational or rotational lift time alteration;
10. Vibrational anharmonicity.

2.6.1.4 The application of Raman spectroscopy analytical technique

The purpose of using Raman spectroscopy is to determine some information, such as identity, composition, form of crystals or the orientation of molecules, of detected samples. This information can be achieved through analysing Raman spectra, for example, the intensity, width, shape, area or position of peaks. Figure 2.37 gives the Raman spectra information of compounds that will be studied in this work. The representative peak position of each compound will be used to determine the change in composition of each compound through experiments. The peak intensity and under peak areas would be useful for the quantitative analysis in future work.
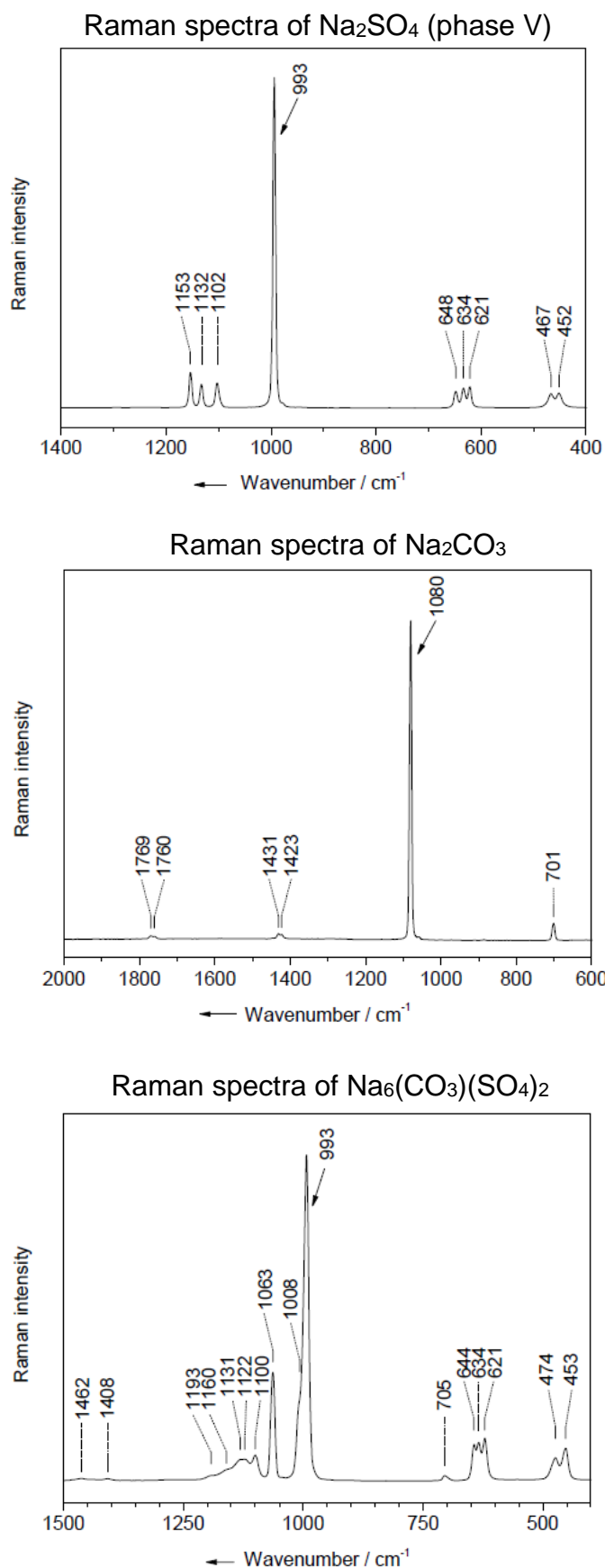
Figure 2.37: Raman spectra of Na₂SO₄, Na₂CO₃ and Burkeite in solid state (138)

2.6.1.4.1 Qualitative analysis

Raman peak position gives the information for determining functional groups. Relative peak height can illustrate the approximate number of different functional groups in the present sample. Shift in position of a functional peak can represent adjacent electron donating or withdrawing groups, or isomerization or phase change. Manual qualitative analysis of spectra is time consuming. Normally a chemometric method can be used such as principal component analysis (PCA). However, the system for this study is a known composition. So qualitative analysis of Raman spectra will not be discussed at length here.

2.6.1.4.2 Quantitative analysis

The quantitative analysis is based upon some measurement of the peak intensity of a detected sample being linearly proportional to the concentration of this sample. A calibration curve is a plot of the area of sample peaks (integrated intensity) vs. concentration, it is better to be a straight line. A least squares fit is normally applied to the calibration curve to generate an equation which can be used for predicting the concentration of the detected sample from the Raman peak area.

Apart from the object concentration, many other factors can influence the measurement of the peak area or intensity, for instance, the colour or material of the container, sample preparation process. Therefore, an internal standard, which would not change with the alternative concentration of the detected sample, must be set up before creating the calibration curve. Raman peak overlap is a very common phenomenon. So the analysed area of the analyte peak may comprise the peak area of other substances Figure 2.38. As long as those other peaks do not vary in shape or area with concentration changes in the detected substance. The calibration curve would still be linear and offering the precise prediction of the analyte concentration (137).

There are many analytical softwares (i.e. Fytik, Origin) which have the function of reducing the effect of the overlap peaks by separating them, such as curve fitting or de-convolution (139) (140) (141). These methods are very useful and practical when the shape and position of peaks are known. For instance, to find out the peak area by curve fitting, when the shape and position are

already known, the result will be more accurate than just using the integration method, especially as there are lots of noises which appear on the spectra (137). Spectra that are pre-processed by this software will be then readily used for developing calibration models.

For instance, in order to achieve the amount of Na_2SO_4 and $Na_2Mg(SO_4)_2 \cdot 4H_2O$ in the mixture in Figure 2.38, one of the possible methods can be processed as follows: 1. Prepare several well mixed powder samples of Na_2SO_4 and $Na_2Mg(SO_4)_2 \cdot 4H_2O$ with different composition; 2. Measure the Raman spectrum of each sample; 3. Apply one of the data processing software (i.e. Fityk) to separate overlapped peaks to achieve the relation of peak intensity vs. concentration for each substance; 4. Apply another software that contains chemometric packages which can be used for developing calibration models, such as GRAMS/AI spectroscopy software.
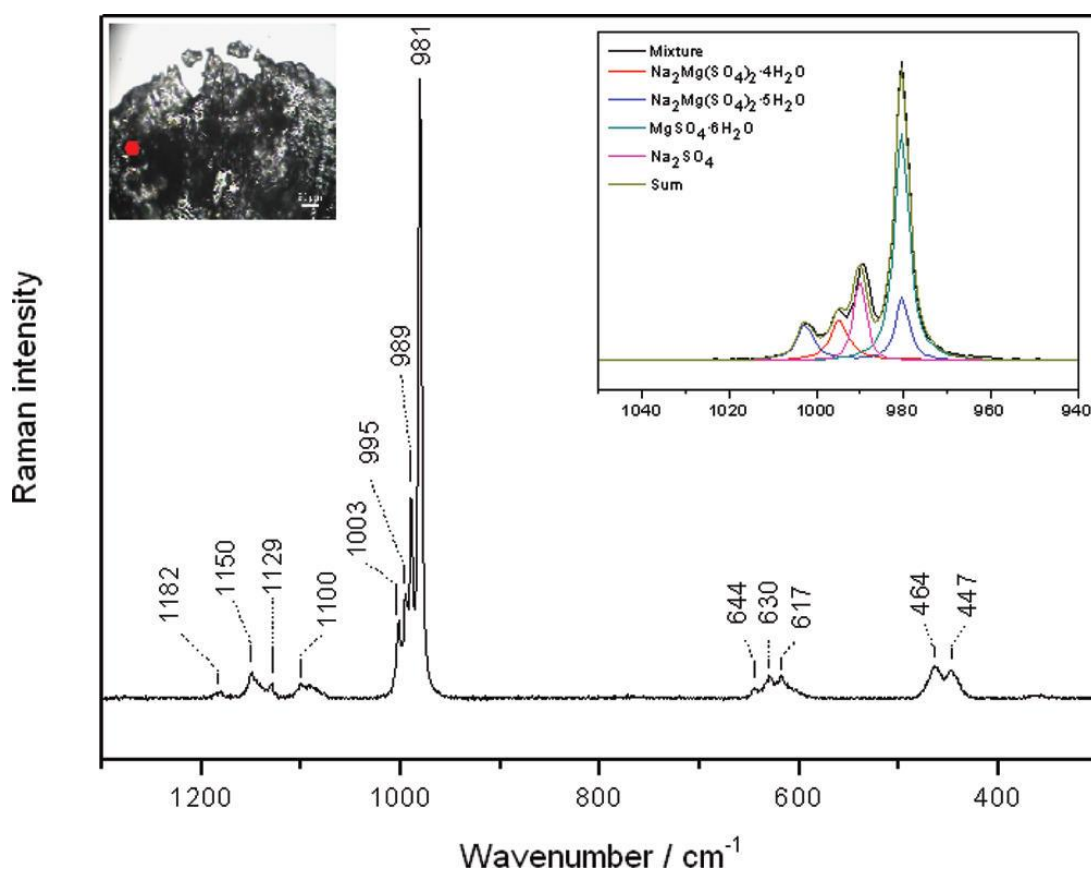
Figure 2.38: Raman spectrum of a dried droplet of $MgSO_4$-Na_2SO_4 solution with a molar ratio of 1:1 (142).

2.6.2 X-Ray Diffraction

X-rays are the products of a type of electromagnetic radiation, which have a wavelength ranging from 0.1-500Å (143). They are produced by rapidly decelerating electrically charged particles and converting the kinetic energy (KE) into radiation. However, the X-rays achieved are only from a small fraction of the total energy, the remaining energy releases as heat. Because only a small portion of electrons can be completely decelerated emitting the highest energy radiation, the rest of the electrons were partially decelerated to diverse stages generating a broad band of radiation known as white radiation. The KE of electrons that were accelerated toward the electrode can be calculated using Equation 2.44.

$$KE = eV = \frac{1}{2}mv^2$$ (Eq. 2.44)

where V represents the voltage across the electrodes, e and m are the charge and mass of an electron, respectively. v is the velocity of the electron on impact.

2.6.2.1   Filters and Monochromators

X-ray diffraction experiments require a monochromatic beam source. However, the source generated in the laboratory contained both K_α, K_β and white radiation (see Figure 2.39), among which only K_α is the desirable one (144). Therefore, a filter is required to remove the unwanted radiations. The principle of choosing a proper filter is to select the one only one atomic number below the target material. So the K absorption edge of the filter would lie between K_α and K_β of the target material, in order to increase the relative intensity of K_α/K_β (Figure 2.40).

In addition, a monochromator should be also used to further separate $K_{\alpha2}$ from $K_{\alpha1}$. A single cut crystal with a strong reflection feature would be the appropriate candidate, such as graphite, this theory follows Bragg's Law.
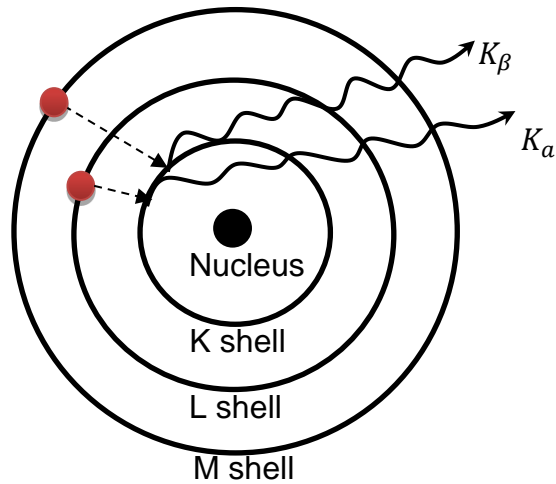
Figure 2.39: Electronic transition produces K_α and K_β X-ray
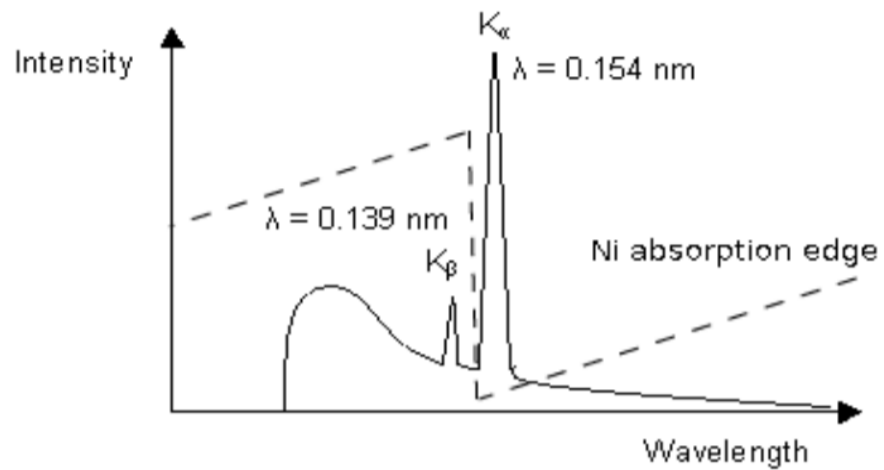
Figure 2.40: Obtaining the characteristic radiation by using a filter (in this case is Ni)(144)

2.6.2.2   Braggs Law
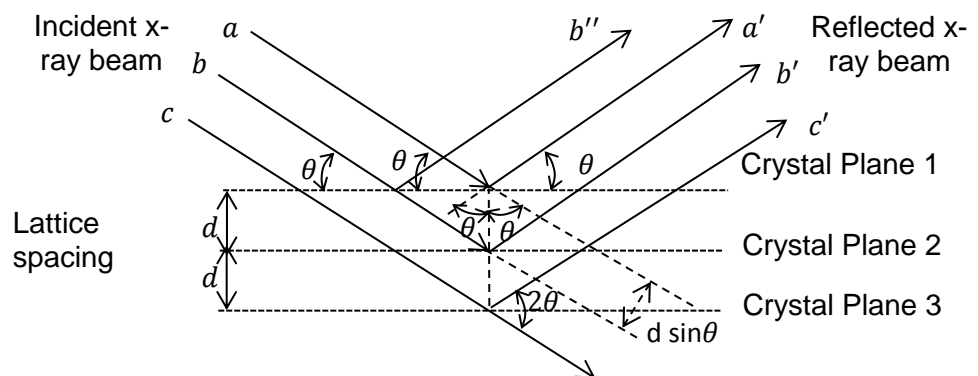
Figure 2.41: Two parallel incident rays on two parallel planes.

Considering a crystal comprises a repeating set of plans with an equal distance d, which is known as interplanar spacing. Assuming a beam of incident x-ray beam irradiates onto the paralleled planes with an angle of θ. The electrons start vibrating after being hit by the beam, then the beam will be radiated in all directions. However, only the ones with a particular direction will be in phase and detected. For instance, in Figure 2.41 reflected beam b' and b'' are in phase. The diffracted ray a', b' and c' will in phase if interplaner spacing is an integral number of wavelengths λ, it is Bragg's law (see Equation 2.45) (145)

$$n\lambda = 2dsin\theta \qquad \text{(Eq. 2.45)}$$

where n is an integer denoting the order of the diffraction beam;

λ is the wavelength of the X-ray beam;

d is the distance between neighbouring planes of atoms;

θ is the angle between incident rays and the surface.

2.6.2.3 Powder X-ray diffraction

Powder X-ray diffraction (PXRD) is a routinely analytical technique for phase identification of crystalline materials, through which the unit cell information can be obtained. It has the advantage of less sample preparation and it is easy to operate. This technique, combined with the Rietveld refinement, can also be applied for the quantitative analysis of a solid mixture.

The measurement is carried out on a collection of microscopic crystals, theoretically, every single crystal is randomly orientated. When the sample is rotated, the diffracted radiation is in a cone shape, and each of the cones represents a crystallographic plane hkl (see Figure 2.42).
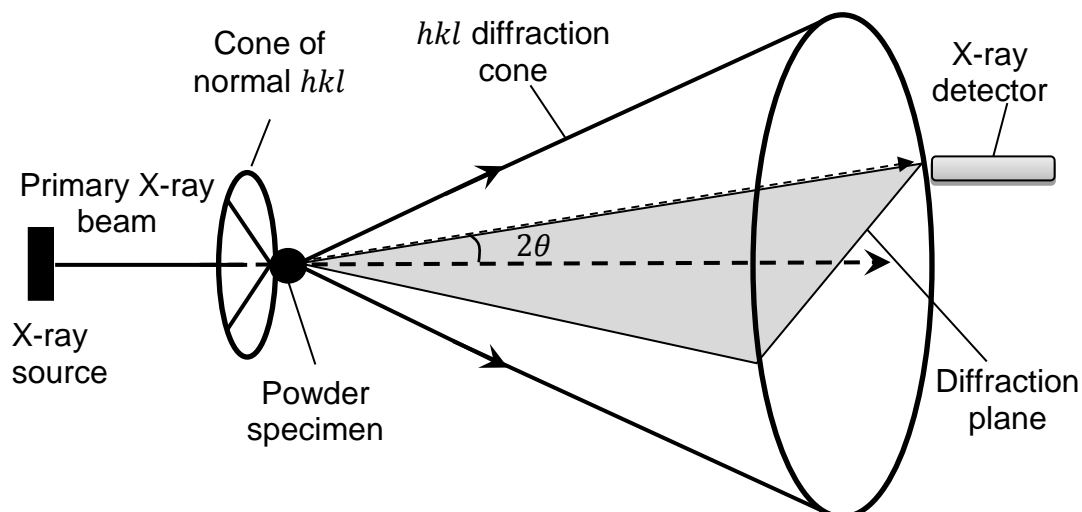
Figure 2.42: A schematic diagram of cone-shaped X-ray diffraction from a powder specimen (146).

The Bragg-Brentano diffractometer uses a different geometry compared with the previous case. As Figure 2.43 illustrates the sample's position is fixed, the source and detector rotate simultaneously in opposite directions via the goniometer circle (147).
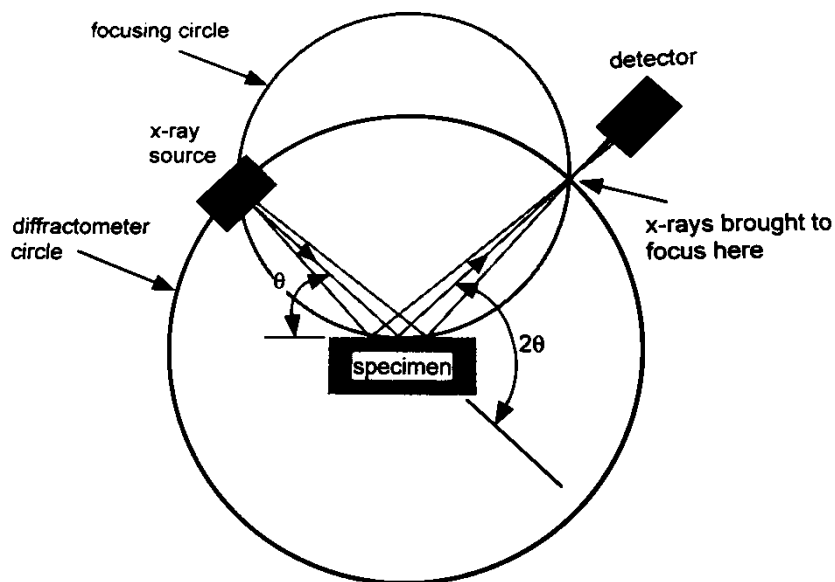
Figure 2.43: Geometry of the Bragg-Brentano diffractometer (146).

2.7 Conclusion

This chapter elaborated the fact that the process condition has a great impact on the composition of a laundry slurry system, which will further alter the property and performance greatly of final dry laundry products. Out of the ordinary thinking and analysis, current study aims to establish an applicable method that allows simultaneous on-line monitoring and studying the phase and composition variation of different components in a multi-component system, which compensates deficiencies of previous arts. The method will allow the laundry industry to follow and record all the changes in the slurry that happened throughout the process, find fundamental causes and further assist to optimise the production protocol.

The crystallisation science was reviewed from both thermodynamic and kinetic aspects that is significantly beneficial to investigate a feasible method for assessing the crystallisation kinetics of a complex multi-type-crystals system. Understanding the concept of solubility product together with sodium silicate properties provides an insight into how solution chemistry interferes with the dissolution and crystallisation process of sodium salts.

The phase equilibrium rules were reviewed, as well as the application of it on the phase diagram development, which has significantly contributed to the ternary phase diagram determination in Chapter 5.

Finally, the primary analytical technique for this work was chosen with regard to its advantages and the characteristic theories were reviewed. This contributes to understanding the instrument working principles comprehensively, thereby eliminating the measurement deviation caused by operating the instrument improperly.

Reference List

1.	Mullin, J.W. 3 - Solutions and solubility. In: *Crystallization (Fourth Edition)*. Oxford: Butterworth-Heinemann, 2001, pp.86-134.

2.	Okorafor, O.C. Solubility and density isotherms for the sodium sulfate-water-methanol system. *Journal of Chemical & Engineering Data.* 1999, **44**(3), pp.488-490.

3.	GESTIS Substance Database. [Online].

4.	Opgrande, J.L., Brown, E. E., Hesser, M. and Andrews, J. *Benzoic Acid. Kirk-Othmer Encyclopedia of Chemical Technology.* . 16-05-2003.

5.	Garrett, D.E. *Sodium sulfate: Handbook of Deposits, Processing, Properties and Use.* California: Academic Press, 2001.

6.	Wells, R.C. *Sodium sulphate: its sources and uses.* US Government Printing Office, 1923.

7.	Bialik, M.A., Sedin, P., Theliander, H., Verrill, C.L. and DeMartini, N.A. Model for Solubility and Solid Phase Composition in High-Temperature Na 2 Co 3-Na 2 So 4 Solutions. In: *The 2006 Annual Meeting*, 2006.

8.	Denbigh, K. The principles of chemical equilibrium. *Cambridge University Press, Cambridge.* 1966, p.287.

9.	Melssner, H. and Kusik, C. Double salt solubilities. *Industrial & Engineering Chemistry Process Design and Development.* 1979, **18**(3), pp.391-394.

10.	Gautier, Q., Bénézeth, P., Mavromatis, V. and Schott, J. Hydromagnesite solubility product and growth kinetics in aqueous solution from 25 to 75° C. *Geochimica et Cosmochimica Acta.* 2014, **138**, pp.1-20.

11.	Outhwaite, C.W. Extension of the Debye–Hückel theory of electrolyte solutions. *The Journal of Chemical Physics.* 1969, **50**(6), pp.2277-2288.

12.	Li, L. and Page, C. Modelling of electrochemical chloride extraction from concrete: influence of ionic activity coefficients. *Computational Materials Science.* 1998, **9**(3), pp.303-308.

13.	Carter, R., Pierson, K.L. and Reynolds, J.G. Binary Pitzer Model Parameters for Predicting the Solubility of Key Electrolytes in Hanford Waste–14215.

14.	Park, H. and Englezos, P. Osmotic coefficient data for Na 2 SiO 3 and Na 2 SiO 3–NaOH by an isopiestic method and modeling using Pitzer's model. *Fluid phase equilibria.* 1998, **153**(1), pp.87-104.

15. Park, H. and Englezos, P. Osmotic coefficient data for NaOH–NaCl–NaAl (OH) 4–H 2 O system measured by an isopiestic method and modeled using Pitzer's model at 298.15 K. *Fluid phase equilibria.* 1999, **155**(2), pp.251-259.

16. Pitzer, K.S. and Mayorga, G. Thermodynamics of electrolytes. II. Activity and osmotic coefficients for strong electrolytes with one or both ions univalent. *The Journal of Physical Chemistry.* 1973, **77**(19), pp.2300-2308.

17. Pitzer, K.S. and Kim, J.J. Thermodynamics of electrolytes. IV. Activity and osmotic coefficients for mixed electrolytes. *Journal of the American Chemical Society.* 1974, **96**(18), pp.5701-5707.

18. Pabalan, R.T. and Pitzer, K.S. Thermodynamics of concentrated electrolyte mixtures and the prediction of mineral solubilities to high temperatures for mixtures in the system Na-K-Mg-Cl-SO 4-OH-H 2 O. *Geochimica et Cosmochimica Acta.* 1987, **51**(9), pp.2429-2443.

19. Pitzer, K.S. Thermodynamics of electrolytes. V. Effects of higher-order electrostatic terms. *Journal of Solution Chemistry.* 1975, **4**(3), pp.249-265.

20. Dokoumetzidis, A. and Macheras, P. A century of dissolution research: from Noyes and Whitney to the biopharmaceutics classification system. *International journal of pharmaceutics.* 2006, **321**(1), pp.1-11.

21. Buckton, G. and Beezer, A.E. The relationship between particle size and solubility. *International journal of pharmaceutics.* 1992, **82**(3), pp.R7-R10.

22. Parfitt, G. Fundamental aspects of dispersion. *Dispersion of powder in liquids, 2nd edn. Wiley & Sons, New York.* 1973, pp.1-43.

23. Skinner, L.M. and Sambles, J.R. The Kelvin equation—a review. *Journal of Aerosol Science.* 1972, **3**(3), pp.199-210.

24. Bentley, A.O. and Rawlins, E.A. *Bentley's textbook of pharmaceutics.* London: Baillière Tindall, 1977.

25. Ricci, J.E. *The phase rule and heterogeneous equilibrium.* Van Nostrand, 1951.

26. Mullin, J.W. 4 - Phase equilibria. In: *Crystallization (Fourth Edition).* Oxford: Butterworth-Heinemann, 2001, pp.135-180.

27. Kobe, K.A. and Sheehy, T.M. Thermochemistry of sodium carbonate and its solutions. *Industrial & Engineering Chemistry.* 1948, **40**(1), pp.99-102.

28. Mullin, J.W. *Crystallization.* Butterworth-Heinemann, 2001.

29. Chiarella, R.A., Davey, R.J. and Peterson, M.L. Making Co-CrystalsThe Utility of Ternary Phase Diagrams. *Crystal Growth & Design.* 2007, **7**(7), pp.1223-1226.

30. Hubert, N., Bouroukba, M. and Schuffenecker, L. Aqueous solution of sodium sulfate. Determination of the dissolution enthalpy at 25, 27.5 and 45 C. *Thermochimica acta.* 1995, **259**(1), pp.41-48.

31. Rodriguez-Navarro, C., Doehne, E. and Sebastian, E. How does sodium sulfate crystallize? Implications for the decay and testing of building materials. *Cement and concrete research.* 2000, **30**(10), pp.1527-1534.

32. Washburn, E.W. Two-Component Systems—Aqueous. In: *International Critical Tables of Numerical Data, Physics, Chemistry and Technology (1st Electronic Edition).* Knovel.

33. Washburn, E.W. B-Table: Standard Arrangement. In: *International Critical Tables of Numerical Data, Physics, Chemistry and Technology (1st Electronic Edition).* Knovel.

34. Washburn, E.W. B-Table: Solutions of More Than One Solute Where at Least One of the Solutes is a Strong Electrolyte. In: *International Critical Tables of Numerical Data, Physics, Chemistry and Technology (1st Electronic Edition).* Knovel.

35. Shaikh, A.A., Salman, A.D., Mcnamara, S., Littlewood, G., Ramsay, F. and Hounslow, M.J. In situ observation of the conversion of sodium carbonate to sodium carbonate monohydrate in aqueous suspension. *Industrial & Engineering Chemistry Research.* 2005, **44**(26), pp.9921-9930.

36. Reddy, L.K. *Principles of engineering metallurgy.* New Age International, 2007.

37. Green, S.J. and Frattali, F.J. The System Sodium Carbonate-Sodium Sulfate-Sodium Hydroxide-Water at 100° 1. *Journal of the American Chemical Society.* 1946, **68**(9), pp.1789-1794.

38. Shi, B. and Rousseau, R.W. Structure of burkeite and a new crystalline species obtained from solutions of sodium carbonate and sodium sulfate. *The Journal of Physical Chemistry B.* 2003, **107**(29), pp.6932-6937.

39. Bayuadri, C. *Stability of Sodium Sulfate Dicarbonate (~ 2Na2CO3• Na2SO4) Crystals.* thesis, Georgia Institute of Technology, 2006.

40. Chalmers, B. *Principles of solidification.* Krieger Pub Co, 1977.

41.   Davey, R.J. and Garside, J. *From molecules to crystallizers.* Oxford: Oxford University Press, 2000.

42.   Myerson, A.S. *Handbook of industrial crystallization.* [Online]. 2nd ed. Boston: Butterworth-Heinemann,, 2002.

43.   Vekilov, P.G. The two-step mechanism of nucleation of crystals in solution. *Nanoscale.* 2010, **2**(11), pp.2346-2357.

44.   Kashchiev, D. *Nucleation: basic theory with applications. 2000.* Butterworth Heinemann: Boston.

45.   Kashchiev, D., Borissova, A., Hammond, R.B. and Roberts, K.J. Effect of cooling rate on the critical undercooling for crystallization. *Journal of Crystal Growth.* 2010, **312**(5), pp.698-704.

46.   Kashchiev, D., Borissova, A., Hammond, R.B. and Roberts, K.J. Dependence of the critical undercooling for crystallization on the cooling rate. *The Journal of Physical Chemistry B.* 2010, **114**(16), pp.5441-5446.

47.   Corzo, D.M.C., Borissova, A., Hammond, R.B., Kashchiev, D., Roberts, K.J., Lewtas, K. and More, I. Nucleation mechanism and kinetics from the analysis of polythermal crystallisation data: methyl stearate from kerosene solutions. *CrystEngComm.* 2014, **16**(6), pp.974-991.

48.   Davey, R. and Garside, J. *From molecules to crystallizers.* Oxford University Press, 2000.

49.   Coupland, J.N. Crystallization in emulsions. *Current Opinion in Colloid & Interface Science.* 2002, **7**(5–6), pp.445-450.

50.   McCabe, W.L., Smith, J.C. and Harriott, P. *Unit operations of chemical engineering.* McGraw-Hill New York, 1993.

51.   Camacho Corzo, D.M. *Crystallisation in Diesel and Biodiesel Fuel in Relation to their Solution Composition.* thesis, University of Leeds, 2015.

52.   Richardson, J.F., Harker, J.H. and Backhurst, J.R. CHAPTER 15 - Crystallisation. In: *Chemical Engineering (Fifth Edition).* Oxford: Butterworth-Heinemann, 2002, pp.827-900.

53.   Kashchiev, D. and Van Rosmalen, G. Review: nucleation in solutions revisited. *Crystal Research and Technology.* 2003, **38**(7- 8), pp.555-574.

54.   Kim, K.-J. and Mersmann, A. Estimation of metastable zone width in different nucleation processes. *Chemical Engineering Science.* 2001, **56**(7), pp.2315-2324.

55. Sangwal, K. A novel self- consistent Nývlt- like equation for metastable zone width determined by the polythermal method. *Crystal Research and Technology.* 2009, **44**(3), pp.231-247.

56. Meenan, P. *Experimental and theoretical studies on the nucleation, growth and habit modification of some inorganic carbonates, phosphates and sulphates.* thesis, University of Strathclyde, 1992.

57. Turner, T.D. *Molecular Self-Assembly, Nucleation Kinetics and Cluster Formation Associated with Solution Crystallisation.* thesis, University of Leeds, 2015.

58. *crystallography.* 1st edition. S.v. ed. s.v., 2003.

59. Choi, B.-K. and Lockwood, D. Raman spectrum of Na2SO4 (phase V). *Solid state communications.* 1989, **72**(1), pp.133-137.

60. Choi, B.-K., Labbé, H. and Lockwood, D. Raman spectrum of Na 2 SO 4 (phase III). *Solid state communications.* 1990, **74**(2), pp.109-113.

61. Kracek, F. and Gibson, R. The Polymorphism of Sodium Sulphate. III. *The Journal of Physical Chemistry.* 1930, **34**(1), pp.188-206.

62. Eysel, W., Höfer, H., Keester, K. and Hahn, T. Crystal chemistry and structure of Na2SO4 (I) and its solid solutions. *Acta Crystallographica Section B: Structural Science.* 1985, **41**(1), pp.5-11.

63. Davies, J.E.D. and Sandford, W.F. Solid-state vibrational spectroscopy. Part IV. A vibrational and differential scanning calorimetry study of the polymorphism of sodium and potassium sulphates. *Journal of the Chemical Society, Dalton Transactions.* 1975, (19), pp.1912-1915.

64. Rasmussen, S.E., Jørgensen, J.-E. and Lundtoft, B. Structures and phase transitions of Na2SO4. *Journal of applied crystallography.* 1996, **29**(1), pp.42-47.

65. Lewin, S. *The solubility product principle: an introduction to its uses and limitations.* Pitman, 1960.

66. Brouns, E., Visser, J. and De Wolff, P. An anomaly in the crystal structure of Na2CO3. *Acta Crystallographica.* 1964, **17**(5), pp.614-614.

67. Meenan, P., Roberts, K., Knight, P. and Yuregir, K. The influence of spray drying conditions on the particle properties of recrystallized burkeite (Na2 CO3·(Na2SO4)2). *Powder technology.* 1997, **90**(2), pp.125-130.

68. Βαβουράκη, A. Crystallization and dissolution of electrolyte salts. 2009.

69.   Hamilton, A. and Menzies, R.I. Raman spectra of mirabilite, Na2SO4· 10H2O and the rediscovered metastable heptahydrate, Na2SO4· 7H2O. *Journal of Raman Spectroscopy.* 2010, **41**(9), pp.1014-1020.

70.   Arakcheeva, A. and Chapuis, G. A reinterpretation of the phase transitions in Na2CO3. *Acta Crystallographica Section B: Structural Science.* 2005, **61**(6), pp.601-607.

71.   Swainson, I., Dove, M. and Harris, M.J. Neutron powder diffraction study of the ferroelastic phase transition and lattice melting in sodium carbonate, Na2CO3. *Journal of Physics: Condensed Matter.* 1995, **7**(23), p.4395.

72.   Harris, M. and Salje, E. The incommensurate phase of sodium carbonate: an infrared absorption study. *Journal of Physics: Condensed Matter.* 1992, **4**(18), p.4399.

73.   Grønvold, F. and Meisingset, K.K. Thermodynamic properties and phase transitions of salt hydrates between 270 and 400 K II. Na2CO3· H2O and Na2CO3· 10H2O. *The Journal of Chemical Thermodynamics.* 1983, **15**(9), pp.881-889.

74.   Kralj, D., Brečević, L. and Kontrec, J. Vaterite growth and dissolution in aqueous solution III. Kinetics of transformation. *Journal of Crystal Growth.* 1997, **177**(3), pp.248-257.

75.   Rosier, M.A. Model to predict the precipitation of burkeite in the multiple-effect evaporator and techniques for controlling scaling. *Tappi journal.* 1997, **80**(4), pp.203-209.

76.   Meenan, P., Roberts, K., Yuregir, K. and Knight, P. The influence of batch processing on the particulate properties of burkeite (Na2CO3 (Na2SO4) 2). *Journal of materials science.* 1995, **30**(12), pp.3115-3122.

77.   Forshag, W. Burkeite, a new mineral species from Searles Lake, California. *Am. Mineral.* 1935, **20**, p.50.

78.   Teeple, J.E. The American Potash Industry and Its Problems. *Industrial & Engineering Chemistry.* 1921, **13**(3), pp.249-252.

79.   Vergouwen, L. Two new occurrences and the Gibbs energy of burkeite. *Mineralogical Magazine.* 1979, **43**(327), pp.341-345.

80.   Giuseppetti, G., Mazzi,F.& Tadini,C. The Crystal Structure of Synthetic burkeite $Na_4SO_4(CO_3)_t(SO_4)_{1-t}$. *Neues Jahrbuch fur Mineralogie.* 1988, **8**.

81. Process for preparing needle-shaped crystal growth modified burkeite detergent additive- patent US4900466.

82. Davey, R. The role of additives in precipitation processes. *Industrial Crystallization.* 1982, **81**, pp.123-135.

83. Nancollas, G. and Zawacki, S. Inhibitors of crystallization and dissolution. *Industrial Crystallization.* 1984, **84**(5), p.1.

84. Davey, R.J. and Mullin, J.W. Growth of the {100} faces of ammonium dihydrogen phosphate crystals in the presence of ionic species. *Journal of Crystal Growth.* 1974, **26**(1), pp.45-51.

85. Shi, B., Frederick, W.J. and Rousseau, R.W. Effects of calcium and other ionic impurities on the primary nucleation of burkeite. *Industrial & Engineering Chemistry Research.* 2003, **42**(12), pp.2861-2869.

86. Euhus, D.D. *Nucleation in Bulk Solutions and Crystal Growth on Heat-Transfer Surfaces during Evaporative Crystallization of Salts Composed of Na_2CO_3 and Na_2SO_4.* thesis, 2003.

87. Bayuadri, C., Verrill, C.L. and Rousseau, R.W. Stability of Sodium Sulfate Dicarbonate (~2Na2CO3·Na2SO4) Crystals Obtained from Evaporation of Aqueous Solutions of Na2CO3 and Na2SO4. *Industrial & Engineering Chemistry Research.* 2006, **45**(21), pp.7144-7150.

88. informatsii, V.u.i.n.i.t., Stephen, H., Stephen, T. and Silcock, H.L. *Solubilities of Inorganic and Organic Compounds: pt. 1-3. Ternary and multicomponent systems of inorganic substance. 1st ed.* Pergamon Press, 1963.

89. Caspari, W.A. The system sodium carbonate–sodium sulphate–water. *Journal of the Chemical Society, Transactions.* 1924, **125**, pp.2381-2387.

90. Harvie, C.E., Møller, N. and Weare, J.H. The prediction of mineral solubilities in natural waters: The Na-K-Mg-Ca-H-Cl-SO 4-OH-HCO 3-CO 3-CO 2-H 2 O system to high ionic strengths at 25 C. *Geochimica et Cosmochimica Acta.* 1984, **48**, pp.723-751.

91. Makarov, S. and Bleiden, V. The polytherm of the Quaternary system Na 2 CO 3-Na 2 SO 4-NaCl-H 2 O and solid solutions of the berkeite type. *Ser. Kim. Izv. Akad. Nauk. SSSR.* 1938, pp.865-892.

92. Shabaline, L.N.M.a.K.N. *Zh. Prikl. Khim.* 1925, **25**, p.1157.

93. Falcone, J.S. The Effect of Degree of Polymerization of Silicates on Their Interactions with Cations in Solution. In: *Soluble Silicates*. American Chemical Society, 1982, pp.133-148.

94. Falcone, J.S. Silicon Compounds: Anthropogenic Silicas and Silicates. *Kirk-Othmer Encyclopedia of Chemical Technology.* 2005.

95. Merrill, R.C. Industrial Applications of the Sodium Silicates-Some Recent Developments. *Industrial & Engineering Chemistry.* 1949, **41**(2), pp.337-345.

96. Deabriges, J. *Process for the manufacture of sodium silicate*. Google Patents. 1982.

97. Weldes, H.H. and Lange, K.R. Properties of soluble silicates. *Industrial & Engineering Chemistry.* 1969, **61**(4), pp.29-44.

98. Bass, J.L. and Turner, G.L. Anion distributions in sodium silicate solutions. Characterization by 29Si NMR and infrared spectroscopies, and vapor phase osmometry. *The Journal of Physical Chemistry B.* 1997, **101**(50), pp.10638-10644.

99. Böschel, D., Janich, M. and Roggendorf, H. Size distribution of colloidal silica in sodium silicate solutions investigated by dynamic light scattering and viscosity measurements. *Journal of colloid and interface science.* 2003, **267**(2), pp.360-368.

100. Dutta, P.K. and Shieh, D.-C. Raman Spectral Study of the Composition of Basic Silicate Solutions. *Applied Spectroscopy.* 1985, **39**(2), pp.343-346.

101. Roggendorf, H., Grond, W. and Hurbanic, M. Structural characterization of concentrated alkaline Silicate Solutions by Si-NMR spectroscopy, FT IR spectroscopy, light scattering, and electron microscopy molecules, colloids, and dissolution artefacts. *Glastech. Ber. Glass Sei. Technol.* 1996, **69**, pp.216-231.

102. Falcone, J.S. *Soluble silicates.* American Chemical Society, 1982.

103. Vail, J.G. and Wills, J.U. Soluble Silicates: Their Properties And Uses, Vol. 2: Technology. 1952.

104. Engelhardt, G. and Michel, D. High resolution 29Si NMR of silicates and zeolites. *J. Wiley, Chichester.* 1987.

105. Belton, D.J., Deschaume, O. and Perry, C.C. An overview of the fundamentals of the chemistry of silica with relevance to biosilicification and technological advances. *FEBS Journal.* 2012, **279**(10), pp.1710-1720.

106. Brawer, S.A. and White, W.B. Raman spectroscopic investigation of the structure of silicate glasses. I. The binary alkali silicates. *The Journal of Chemical Physics.* 1975, **63**(6), pp.2421-2432.

107. Harris, R.K. and Knight, C.T. Silicon-29 nuclear magnetic resonance studies of aqueous silicate solutions. Part 6.—Second-order patterns in potassium silicate solutions enriched with silicon-29. *Journal of the Chemical Society, Faraday Transactions 2: Molecular and Chemical Physics.* 1983, **79**(10), pp.1539-1561.

108. Svensson, I.L., Sjöberg, S. and Öhman, L.-O. Polysilicate equilibria in concentrated sodium silicate solutions. *Journal of the Chemical Society, Faraday Transactions 1: Physical Chemistry in Condensed Phases.* 1986, **82**(12), pp.3635-3646.

109. Hunt, J.D., Kavner, A., Schauble, E.A., Snyder, D. and Manning, C.E. Polymerization of aqueous silica in $H_2O–K_2O$ solutions at 25–200° C and 1bar to 20kbar. *Chemical Geology.* 2011, **283**(3), pp.161-170.

110. Le Losq, C. and Neuville, D.R. Effect of the Na/K mixing on the structure and the rheology of tectosilicate silica-rich melts. *Chemical Geology.* 2013, **346**, pp.57-71.

111. Mähler, J. and Persson, I. A study of the hydration of the alkali metal ions in aqueous solution. *Inorganic chemistry.* 2011, **51**(1), pp.425-438.

112. WU, C.K. Nature of incorporated water in hydrated silicate glasses. *Journal of the American Ceramic Society.* 1980, **63**(7- 8), pp.453-457.

113. Scholze, H. Incorporation of Water in Glasses: I. *Glastech. Ber.* 1959, **32**(3), pp.81-88.

114. Harman, R. Aqueous Solutions of Sodium Silicates. VIII. General Summary and Theory of Constitution. Sodium Silicates as Colloidal Electrolytes. *The Journal of Physical Chemistry.* 1928, **32**(1), pp.44-60.

115. Cann, J.Y. and Gilmore, K. The System Na2O: SiO2: H2O. Relationship between Composition and Boiling Point of Aqueous Solutions of Sodium Silicate. II. *The Journal of Physical Chemistry.* 1928, **32**(1), pp.72-90.

116. Ganguly, P. The Scattering of Light by Aqueous Sodium Silicate Solutions. *The Journal of Physical Chemistry.* 1926, **30**(5), pp.706-712.

117. Nauman, R. and Debye, P. Light-scattering investigations of carefully filtered sodium silicate solutions. *The Journal of Physical Chemistry.* 1951, **55**(1), pp.1-9.

118. Ray, N.H. and Plaisted, R.J. The constitution of aqueous silicate solutions. *Journal of the Chemical Society, Dalton Transactions.* 1983, (3), pp.475-481.

119. Tarutani, T. Chromatographic studies in the field of silicate chemistry. *Journal of Chromatography A.* 1984, **313**, pp.33-45.

120. Gharzouni, A., Joussein, E., Samet, B., Baklouti, S., Pronier, S., Sobrados, I., Sanz, J. and Rossignol, S. The effect of an activation solution with siliceous species on the chemical reactivity and mechanical properties of geopolymers. *Journal of Sol-Gel Science and Technology.* 2015, **73**(1), pp.250-259.

121. Tognonvi, M.T., Massiot, D., Lecomte, A., Rossignol, S. and Bonnet, J.-P. Identification of solvated species present in concentrated and dilute sodium silicate solutions by combined 29 Si NMR and SAXS studies. *Journal of colloid and interface science.* 2010, **352**(2), pp.309-315.

122. Alvarez, R. and Sparks, D.L. Polymerization of silicate anions in solutions at low concentrations. 1985.

123. Malfait, W., Zakaznova-Herzog, V. and Halter, W. Quantitative Raman spectroscopy: High-temperature speciation of potassium silicate melts. *Journal of Non-Crystalline Solids.* 2007, **353**(44), pp.4029-4042.

124. Malfait, W.J. Quantitative Raman spectroscopy: speciation of cesium silicate glasses. *Journal of Raman Spectroscopy.* 2009, **40**(12), pp.1895-1901.

125. Zakaznova-Herzog, V., Malfait, W., Herzog, F. and Halter, W. Quantitative Raman spectroscopy: Principles and application to potassium silicate glasses. *Journal of Non-Crystalline Solids.* 2007, **353**(44), pp.4015-4028.

126. Vidal, L., Joussein, E., Colas, M., Cornette, J., Sanz, J., Sobrados, I., Gelet, J., Absi, J. and Rossignol, S. Controlling the reactivity of silicate solutions: A FTIR, Raman and NMR study. *Colloids and Surfaces A: Physicochemical and Engineering Aspects.* 2016, **503**, pp.101-109.

127. Halasz, I., Agarwal, M., Li, R. and Miller, N. Vibrational spectra and dissociation of aqueous Na2SiO3 solutions. *Catalysis Letters.* 2007, **117**(1-2), pp.34-42.

128. Halasz, I., Agarwal, M., Li, R. and Miller, N. Monitoring the structure of water soluble silicates. *Catalysis Today.* 2007, **126**(1), pp.196-202.

129. Andersson, K.R., Dent Glasser, L.S. and Smith, D.N. Polymerization and Colloid Formation in Silicate Solutions. In: *Soluble Silicates*. American Chemical Society, 1982, pp.115-131.

130. Katsanis, E., Krumrine, P. and Falcone Jr, J. Chemistry of precipitation and scale formation in geological systems. In: *SPE Oilfield and Geothermal Chemistry Symposium*: Society of Petroleum Engineers, 1983.

131. Iler, R.K. The colloid chemistry of silica and silicates. *Soil Science.* 1955, **80**(1), p.86.

132. Brady, A., Brown, A. and Huff, H. The polymerization of aqueous potassium silicate solutions. *Journal of Colloid Science.* 1953, **8**(2), pp.252-276.

133. Marshall, W.L. and Warakomski, J.M. Amorphous silica solubilities—II. Effect of aqueous salt solutions at 25 C. *Geochimica et Cosmochimica Acta.* 1980, **44**(7), pp.915-924.

134. Marshall, W.L. Amorphous silica solubilities—III. Activity coefficient relations and predictions of solubility behavior in salt solutions, 0–350 C. *Geochimica et Cosmochimica Acta.* 1980, **44**(7), pp.925-931.

135. Dove, P.M. and Crerar, D.A. Kinetics of quartz dissolution in electrolyte solutions using a hydrothermal mixed flow reactor. *Geochimica et Cosmochimica Acta.* 1990, **54**(4), pp.955-969.

136. Smith, E. and Dent, G. *Modern Raman spectroscopy: a practical approach.* Wiley. com, 2005.

137. Pelletier, M.J. *Analytical Applications of Raman Spectroscopy.* Wiley, 1999.

138. Vargas Jentzsch, P., Ciobotă, V., Rösch, P. and Popp, J. Reactions of alkaline minerals in the atmosphere. *Angewandte Chemie International Edition.* 2013, **52**(5), pp.1410-1413.

139. Smith, C.A., Want, E.J., O'Maille, G., Abagyan, R. and Siuzdak, G. XCMS: processing mass spectrometry data for metabolite profiling using nonlinear peak alignment, matching, and identification. *Analytical chemistry.* 2006, **78**(3), pp.779-787.

140. Wojdyr, M. Fityk: a general-purpose peak fitting program. *Journal of applied crystallography.* 2010, **43**(5 Part 1), pp.1126-1128.

141. Sánchez-Pastor, N., Oehlerich, M., Astilleros, J.M., Kaliwoda, M., Mayr, C.C., Fernández-Díaz, L. and Schmahl, W.W. Crystallization of ikaite and its

pseudomorphic transformation into calcite: Raman spectroscopy evidence. *Geochimica et Cosmochimica Acta.* 2016, **175**, pp.271-281.

142. Vargas Jentzsch, P., Kampe, B., Rösch, P. and Popp, J.r. Raman spectroscopic study of crystallization from solutions containing MgSO4 and Na2SO4: Raman spectra of double salts. *The Journal of Physical Chemistry A.* 2011, **115**(22), pp.5540-5546.

143. Evans, H.T. Essential of Crystallography. *Eos, Transactions American Geophysical Union.* 1988, **69**(11), pp.156-156.

144. Aichinger, H., Dierker, J., Joite-Barfuß, S. and Säbel, M. Production and Measurement of X-rays. In: *Radiation Exposure and Image Quality in X-Ray Diagnostic Radiology.* Springer, 2012, pp.13-20.

145. Harding, M.M. X-ray structure determination, a practical guide edited by GH Stout and LH Jensen. *Acta Crystallographica Section A: Foundations of Crystallography.* 1992, **48**(3), pp.407-407.

146. Aslanov, L.A., Fetisov, G.V. and Howard, J. *Crystallographic instrumentation.* Oxford University Press, 1998.

147. Ladd, M.F.C., Palmer, R.A. and Palmer, R.A. *Structure determination by X-ray crystallography.* Springer, 1985.

Chapter 3 **Material and Methodology**

3.1 Introduction

This chapter provides information on the materials used in this study together with the experimental methodologies in order to address the aims and objectives set by this project. This chapter starts with introducing the materials used in the subsequent experiments; the procedures of each experiment are also described in detail (see Figure 3.1).

Chapter 4	Chapter 5	Chapter 6
• High purity Burkeite generation; • Solution, slurry and solid state Raman spectroscopy; • X-ray diffraction of the preferable orientation elimination	• Na_2CO_3-H_2O-Na_2SO_4 ternary phase diagram determination; • Kinetics studies of the sodium double salt Burkeite	• The impact of solution conditions (i.e. water level, pH & sodium silicate) on Na_2CO_3 and Na_2SO_4 slurry system; • Sodium silicate (de-)polymerisation

Figure 3.1: Experimental work involved in this study.

3.2 Materials

The experimental work was carried out using sodium carbonate (Na_2CO_3) and sodium sulphate (Na_2SO_4) inorganic salt with a size cut of 150-250 μm and 45 wt% sodium silicate solution (1.6 and 3.2 ratios) provided by Procter & Gamble (UK). The polymorphic form V of Na_2SO_4 was detected and confirmed using Bruker D8 advance powder X-ray diffraction. Sodium carbonate monohydrate ($Na_2CO_3 \cdot H_2O$) > 99.9% was purchased from Sigma Aldrich.

Burkeite was synthesised following the procedure in section 3.3.1, and the purity was also confirmed by XRD.

3.3 Experimental Methodology

3.3.1 High Purity Burkeite Generation

An automated reactor system was used to carry out the Burkeite crystallisation experiments (Figure 3.2). This set-up consists of 4 separate glass reactors that operate with glass impellers (2.5 cm in diameter). The rotation speed of the impeller can be adjusted individually through a switch box connected to the automated system. A turbidity probe can also be added to the system if required. The system was temperature controlled using an oil heating system known as 'HEL Julabo oil bath' and measured via internal thermocouples. The system operating plans/steps were set up and monitored through the 'winISO' computer software program.
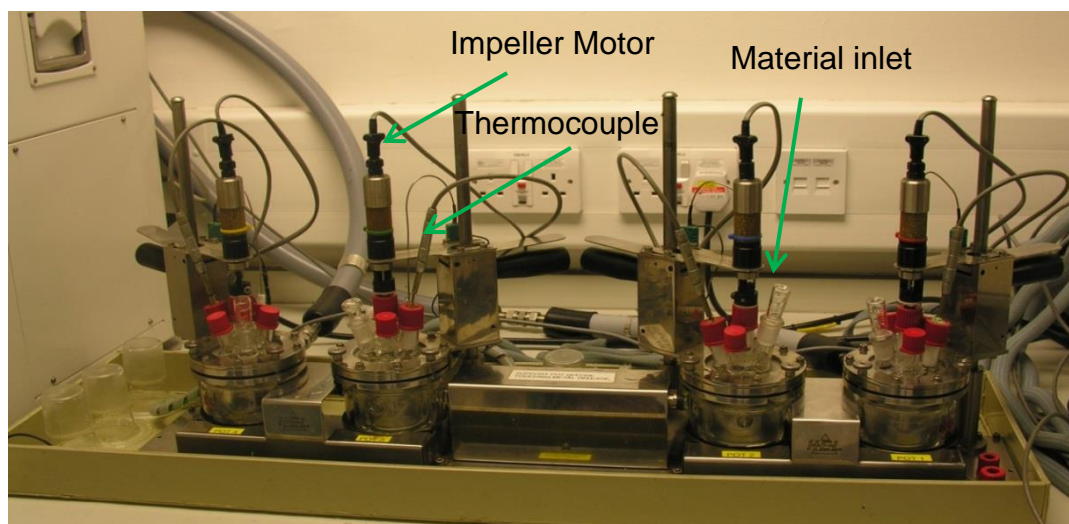
Figure 3.2: The Automate reactor system.

One of the reactors was filled with 30 ml of deionized water, loaded into the Automate system and the lid was secured over the top to prevent any solution evaporation from occurring. The Automate was switched on via the software and the temperature fixed at a constant point of 75°C. The impeller was turned on and set to the 5th position on the control box. Once the water reached the set temperature, 4.4 g Na_2CO_3 was introduced into the reactor followed by 13.5 g Na_2SO_4 10 minutes later. The reaction was then left for 20 hours ensuring it reached the equilibrium state. Next, the mixture was filtered out through a hot vacuum system; the undissolved residue was weighed and placed in the oven at 80°C. The filtrate of the saturated solution was covered with pierced

paraffin film and put in the same oven conditions allowing the evaporative crystallisation to occur. After approximately 36-48 hours the crystals formed were removed from the solution and left in the oven to dry. The filtered residues and the crystallised sample was then prepared for the subsequent XRD measurement.

3.3.1.1 Optical Microscopy

The microscope was connected to a computer; the operating software system is called "QCapture Pro". The microscope has 5x and 10x objective lenses. It was not only used to analyse the final product powder but also applied to observe the slurry sample which was taken straight away from the vessel at the end of a reaction. Slurry samples were taken by using a pipette and placing them on a glass slide, then located on the sample stage of microscope. Micrographs could be taken by clicking the snap icon on the "QCapture Pro" window. The focus and light could be adjusted from the side of the microscope, see Figure 3.3.
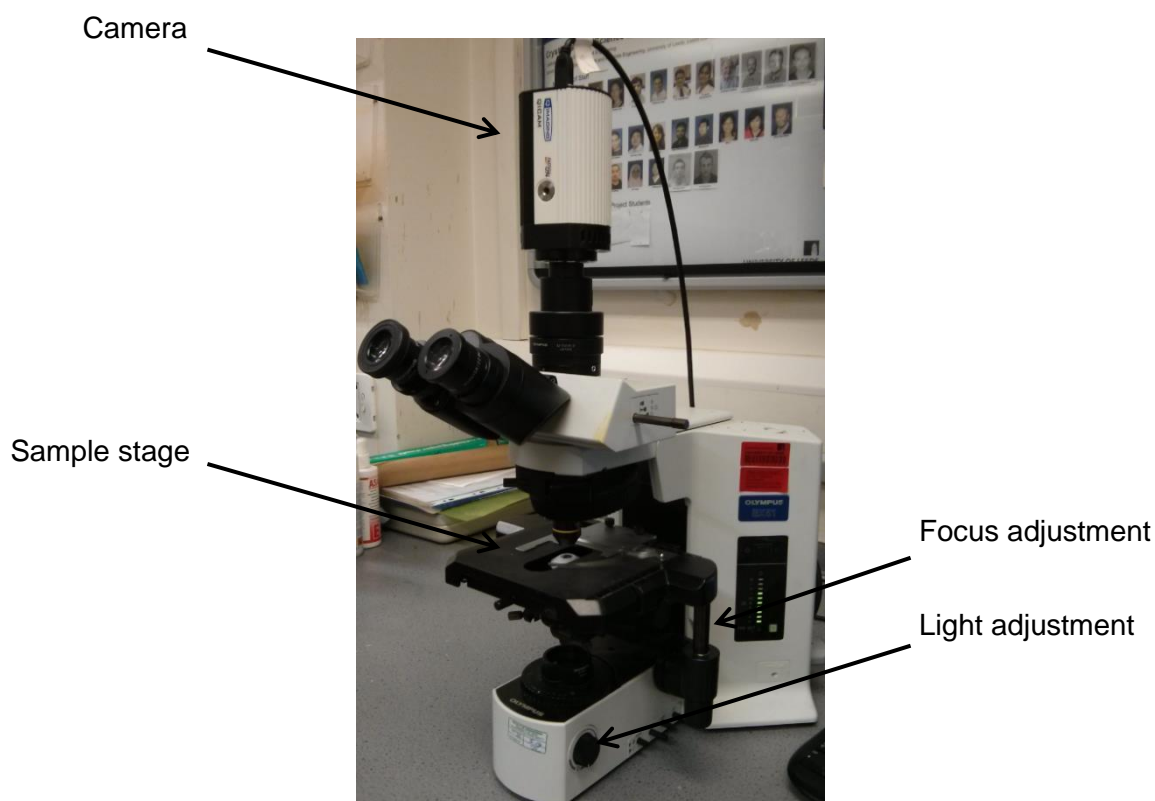
Figure 3.3: Showing the OLYMPUS microscope (BX51)

3.3.2 Slurry State and Solid State Raman Spectroscopy

3.3.2.1   Raman Spectroscopy

In-situ measurements were monitored by a Raman RXN1 spectrometer purchased from Kaiser Optical Systems Inc., covering a spectral wavelength range of 100-3425 cm^{-1}. The high powder NIR laser was emitted through a fibre-optic probe with the wavelength of 785 nm; fluorescent effects can be reduced significantly under this wavelength. The time interval of each measured spectrum can be minimised to a few seconds, which allows capturing the dynamics of processes with characteristic times larger than 10 seconds.
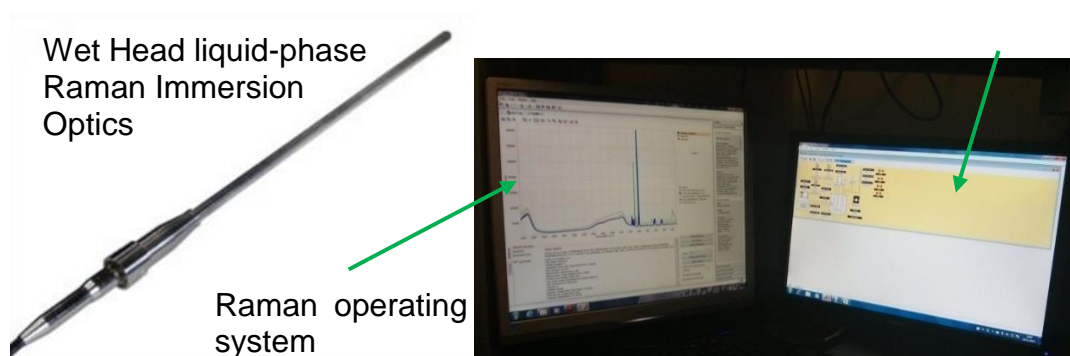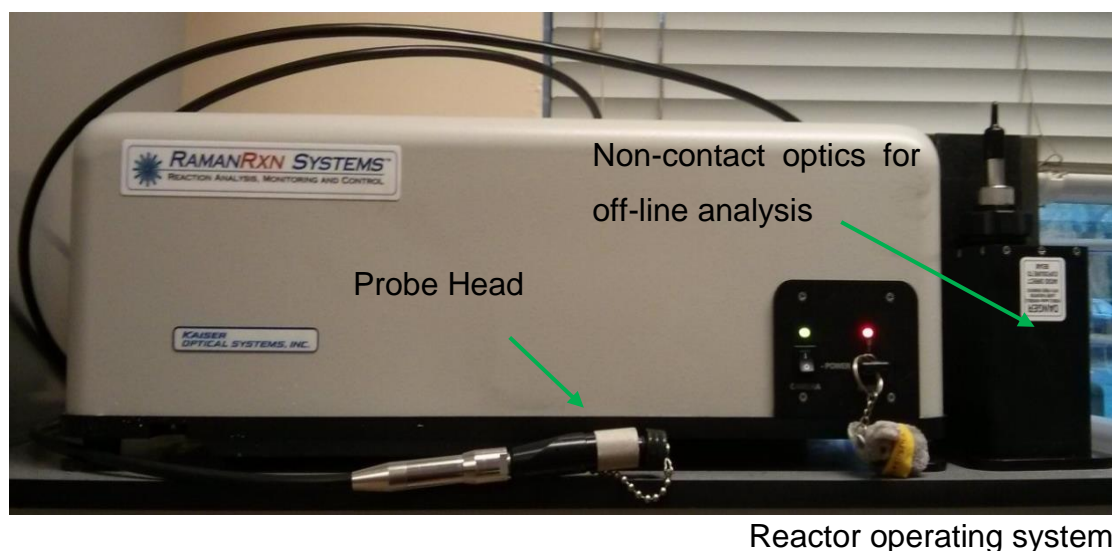
Figure 3.4: Raman spectroscopy set-up

3.3.2.2 Solubility of Sodium Salt in Water

A half-litre glass jacket reactor was used (Figure 3.5 left). The system was operated at 100 rpm using a curved blade PTFE impeller (7 cm in diameter). 300 ml of deionized water was added to the reactor and heated to 75°C using a Julabo FP-50 heating circulator, equipped with Thermal H10 bath fluid (Figure 3.5 right).

Figure 3.5: Half-litre reactor system (left figure: jacket reactor, right figure: Julabo heating circulator)

The reactor needs to be assembled properly before starting the experiment to ensure the mixing efficiency, the height between the impeller and the reactor bottom should be no more than 1 cm. The impeller must point at the middle of the reactor, and the reactor lid must seal well in case of solution evaporation occurring during the experiment operation.

The Raman probe was inserted via one of the reactor pots and secured with a clamp. The reactor was covered up with foils to prevent the impact of any light sources on collecting Raman spectra. 300 ml of deionized water was added to the reactor; the system was then heated up to 75°C. A single

spectrum was collected at 30 seconds intervals, each with a scan time of 5 seconds and three accumulations. Each material was incrementally added to the solution; the additional material was only added when the previous aliquot had dissolved entirely and there was no change in the Raman spectra. When approaching the saturation point, 1g/100g H_2O of the salt was added, until the solid peak appeared on the spectrum and was not disappearing with time. Thus, the solubility of the material should be equal to the total amount that was added, but excluding the last addition. An example is given in section 4.2.2.

3.3.2.3   Slurry System Calibration

Repeat the procedure as in 3.3.2.2, however after the saturation point, solid was continuously added into the solution incrementally. The interval of the addition was set to 15 minutes to ensure a homogenous system was reached before collecting the spectra. The volume fraction of the input material was calculated for the purpose of creating the calibration model.

3.3.2.3.1 Partial Least Square (PLS) Model Development

PLS models were created using GRAMS/AI-PLS Plus/IQ spectroscopy software from Thermo Scientific. GRAMS/AI has been recognised as a comprehensive data processing, visualisation and reporting suite, with the add-in application applied for PLS and principal component regression (PCR) analysis and to develop chemometric models (1, 2). Calibration achievement was evaluated as the coefficient of correlation (R^2) and the standard error of the cross validation (3) (4). The cross validation was applied to reduce the possibility of over fitting when assessing the precision of calibration models. The best number of factors obtained using PLS was stated, and the number of factors adopted is the one that gives the smallest value of the predicted residual sum of squares (PRESS) with the highest R^2 (5). The functions and factors that were chosen to generate the models was described in this section.

In the calibration experiment, a single spectrum was obtained for each concentration by averaging at least 15 spectra (across three repeat experiments) from those achieved from the on-line monitoring system and applying the 1st order derivative baseline correction. In the process of model establishment, a 100-point second gap derivative was applied to account for

differences in compositional profiling during the analysis of future spectra. Factor loadings of 2 for Na_2SO_4 and Na_2CO_3 solution and 1 for Na_2SO_4, $Na_2CO_3 \cdot H_2O$ and Burkeite solid were recommended by the software. Data was written to a single file for process via iC Raman software linked to the Raman Rxn1 spectrometer. Five separate models were created for the slurry systems, which were the solution models for Na_2SO_4 and Na_2CO_3 and the solid models for Na_2SO_4, $Na_2CO_3 \cdot H_2O$ and Burkeite models. The model development followed the leave-n-out principle; two random spectra were omitted from each calibration, which would be used in the final step of the model development. The known responses of these samples were predicted to identify the optimum PLS parameters for each species.

The model development procedure is given in a flow chart in Figure 3.6.
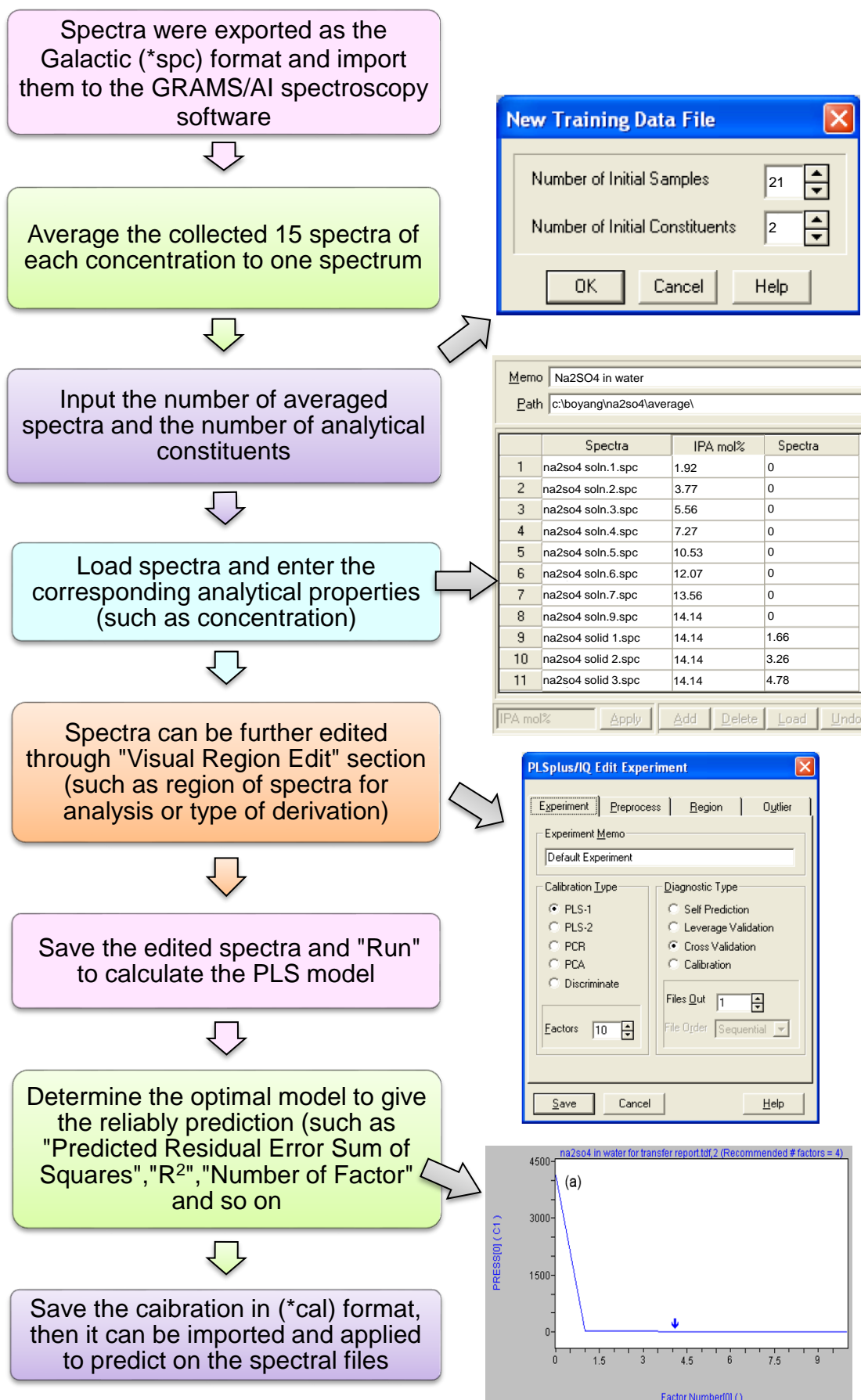
Figure 3.6: Simplified procedure of developing the calibration model using GRAMS/AI spectroscopy software

3.3.2.3.2 PLS Model Validation

Repeat the solubility and slurry calibration experiment again with a different set-up (Figure 3.7). The instrument was programmed with the completed calibration models to obtain concentrations of specie(s) in real time. This validation experiment can also provide the indication of the sensitivity of the calibration model on different experimental set-ups.

Magnetic
stirrer: 7cm

Wide neck flask: 500 ml

Hot plate: 75℃, 250 rpm

Figure 3.7: Experiments for PLS model validation

3.3.2.4   Inorganic solid mixture calibration

Na_2SO_4, Na_2CO_3 and $Na_2CO_3 \cdot H_2O$ was milled before usage. Using the in-situ Raman spectroscopy method to measure five known composition mixtures of these three materials (Table 3.1) with a fixed total sample volume (68 ml) and impeller rotation speed (100 rpm), which is enough to mix the sample properly without having any vortex. The measurement was processed in a 150 ml beaker and fully covered with foil. The Raman probe was immersed in the beaker at a 30-degree angle. The tip of the probe was located 1 cm below the mixture surface. Spectra were collected using 5 second exposure times with three times accumulation. The time interval of taking each spectrum was 20 seconds. The density of the mixture was evaluated after each sample measurement, in order to include the effect of powder packing density in the model.

Figure 3.8: The set-up for the Raman solid mixture calibration experiment.

Table 3.1: The composition of solid mixtures was applied for Raman solid model calibration

Material	Solid mixture composition_wt%				
Na_2SO_4	70	70	55	55	40
Na_2CO_3	10	20	15	30	30
$Na_2CO_3{\cdot}H_2O$	20	10	30	15	30

3.3.3 Eliminating Artificial Effects Caused by Crystal Orientation Preference in XRD Measurement

3.3.3.1   Powder X-ray Diffraction

Powder X-ray diffraction (PXRD) was applied to identify the phases present in the solid samples and the analysis software (PANalytical X'Pert Highscore software) utilised to help analyse the composition of powder mixtures quantitatively.

The measurement was implemented using the Bruker D8 advanced XRD diffractometer which utilised copper (Cu) Kα radiation with a germanium (Ge) primary monochromator in a Bragg-Brentano configuration (Figure 3.9). The step size applied was $0.033 2\theta$ and the step time was 0.664 s/step over a 2 θ range of 15-60. The spinner configuration was set at a tension of 40kV.
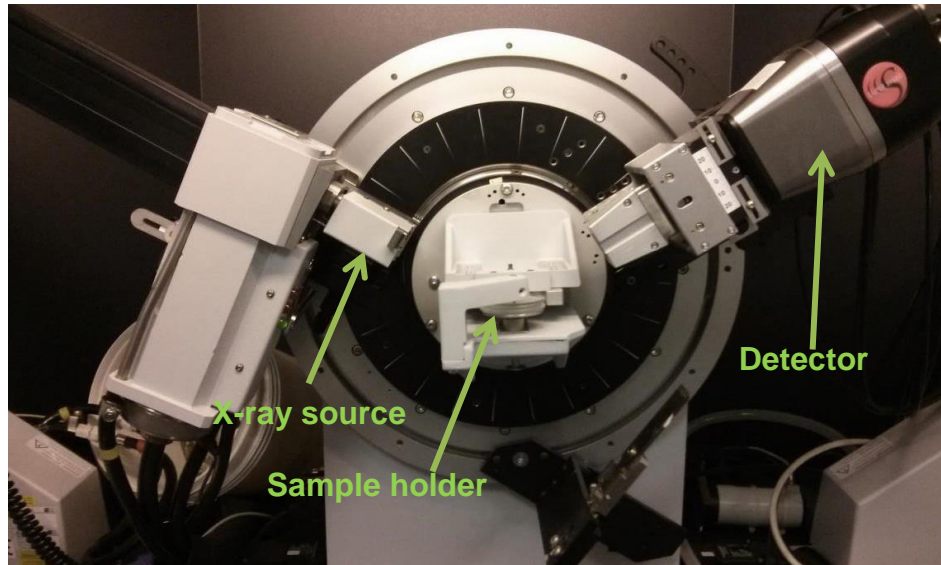
Figure 3.9: D8 X-ray diffractometer in Bragg-Brentano configuration

3.3.3.2 Declining the Preferred Orientation Manner via a Potting Method

Epoxy resin was used in the process to immobilise the crystal and prevent powder from orientating itself in its preferential manner. There are two components of the glue, a resin and a hardener. The powder to be detected was split into two equal portions and each portion was mixed with the resin and hardener, respectively; and then these two portions were further mixed together on a PTFE surface, and the final mix would harden with time (within a few minutes). Once it hardens, it could be removed from the PTFE surface very easily.
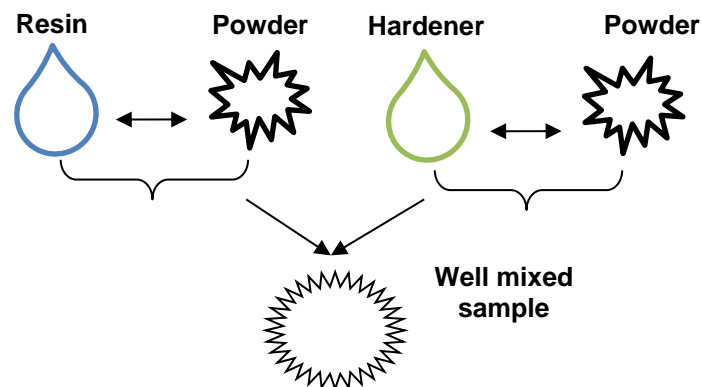
Figure 3.10: Schematic diagram of the epoxy resin and sample powder mixing process for eliminating the crystals from orientating in a preferential manner.

The hardened sample was then ground down into particles with a diameter of approximately 100-200 µm using a pestle and mortar. No more than 1 g of powder sample should be used in the mix, as the high powder content can cause poor distribution in the resin and hardener; the amount of resin and hardener was around 1-2 ml, respectively.

3.3.3.3 Rietveld refinement for quantitative analysis

There are many available methods which can be applied for quantitatively analysing the composition within a sample, such as the Internal standard method, the absorption diffraction method, however, the Rietveld refinement was the most common approach (6). This method can only be applied if the structure of all present phases is known. The equation below Equation 3.1 was used in the quantitative analysis for predicting the composition (wt%) of crystal x in a multi-component solid mixture.

$$W_x = \frac{S_x(ZMV)_x}{\sum S_i\,(ZWV)_i} \qquad\qquad \text{Eq. (3.1)}$$

where W_x is the wt% of phase x, S is the scale factor, Z is the number of formula units per cell, M is the mass of the formula unit and V is the volume of the unit cell.

The full diffraction pattern would be taken into account during the Rietveld refinement, where the measured profile was compared to a calculated profile. Next, some parameters (i.e. scale factors, cells, symmetric factor) can be adjusted either automatically or semi-automatically to minimise the discrepancy between these two profiles to give quantification values, such as the weight R profile and the goodness of fit.

The Rietveld method was established upon:

$$I_{ic} = I_{ib} \sum_P \sum_{k=k_1^P}^{k_2^P} G_{ik}^P I_k \qquad\qquad \text{Eq. (3.2)}$$

where I_{ic} denotes the net intensity calculated from point I in the pattern, I_{ib} denotes the intensity of the background, G_{ik} is the normalised peak profile function, I_k is the intensity of the kth Bragg reflection, P represents the possible phases in the sample examined.

Here,

$$I_k = SM_k L_k |F_k|^2 P_k A_k E_k \qquad\qquad \text{Eq. (3.3)}$$

where M_k represents the multiplicity, L_k is the Lorentz polarization factor, F_k illustrates the structural factor, P_k indicates the preferred orientation influence ($P_k = 1$ illustrates no preferred orientation presence), A_k and E_k are the absorption and extinction correction factor respectively.

If preferred orientation does exist in the sample, then the peak intensity will be altered. However, it can be compensated through Rietveld refinement by following the theory in Equation 3.4.Eq. (3.4)

$$P_k = [P1^2 cos^2\alpha_k + P1^{-1}sin^2\alpha_k]^{-3/2} \qquad\qquad \text{Eq. (3.4)}$$

where $P1$ is a refinable value, α_k is the acute angle between the scattering vector and the normal to the crystallites.

3.3.4 Process Conditions Effect on the Slurry System of Na_2CO_3-H_2O-Na_2SO_4 Slurry

Two variables were considered on investigating the impact of process condition on the slurry composition of a Na_2CO_3-H_2O-Na_2SO_4 system, which are mass ratio and the order of addition (OOA) of the raw materials. Six experiments were considered to conduct this investigation see Table 3.2.

The instrumental set-up was identical as in 3.3.2.2. First of all, 300 ml of deionized water was heated up to 75°C with 100 rpm. Turn on the Raman instrument and a single spectrum was collected at 30 second intervals, each with a scan time of 5 seconds and three accumulations. Next, the first salt was added to the solution, around 10 minutes later the second salt was added. Then, the system was left to run for 20-30 minutes. The slurry produced was filtered through a pre-heated vacuum system; the residues were placed in an 80°C oven to dry preparing for the XRD measurement.

Table 3.2: The impact of the order of addition (OOA) and the mass ratio of raw materials on final slurry composition (C+S= Add Na$_2$CO$_3$ first then Na$_2$SO$_4$; S+C= Add Na$_2$SO$_4$ first then Na$_2$CO$_3$)

Experiment number	OOA	Mass ratio	Composition_wt%		
			Na$_2$CO$_3$	H$_2$O	Na$_2$SO$_4$
1	C:S	1:1	33	34	33
2	S:C	1:1	33	34	33
3	C:S	1:3	16.5	34	49.5
4	S:C	3:1	49.5	34	16.5
5	C:S	6:1	56.6	34	9.4
6	S:C	1:6	9.4	34	56.6

3.3.5 Na$_2$CO$_3$-H$_2$O-Na$_2$SO$_4$ Ternary Phase Diagram Determination

3.3.5.1   Solubility Line Determination of the Sodium Salt Mixtures

The comparable experimental theory and set-up were applied as described in 3.3.2.2. Nine solutions with different amounts of pre-dissolved Na$_2$CO$_3$ salt were heated to 75°C individually. Na$_2$SO$_4$ was then incrementally added to each Na$_2$CO$_3$ solution, and the total quantity added was recorded (Figure 3.11). Each addition was only added when the previous portion had dissolved entirely, and no change in the Raman peak intensity was observed. Upon reaching saturation state, the system was run overnight to ensure solubility equilibrium was reached. Then the total amount of salt (Na$_2$CO$_3$+Na$_2$SO$_4$) in each solution would be the solubility for the corresponding mixture system.
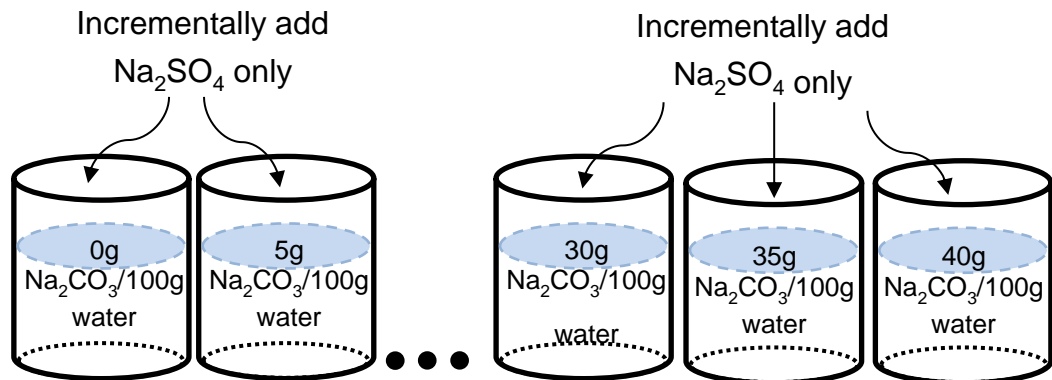
Figure 3.11: Experimental design for determining the mixture solubility line for the Na$_2$CO$_3$-H$_2$O-Na$_2$SO$_4$ ternary phase diagram.

3.3.5.2 Region Boundary Lines Determination for the Phase Diagram

Two Na_2SO_4 and Na_2CO_3 solutions were prepared, then Na_2CO_3 (or Na_2SO_4) was incrementally added into the Na_2SO_4 (or Na_2CO_3) salt solutions (Figure 3.12) until there were no further changes in the solid phase constitution. PLS slurry models, which were established in 3.3.2.3, were applied for simultaneous on-line monitoring the real-time composition variation in both solution and slurry phases. The phenomenon of appearance or disappearance in solid phases was recorded over the experiment. The procedure was explained in detail in section 5.2.2.
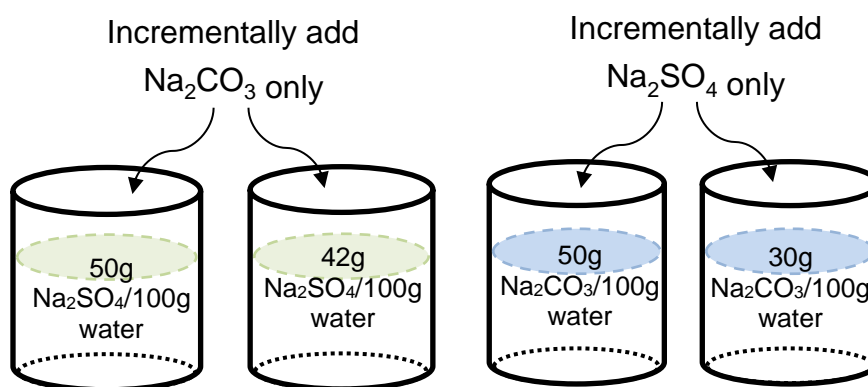
Figure 3.12: Experimental design for Na_2CO_3-H_2O-Na_2SO_4 boundary lines determination (the solution and slurry composition variation after each time salt was added was monitored by in-situ Raman)

3.3.6 Kinetics Studies of the Double Salt (Burkeite)

In-situ Raman and Focus Beam Reflectance Measurement (FBRM) techniques were both applied in this part of the study.

3.3.6.1 FBRM Experiments

FBRM follows the principle of laser backscattering. A focused laser beam spins at a constant velocity. The chord length is the product of the scanning speed velocity multiplied by the time pulse (Figure 3.15). As the laser scans across a particle, the time duration of detected reflectance from the particle is resolved and correlated with the chord length. However, the chord length does not always represent the particle length, for instance, in the case of needle/plate-like particles, the detected chord length may vary and that

depends on the way the particle passes through the beam measurement area (Figure 3.15).
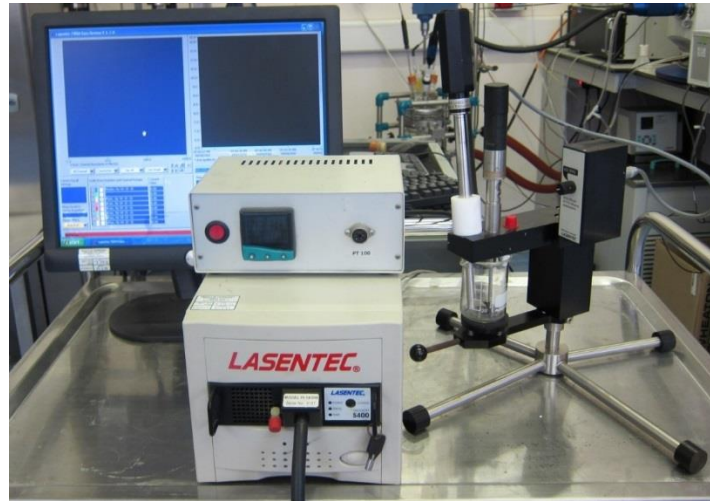
Figure 3.13: FBRM instrument for on-line monitoring of the chord length distribution.
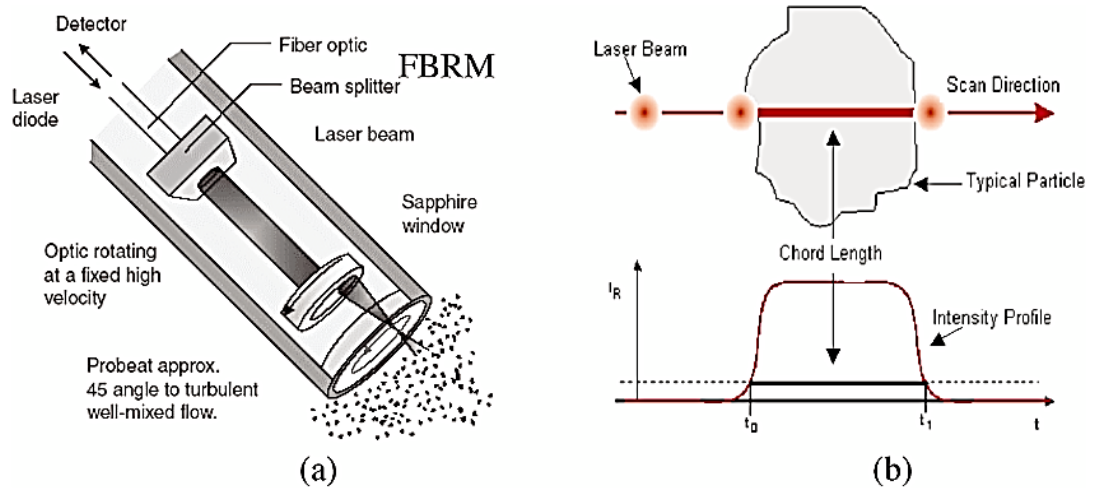
Figure 3.14: A schematic diagram of FBRM (6)
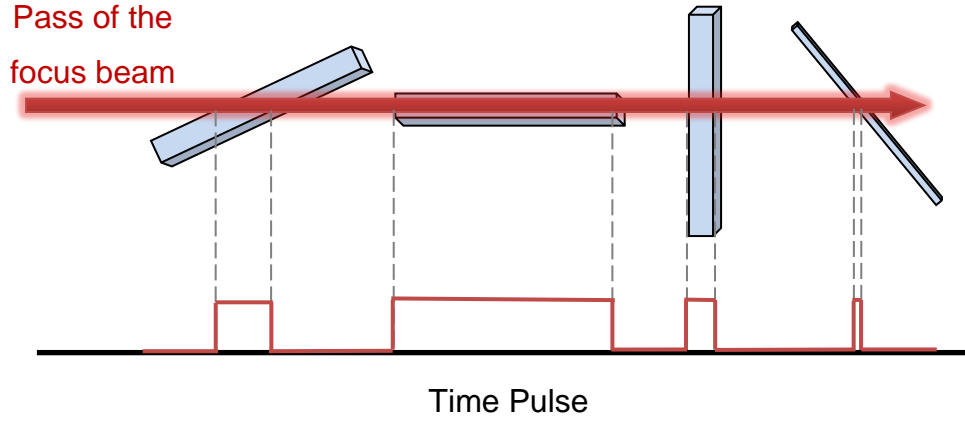
Figure 3.15: Chord length varies with different particle orientations.

In general, thousands of chord lengths will be measured every second, and the counts of chord lengths can be partitioned up to 1000 channels. The measuring range of the chord length (particle length) is from $0.5\,\mu m$ to $1000\,\mu m$, and the operating temperature of the device is -20-150ºC.

3.3.6.1.1 Chord Length Distribution to Particle Size Distribution

As already mentioned, the beam can scan through anywhere on the particles. Therefore, the chord length (l_i) will be larger than zero but smaller than the largest particle dimension (d_i).

In the case of known crystal population, the size distribution can be expressed as a function of chord count density,

$$n(L) = \lim_{\Delta L \to 0} \frac{\Delta N(L)}{V_S \Delta L} \tag{3.5}$$

where L is the specific length of the crystal, $\Delta N(L)$ represents the number of crystals possessing a length between L and $L + \Delta L$, V_S is the volume of the sample. This relationship assumes that all crystals have the same geometric shape even if their sizes are diverse (7).

Following the same principle; the particle size distribution can be written as a function of the chord length density,

$$c(l) = \lim_{\Delta l \to 0} \frac{\Delta C(l)}{V'_S \Delta l} \tag{3.6}$$

where $\Delta C(l)$ represents the number of the chord counts with a length between l and $l + \Delta l$, V'_S is the volume that was detected by the laser beam.

3.3.6.1.2 Moments of Population Density Functions

According to Randolph (8), moments of the population density equations can have real physical meaning, for instance,

$$m_j = \int_0^\infty L^j n dL \qquad (3.7)$$

when $m_0 = N_{total}$ = total number of particles/unit volume;

$m_1 = L_{total}$ = total length of particles/unit volume;

$k_A m_2 = A_{total}$ = overall surface area of particles/unit volume;

$\rho k_V m_3 = M_{total}$ = overall mass of particles/unit volume.

Here, k_A and k_V are the area and volume factors for a specific particle geometry.

In FBRM measurements, the total counts of the chords should be equal to the amount of particles, hence:

$$N_{total} = m'_0 = \int_0^\infty c dL = \int_0^\infty n dL \qquad (3.8)$$

3.3.7 Impact of Solution Conditions on the Composition of the Na₂CO₃ and Na₂SO₄ Slurry System

3.3.7.1 Water content and solution pH effects

Two water levels (25% and 48%) were chosen for investigating the impact of water content on sodium salt slurry composition.

Water was added to a two litre stainless steel IKA reactor (Figure 3.16). The system was stirred at 100 rpm using an anchor impeller and heated to 75°C. The reactor was connected to a water bath. The temperature and rotation speed can be controlled either via the software or the control panel that is indicated in Figure 3.16.

The Raman on-line monitoring probe was inserted through one of the reactor ports and secured by a customised clamp. The operating parameters remained the same as applied in 3.3.2.2.

Once the system reached thermal equilibrium, the sodium salt was added in following the sequence given in Table 3.3. The second salt was introduced when the system regained its equilibrium after the first addition.

Table 3.3: Formulas for studying the impact of solution conditions on the final slurry composition of Na_2CO_3 and Na_2SO_4 double salts system (i.e. W-C-S indicates the order of addition of water followed by Na2CO3 then follow by Na_2SO_4)

Experiment	1	2	3	4	5
OOA	**W-C-S**	**W-S-C**	**W-C-S**	**W-S-C**	**W-Caustic Soda-S-C**
Water_wt%	25	25	48	48	48
Na_2CO_3_wt%	20.3	20.3	14.2	14.2	14.2
Na_2SO_4_wt%	54.9	54.9	38.3	38.3	38.3

Experiment five was designed for verifying the hypothesis that high pH solution environment promotes the Burkeite crystallisation to occur. Caustic soda was used to increase the solution pH to 11 ahead of any material being added.

3.3.7.1.1 Scanning Electron Microscopy (SEM)
Images of crystals collected from the FBRM experiment in Chapter 4 were provided using the Hitachi SU8230 high performance cold field emission SEM. It has an Aztec Energy EDX system and 80mm X-max SDD detector, providing nanoscale resolution as well as nanoscale EDX.

Images of Burkeite presented in Chapter 6 were taken using a Hitachi TM3030 Plus table top microscope which is designed for quick and easy imaging up to 3.0×10^4 magnification.
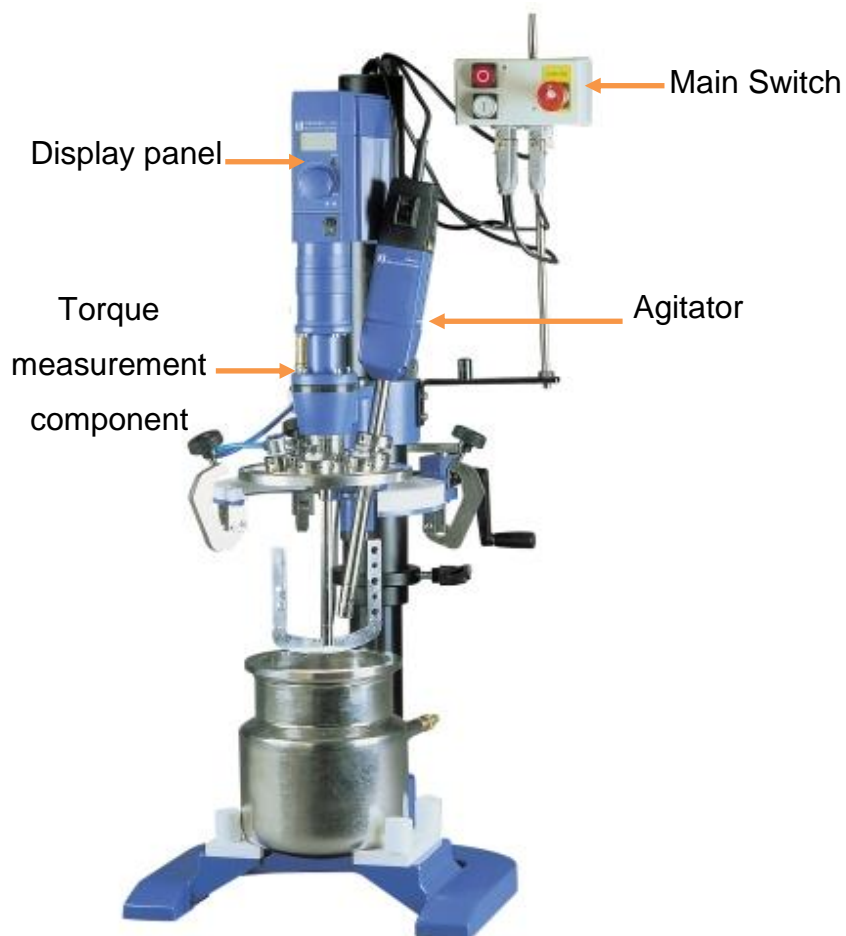
Figure 3.16: IKA 2 litre stainless steel reactor with an anchor impeller.

3.3.7.2 Other Chemical Effects

3.3.7.2.1 Order of Addition Experiments in Sodium Silicate Solutions
The OOA experiment in section 3.3.4 was partially repeated following the formula that was given in Table 3.4.

The sodium silicate (1.6 R, 45 wt%) solution was mixed with deionized water first and heated to 75°C, then followed the procedure that was described in section 3.3.4.

Table 3.4: The impact of the OOA and the mass ratio of raw materials on final slurry composition in the sodium silicate solution system (C+S= Add Na₂CO₃ first then Na₂SO₄; S+C= Add Na₂SO₄ first then Na₂CO₃)

Experiment number	OOA	Mass ratio	Composition_wt%			
			Na_2CO_3	H_2O	Sodium silicate	Na_2SO_4
1	C:S	1:1	30	30	10	30
2	S:C	1:1	30	30	10	30
3	C:S	1:3	15	30	10	45
4	S:C	3:1	45	30	10	15

3.3.7.2.2 The Solubility of Sodium Salts in Sodium Silicate (1.6R) Solutions

In this section of the study, the solution system was changed to different compositions of sodium silicate solutions (i.e. 10, 15, 25, 35 and 45 wt%), and the procedure was repeated as already described in section 3.3.2.2.

3.3.7.2.3 Impact of changing pH on sodium silicate solutions

In this section of study, the solution system was changed to different composition of sodium silicate solutions (i.e., 10, 15, 25, 35 and 45wt%), and repeated the procedure as described Solubility of Sodium Salt in Water3.3.2.2.

3.3.7.2.4 Impact of changing pH on sodium silicate solutions

❑ De-polymerisation of sodium silicate 3.2R (10wt%)

4 M NaOH solution was used to increase the pH of the 3.2R sodium silicate solution. The Raman spectra were taken for solutions with different pH, i.e. 11.34, 12.11 and 12.77. Raman instrument was setup to a 5 seconds exposure time with 1 accumulation per measurement. The experiment was carried out at 75°C.

❑ Polymerisation of sodium silicate 1.6R (10wt%)

H_2SO_4 diluted to 49% as used to decrease the pH of the 1.6R sodium silicate solution. The Raman spectra were taken for solutions with different pH, i.e. 12.56, 11.53, 11 and less than 7. The Raman was setup to a 5 seconds

exposure time with 1 accumulation for each spectrum taken. The experiment was carried out at 75ºC.

3.4 Conclusion

This chapter has provided the materials information together with detailed experimental methodologies which were applied in this project. Raman spectroscopy was used as the main instrument throughout this research. Some matters needed attention for applying this technique. For instance, the influence from other light sources should be prevented during measurements. Laser safety goggles was required while the instrument operation, the class 3b laser beam could cause eye-damaging. The immersion optical has to be cleaned gently before and after each experiment, ensuring no damage would occur to the crystal on the tip of Raman probe. Last not the least, in the case of experimental setups for quantitative analysing, the exposure time and the number of accumulation for each measurement have to be consistent with the value that applied in the calibration experiments.

Reference List

1. Martens, H. and Naes, T. *Multivariate calibration.* John Wiley & Sons, 1992.

2. Haaland, D.M. and Thomas, E.V. Partial least-squares methods for spectral analyses. 1. Relation to other quantitative calibration methods and the extraction of qualitative information. *Analytical chemistry.* 1988, **60**(11), pp.1193-1202.

3. Williams, P. and Norris, K. *Near-infrared technology in the agricultural and food industries.* American Association of Cereal Chemists, Inc., 1987.

4. Shim, J., Cho, I., Khurana, H., Li, Q. and Jun, S. Attenuated Total Reflectance–Fourier Transform Infrared Spectroscopy Coupled with Multivariate Analysis for Measurement of Acesulfame- K in Diet Foods. *Journal of food science.* 2008, **73**(5), pp.C426-C431.

5. Geladi, P. and Kowalski, B.R. Partial least-squares regression: a tutorial. *Analytica chimica acta.* 1986, **185**, pp.1-17.

6. McCusker, L., Von Dreele, R., Cox, D., Louër, D. and Scardi, P. Rietveld refinement guidelines. *Journal of applied crystallography.* 1999, **32**(1), pp.36-50.

7. Boxall, J.A., Koh, C.A., Sloan, E.D., Sum, A.K. and Wu, D.T. Measurement and calibration of droplet size distributions in water-in-oil emulsions by particle video microscope and a focused beam reflectance method. *Industrial & Engineering Chemistry Research.* 2009, **49**(3), pp.1412-1418.

8. Euhus, D.D. Nucleation in bulk solutions and crystal growth on heat-transfer surfaces during evaporative crystallization of salts composed of NaCO and NaSO. 2003.

9. Ranodolph, A. *Theory of Particulate Processes 2e: Analysis and Techniques of Continuous Crystallization.* Elsevier, 2012.

Chapter 4 **Raman Calibration Model Development, Verification, and Applications**

4.1 Introduction

The purpose of this research was to understand the dissolution and crystallisation of the common inorganic ingredients in a dry laundry system. Dissolution and crystallisation of the inorganic materials, i.e. Na_2CO_3, Na_2SO_4 and Burkeite, in the slurry mixture are process dependent, which leads to the formation of different solid compositions that have a significant impact on the final product properties, such as solid composition, particle size distribution, porosity, stability and so on. Until now, the scientific methodology for characterising the inorganic crystalline composition in slurry conditions has been established by employing chemical analysis, XRD and EDX (1-3). However, these were all ex-situ techniques which may not entirely reflect the real-time variation of the slurry composition during the operation.

To monitor the slurry composition changing along with the experimental/processing time, calibration model development for in-situ analysis of the slurry system was considered as the entry point for this project. The Raman spectroscopy technique was applied due to its many obvious advantages such as minimal sample preparation, less interference by water and glassware, fast spectra collection and less complex data-processing.

This chapter involves five sub-sections. 1. Firstly, due to there being no commercial Burkeite available, at the beginning of the research Burkeite was generated and analysed by XRD for the purity examination. Secondly, the solubility of raw material Na_2CO_3 and Na_2SO_4 was determined by using an in-situ Raman technique at 75°C experimental conditions. Further, calibration models were created for the Na_2CO_3 and Na_2SO_4 solution system, respectively. Thirdly, solid calibration models for the individual substance of a Na_2CO_3, Na_2SO_4 and Burkeite slurry system were developed. 2. The second section expounded how to implement the technique of XRD quantitative analysis on verifying the accuracy of Raman slurry models, a mass-balance calculation was also delivered. 3. This section illustrates the application of

slurry models on the real process. 4. Section four describes the procedure of developing calibration models for dry solid mixtures, followed by the model verifications and applications. In some cases, the composition of amorphous phases can also be determined. 5. The conclusion section has indicated the matters needing attention for developing different models. It also proposed the benefits that can be obtained from the model application.

A flow chart is displayed in Figure 4.1 with the purpose of explaining the relationship of the first three sections.
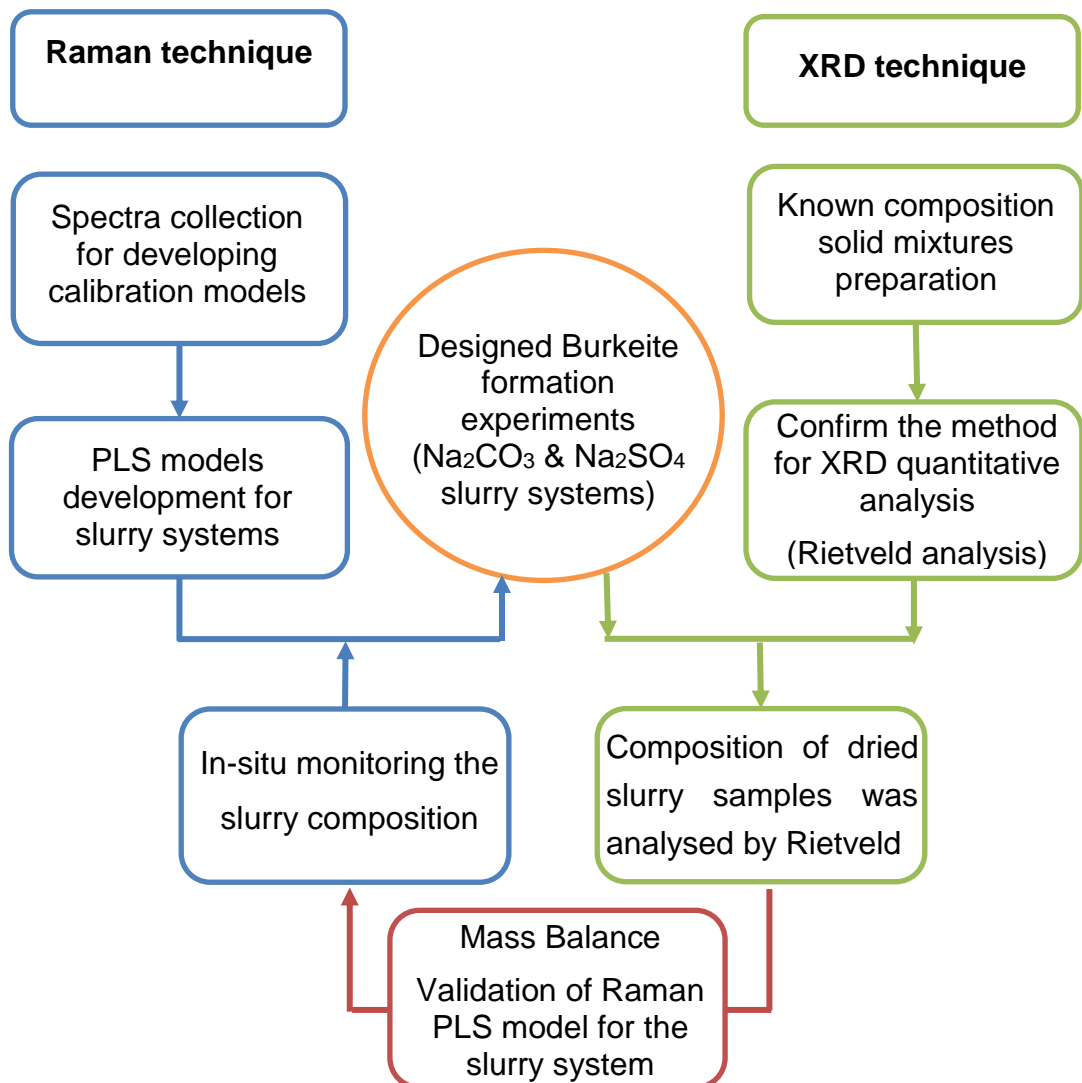
Figure 4.1: The flowchart illustrates the structure of the first three sections of Chapter 4.

4.2 Development of Quantitative Calibration Models for the Slurry System by Applying the Raman Spectroscopy Technique

4.2.1 High Purity Burkeite Preparation

Burkeite was produced by the evaporative crystallisation method from Na_2CO_3 and Na_2SO_4 saturated solution mixtures at 80°C. The purity of the crystals obtained was then confirmed by XRD analysis; high purity products were stored in dry room conditions (~25 °C) for further calibration use.

According to the literature (4-7), Burkeite commonly presents as the following formula $Na_6(CO_3)(SO_4)_2$ and only precipitates when solutions are over the saturation limit. Hence, firstly a saturated solution of Na_2CO_3 and Na_2SO_4 was prepared using a molar ratio of 1:2 respectively. The solubility of Na_2CO_3 and Na_2SO_4 in water at 75°C was reported as 41 and 45 respectively (8), which were applied to find the quantity of each material required to make a saturated solution in 30 ml of water. The 30 ml water was firstly heated up to 75°C in the automate reactor (see Figure 3.2), following by 4.4 g Na_2CO_3 being added to the water. Once this had completely dissolved, 13.5 g Na_2SO_4 was introduced and left in the reactor for 20 hours to make sure the system reached the equilibrium state. Theoretically, all materials should have dissolved if the correct solubility data was applied. However, after 20 hours there were still undissolved particles suspending, which was around 4 g. The residues were filtered out through a hot vacuum system and dried in an oven at 80°C. Through the XRD phase identification, the suspended solid was confirmed as the undissolved Na_2SO_4 other than precipitated Burkeite crystals (Figure 4.2). The filtrate of the saturated solution was covered with pierced paraffin film and placed in the oven at 80°C for evaporative crystallisation to occur. After approximately 36-48 hours the formed crystals were removed from the solution and left in the oven to dry.
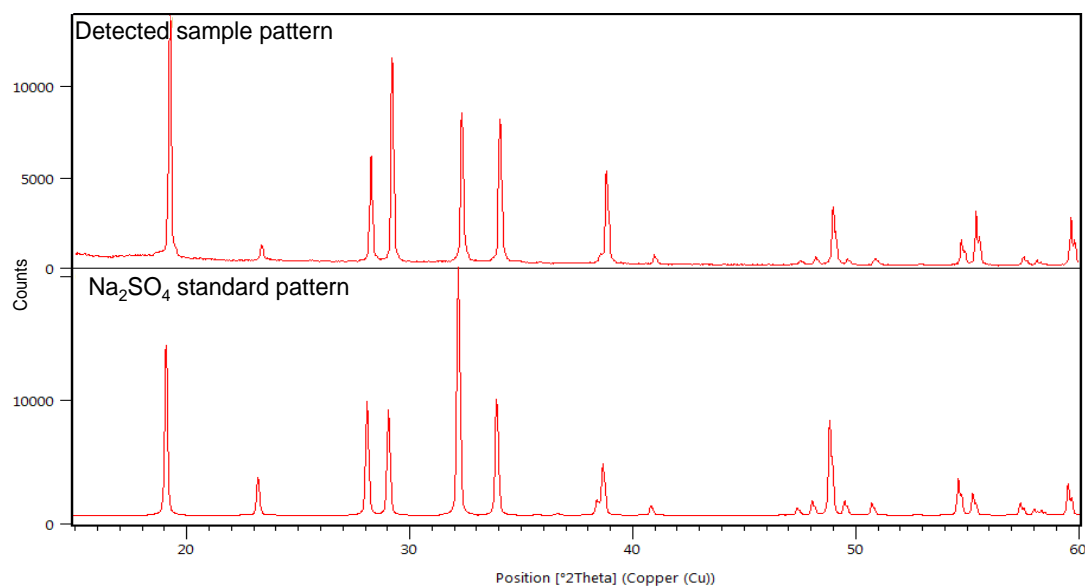
Figure 4.2: XRD phase verification on the filtered and dried undissolved particles obtained from pure Burkeite generation. (ICDD Na₂SO₄ (V) pattern number: 00-036-0397)
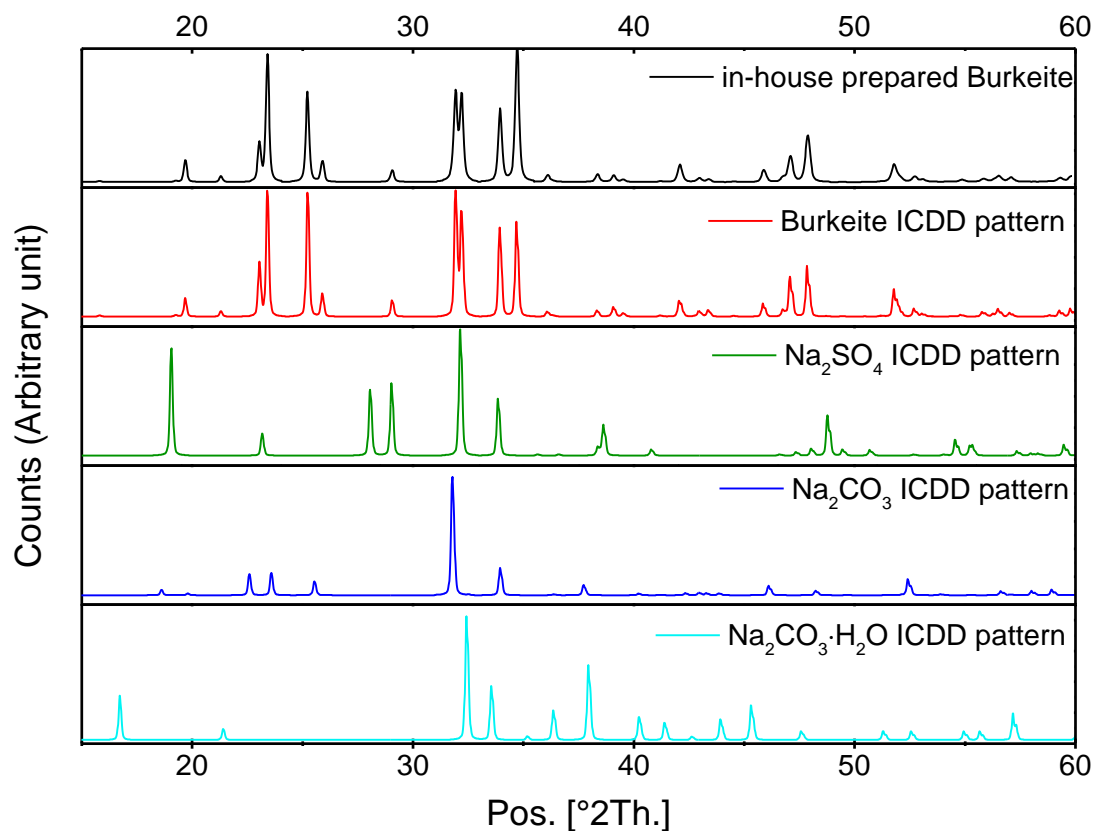
Figure 4.3: XRD pattern of in-house prepared Burkeite in comparison with the ICDD database (Na₂SO₄ (V) 00-036-0397, Na₂CO₃ 01-075-6816 and Burkeite 04-014-9945).
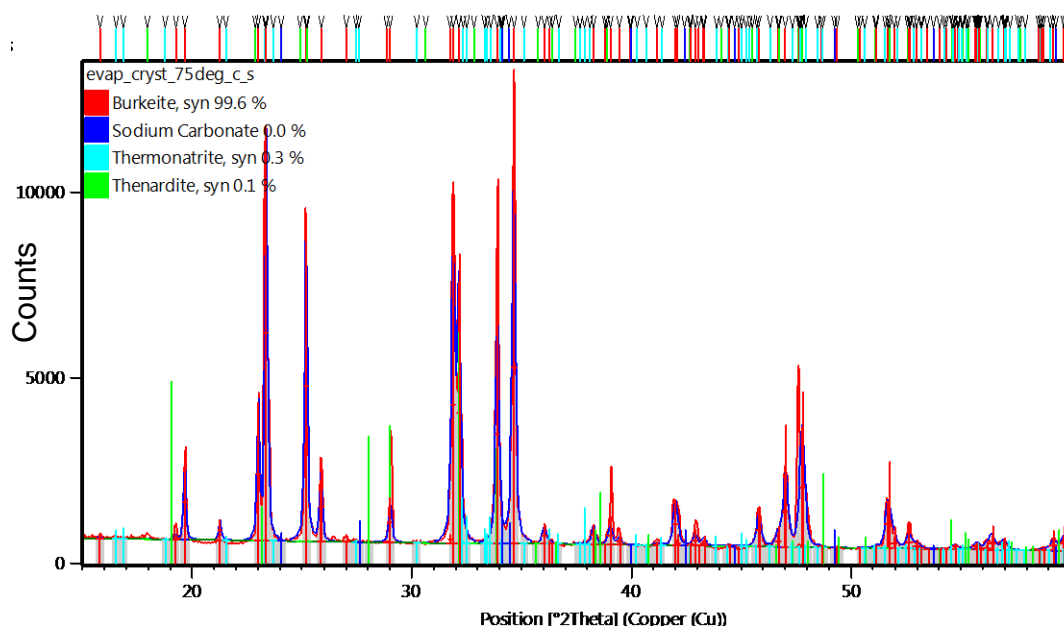
Figure 4.4: The quantitative analysis by Rietveld refinement of a powder sample obtained from evaporating a saturated solution with Na_2CO_3: Na_2SO_4 =1:2 molar ratio at 80ºC)

Figure 4.3 shows the X-ray diffraction pattern from the experiment. Rietveld analysis of this powder denoted 99.6% Burkeite, 0.3% Na_2CO_3 and 0.1% $Na_2CO_3 \cdot H_2O$ (Figure 4.4), which indicated this was a feasible method in precipitating Burkeite to a high degree of purity. Guiseppetti et al. believed that Burkeite could present in different stoichiometric variations (9), according to the Rietveld analysis the best fitting for the Burkeite sample achieved in this experiment was $Na_4(CO_3)_{0.61}(SO_4)_{1.39}$. Therefore this stoichiometric ratio will be used to perform quantitative analysis in the later study. A comparison of the XRD pattern of different ratios of Burkeite was given in Figure 4.5. The SEM image of the Burkeite obtained is shown in Figure 4.6. The morphology agreed with one of the predicted morphologies, that proposed by Meenan P. in 1992 (10). So, in this study, Burkeite presents with the predominant faces (020), (002) and side faces of ($\bar{1}11$), ($\bar{1}01$) and ($1\bar{1}0$).
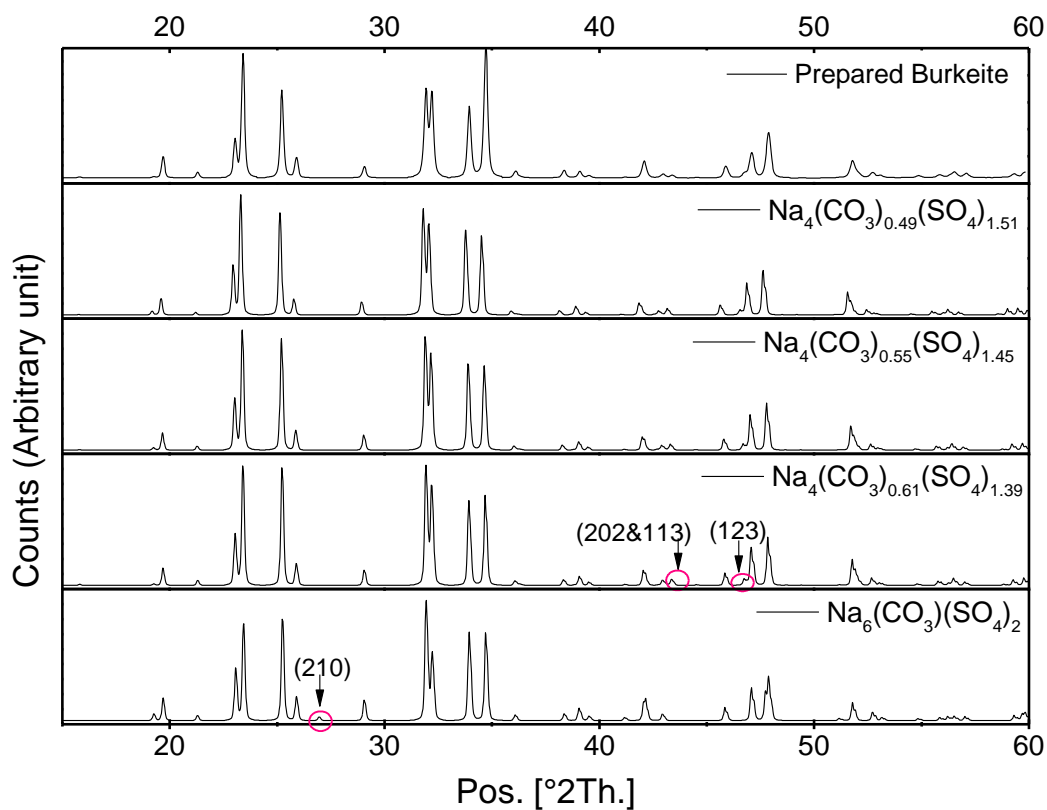
Figure 4.5: XRD comparison of experimental Burkeite pattern with standard patterns of Burkeite in different stoichiometric variations
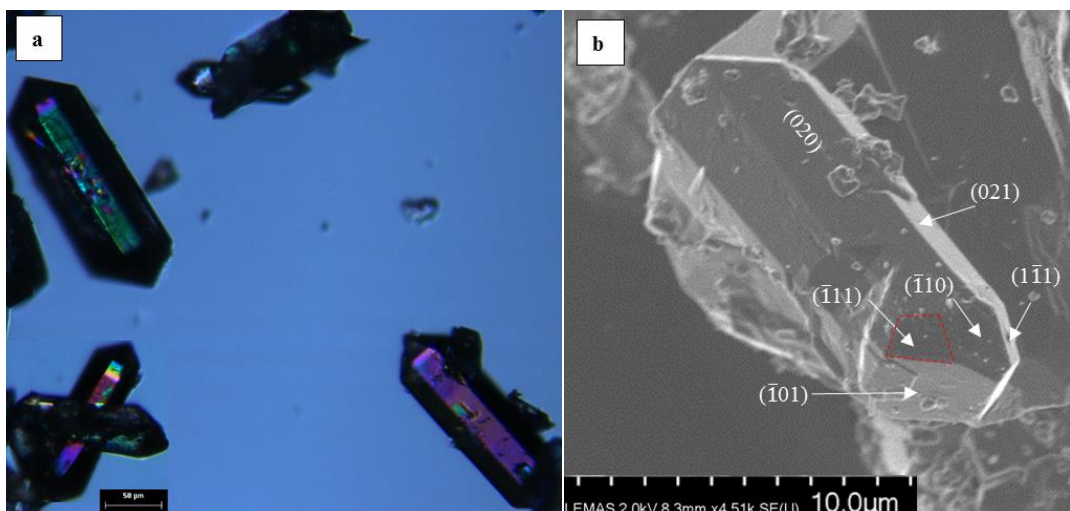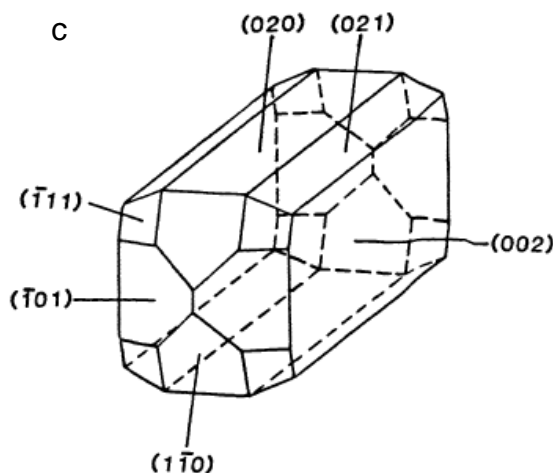
Figure 4.6: Burkeite crystal images from (a) Microscopy and (b) LEMAS SEM; (c) shows the predicted morphology of the 6X Na$_6$(CO3)(SO$_4$)$_2$ supercell, based on the BFDH laws (10).

4.2.2 Determining the solubility of Na$_2$SO$_4$ and Na$_2$CO$_3$ in water

In the previous section, the amount of Na$_2$CO$_3$ and Na$_2$SO$_4$ that was used to create the saturated solution was not completely dissolved. A repeat experiment was left to run for over 24 hours; residues still existed at the end of the experiment. Thus, there must be discrepancies in the solubility of the raw materials provided. It is possible the raw materials or experimental conditions used were different from the reported data. Therefore, it is necessary to determine the solubility of Na$_2$CO$_3$ and Na$_2$SO$_4$ under current experimental conditions (i.e. 75°C and 100 rpm), Raman spectroscopy was used to carry out the measurement, the collected spectra were also used to create solution calibration models for Na$_2$CO$_3$ and Na$_2$SO$_4$ individually. However, these models will only be accurate for predicting solution concentrations with no solid present. Volume expansion was considered during the dissolution process; the composition was expressed as concentration per unit volume.

300 ml of deionized water was added to a half litre reactor. The system was operated at 100 rpm using a retreat curved pitched blade PTFE agitator and heated up to 75°C. The Raman probe was inserted directly into the solution; upon reaching the set temperature, the raw material was introduced. For example, initially Na$_2$SO$_4$ was added in 5 g (per 100 ml H$_2$O) increments; but when close to the saturation point (i.e. 40 g/100 ml H$_2$O) the amount was

altered to 1 g (/100 ml H_2O) each time until the appearance of the solid peak on Raman spectra. The additional material was only added when the previous aliquot had dissolved completely and no change in the Raman spectrum was observed. The dissolution of Na_2CO_3 followed a similar procedure.
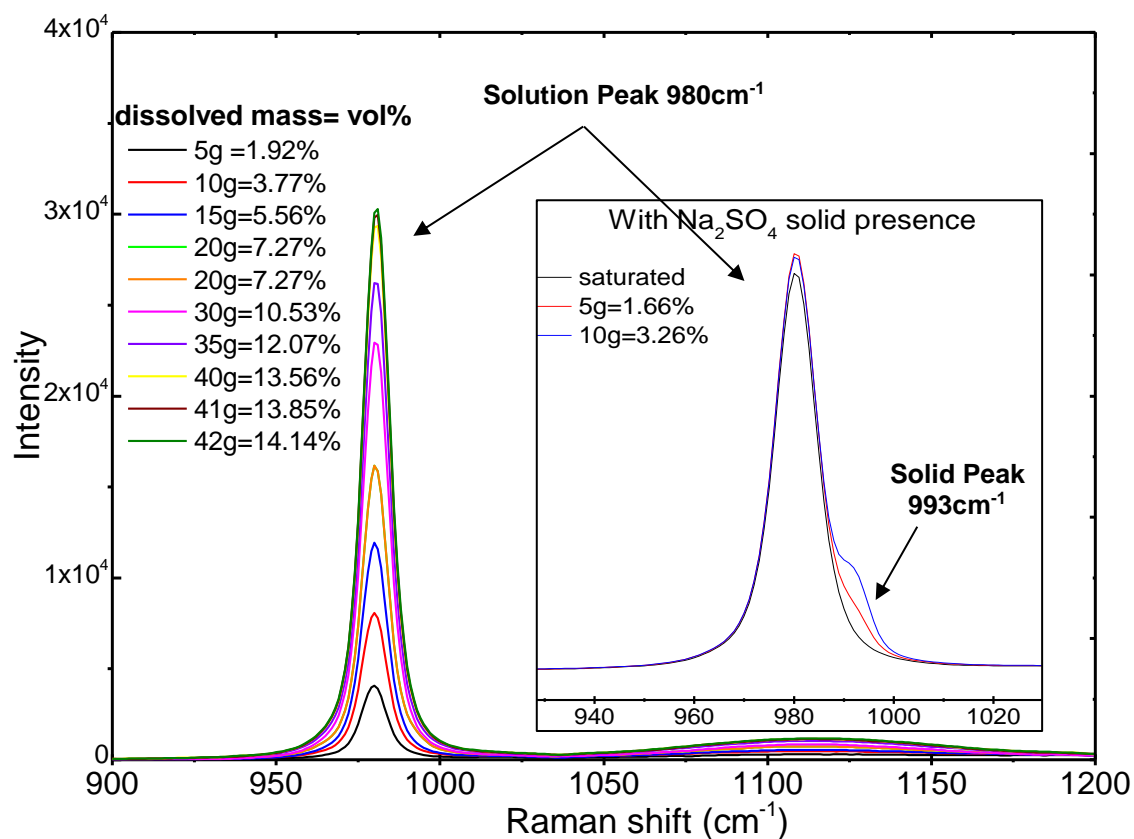
Figure 4.7: Solubility determination of Na₂SO₄ in water at 75°C, detected by in-situ Raman spectroscopy. Spectra were obtained at 75°C and 100 rpm. Each plot represents an average of 15 raw spectra, collected at 30 second intervals. Values in legends are the volume fraction = volume of the salt/total volume of the solution system.
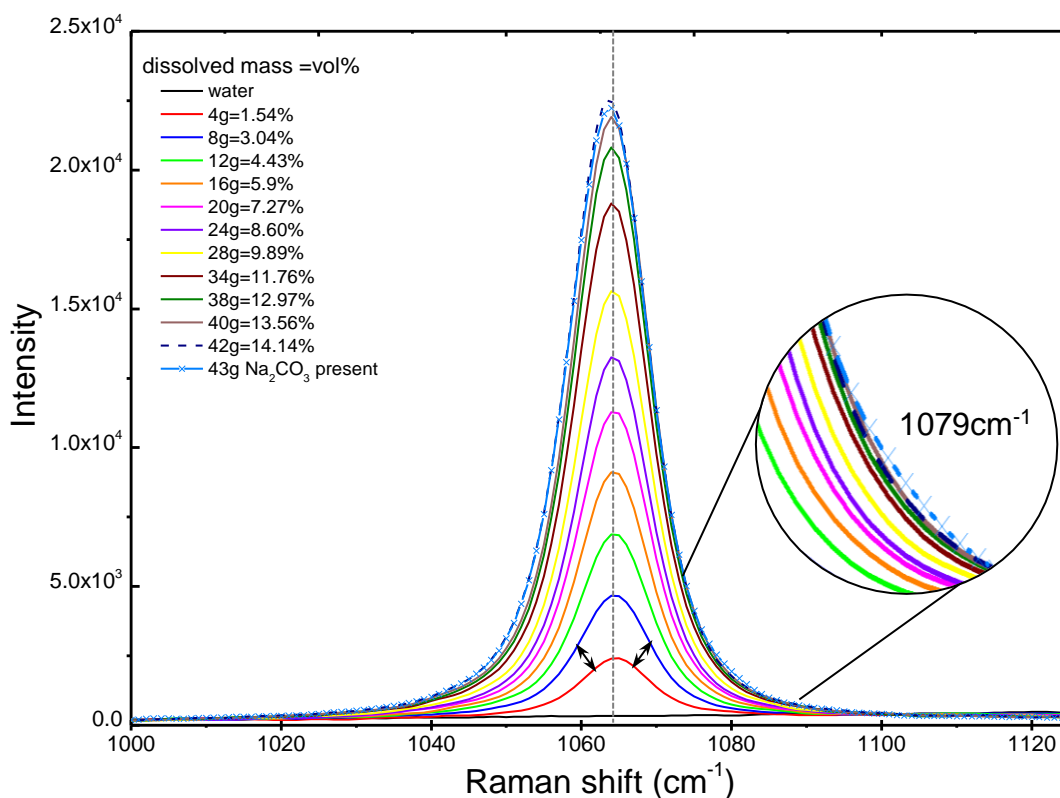
Figure 4.8: Solubility determination of Na$_2$CO$_3$ in water at 75°C, detected by in-situ Raman spectroscopy. Spectra were obtained at 75°C and 100 rpm. Each plot represents an average of 15 raw spectra, collected at 30 second intervals. Values in legends are the volume fraction = volume of the salt/total volume of the solution system.

Figure 4.7 and Figure 4.8 illustrate that peak intensity increased incrementally with the addition of material. This increasing trend would reach a plateau when the salt was close to its solubility. Beyond the solubility point, with the addition of the exceeded substance, the solid peak would appear as a shoulder of the solution peak, and then gradually increased with more salt being introduced (Figure 4.7). This is because, for the same chemical bonds, the vibrational energy is higher in solid phase compared to in its liquid phase.

In the case of the Na$_2$CO$_3$ system, the solution peak appeared around 1064 cm^{-1} as expected by comparing with the previous study (11). Before the precipitation of the Na$_2$CO$_3$ solid occurred, the shape of the solution peak should grow symmetrically (Figure 4.8). From the inset image of Figure 4.8, the shoulder of the Na$_2$CO$_3$ solid peak ~1079 cm^{-1} (Figure 2.37) can be seen clearly when there were 43 g Na$_2$CO$_3$ presenting in the system, which illustrates the system did not reach its equilibrium. However, one thing was sure, that the system has already beyond its solubility limit with the amount of

material involved. It was just a matter of anhydrous to monohydrates conversion. Because, theoretically beyond the solubility limit, under this experimental condition, Na_2CO_3 monohydrate should precipitate and stay as the solid phase upon reaching the dissolution equilibrium state (Figure 2.6).

Tracking backwards to the second last addition of Na_2CO_3 salt, in Figure 4.8 when the total Na_2CO_3 content increased from 40 g to 42 g in the system, the spectrum (or solution peak of Na_2CO_3) did not retain its symmetrical growth form. At the range of 1040-1060 cm^{-1} (on the left side of the peak), the intensity of 42 g spectrum still maintained an increasing tendency compared with the spectrum of 40 g. However, on the right side of the peak (~1065 - 1080 cm^{-1}) these two spectra mostly overlapped each other. This phenomenon implies there must be an additional peak appearing near the Na_2CO_3 solution peak (1064 cm^{-1}), which contributed to broadening or increasing the peak information around 1065 - 1080 cm^{-1}. In this case, the formation of $Na_2CO_3 \cdot H_2O$ (1069 cm^{-1}) solid phase was assumed. A detailed deconvolution to the spectrum was proceeded to the peak and displayed in Figure 4.9 to prove this hypothesis. The spectral region of 1000-1125 cm^{-1} was chosen to be able to clearly observe this phenomena. The fitted spectrum presented high consistency with the raw spectra in all three cases. This peak separation was completed by using Fityk software, the operational procedure of this action is given in the appendix.
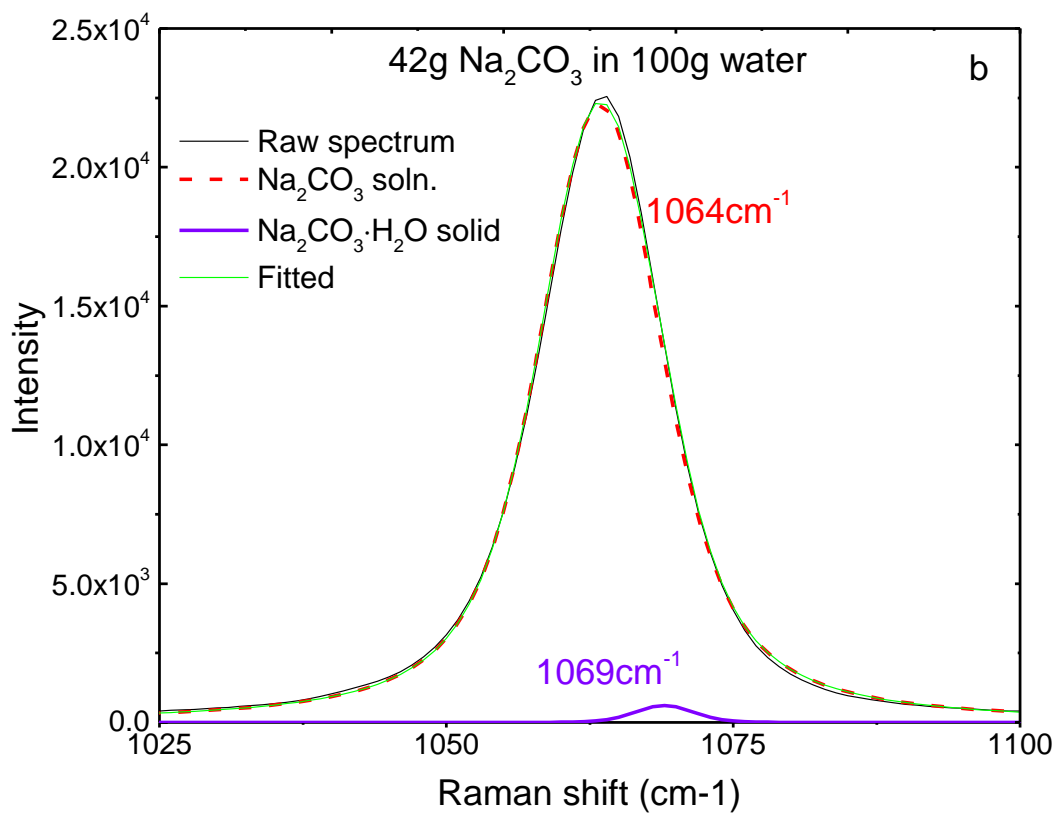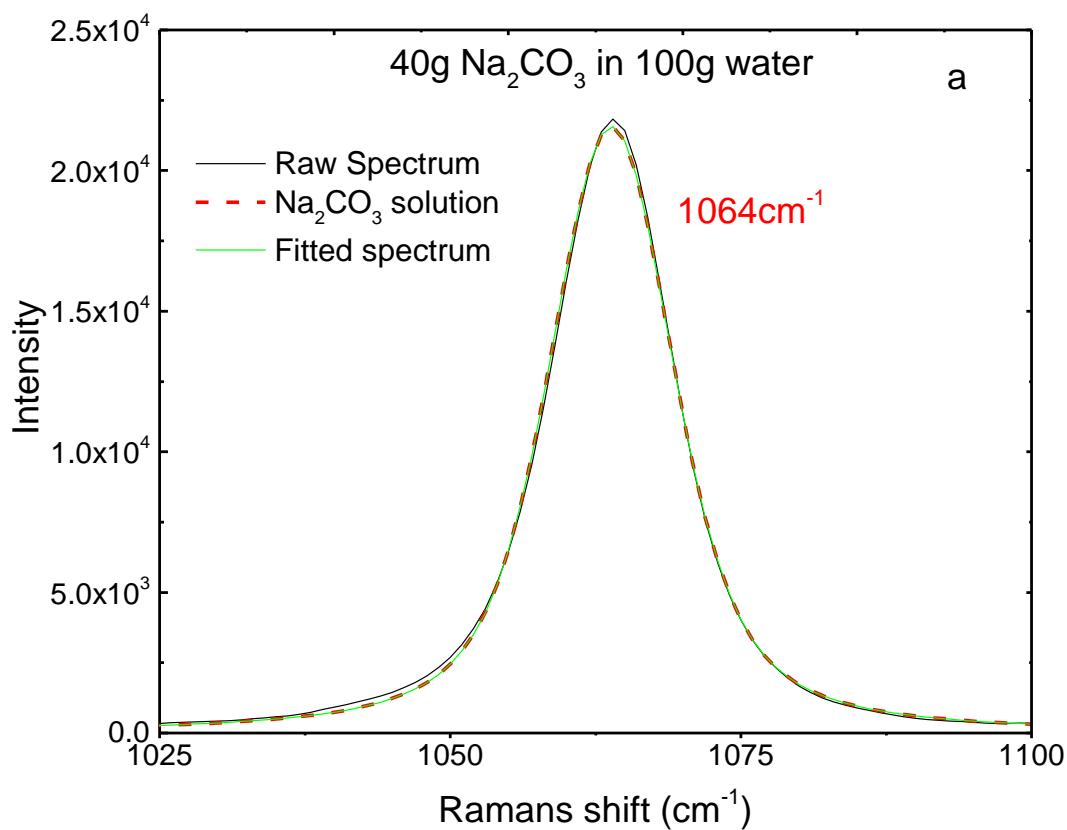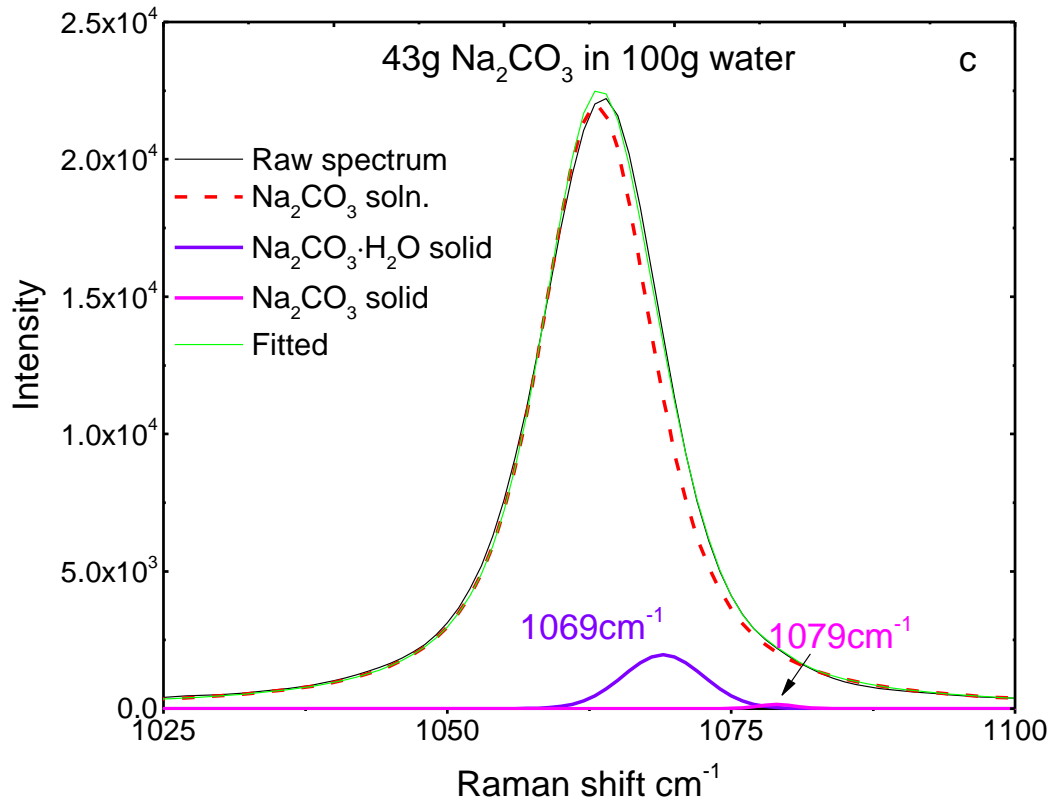
Figure 4.9: **The interpretation of Na_2CO_3 Raman spectra by peak separation. a) Unsaturated Na_2CO_3 solution spectrum; b) Saturated Na_2CO_3 solution in the presence of $Na_2CO_3 \cdot H_2O$ solids; c) Saturated Na_2CO_3 solution in the presence of $Na_2CO_3 \cdot H_2O$ & un-hydrated Na_2CO_3 solids. (for the procedure for peak separation see the Appendix)**

As explained above, with more salt added to water, the more the system went from an unsaturated state to a saturated solution then became a saturated system with a small amount of undissolved particles. This change reflected on the Raman spectra as solution peak intensity progressively increased with the addition of material, once the system went beyond its solubility limit, the solid peak information would appear. Hence, before the solid peak emerged, the record amount of salt added to the system was determined as the solubility of this material. Therefore, the solubility of Na_2SO_4 and Na_2CO_3 was determined as 44 g (/100 g water) and 41 g (/100 g water).

4.2.3 Development of Calibration Model for Slurry Systems

This section focused on the development of partial least square (PLS) calibration models for slurry systems. The concentration (in vol%) of the Burkeite solid phase, Na_2CO_3 and Na_2SO_4 in both solution and solid phases

was monitored via on-line Raman spectroscopy. The resulting spectral information was used to create 5 PLS regression models, which aim to predict the compositions of these species within slurry systems. The model was subsequently verified by monitoring concentrations of Na_2CO_3 and Na_2SO_4 via a simpler laboratory glassware set-up (Figure 3.7). Altering the set-up of the reaction system for the model validation can provide an insight into transferability of the model between different reactor set-ups and determine the feasibility of applying this model for the prediction of unknown concentrations in an industrial reactor.

4.2.3.1 Raman Calibration of Na_2CO_3, Na_2SO_4 and Burkeite

Table 4.1 provided the characteristic peak positions and the vibrational information for the solid phase of each material.

Table 4.1: Raman shifts and vibrational information of the solid phase of Na_2SO_4, Na_2CO_3, $Na_2CO_3 \cdot H_2O$ and Burkeite (12-15)

Material	Assignments	Raman shift (cm^{-1})
Na_2SO_4 (v)	SO_4^{2-} symmetric stretching ν_1	993
	SO_4^{2-} asymmetric stretching ν_3	1102, 1132 & 1152
Na_2CO_3	CO_3^{2-} symmetric stretching ν_1	1079
$Na_2CO_3 \cdot H_2O$	CO_3^{2-} symmetric stretching ν_1	1069
Burkeite	SO_4^{2-} symmetric stretching ν_1	1008 (shoulder) & 993
	CO_3^{2-} symmetric stretching ν_1	1063

Saturated solutions were prepared for the individual material of Na_2CO_3, Na_2SO_4 and Burkeite at 75°C. Based on understanding the procedure of creating solution models, materials were incrementally added to their corresponding saturated solution. For instance, 5 vol% of Na_2SO_4 solid was added to a Na_2SO_4 saturated solution every 15 minutes, until 60 vol% of the solid phase was reached. Meanwhile, the concentration change of Na_2SO_4 solutions in volume fraction was also recorded. An Excel table was used to calculate the required amount of Na_2SO_4 for each addition; an example is given in Table 4.3. To be able to observe a clear trend of the increasing peak

intensity, only some of the collected spectral information were shown in Figure 4.10. All spectra were collected in-situ once the system reached the instrumentally detectable equilibrium, that means no further change in the peak intensity.

Figure 4.10 illustrates beyond the solution saturated point, the solution peak (981 cm^{-1}) intensity linearly decreased with the addition of exceeding Na_2SO_4 solid, at the same time the higher energy solid peak (993 cm^{-1}) appeared as a distinct shoulder and increased with the solid concentration. Table 4.2 provides the correlation of the peak intensity with the concentration variation. The volume fraction of the dissolved Na_2SO_4 was calculated from Table 4.3.

Table 4.2: Na_2SO_4 solution vol% vs. 981cm^{-1} peak intensity; Na_2SO_4 solid vol% vs. 993cm^{-1} peak intensity (the vol% of dissolved Na_2SO_4 was obtained from the calculation of Table 4.3)

Vol% of Na_2SO_4 solid in slurry	Intensity of Na_2SO_4 solid in slurry	Vol% of Dissolved Na_2SO_4	Intensity of Dissolved Na_2SO_4
10.00	20954.97	13.25	23032.48
20.00	31372.00	11.79	20694.56
25.00	39215.00	11.06	19121.30
30.00	52595.75	10.32	19044.19
35.00	60840.31	9.59	16425.98
40.00	62696.00	8.85	15310.26
45.00	70533.00	8.12	14925.78
50.00	77152.01	7.38	12626.41
55.00	83638.18	6.66	10374.78
60.00	90241.49	5.91	9235.46

Table 4.3: The table was applied in Excel for calculating the amount of material required to be added in the system to obtain the desired volume fraction (m_{water}, $m_{S.\ diss.}$, ρ_{water} and $\rho_{Na_2SO_4}$ are fixed value; the $vol\%_{S.solid}$ was the input value; the $m_{S.\ solid}$ is the value wanted to calculate)

Considered Parameters	Symbol	Equation	Final value
Mass of Water (g)	m_{water}	Input value	300.00
Dissolved Na₂SO₄ in solution (g)	$m_{S.\ diss.}$	Input value	132.00
Extra Na₂SO₄ solid added into saturated solution (g)	$m_{S.\ solid.}$	$= V_{S\ solid} * \rho_{Na_2SO_4}$	99.67
Total mass (g)	m_{total}	$= m_{water} + m_{S.\ diss.} + m_{S.\ solid.}$	531.67
Density of water (g/cm³)	ρ_{water}	Input value	1.00
Density of Na₂SO₄ (g/cm³)	$\rho_{Na_2SO_4}$	Input value	2.55
Vol. of water	V_{water}	$= \dfrac{m_{water}}{\rho_{water}}$	300.00
Vol. of dissolved Na₂SO₄	$V_{S\ diss.}$	$= \dfrac{m_{S.\ diss.}}{\rho_{Na_2SO_4}}$	51.76
Vol. of Na₂SO₄ solid	$V_{S\ solid}$	$= \dfrac{vol\%_{S.\ solid} * (V_{water} + V_{S\ diss.})}{(1 - vol\%_{S.\ solid})}$	39.08
System total Vol. cm³	V_{total}	$= V_{water} + V_{S\ diss.} + V_{S\ solid}$	390.85
Vol% of water	$vol\%_{water}$	$= \dfrac{V_{water}}{V_{total}}$	76.76%
Vol% of dissolved Na₂SO₄	$vol\%_{S.\ diss.}$	$= \dfrac{V_{S.\ diss.}}{V_{total}}$	13.24%
Vol% of Na₂SO₄ solid	$vol\%_{S.\ solid}$	Input value	10.00%
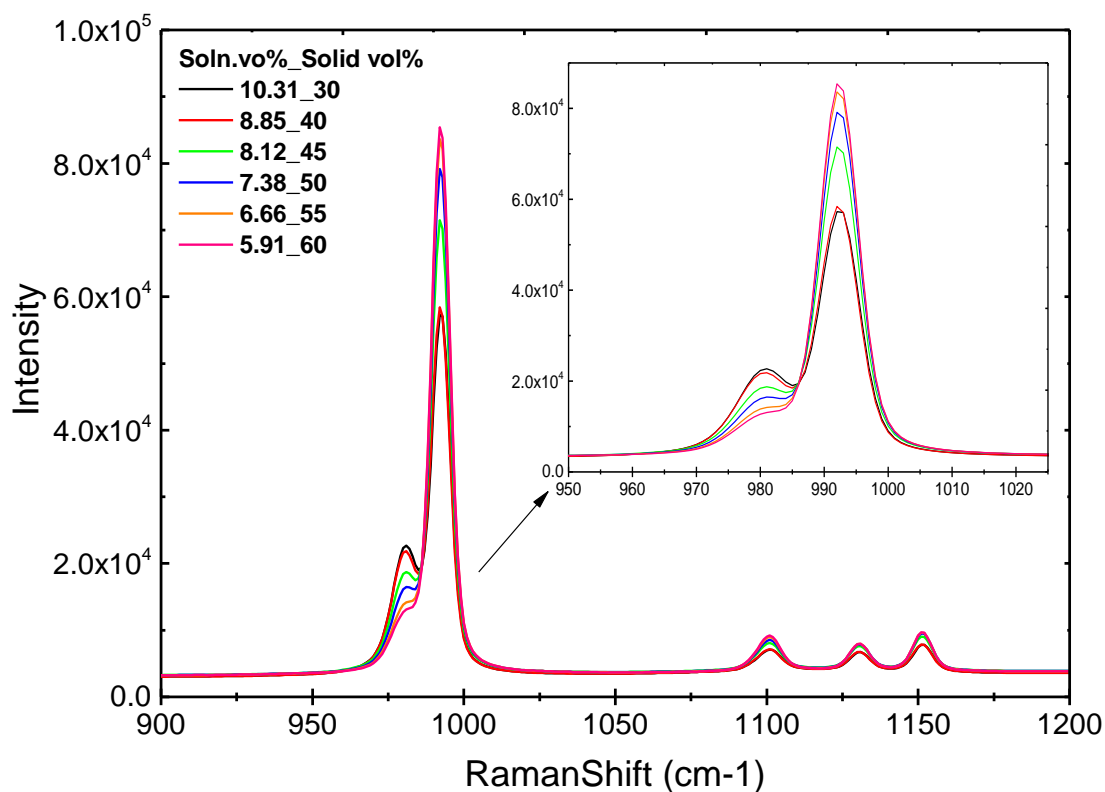
Figure 4.10: Spectra collections for the calibration use of Na$_2$SO$_4$, solid in slurry systems. Figure illustrates the change in peak intensity and position with concentration and phase respectively. Spectra were obtained at 75°C and 100 rpm. Each plot represents an average of 15 raw spectra, collected at 30 second intervals. Values in legends are the volume fraction of solution phase and solid phase respectively.

The calibration of the Burkeite solid phase should follow the same method. A peak around 1008 cm^{-1} was chosen as the characteristic information, see Figure 4.11.
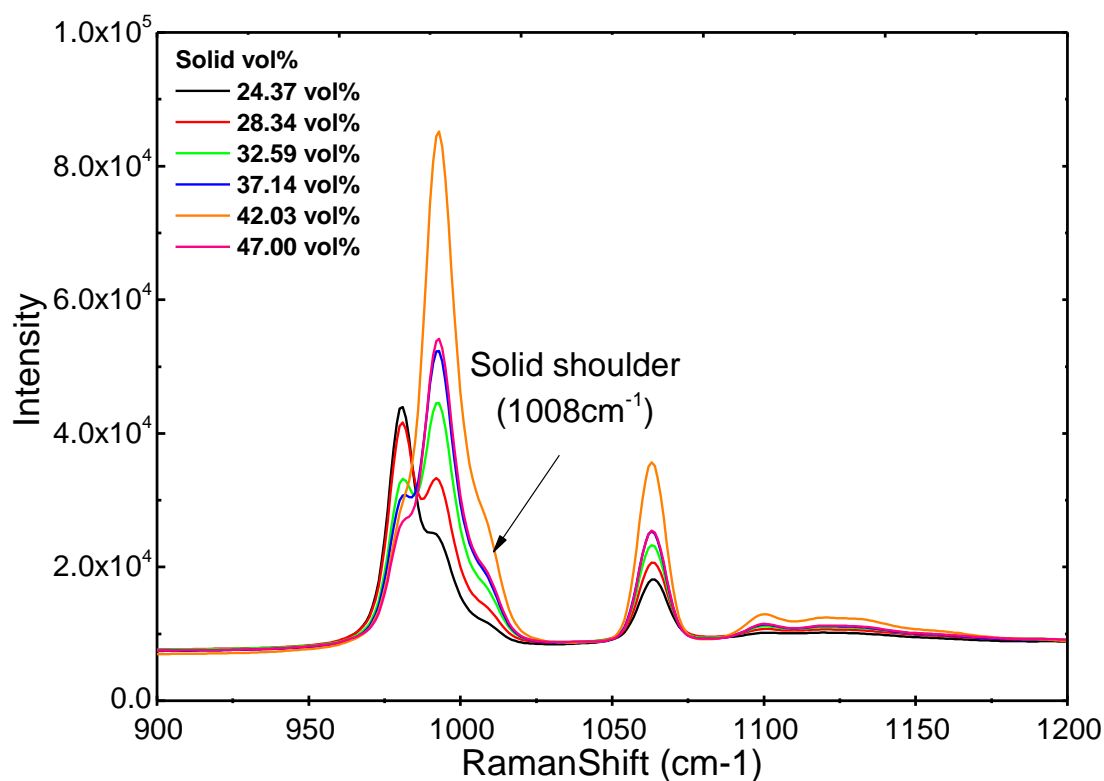
Figure 4.11: Spectra collections for the calibration use of Burkeite solid in slurry systems. Figure illustrates the change in peak intensity and position with concentration and phase respectively. Spectra were obtained at 75ºC and 100 rpm. Each plot represents an average of 15 raw spectra, collected at 30 second intervals. Values in legends are the volume fraction of solution phase and solid phase respectively.
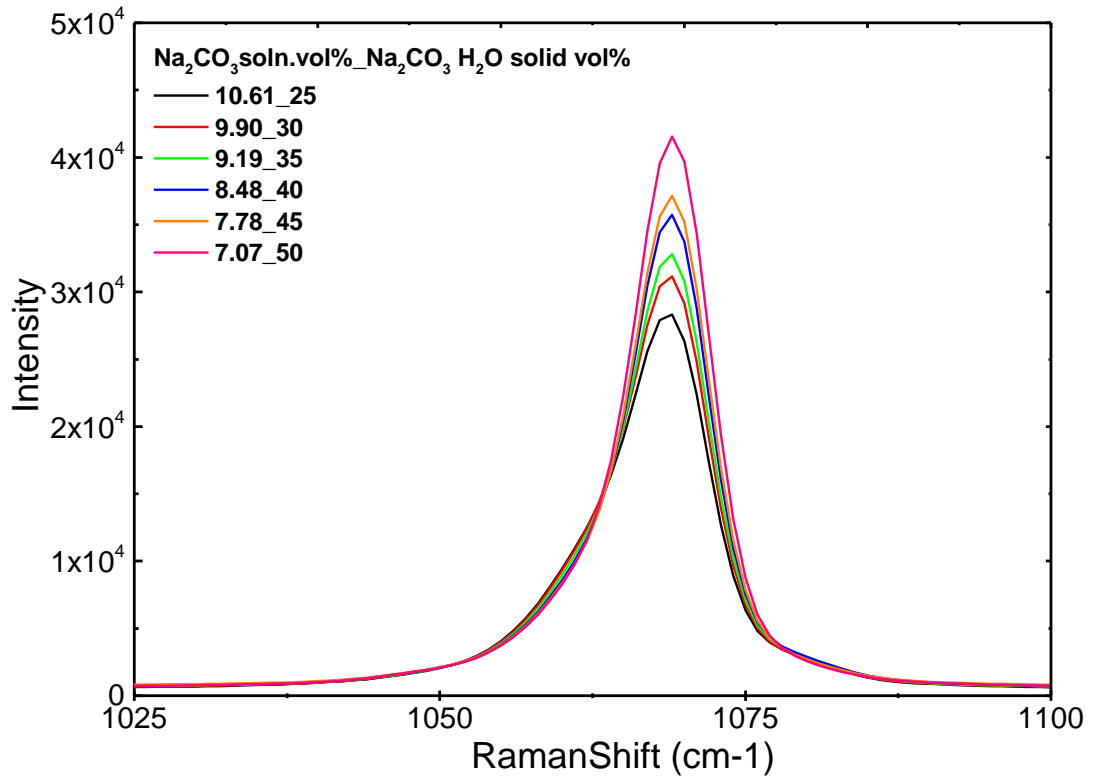
Figure 4.12: Spectra collections for the calibration use of Na₂CO₃·H₂O, solid in slurry systems. Figure illustrates the change in peak intensity and position with concentration and phase respectively. Spectra were obtained at 75°C and 100 rpm. Each plot represents an average of 15 raw spectra, collected at 30 second intervals. Values in legends are the volume fraction of solution phase and solid phase respectively.

In the case of the Na_2CO_3 system, the situation is a little complex due to the peak position of the solid phase being very close to the solution peak, see Figure 4.12. According to the empirical concentration-temperature 2D phase diagram of Na_2CO_3 (Figure 2.6), under this experimental condition, the solid phase should be $Na_2CO_3 \cdot H_2O$ upon reaching the system equilibrium state. Therefore Na_2CO_3 monohydrate solids were used instead of adding Na_2CO_3 anhydrous. By doing so, firstly the slurry composition of the Na_2CO_3 system was simplified, there would be no interference information from the anhydrous phase, hence it will be beneficial to the later model manipulation. Secondly, the overall time for collecting the Raman spectra would be shortened, because the process of anhydrous to monohydrate solid phase transition was avoided. If a system did not reach the equilibrium, in other words the Na_2CO_3 anhydrous solid still existed in the slurry system, then the composition of the

anhydrous phase can be calculated manually by applying the mass balance rule after the peak separation. For instance, in Figure 4.12 the amount of undissolved Na_2CO_3 anhydrous ($m_{c-an.}$) would be calculated by applying the equation below:

$$m_{c-an.} = m_{c-T.} - (m_{c-diss.} + m_{c-mono.})$$

where, $m_{c-T.}$ denotes the total amount of Na_2CO_3 that was added to the solution;

$m_{c-diss.}$ is the amount of dissolved Na_2CO_3;

$m_{c-mono.}$ represents the amount of $Na_2CO_3 \cdot H_2O$.

The last two terms $m_{c-diss.}$ and $m_{c-mono.}$ can be calculated from vol% that will be obtained from the PLS models.

4.2.3.2   PLS model development

Raman spectra for each material at different concentrations was collected and the characteristic peak of both solution and solid phase of Na_2SO_4, Na_2CO_3 and Burkeite were determined. The averaged spectra representing each composition in the calibration experiments (Figure 4.10, Figure 4.11 and Figure 4.12) were inputted to the GRAMS/PLSplusIQ plug-in software, following the operating procedure and applying the modelling parameters that were described in section 3.3.2.3.1.

The accuracy of the model can be displayed by creating an output of the validation plot. Figure 4.13 demonstrates the correlation relationship of the predicted and actual amount of Na_2SO_4 in detected samples as achieved from region 900-1050cm^{-1}. Both correlation coefficients R^2 exhibited in excess of 0.95 suggested good agreement between predicted and actual concentrations of Na_2SO_4.
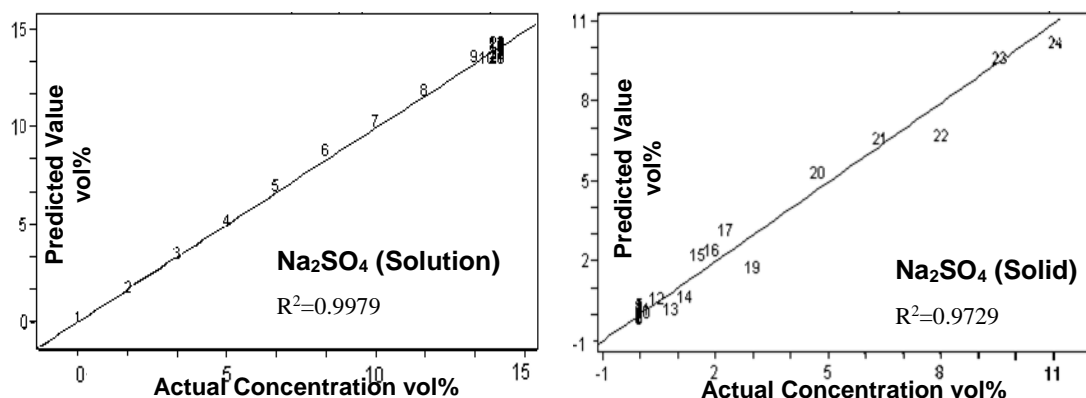
Figure 4.13: An example of PLS predicted concentrations of Na₂SO₄ vs. actual responses obtained in the calibration process. $vol\% = vol\ of\ Na_2SO_4\ suspended\ solid/vol\ of\ total\ slurry$. **Figures were outputted using GRAMS/AI spectroscopy software as a measure of fit of PLS models to the original calibration data.**

4.2.4 Validation of PLS models

The dissolution and adding of solid in the slurry experiments was repeated, and the PLS model was applied for on-line monitoring of the solution and slurry composition change for each addition. The results are displayed in Figure 4.14; the predicted concentration was aligned with the actual amount of added materials; this consistency indicated the predictive accuracy of the PLS slurry models.
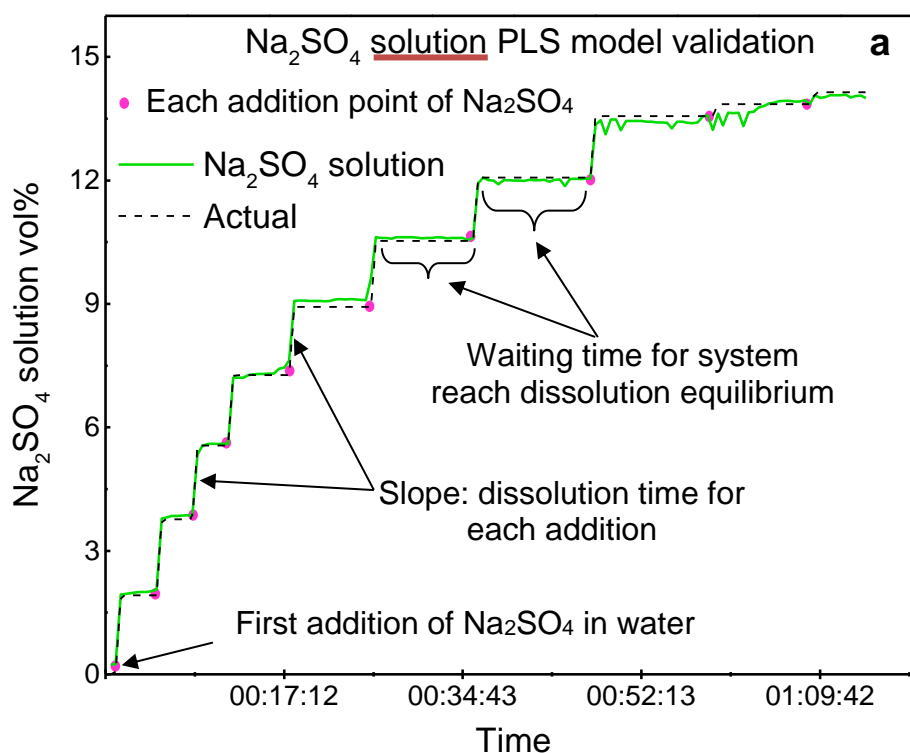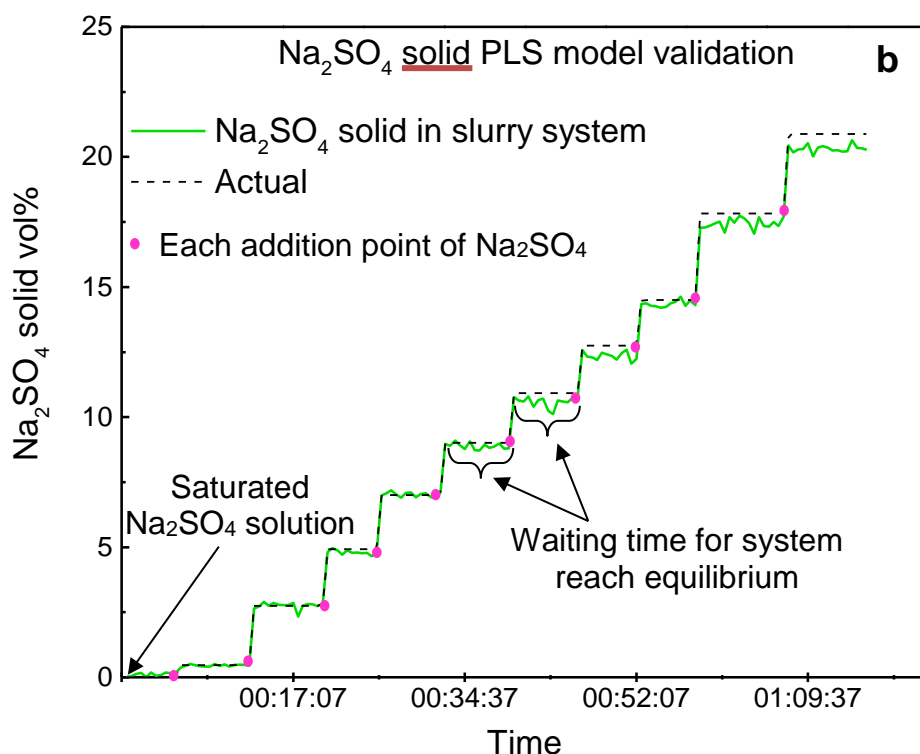
Figure 4.14: Validation of the PLS model by on-line detecting Na₂SO₄ dissolution (a) and precipitation (b) process. Green solid line illustrates predicted concentration from PLS model. The black dashed line stands for the actual amount of Na₂SO₄ introduced in each addition.

4.3 Quantitative analysis of solid mixtures using XRD Rietveld Refinement

XRD has been much used as an analytical technique to understand the crystalline properties of both organic and inorganic contained in powder form. This technique was applied for both qualitative and quantitative analysis. In this work, it was used to verify the reliability of the Raman PLS models. However, firstly the reliability and feasibility of the XRD quantitative analysis method for current materials (i.e. Na_2SO_4, Na_2CO_3 and Burkeite) needs to be confirmed.

4.3.1 Eliminating Artificial Effect Caused by Crystal Orientation Preference in XRD Measurement

First of all, XRD patterns of raw materials and in-house-synthesised Burkeite were compared with the International Centre for Diffraction Data (ICDD) standard patterns, see Figure 4.15; the most peak positions were matched that indicated Na_2CO_3 was in its monoclinic β form with the space group of C2/m and Na_2SO_4 presented in its orthorhombic stable form V with the space

group Fddd. However, the most intense peaks for the raw materials did not match with the standard patterns from the ICDD database. For instance, the peak of (111) face has higher intensity than the (112) face for Na_2SO_4 raw material, and for Na_2CO_3, the most intense peak appeared as face (002) instead of (310) in the reference pattern. The most possible reason should be due to the preferential orientation of the tested sample on the sample holder. Similar effects were also experienced by other researchers (10, 16). Linnow et al. pointed out for the stable phase V of Na_2SO_4 several faces that can give the preferential orientation effect (17). Also, Meenan's research denoted the (111) face of Na_2SO_4 is the fast growing one (10), so not surprisingly most of the Na_2SO_4 crystals would prefer to align in this face and provide strong intensity in the measurements of this research.
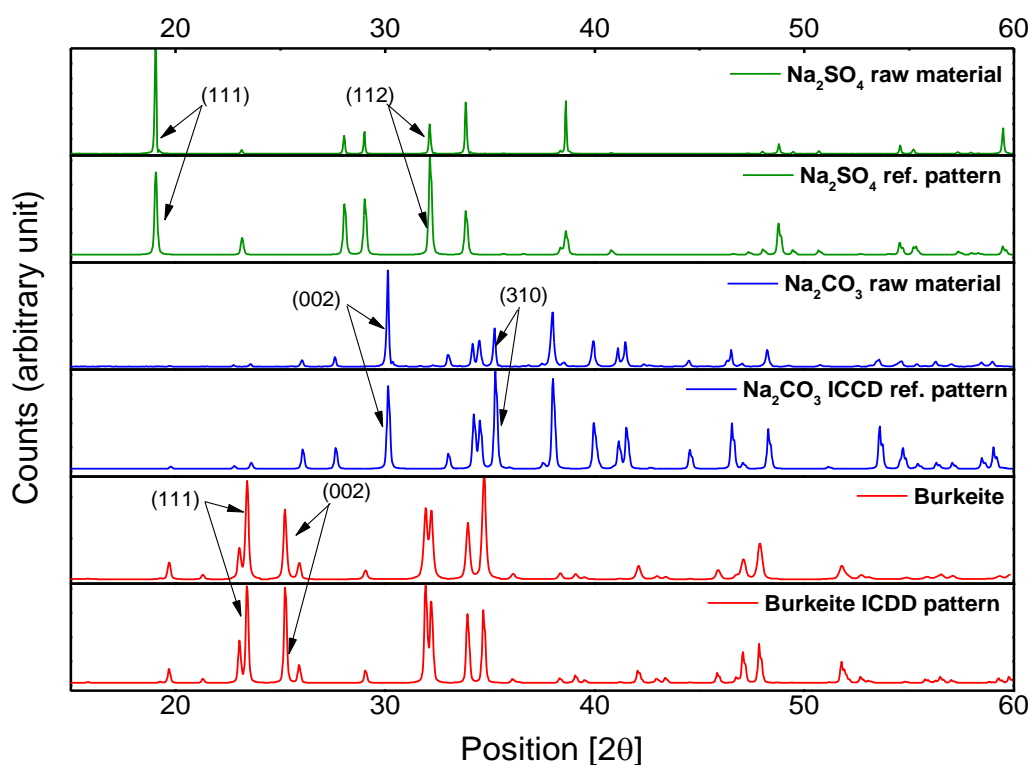
Figure 4.15: XRD pattern for Na₂CO₃, Na₂SO₄ raw materials and self-crystallised Burkeite with the comparison of the ICDD database. (Na₂SO₄ (V) 00-036-0397, Na₂CO₃ 01-075-6816 and Burkeite 04-014-9945).

The shape of crystals (i.e. needle-like, plate-like) turn to pack in a preferred orientation during measurement and cause an adverse impact on the XRD pattern, which could introduce errors to the qualitative analysis and give an

inaccurate conclusion. Therefore, there is a need to develop a method which can be used to eliminate the packing orientation issue. A plotting? method was described in the MEng final report by Matthew Kilner, which has also been applied previously by other researchers (16, 18).

By repeating the method that Kilner mentioned (19), 0.5-1 g was determined as the proper amount of powder that will be mixed with resin to provide an efficient reduction in the preferable orientation influence (see Figure 4.16).
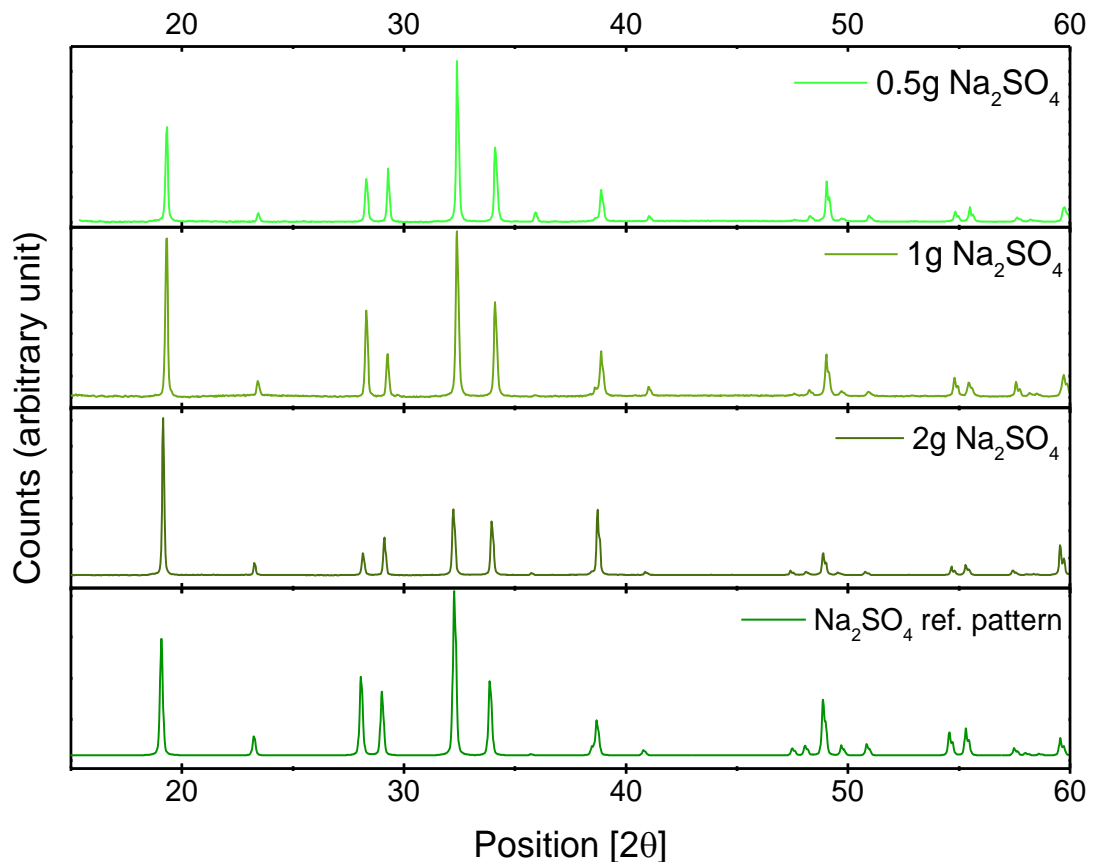
Figure 4.16: Determining the effective amount of powder that will mix with resin to reduce the preferable orientation effect.

4.3.2 Rietveld quantitative analysis

As illustrated in Figure 4.16 the plotting method minimised the extent of the preferred orientation. However, if the effect still exists in the analysed sample, the deviation can be further tuned and compensated through Rietveld refinement, thereby improving the accuracy of the quantitative analysis outcomes.

Ten out of twenty known compositions of solid mixtures were pre-treated by using epoxy resin as described in the method section, then the XRD and the Rietveld analysis were applied to all the twenty samples individually. The final comparison outcomes are presented in Table 4.4 and Table 4.5.

Table 4.4: Semi-quantitative Rietveld refinement on known composition of Na_2CO_3 & Na_2SO_4 solid mixtures and the deviation before and after the epoxy resin treatment

Weight Ratio Na_2CO_3: Na_2SO_4	Non-pre-treated powders (wt%)		Dev. (%)	Pre-treated powders (wt%)		Dev. (%)
6:1	90.72	9.28	20.44	84.06	15.94	6.75
3:1	80.63	19.37	15.01	76.55	23.45	4.13
1:1	87.41	12.59	74.82	47.31	52.69	5.38
1:3	45.19	54.81	53.84	25.78	74.22	2.08
1:6	47.67	52.33	136.3	16.29	83.71	8.18
			Average:60.09%			Average:5.31%

Table 4.5: Semi-quantitative Rietveld refinement on known composition of Na_2CO_3, Na_2SO_4 and Burkeite solid mixtures and the deviation before and after the epoxy resin treatment

Weight Ratio Na_2CO_3: Na_2SO_4: Burkeite	Non-pre-treated powders (wt%)			Dev. (%)	Pre-treated powders (wt%)			Dev. (%)
1:1:1	56.76	22.46	20.78	46.85	33.34	35.6	32.10	3.51
1:3:1	15.38	39.80	44.88	60.49	21.97	59.8	18.23	6.34
1:3:2	9.09	52.63	38.28	21.85	16.40	47.30	36.30	5.30
6:1:1	85.26	12.17	2.57	31.92	77.28	10.64	12.08	7.09
				Average:40.28%				Average:5.56%

The results denoted that with the combination of sample pre-treatment and Rietveld refinement a dramatic improvement was achieved in quantitative analysing of solid mixtures.The average deviation of 5.31% and 5.56% was achieved for the double and triple solid mixture systems respectively. These two methods were, therefore, employed to evaluate the products from the slurry experiments. In addition, the concentrations of phases present in the samples were then used to calculate the amount of Na_2CO_3 and Na_2SO_4 dissolved in the solution, which contributes to the verification of PLS slurry models.

4.4 Impact of process conditions on slurry compositions - a validation of the PLS models

This part of the experiments was designed for two purposes, one of which was for validating the PLS slurry models. The other important reason was for finding the dependency of the Burkeite yield on the process conditions, such as the impact of the order of addition (OOA) of raw materials on Burkeite crystallisation. The solids in the slurry were filtered and dried around at 80°C ready for the XRD quantitative determination as described in section 4.3, through which the preferable orientation effect in powder samples should be diminished. The results were further compared with the outcomes from PLS prediction.

4.4.1 The impact of the mass ratio and order of addition (OOA) of raw materials on the Burkeite formation

Na_2CO_3 and Na_2SO_4 were weighed separately with the mass ratio of 1:1, 1:3 and 6:1. For each experiment, Na_2CO_3 was firstly added in the pre-heated deionized water (75°C), after the system reached thermal equilibrium again, Na_2SO_4 were added. These three experiments were repeated with a converse adding sequence. (The detailed procedure was given in section 3.3.4. Results are presented in Figure 4.17, Table 4.6 and Table 4.7.
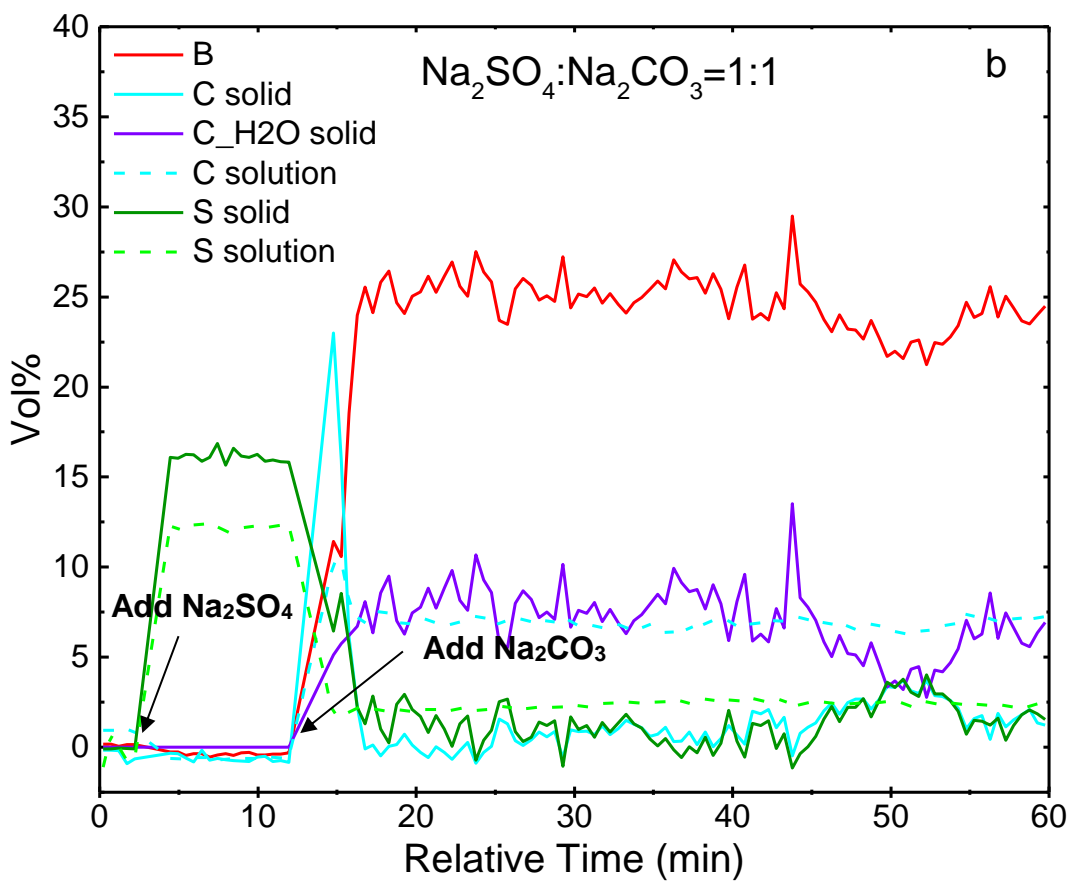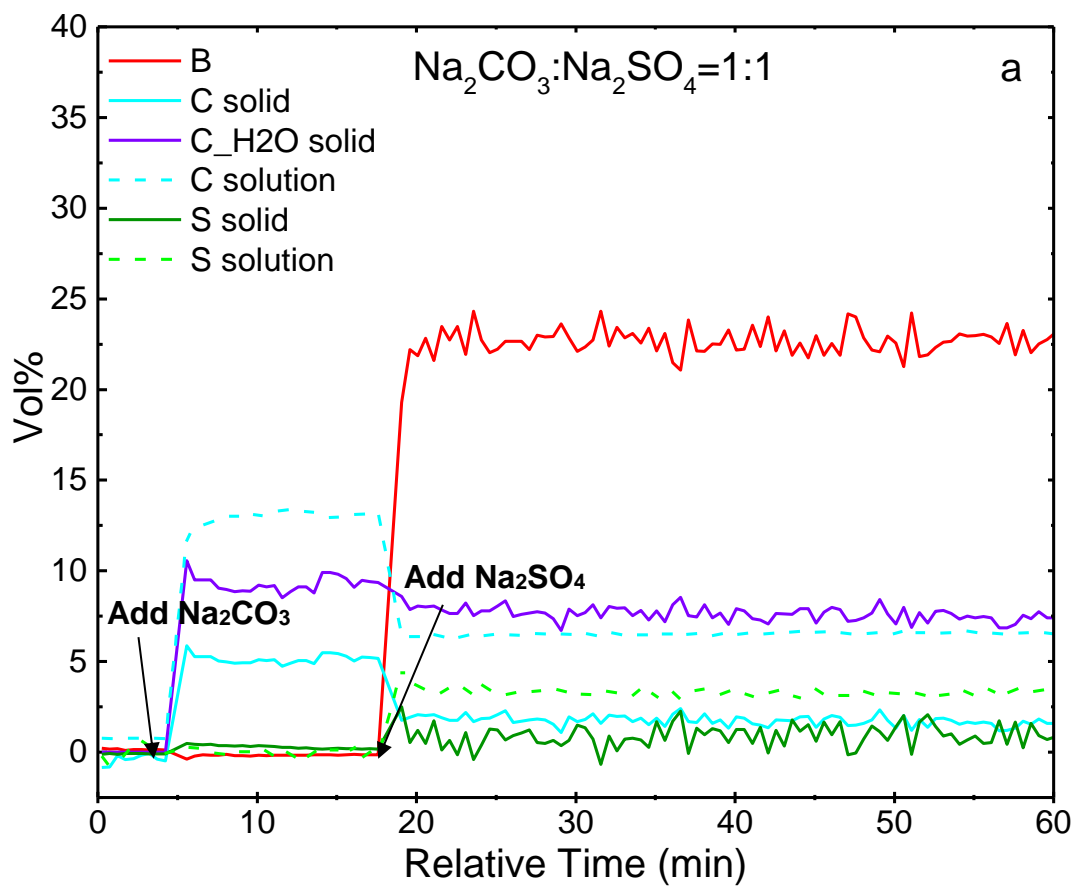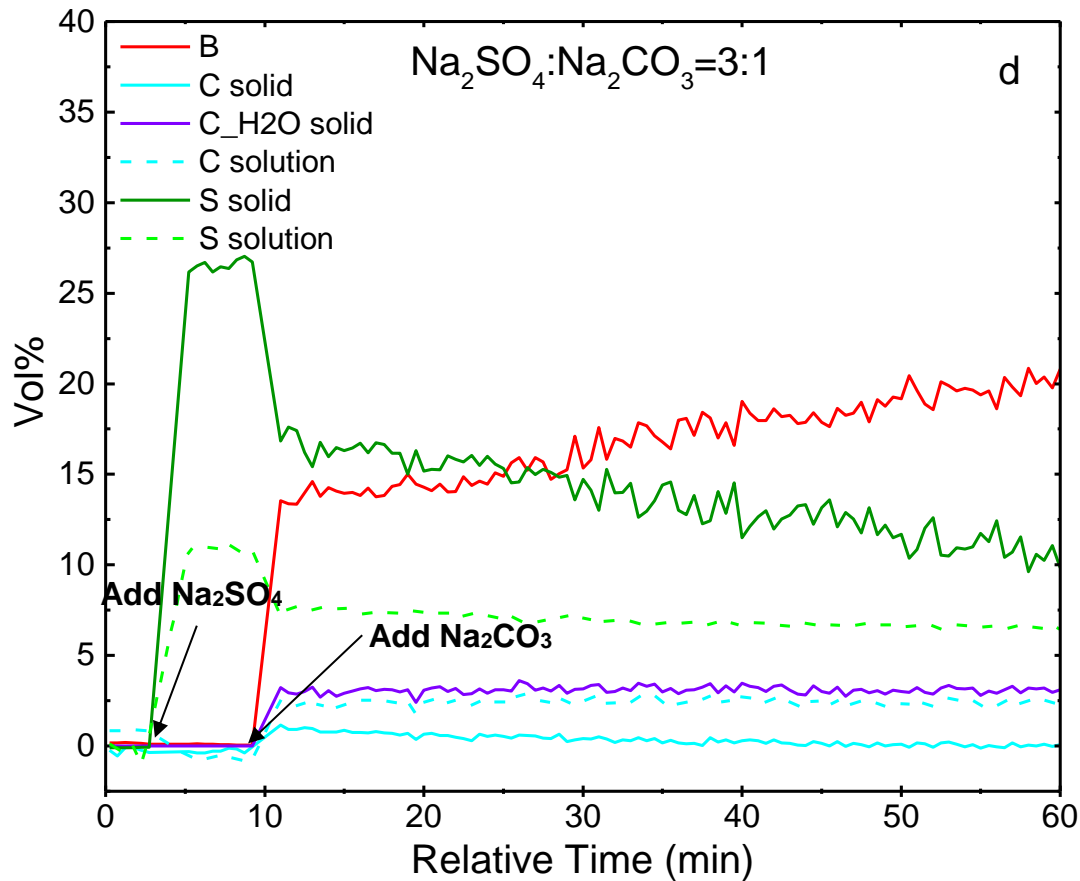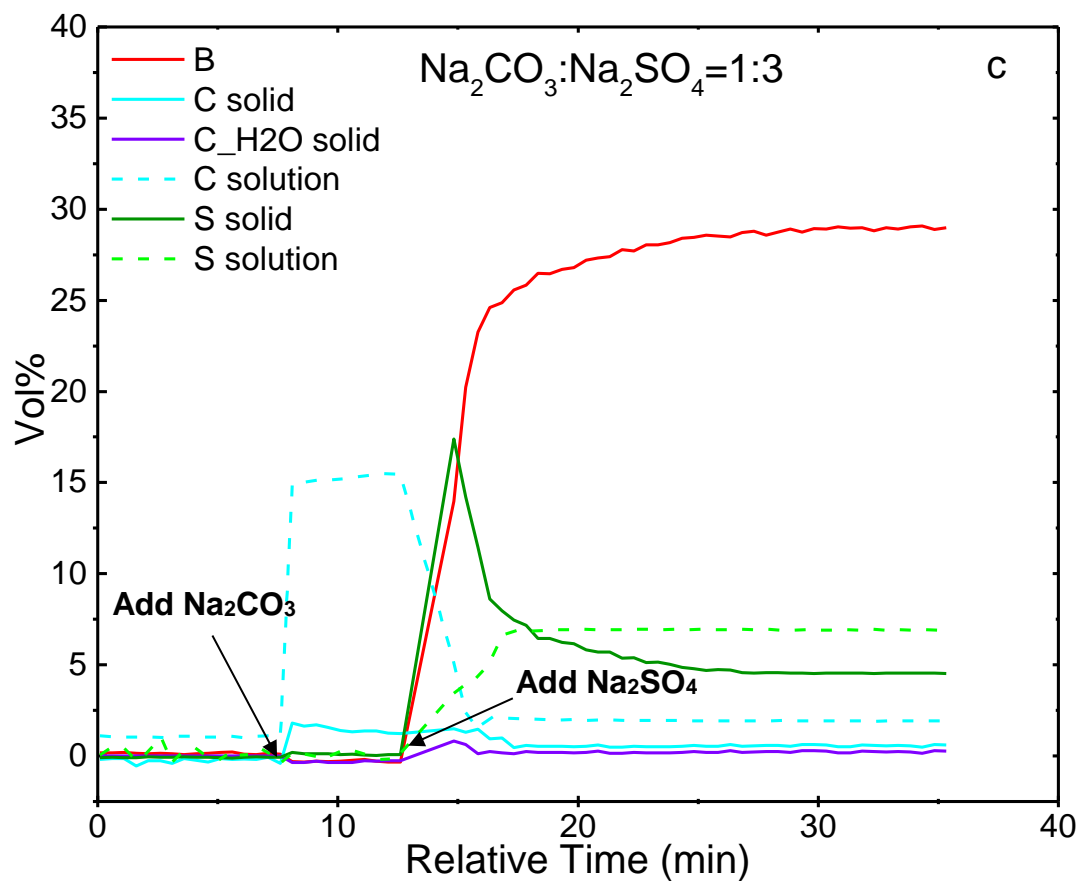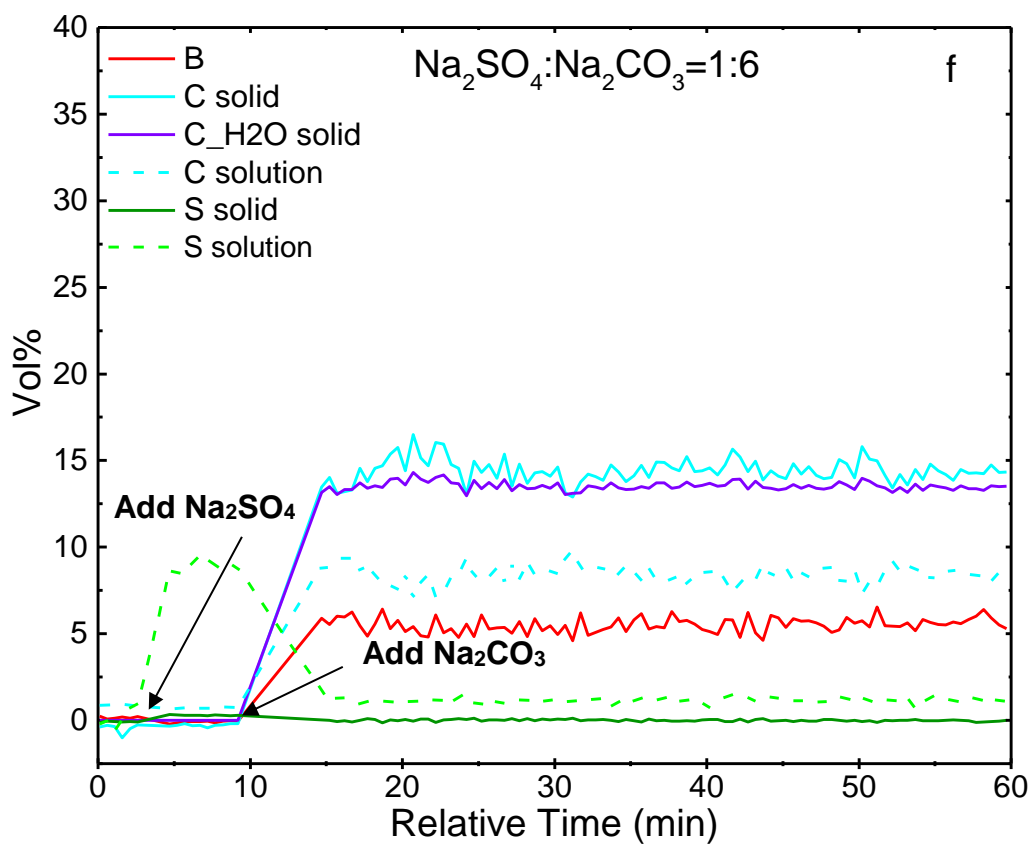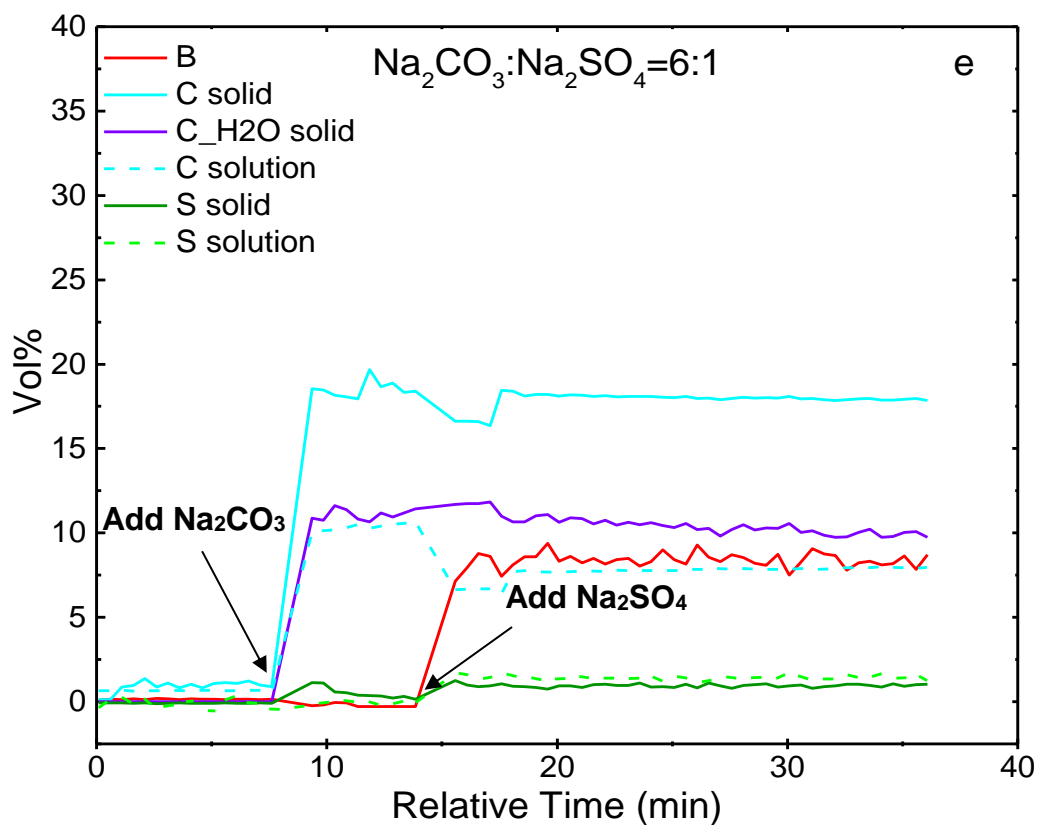
Figure 4.17: Impact of process operation on Burkeite crystallisation monitored by in-situ Raman (experimental variables: Na₂CO₃ to Na₂SO₄ mass ratio and the additional sequence; fixed condition: 75°C and 100rpm);

Figure 4.17 shows the fast crystallisation kinetic of Burkeite. A significant amount of this new solid phase was achieved within a minute after the second material was added to the system. In the case of adding Na_2CO_3 first, the exceeded solid existed in both anhydrous and monohydrate phase (Figure 4.17 a and e). The concentration of Na_2CO_3 anhydrous solids reduced sharply with the addition of Na_2SO_4, however, the vol% of the $Na_2CO_3 \cdot H_2O$ phase remained constant. This could be due to the existence of co-ordinate covalent bonds (i.e. the bonding between water and the sodium ion) in the crystal structure of monohydrates as compared to the anhydrous. Energy input would be required to break the structure of monohydrates. So the dissolution of the anhydrous was preferable.

At the weight ratio of $Na_2CO_3 : Na_2SO_4 = 1:3$, the most Burkeite was obtained (~28.95 vol%) when Na_2CO_3 was first introduced to the aqueous solution. On the contrary, with the same ratio, if Na_2SO_4 was added first, the final volume fraction of Burkeite was approximately 20.16%. In addition, a relatively slow crystallisation process was achieved, the concentration of Burkeite was continuously increasing, see Figure 4.17 (d). In other ratio cases, it was probably because either there was not enough Na_2CO_3 (i.e. 1:1 ratio) or Na_2SO_4 (i.e. 6:1 ratio) to effectively react, furthermore regarding the stoichiometric ratio of Burkeite ($Na_4(CO_3)_{0.61}(SO_4)_{1.39}$), therefore raw material residues were left in both cases. Table 4.6 lists the composition of the final slurry of each experiment by PLS model, weight percentage was applied in order to correlate with the XRD analysis in Table 4.7.

Table 4.6: Quantitative analysis by Raman PLS models represents the dependency of the slurry composition on the OOA of raw materials

Raw material OOA & ratio	Burkeite (wt%)	Na_2CO_3 (C) (wt%)			Na_2SO_4 (S) (wt%)	
		Solid	$Na_2CO_3 \cdot H_2O$ solid	Soln.	Solid	Soln.
C+S 1:1	34.23	2.27	10.98	9.87	1.44	5.02
S+C 1:1	37.11	2.19	10.11	10.95	2.12	3.54
C+S 1:3	44.15	0.86	0.35	2.92	6.92	10.54
S+C 3:1	30.82	0.03	4.70	3.70	16.25	10.96
C+S 6:1	7.25	27.20	15.04	12.05	1.48	2.19
S+C 1:6	8.75	21.79	20.45	12.86	-0.05	1.81

$Na_2CO_3:Na_2SO_4=1:3$ provided the most Burkeite, this result was very close to the most desirable ratio for the Burkeite formation that was discovered by previous researchers (4, 5). However, the conclusion of the desirable order of addition was in conflict with the discovery from Colin et al. (20). The reason will be discussed in Chapter 6.

In this study, after Na_2CO_3 was primarily introduced into the aqueous system, the pH of the solution increased above 10 immediately. Therefore most of the salt stayed as free CO_3^{2-} in the solution ready to form Burkeite. However, when Na_2SO_4 was added first, theoretically it will slow down the dissolution of Na_2CO_3 to a certain extent on the common ion effect of Na^+ from the already dissolved Na_2SO_4. Apart from that, with the high water content (34 wt%) and the operational temperature (75°C), the Na_2CO_3 anhydrous to monohydrate transition would take place instantaneously after the exceeded amount of this salt was added (Figure 2.6). With the additional process of crystal transition and dissolution involved, the formation of Burkeite certainly would be slowed or delayed. More experiments and discussion are detailed in Chapter 6.

Table 4.7 shows a comparison of the quantitative analysis results between the PLS predictions and Rietveld refinements. The PLS results of the solid phases were re-calculated from Table 4.6. The standard deviation of each material was less than 5%, which represents the high consistency between these two analytical methods which further verified the reliability of the PLS models.

Table 4.7: Comparison of the quantitative analysis results between Rietveld refinement and PLS models prediction on the solid phase of the slurries (samples for the XRD analysis were filtered at the end of the OOA experiments and dried in a pre-heated oven at 80°C)

Raw material OOA & ratio	Burkeite wt% in the total solid		Na_2CO_3 wt% in the total solid		$Na_2CO_3 \cdot H_2O$ wt% in the total solid		Na_2SO_4 wt% in the total solid	
	Raman	XRD	Raman	XRD	Raman	XRD	Raman	XRD
C+S 1:1	69.97	69.50	4.64	5.70	22.45	24.00	2.95	0.90
S+C 1:1	72.01	70.40	4.25	5.40	19.62	23.70	4.12	0.50
C+S 1:3	84.45	83.10	1.65	1.90	0.67	3.40	13.23	11.60
S+C 3:1	59.50	63.90	0.07	0.70	9.06	14.50	31.37	20.90
C+S 6:1	14.22	-	53.36	-	29.51	-	2.90	-
S+C 1:6	17.18	-	42.78	-	40.15	-	-0.10	-
Dev.	1.38		0.55		2.44		3.14	

4.5 Raman Calibration Model for Solid Mixtures

4.5.1 Raman spectra collection for calibration

XRD is the most popular way for quantitative analysis of powder mixtures for both the organic and inorganic phases. Here with the advantages of minimum sample preparation, the fast scanning time and lower sensitivity to the crystal orientation effect, creating the Raman solid mixture model for the quantitative analysis was attempted.

Five mixtures with different ratios of Na_2SO_4, Na_2CO_3 and $Na_2CO_3 \cdot H_2O$ (see Table 4.8) were used.

Table 4.8: The composition of solid mixtures was utilised for the Raman solid model calibration

Material	Experiments_wt%					Experiments _mass_g				
	1	2	3	4	5	1	2	3	4	5
Na_2SO_4	70	70	55	55	40	65.00	65.00	50.00	50.00	35.00
Na_2CO_3	10	20	15	30	30	9.29	18.57	13.64	27.27	26.25
$Na_2CO_3.$ H_2O	20	10	30	15	30	18.57	9.29	27.27	13.64	26.25
Measured density of mixtures (kg/m^3)						1240.33	1128.50	1160.00	1074.33	1021.17

$$wt\%_{predicted} = \frac{I_{measured} * F_{packing}}{k}$$

The calibration model equation is given above. $I_{measured}$ is the Raman peak intensity of a single component, k is the calibration gradient of a single component, $F_{packing}$ is the volume correction factor, which illustrates the absolute volume difference between the measured sample and the samples used in calibration.

In general, Raman peak intensity increases with the material mass fraction. However, in powder mixtures there are other factors which could also impact on the peak intensity, e.g. particle size distribution, packing density and so on. It is because the size of Raman measuring area is fixed, for the same powder mixture, lower packing density would result in a lower peak intensity due to the presence of a higher volume fraction of the void.

The schematic diagrams below (Figure 4.18) demonstrate how the packing density difference was caused by different intra-porosity and different particle size distribution (PSD).
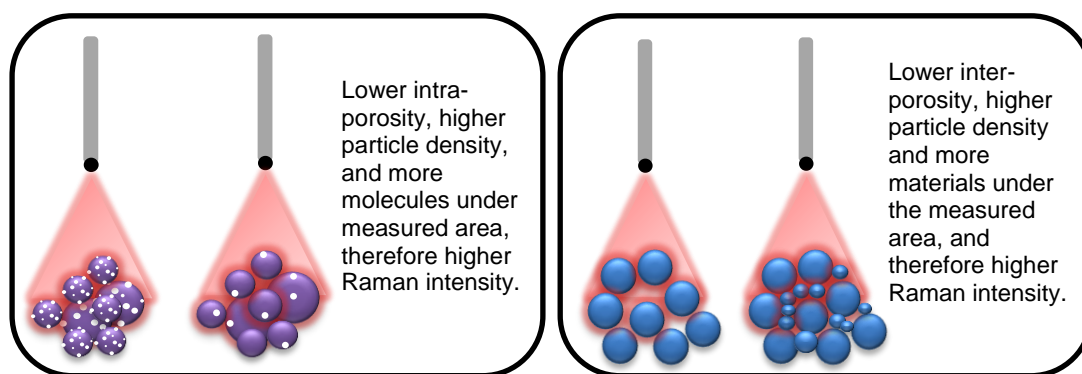
Figure 4.18: Schematic diagrams of how sample density or packing could impact on the peak intensity of Raman spectra.

4.5.2 Calibration Model Development and Validations for Solid Mixtures

To generate the model, five different compositions of Na_2SO_4, Na_2CO_3 and $Na_2CO_3 \cdot H_2O$ were measured and analysed. The full Raman spectra of these five mixtures are shown in Figure 4.19(a), and three different characteristic peaks can be seen for these materials, Na_2SO_4 (993 cm^{-1}), Na_2CO_3 (1080cm^{-1}) and $Na_2CO_3 \cdot H_2O$ (1069 cm^{-1}). A clear linear relationship was found between the peak intensity and the mass fraction of each component (Figure 4.19 (b)). The slope of Na_2SO_4 and Na_2CO_3 are similar, but the gradient of $Na_2CO_3 \cdot H_2O$ is just half of the number compared with the other two. The present water molecule within the $Na_2CO_3 \cdot H_2O$ crystals must reduce the density of the carbonate under the focused laser beam, therefore appeared a lower gradient of the peak intensity of its Raman spectra. The slight difference in the peak intensity of two samples that both contained 70% Na_2SO_4 may be because of the different particle arrangement in the sample.
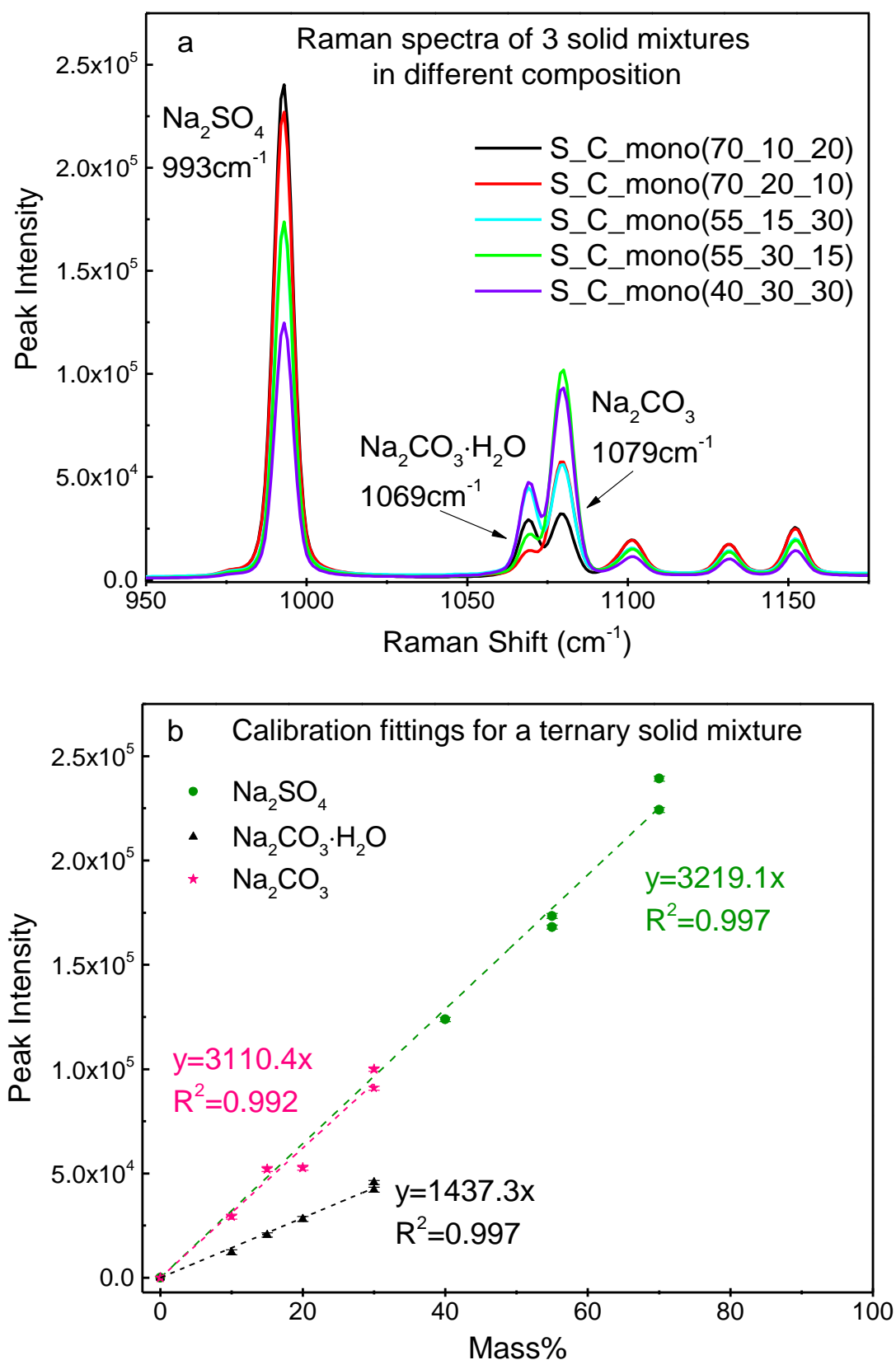
Figure 4.19: (a) Raman spectra of three materials mixed in various compositions, the standard peak position for each material was listed; (more experimental detail see section 3.3.2.4); (b) illustrates the linear relationship between the peak intensity and the mass percentage of each component in the mixture.

Figure 4.20 displays the difference between the actual composition and the predicted composition by using the Raman solid mixture calibration models. The overall predicted composition root-mean-square error (RMSE) was below 2%, which indicates the model has relatively high accuracy. Two different samples of spray drying granules (provided by Procter & Gamble) were analysed by XRD and both spray drying granules contained Na_2CO_3 amorphous which will not directly provide a sharp peak in the Raman spectra. This finding can extend the capability of the application of the Raman spectroscopy technique, especially for processes which have spray drying involved, whereby amorphous would be easily achieved (21-23). Therefore, the composition variation of a slurry mixture would be able to be compared before and after the process. Moreover, the composition of the achieved samples can also be traced under specific storage conditions.
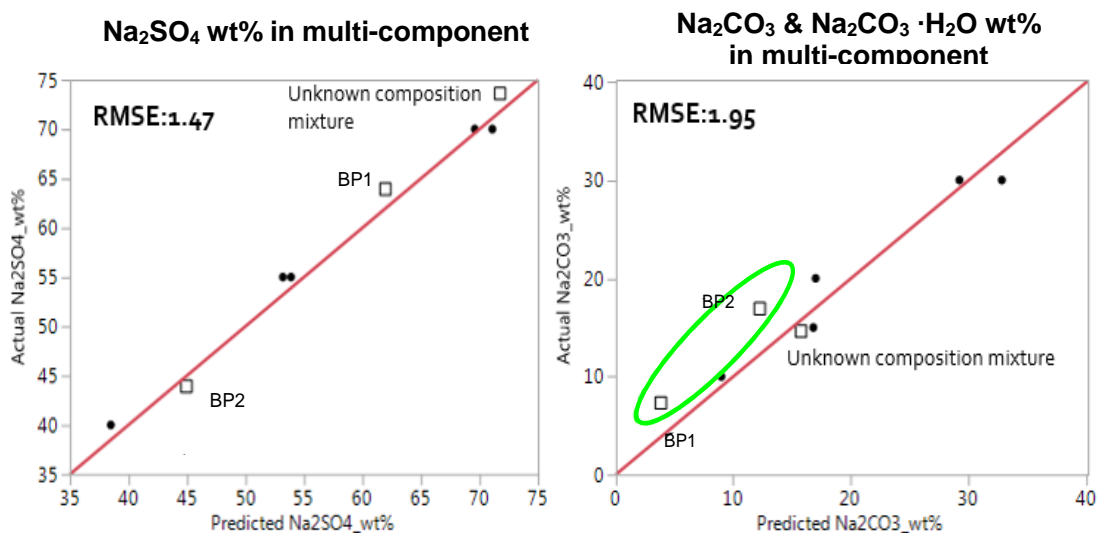
Figure 4.20: Validation results of known powder mixtures and spray drying granule samples (BP). (The BP samples were supplied by P&G, unknown composition sample was a mixture prepared by another researcher who was the only person who knows the actual composition)

4.5.3 The Application of Raman Solid Models

An example was given to illustrate the possibility of using Raman dry solid models to monitor the evolution from amorphous to the crystalline phase of materials under stable conditions.

The solid model of two inorganic crystalline materials A and B were generated by following the previous method. According to the model, crystals A and B would appear as sharp peaks in the Raman spectra. However, if the detected sample contained a certain level of amorphous, then the composition of the amorphous will be calculated by subtracting the detected total amount of crystalline from the initial mixture composition.

A slurry mixture of the Na_2CO_3 and Na_2SO_4 was spray dried (above 200°C) and separated into four equal portions. Amorphous could be obtained during the spray drying process (21). The separated samples were kept under identical laboratory conditions. As time went on (i.e. a few months), each time one sample was taken out for Raman measurement, at least 15 spectra were collected for each sample, assuming all the samples initially had the same level of amorphous and crystalline content. Sample one had the shortest conditioning time, and sample four was the last sample that was taken out of the conditioning oven.

A clearly crystalline to amorphous transition tendency can be observed from Figure 4.21. As the total crystalline of Na_2CO_3 and Na_2SO_4 increased, which is indicated in black, the amount of amorphous phase decreased, denoted by the green colour.

This experiment was performed just to give a taste of the capability of the Raman technique. With this help, more experiments can be designed, such as accelerating or eliminating the transition process, which would be purely dependent on the real case requirements.
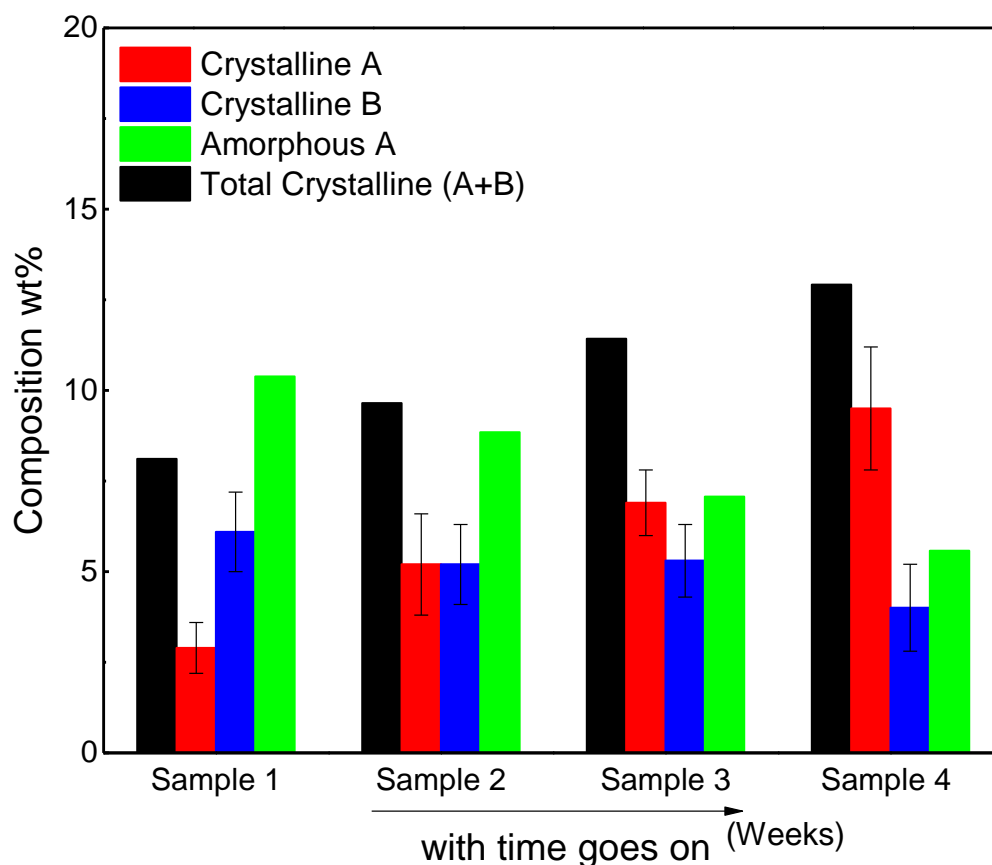
Figure 4.21: Applying the Raman model for solid mixtures on estimating the amount of amorphous to crystalline transition with the change of time (A: Na$_2$CO$_3$，B: Na$_2$SO$_4$).

4.6 Conclusions

The emphasis of this chapter was on developing the calibration models for quantitatively analysing the detected samples.

The solution calibrations of Na$_2$CO$_3$ and Na$_2$SO$_4$ were achieved by monitoring the peak intensity changing with the solution concentration through the dissolution process, respectively. A linear relationship was attained for both materials with the R^2 values in excess of 0.99. These calibrations are better used for solution systems with no solid present, so the volume expansion is only caused by raw material dissolving.

In the case of slurry model development, firstly five PLS models were created, next a set of experiments was designed with the intention of verifying the accuracy of PLS models as well as finding the optimal strategy for producing the most Burkeite. The model verification was carried out by comparing the

PLS monitoring outcomes of the final slurry composition with the quantitative analysis results from the XRD Rietveld refinement of the dried end product from each experiment. A good agreement was obtained from these two methods with the deviation smaller than 5 wt% on each substance, which indicates the reliability of the PLS models. Apart from that, by comparing the slurry composition dependency on the designed experimental variables, i.e. raw material mass ratios and raw material order of addition to the system, found out the most Burkeite would be achieved by adding Na_2CO_3 first Na_2SO_4 after with the mass ratio of 1:3.

There are some matters needing attention for developing slurry model which are:

1. Spectra for calibration use needs to be collected upon the system reaching equilibrium;
2. Ensure system mixing is efficient, no sedimentation at the bottom of the reactor;
3. Raw material sampling, minimise the impact of particle size distribution on the peak intensity.

Models for dry solid mixtures were also established. The accuracy was verified by detecting the solid mixture with known compositions. The overall predicted RMSE was below 2%, which proves the veracity of the solid models. The essential matter for creating the solid model is to record the sample density, which helps to calculate the volume correction factor $F_{packing}$ that was defined in section 4.5.1, thereby diminishing the impact of packing density on the peak intensity.

All of the accomplished models would contribute to investigating the influence of the experimental, processing or storage conditions on the composition variation of the samples studied, which can further affect the experiment optimisation. In the following chapters, these models were applied to some practical studies, such as ternary phase diagram determination, kinetics study for the new solid phase precipitation (i.e. Burkeite) and the speciation study for sodium silicate solutions.

Reference List

1.   Green, S.J. and Frattali, F.J. The System Sodium Carbonate-Sodium Sulfate-Sodium Hydroxide-Water at 100° 1. *Journal of the American Chemical Society.* 1946, **68**(9), pp.1789-1794.

2.   Meenan, P., Roberts, K., Knight, P. and Yuregir, K. The influence of spray drying conditions on the particle properties of recrystallized burkeite (Na2 CO3·(Na2SO4)2). *Powder technology.* 1997, **90**(2), pp.125-130.

3.   Meenan, P., Roberts, K., Yuregir, K. and Knight, P. The influence of batch processing on the particulate properties of burkeite (Na2CO3 (Na2SO4) 2). *Journal of materials science.* 1995, **30**(12), pp.3115-3122.

4.   Harvie, C.E., Møller, N. and Weare, J.H. The prediction of mineral solubilities in natural waters: The Na-K-Mg-Ca-H-Cl-SO 4-OH-HCO 3-CO 3-CO 2-H 2 O system to high ionic strengths at 25 C. *Geochimica et Cosmochimica Acta.* 1984, **48**, pp.723-751.

5.   Makarov, S. and Bleiden, V. The polytherm of the Quaternary system Na 2 CO 3-Na 2 SO 4-NaCl-H 2 O and solid solutions of the berkeite type. *Ser. Kim. Izv. Akad. Nauk. SSSR.* 1938, pp.865-892.

6.   Shi, B., Frederick, W.J. and Rousseau, R.W. Effects of calcium and other ionic impurities on the primary nucleation of burkeite. *Industrial & Engineering Chemistry Research.* 2003, **42**(12), pp.2861-2869.

7.   Shi, B. and Rousseau, R.W. Structure of burkeite and a new crystalline species obtained from solutions of sodium carbonate and sodium sulfate. *The Journal of Physical Chemistry B.* 2003, **107**(29), pp.6932-6937.

8.   Gamble, P. 2011.

9.   Giuseppetti, G., Mazzi,F.& Tadini,C. The Crystal Structure of Synthetic burkeite $Na_4SO_4(CO_3)_t(SO_4)_{1-t}$. *Neues Jahrbuch fur Mineralogie.* 1988, **8**.

10.   Meenan, P. *Experimental and theoretical studies on the nucleation, growth and habit modification of some inorganic carbonates, phosphates and sulphates.* thesis, University of Strathclyde, 1992.

11.   Odziemkowski, M., Flis, J. and Irish, D. Raman spectral and electrochemical studies of surface film formation on iron and its alloys with carbon in Na2CO3/NaHCO3 solution with reference to stress corrosion cracking. *Electrochimica acta.* 1994, **39**(14), pp.2225-2236.

12. Brooker, M. and Bates, J.B. Raman and infrared spectral studies of anhydrous Li2CO3 and Na2CO3. *The Journal of Chemical Physics.* 1971, **54**(11), pp.4788-4796.

13. Choi, B.-K. and Lockwood, D. Raman spectrum of Na2SO4 (phase V). *Solid state communications.* 1989, **72**(1), pp.133-137.

14. Korsakov, A.V., Golovin, A.V., De Gussem, K., Sharygin, I.S. and Vandenabeele, P. First finding of burkeite in melt inclusions in olivine from sheared lherzolite xenoliths. *Spectrochimica Acta Part A: Molecular and Biomolecular Spectroscopy.* 2009, **73**(3), pp.424-427.

15. Hamilton, A. and Menzies, R.I. Raman spectra of mirabilite, Na2SO4· 10H2O and the rediscovered metastable heptahydrate, Na2SO4· 7H2O. *Journal of Raman Spectroscopy.* 2010, **41**(9), pp.1014-1020.

16. Nesterenko, S.N., Meshkov, L.L., Zosimova, P.A. and Nesterenko, N.S. Composition and structure of the oxidation products of Mo-Pt alloys. *Inorganic Materials.* 2009, **45**(2), pp.145-150.

17. Linnow, K., Zeunert, A. and Steiger, M. Investigation of sodium sulfate phase transitions in a porous material using humidity-and temperature-controlled X-ray diffraction. *Analytical chemistry.* 2006, **78**(13), pp.4683-4689.

18. Taylor, J. and Pecover, S. Quantitative analysis of phases in zeolite bearing rocks from full X-ray diffraction profiles. *Australian Journal of Physics.* 1988, **41**(2), pp.323-336.

19. Kilner, M. Crystallisation of Burkeite from Detergent Slurry. 2012.

20. Atkinson, C., Heybourne, M.J., Iley, W.J., Knight, P.C., Russell, P.J., Taylor, T. and Jones, D.P. *Process for preparing needle-shaped crystal growth modified burkeite detergent additive.* Google Patents. 1990. Available from: https://www.google.be/patents/US4900466

21. Leaper, M.C., Leach, V., Taylor, P. and Prime, D.C. A comparison of compacting and caking behavior of carbonate-based washing powders. *Drying technology.* 2013, **31**(7), pp.769-774.

22. Cleaver, J., Karatzas, G., Louis, S. and Hayati, I. Moisture-induced caking of boric acid powder. *Powder technology.* 2004, **146**(1), pp.93-101.

23. Burnett, D., Thielmann, F. and Booth, J. Determining the critical relative humidity for moisture-induced phase transitions. *International journal of pharmaceutics.* 2004, **287**(1), pp.123-133.

Chapter 5 In-situ Raman Spectroscopy Determining a Ternary Phase Diagram of Na_2CO_3-H_2O-Na_2SO_4 and a Kinetic Study of Burkeite Formation

5.1 Introduction

Solubility studies of the Na_2CO_3-Na_2SO_4-H_2O ternary system by Harvie *et al.* have displayed limited information on the crystallisation behaviour of Burkeite at 25°C through semi-empirical modelling (1). One method of applying this solubility data to the solid-liquid composition of the Na_2CO_3-Na_2SO_4-H_2O slurry is to create a ternary phase diagram, which displays the phase of components as a function of their concentration. Green *et al.* incrementally added Na_2CO_3 and Na_2SO_4 to various concentrations of aqueous solutions at 100°C to develop a ternary phase diagram of Na_2CO_3-Na_2SO_4-H_2O.(2) In his work, in order to achieve the solution equilibrium, each experiment took more than 20 hours to ensure the system equilibrium was attained. Then after filtration, the filtrate and wet residue were studied using a chemical analysis method. According to this method, to carry out a complete phase diagram was time-consuming.

In the present study, the in-situ Raman technique was applied with the aid of the developed PLS models for slurry systems, which were accomplished and verified in the previous chapter, to quickly determine the ternary phase diagram of Na_2CO_3-Na_2SO_4-H_2O at 75°C. The advantages of this method were less time consuming, minor sample preparation and loss, easy to operate, last but not least the composition of each material involved was monitored over the entire experimental period. Therefore, the kinetics of the dissolution and crystallisation process for the individual substances investigated was obtained. In this chapter, the kinetics of Burkeite formation is studied.

5.2 Na$_2$CO$_3$-H$_2$O-Na$_2$SO$_4$ Ternary Phase Diagram Determination

5.2.1 Solubility line determination of Na$_2$CO$_3$ and Na$_2$SO$_4$ solution mixtures

As shown in section 2.2.5.2, Figure 2.11, the solubility lines, A'D, DE and EB', of the solution mixtures with the various compositions of Na$_2$CO$_3$ and Na$_2$SO$_4$ were determined, after which the ternary phase diagram was separated into an unsaturated solutions region and a slurry region. In the saturated region, solutions contained both dissolved Na$_2$CO$_3$ and Na$_2$SO$_4$ raw materials. However, the composition of the slurry systems was complex, and each section contained up to 3 different solid components, such as Na$_2$CO$_3$·H$_2$O Burkeite and Na$_2$CO$_3$.

The way of determining the solubility of a salt mixture system was similar to a single salt solubility determination, by observing the appearance of solid peaks on the Raman spectra (see section 4.2.3).

The total dissolved amount of each material was recorded and also measured using the PLS model at the saturated state and displayed in Figure 5.1.
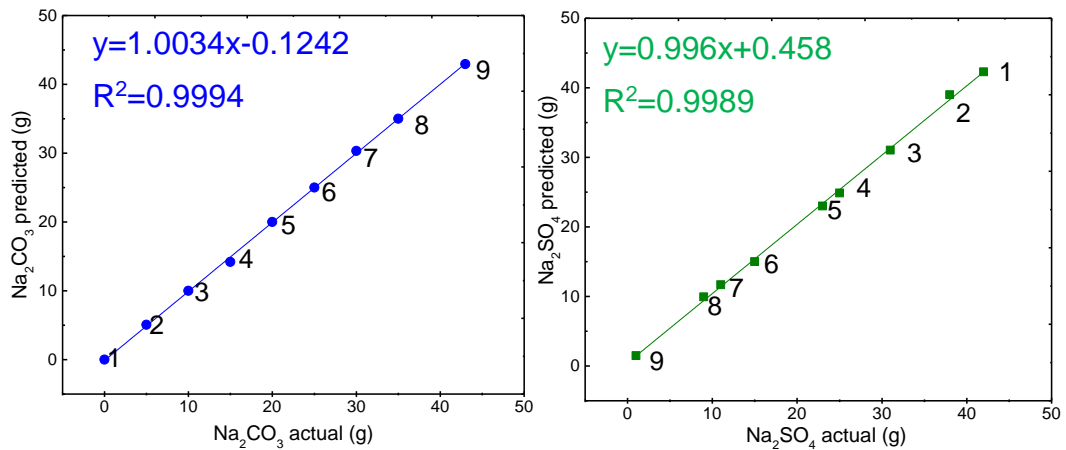
Figure 5.1: Solubility determination of Na$_2$CO$_3$ and Na$_2$SO$_4$ salt mixtures. Numbers next to the fitting line represent experimental solution numbers that corresponds to the first column of Table 5.1 (actual value: the recorded amount of salt was added to dissolve; predicated value: the estimated amount of salt was dissolved from PLS model).

Nine solutions with different amounts of pre-dissolved Na_2CO_3 salt were prepared, Na_2SO_4 was then incrementally added into each Na_2CO_3 solution and the amount added was recorded. In Table 5.1, the total quantity of dissolved Na_2CO_3 and Na_2SO_4 was given, and the individual composition of each solution was also obtained from in-situ Raman measurements. The overall amount of salts involved in the system was estimated by PLS models (see Figure 5.1), which had an average of approximately 0.61 g deviation from the real input value. The average amount of salt dissolved in the water was around 44g/100g. For the exceeded solid phase, see Table 5.1, in solution 1, most of the solids were undissolved Na_2SO_4 that was around 93.06 wt% of the entire remaining solid. In the case of solutions 3 to 8, Burkeite was the dominant crystal of the solid phase. In solution 4, due to more Na_2SO_4 being introduced in the solution, therefore more Burkeite precipitated out as the new phase.

After each experiment, the remaining particles were filtered and dried for XRD quantitative analysis, see Table 5.2. The result was mostly consistent with the Raman data. However, in the case of solutions 3 and 7, $Na_2CO_3 \cdot H_2O$ solid existed in the mixture, probably because the temperature difference led Na_2CO_3 to withdraw from the solution and it stayed in its monohydrate form during the filtration process.
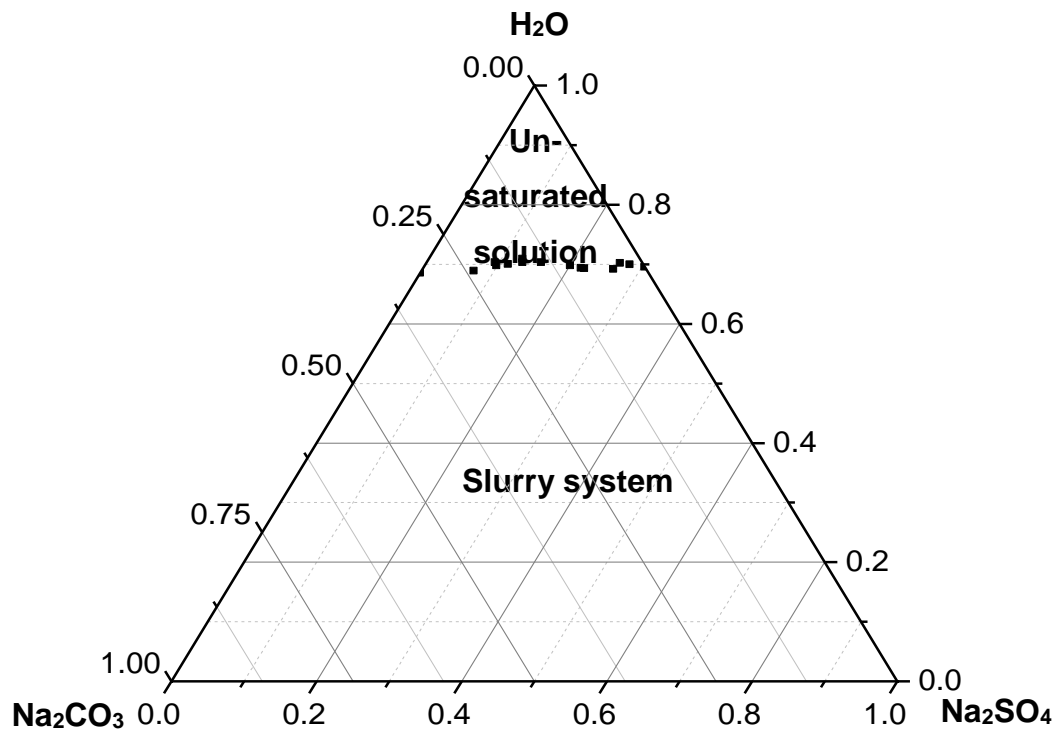
Figure 5.2: Solubility line determination of Na_2CO_3 and Na_2SO_4 solution mixtures on the ternary phase diagram. Different concentrations of Na_2CO_3 solution were prepared; Na_2SO_4 was then added to create saturated solutions. The weight of dissolved Na_2CO_3 and Na_2SO_4 at the saturated state point was recorded separately and used to calculate the wt% by counting in the water weight. The solubility points were located on the phase diagram by applying Origin software. All the solubility points in this figure are corresponding to the orange start points in Figure 5.3. (Experiments were taken under 75 ℃ with 100 rpm)

Table 5.1: PLS model monitored solubilities of Na_2CO_3 and Na_2SO_3 double inorganic solution systems

Soln.	Actual input into the system (**g**)			Raman PLS model predicted concentration (**vol%**)					Mass balance calculation according to the Raman PLS model (**g**)			Deviation
	Na_2CO_3	**Na_2SO_4**	**total**	**Na_2CO_3 soln.**	**Na_2SO_4 soln.**	**Na_2CO_3 & $Na_2CO_3 \cdot H_2O$ solid**	**Na_2SO_4 solid**	**Burkeite solid**	**Total dissolved solid**	**Total Undissolved solid**	**Total amount of salts**	
1	0.00	44.00	44	0.00%	14.56%	0.00%	0.47%	0.00%	43.68	1.41	45.09	0.77
2	5.00	45.00	50	1.45%	12.50%	0.06%	2.01%	0.09%	42.42	6.56	48.98	0.72
3	10.00	35.00	45	3.27%	10.41%	0.13%	0.02%	1.10%	41.00	3.73	44.73	0.19
4	15.00	40.00	55	3.86%	10.20%	0.05%	0.06%	3.77%	43.67	12.07	55.74	0.52
5	20.00	26.00	46	6.51%	7.23%	0.01%	0.01%	1.30%	42.15	4.01	46.17	0.12
6	25.00	20.00	45	7.60%	6.05%	0.00%	0.03%	1.46%	41.01	4.47	45.48	0.34
7	30.00	15.00	45	9.59%	4.43%	0.13%	0.04%	0.95%	42.11	3.33	45.44	0.31
8	35.00	12.00	47	11.46%	3.45%	0.06%	0.00%	0.76%	45.13	2.48	47.61	0.43
9	45.00	0.00	45	14.32%	0.00%	0.30%	0.00%	0.00%	42.76	0.89	43.65	0.95

Table 5.2: The deviation of XRD Rietveld and Raman PLS model analysis (the sample for XRD analysis was the filtered sample from experiments in Table 5.1):

Soln.	XRD Rietveld analysis (wt%)			XRD results converted to mass (g)				Deviation between XRD and Raman analysis			
	Na_2CO_3 & $Na_2CO_3 \cdot H_2O$ solid	Na_2SO_4 solid	Burkeite solid	Na_2CO_3 & $Na_2CO_3 \cdot H_2O$ solid	Na_2SO_4 solid	Burkeite solid	Cal. Dissolved solids	Na_2CO_3 & $Na_2CO_3 \cdot H_2O$ solid	Na_2SO_4 solid	Burkeite solid	Dissolved solids
1	0.00%	100.00%	0.00%	0.00	0.97	0.00	43.03	0.00	0.31	0.00	0.46
2	11.20%	86.50%	2.3%	0.73	5.67	0.15	43.44	0.39	0.32	0.08	0.72
3	13.20%	2.50%	84.30%	0.49	0.09	3.14	41.27	0.07	0.03	0.10	0.19
4	3.90%	1.20%	94.90%	0.47	0.14	11.45	42.93	0.22	0.03	0.19	2.00
5	0.50%	0.20%	99.00%	0.02	0.01	3.98	41.99	0.02	0.01	0.02	0.12
6	0.90%	0.40%	98.80%	0.04	0.02	4.42	40.53	0.03	0.04	0.02	0.34
7	39.40%	4.30%	56.30%	1.31	0.14	1.87	41.67	0.66	0.02	0.68	0.31
8	6.60%	0.10%	91.40%	0.16	0.00	2.27	44.52	0.01	0.00	0.02	0.43
9	100.00%	0.00%	0.00%	0.89	0.00	0.00	44.11	0.00	0.00	0.00	0.96

According to the Raman measurement results of solution composition at the saturation point provided in Table 5.1, solubility points could be located on the phase diagram as shown in Figure 5.2. Above these points solution mixtures stay un-saturated, below these points systems presented as slurries. So, if a line was drawn linking through these points, then it would be the mixture solubility (MS) line for solution mixtures that contain both Na_2CO_3 and Na_2SO_4. The MS also compared with data reported from literature at different temperatures. In Figure 5.3, the MS line for 30°C, 50°C and 100°C were drawn by relocating solubility points from the literature on the phase diagram. It was changed following a trend that the higher the temperature, the shorter the MS line. In addition, all MS lines were almost parallel to each other. So, theoretically the MS at 75°C should locate in parallel in between the purple (100°C) line and the red line (50°C) (Figure 5.3). Moreover, it is worth noting that the eutectic point for the Na_2SO_4-H_2O-Na_2CO_3 system was changing along a straight line which is indicated as line AB and CD in Figure 5.3, therefore the eutectic points of 75°C had to be on AB and CD too. The experimental data showed high agreement. (1-3)
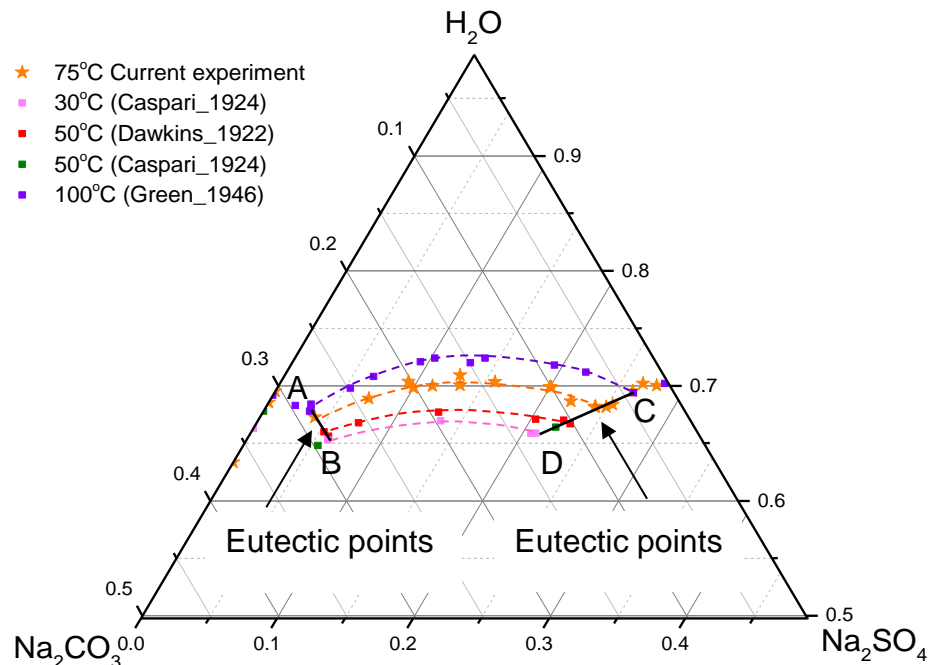
Figure 5.3: A comparison on the solubility of Na_2CO_3 and Na_2SO_4 solution mixtures at different temperature. Orange star points were achieved from this work under 75°C, see Figure 5.2. Solubility lines of sodium solution mixtures at other temperatures (30°C, 50°C and 100°C) are reproduced from literatures (1-3) Eutectic points of the Na_2SO_4-H_2O-Na_2CO_3 are changing with temperature along AB and CD lines.

5.2.2 Boundary line determination in the slurry region

Four experiments were carried out to determine the boundary lines (i.e. line FB, FD, ED, and EA in Figure 2.11) in the slurry region. Two Na_2SO_4 and Na_2CO_3 solutions were prepared, then Na_2CO_3 or Na_2SO_4 was incrementally added into the opposition salt solutions, see Figure 5.4. PLS slurry models were applied for on-line monitoring of the real-time composition variation in both solution and slurry phases. The phenomenon of appearance or disappearance in solid phases was recorded. One of the experiments is given here as an example, Na_2CO_3 was gradually added into a solution of 33.3 wt% Na_2SO_4.

Incrementally add Na_2CO_3 only

Incrementally add Na_2SO_4 only

50g Na_2SO_4/100g water

42g Na_2SO_4/100g water

50g Na_2CO_3/100g water

30g Na_2CO_3/100g water
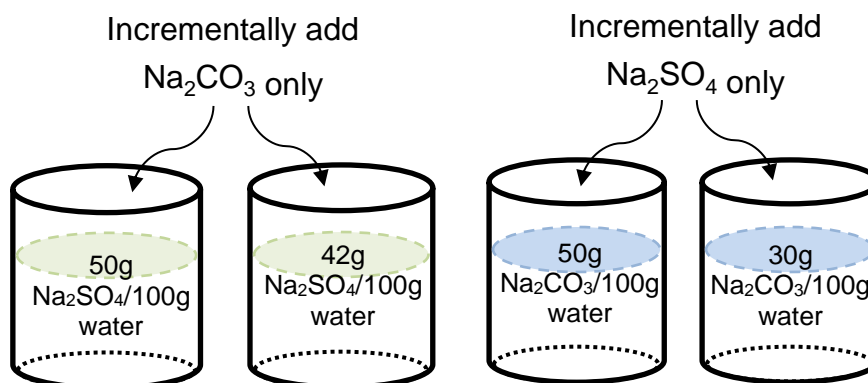
Figure 5.4: Experimental design for Na_2CO_3-H_2O-Na_2SO_4 boundary lines determination. (The solution and slurry composition variation after each time's salt addition was monitoring by in-situ Raman)

The real-time PLS composition analysis profile was obtained and converted to wt%, which is illustrated in Figure 5.5. The corresponding Raman spectra is displayed Figure 5.7. Points F, G & H represent phase-transition points, in other words a new phase was precipitating as a solid or disappearing. For instance, before point F, with the addition of Na_2CO_3 salt, there was no phase change in the system, the composition was a saturated solution with suspended Na_2SO_4 particles.   Beyond point F, Burkeite particles started precipitating out from the solution and co-existed with Na_2SO_4 particles in the saturated solution. Therefore, point F was considered as one of the phase transition points; it must be on one of the region boundaries of the phase diagram. If Na_2CO_3 kept being added it would achieve the phase changing point G and H. Before point G, there were two kinds of particles suspended, which are Burkeite and Na_2SO_4. After point G, only Burkeite crystals were

present in the saturated system and the concentration of its solid phase increased with the increasing amount of Na_2CO_3 added into the system. H was another phase transition point; here $Na_2CO_3 \cdot H_2O$ started taking part in the solid phase. Further adding of Na_2CO_3 showed no change occurred in the phase composition, but solid concentration.
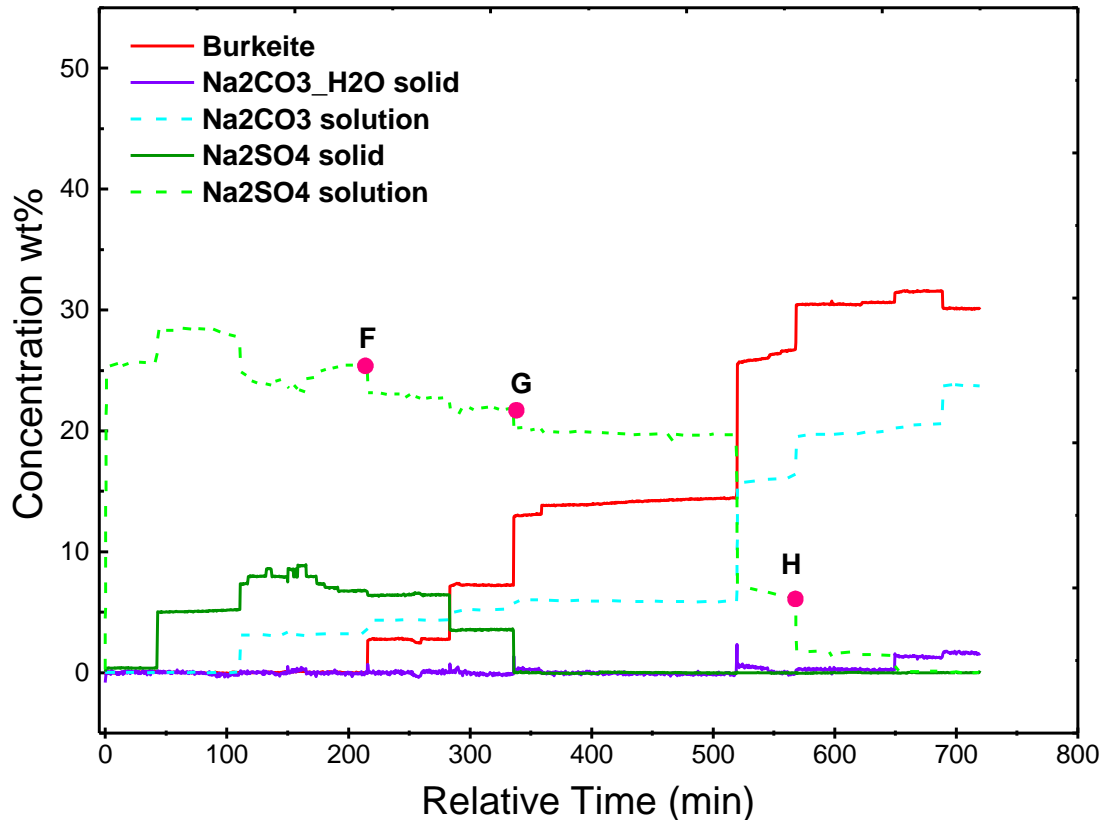
Figure 5.5: An example of the phase boundary determination experiment. Real-time PLS analysis of the changing composition, while incrementally adding Na_2CO_3 into an aqueous slurry system that originally contained 33.3wt% of Na_2SO_4. Each plateau represents the waiting time for the system to reach equilibrium; Na_2CO_3 was introduced to the system at the end of each plateau. F, G & H are the phase transition points, the phase composition of the system are different before and after this point (addition of Na_2CO_3), such as a new phase appearing or the present phase disappearing. The change in spectra is displayed in Figure 5.6.
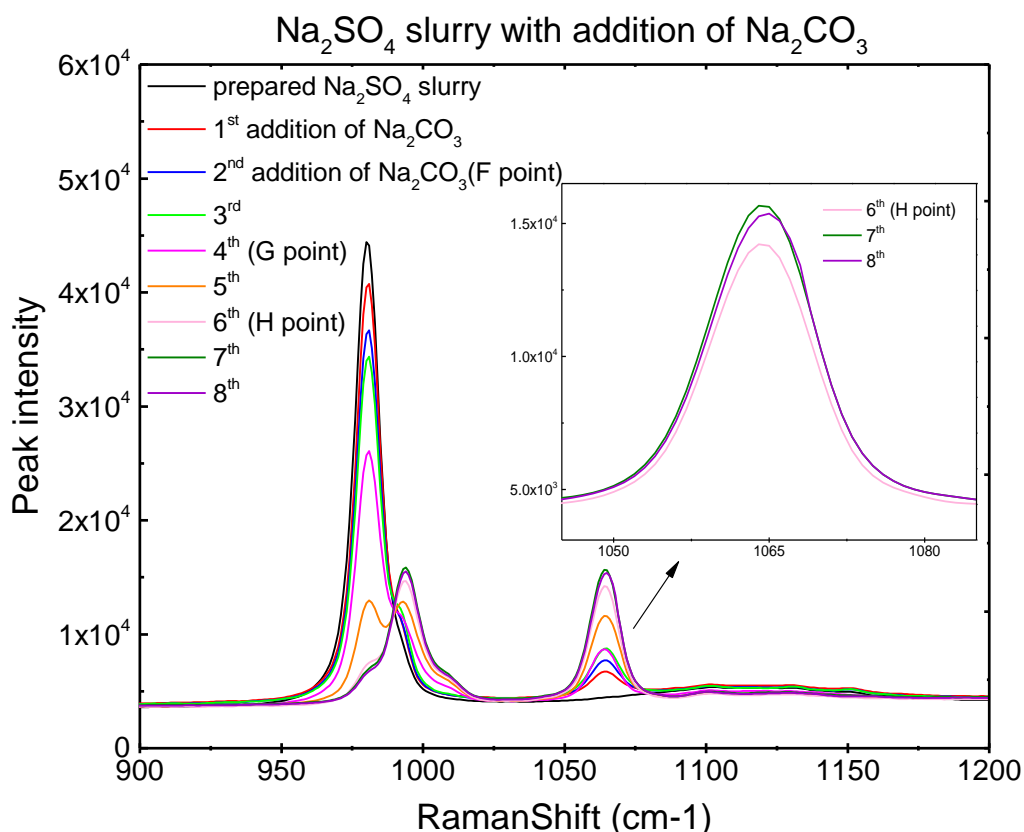
Figure 5.6: Raman spectra of incrementally adding Na_2CO_3 into an aqueous slurry system that originally contained 33.3 wt% of Na_2SO_4. Each spectrum indicates the equilibrium state after the corresponding addition of Na_2CO_3. The phase transition points F, G & H can correlate with Figure 5.5 and Figure 5.7.

Figure 5.6 illustrates the change in Raman spectra with the addition of Na_2CO_3; from the inset figure it can be observed that there was no Na_2CO_3 solid peak ($1079 cm^{-1}$) in existence. After the 6th addition peak around 1065 cm^{-1} started shifting to a higher wavelength, which indicated the formation of $Na_2CO_3 \cdot H_2O$ solid. The results of presenting $Na_2CO_3 \cdot H_2O$ also supported the data from the literature (4-6).

Next, when the system reached its equilibrium after each salt addition, the total weight percentage of Na_2CO_3, Na_2SO_4 and water, respectively were calculated according to the PLS on-line measurement presented in Figure 5.5, and located all the equilibrium points on the ternary phase diagram, see Figure 5.7 (points along the red line). Marking out phase transition points F, G and H for the experiment of adding Na_2CO_3 to Na_2SO_4 solution that had an initial concentration of 33.3 wt% of Na_2SO_4. This kind of phase transition point was also recorded for the other three experiments, which were solutions with an

initial concentration of 23.08 wt% Na_2CO_3 (orange line), 33.33 wt% Na_2CO_3 (blue line) and 29.58 wt% Na_2SO_4 (green line), the real-time PLS measurement plots for these three experiment are displayed in the Appendix.
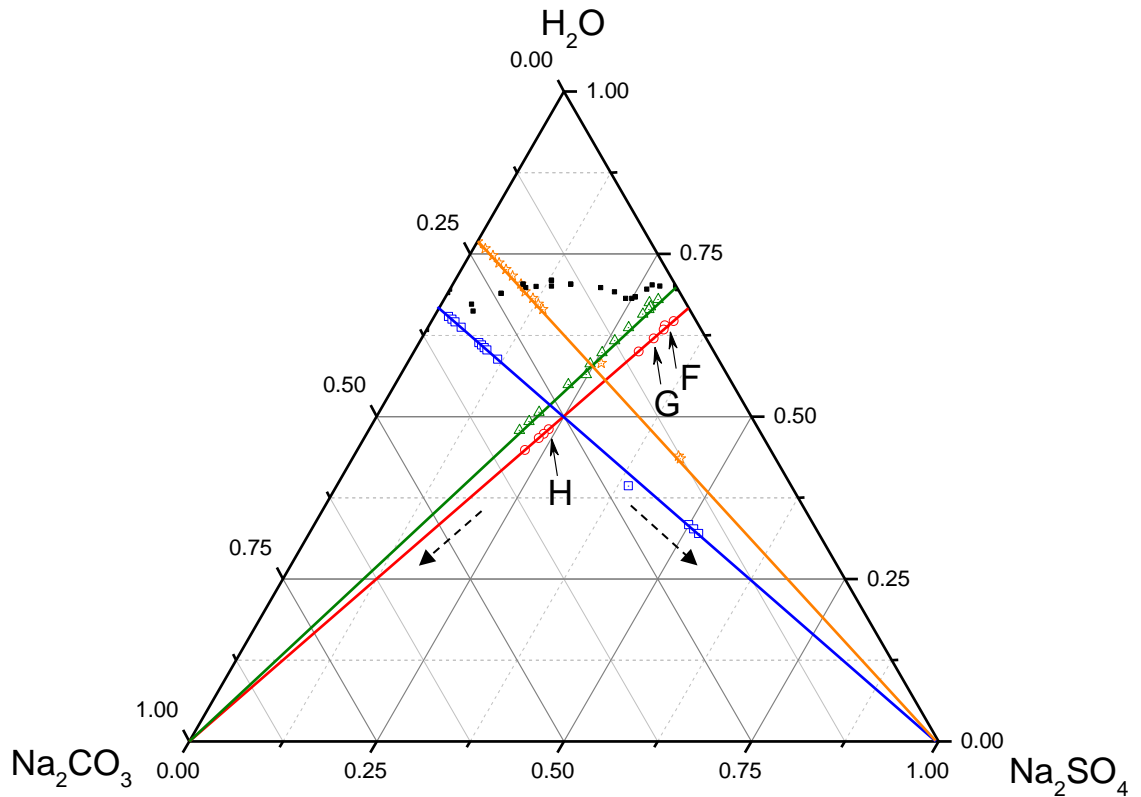
Figure 5.7: Boundary line determination in the slurry section of the ternary phase diagram of Na_2CO_3-H_2O-Na_2SO_4 at 75°C (each coloured line stands for one designed experiment; F, G & H represent the solid phase transition point for one of the experiments; the dotted arrows indicate the direction of the slurry composition change with the addition of sodium salt over the experiment)

Boundary lines between each region were determined by linking the corresponding phase transition points from each experiment together. For instance, according to Figure 5.5 and Figure 0.6 (from the appendix), F and K are the transition points from two different experiments. They both represent the slurry system transferring from a pure Na_2SO_4 composition to a bi-solid (Na_2SO_4 and Burkeite) suspension, see Figure 5.8. Therefore, drawing a line through F and K should achieve one of the region boundary ES. Similarly, the boundary line between region "Na_2SO_4 + Burkeite + solution" and "pure Burkeite + solution" was also obtained through linking transition points J & G (Figure 5.5 and Figure 0.6 from the appendix). The intersecting point of these

two boundary lines would be one of the eutectic points for the Na_2CO_3-H_2O-Na_2SO_4 system. Another eutectic point D in Figure 5.8 was determined in an analogous way.

Figure 5.8: Eutectic points determined by linking together the corresponding phase transition points from different experiments. For instance, one of the boundary lines EI was determined by connecting the phase transition points J, G and N together. It intersects with another boundary line that was achieved from linking K and F together. The intersecting point E was one of the eutectic points of the Na_2CO_3-H_2O-Na_2SO_4 system. Points K and F are transitional points from two different experiments, which indicates the system is transferring from a pure Na_2SO_4 slurry system to a system containing both Na_2SO_4 and Burkeite particles. Points J and G then denote the system is changing from a Na_2SO_4 and Burkeite slurry to a pure Burkeite slurry system.

Any slurry located within the area of solution + Burkeite & Na_2CO_3·H_2O or solution + Burkeite & Na_2SO_4 in Figure 5.9 would stay in equilibrium with the eutectic points D or E. The pink dotted line is the Burkeite component stoichiometric ratio line, which means that the co-crystal achieved along this line is in thermodynamically stable form. Point I represents the composition of

Burkeite in the solid phase, for instance the molar ratio of Na_2CO_3 to $Na_2SO_4 \approx 1:2$. Besides, it is very likely to achieve pure Burkeite crystals by evaporating an unsaturated solution or a slurry system that is located on the dotted line (EI). In addition, the dissolution of the co-crystal obtained along this line would also follow the stoichiometric ratio.

Theoretically, there should have been another small region with the composition of solution + Na_2CO_3 solid + $Na_2CO_3 \cdot H_2O$ and Burkeite at the bottom of the ternary phase diagram (3-8), see Figure 5.9. However, due to the low water level the agitation was not efficient. So, an alternative methodology needs to be considered to define this area.
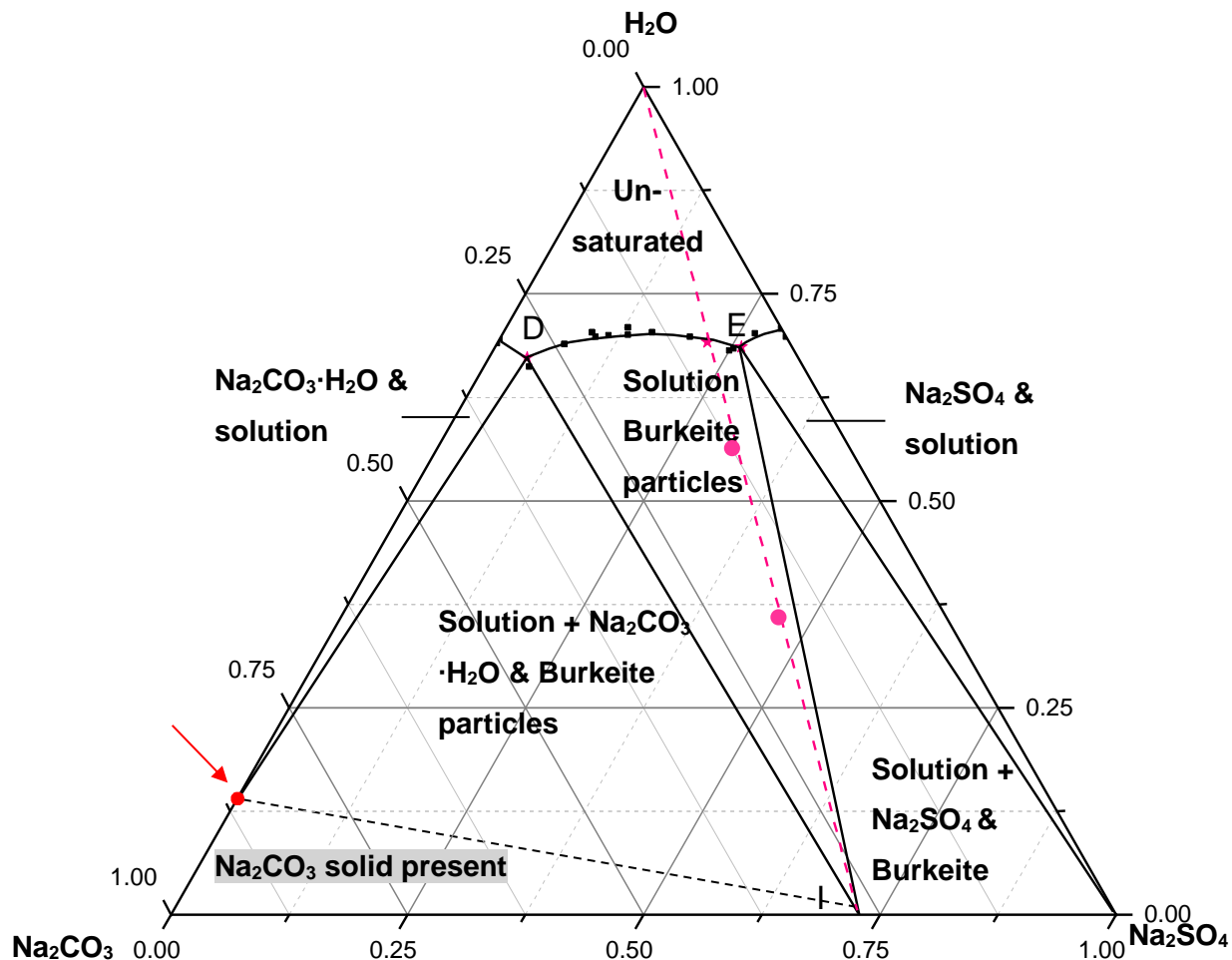
Figure 5.9: The ternary phase diagram of Na_2CO_3-H_2O-Na_2SO_4 at 75°C, the phase compositions are indicated on the graph, D & E are two eutectic points. The pink dotted line is the stoichiometric ratio line for Burkeite. Below the red point, there should be a region with the composition of solution + Na_2CO_3 solid + $Na_2CO_3 \cdot H_2O$ and Burkeite. Two pink points on line EI indicate the current water usage in the laundry industry.

5.3 Investigation of Burkeite Nucleation Kinetics in the slurry system

Metastable Zone Width (MSZW) determination was the preliminary step for nucleation kinetic studies. Commonly, either the isothermal or polythermal method would apply as reviewed in section 2.3.3.
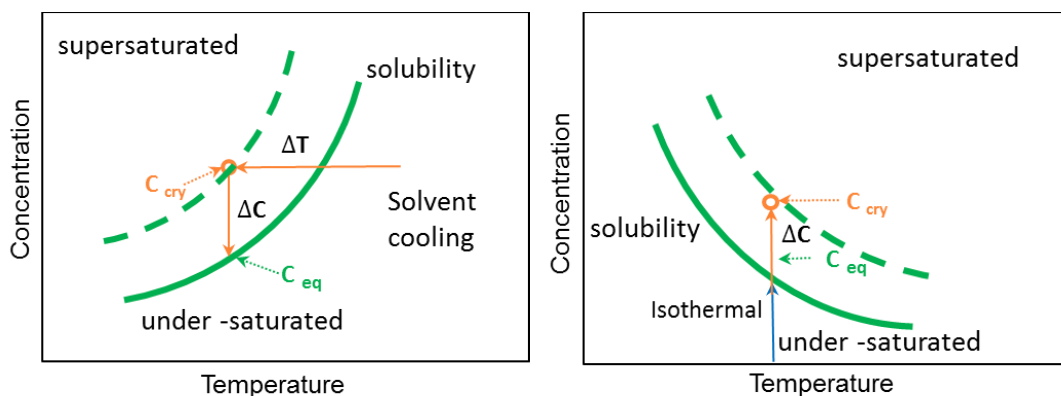
Figure 5.10: Approaches to nucleation study through MSZW determination (left: apply the polythermal method to a substance where solubility increases with the temperature; right: under isothermal conditions, determine the MSZW for a substance that possesses inverse solubility behaviour)

In Figure 5.10, the figure on the left illustrated a material with normal solubility behaviour (solubility increased with the temperature); a temperature cooling method was employed to induce the nucleation. The MSZW or supersaturation degree varies with the cooling rate. The figure on the right indicated the metastability of a material with inverse solubility behaviour (solubility decreased with increasing temperature), such as Na_2CO_3, Na_2SO_4 and Burkeite in this study.

Burkeite can only be obtained when a solution mixture is beyond its supersaturation limit and the dissolved Na_2CO_3 and Na_2SO_4 are in a proper ratio (i.e. around 1:2 molar ratio). According to Shi, et al., the supersaturation degree of the system has an impact on the Burkeite crystallisation (9).

Due to the difficulties in monitoring the on-set of crystallisation in this complex multi-type-crystals system, together with its nature of reaction crystallisation, the application of traditional methodologies to study crystallisation kinetics is not straightforward. In this research, attempting to assess the mechanism and

kinetics of nucleation for Burkeite were carried out. This was done by analysing the dependence of supersaturation on Na_2SO_4 dissolution rate (Figure 5.10 left) in connection with Nyvlt's approach, as well as the recently developed KBHR approach. The kinetics study would provide a fundamental base for modelling nucleation rate and crystal size control for industrial processing of inorganic mixture systems.

One set of experiments was designed here. A similar concept to the cooling crystallisation, however here the temperature was kept constant at 75℃, the metastable zone was achieved by controlling the raw material dissolution rate near the solution saturation point. For instance, initially four Na_2CO_3 unsaturated solutions with the same concentration of 13 wt% were prepared. Na_2SO_4 sieved to four different particle size cuts that were < $75\mu m$, 75-100 μm, 100-150 μm and > 200 μm. Each of the size cuts then incrementally added in one of the prepared Na_2CO_3 solutions. The solution composition variation and saturation points were monitored on-line by the PLS models. The initial concentration of Na_2CO_3 was chosen in accordance with the completed phase diagram Figure 5.9, in order to be sure that the precipitated crystals would be only Burkeite.
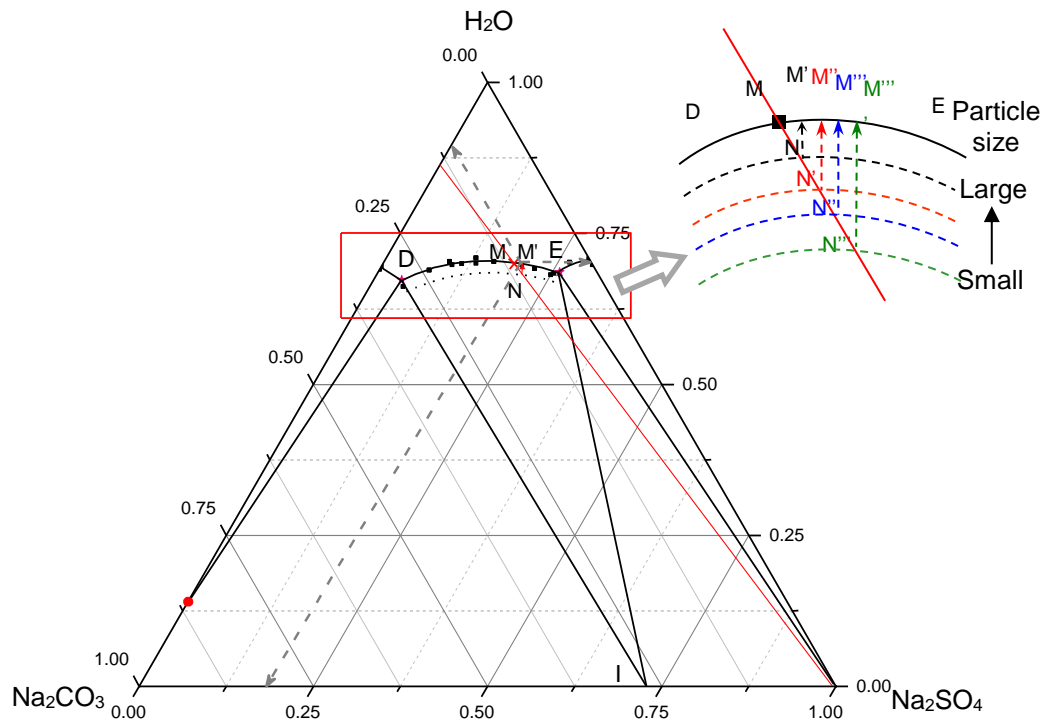
Figure 5.11: The impact of raw material particle size on Burkeite MSZW determination.

Figure 5.11 illustrates the primary experimental intention. DE was determined as the Burkeite solubility line that was achieved by adding Na_2SO_4 to Na_2CO_3 solutions. It was known that smaller particles have relatively larger surface areas than the bigger ones, which leads to obtaining a fast dissolution rate and a higher kinetic solubility (10, 11). Hence, theoretically using different sizes of Na_2SO_4 would create different degrees of supersaturation due to the dissimilar dissolution rate, which is analogous to changing the cooling rate to generate different supersaturation levels.

For instance, an exaggerated solubility area of Burkeite is represented in Figure 5.11. The coloured dotted lines illustrate the different supersaturation levels. At the beginning, with more Na_2SO_4 dissolved, the system reached its equilibrium saturation point M. Further adding a small amount of Na_2SO_4 solid (i.e. 0.3 or 0.7 wt%) would drive the system away from the equilibrium state and lead to Burkeite crystallising out, such as point N. This point was considered as the supersaturated point of the saturated solution M', the solution composition of Na_2CO_3 and Na_2SO_4 can be traced back to axes that are indicated as a dotted grey line on the phase diagram in Figure 5.11.

5.3.1 Nyvlt's approach

Table 5.3: Summary of the impact of the raw material particle size (or dissolution rate) on the metastability of Burkeite.

Na2SO4 Particle size (μm)	Na_2SO_4 dissolution rate at the solubility limit (g/min)	Crystallisation g/100g water content	Dissolution g/100g water content	$\log \sigma$	$\log r$
<75	9.64	43.11 ± 0.15	41.03 ± 0.11	0.32 ± 0.02	0.98
75-100	3.02	41.85 ± 0.12	40.67 ± 0.10	0.07 ± 0.01	0.48 ± 0.01
100-150	1.44	40.78 ± 0.06	40.02 ± 0.15	-0.12 ± 0.01	0.16 ± 0.04
150-200	0.54	40.81 ± 0.08	40.10 ± 0.09	-0.15 ± 0.01	-0.27 ± 0.02

The experimental results were summarised in Table 5.3, Figure 5.12 and Figure 5.14. Figure 5.12 is showing the composition analysis result from in-situ Raman spectroscopy, from which it was noticed that the formation of

Burkeite crystals was almost simultaneous with the addition of Na₂SO₄, the induction time could not be determined. Therefore, the classical isothermal nucleation method could not be applied. However, according to these figures (Figure 5.12), the supersaturation (i.e. N, N', N'' and N''') and their corresponding saturation points (i.e. M', M'', M''' and M'''') in Figure 5.11 can be calculated. Thus, a metastable zone was obtained (see Figure 5.13 and Figure 5.14). Furthermore, Nyvlt's theory was then applied for determining the kinetics of Burkeite nucleation.
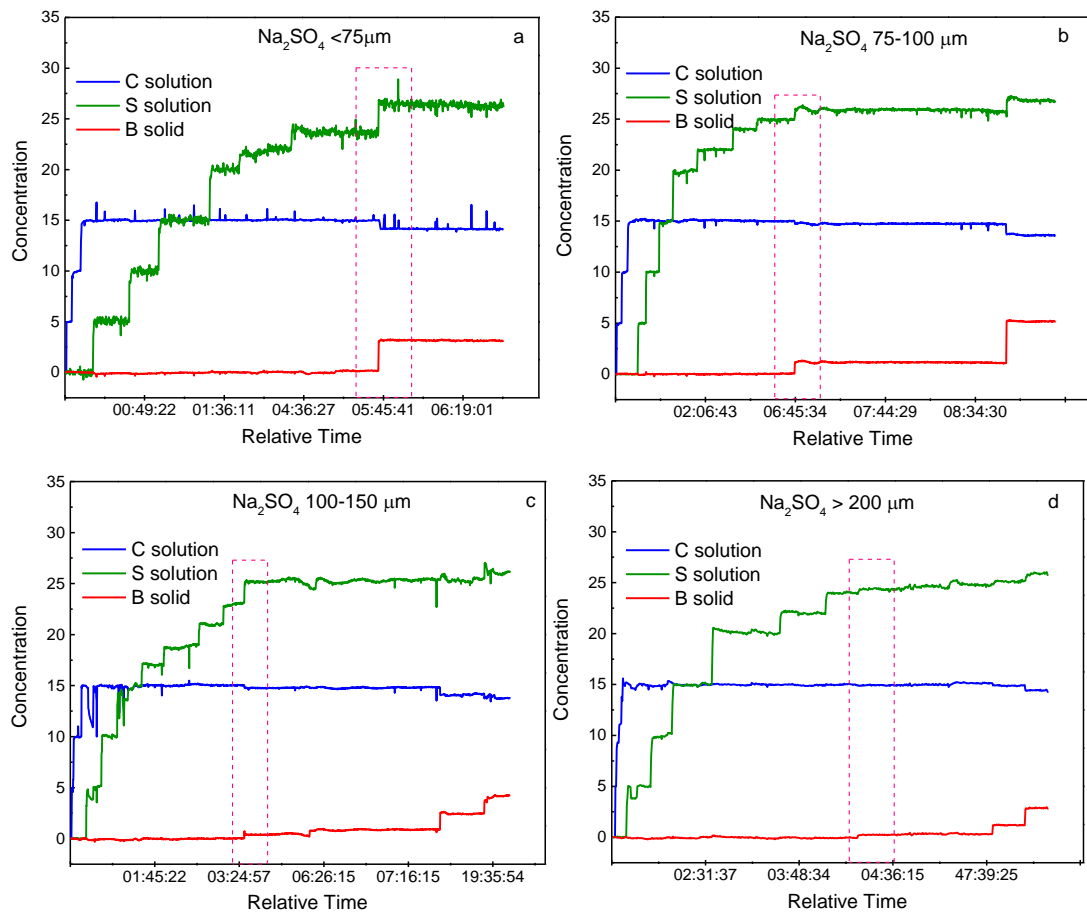
Figure 5.12: Burkeite MSZW determination by dissolving different sizes of Na₂SO₄ in the prepared Na₂CO₃ solutions.

In Nyvlt's equation, the experimental variable was the cooling rate (q) and MSZW represented as temperature difference (ΔT) between the solubility and supersolubility limits (12-14). A linear relationship will be found between the $\ln q$ and the $\ln \Delta T$. However, in current research, the experimental variable was the raw material dissolution rate r and MSZW expressed as the solution concentration difference ($\sigma = \Delta C_{max}$) between the saturation and supersaturation states. The dissolution rate was calculated from Figure 5.12

and its logarithmic values were concluded in Table 5.3. The value of ΔC_{max} was obtained from Figure 5.13, and presented in Figure 5.14 & Table 5.4.
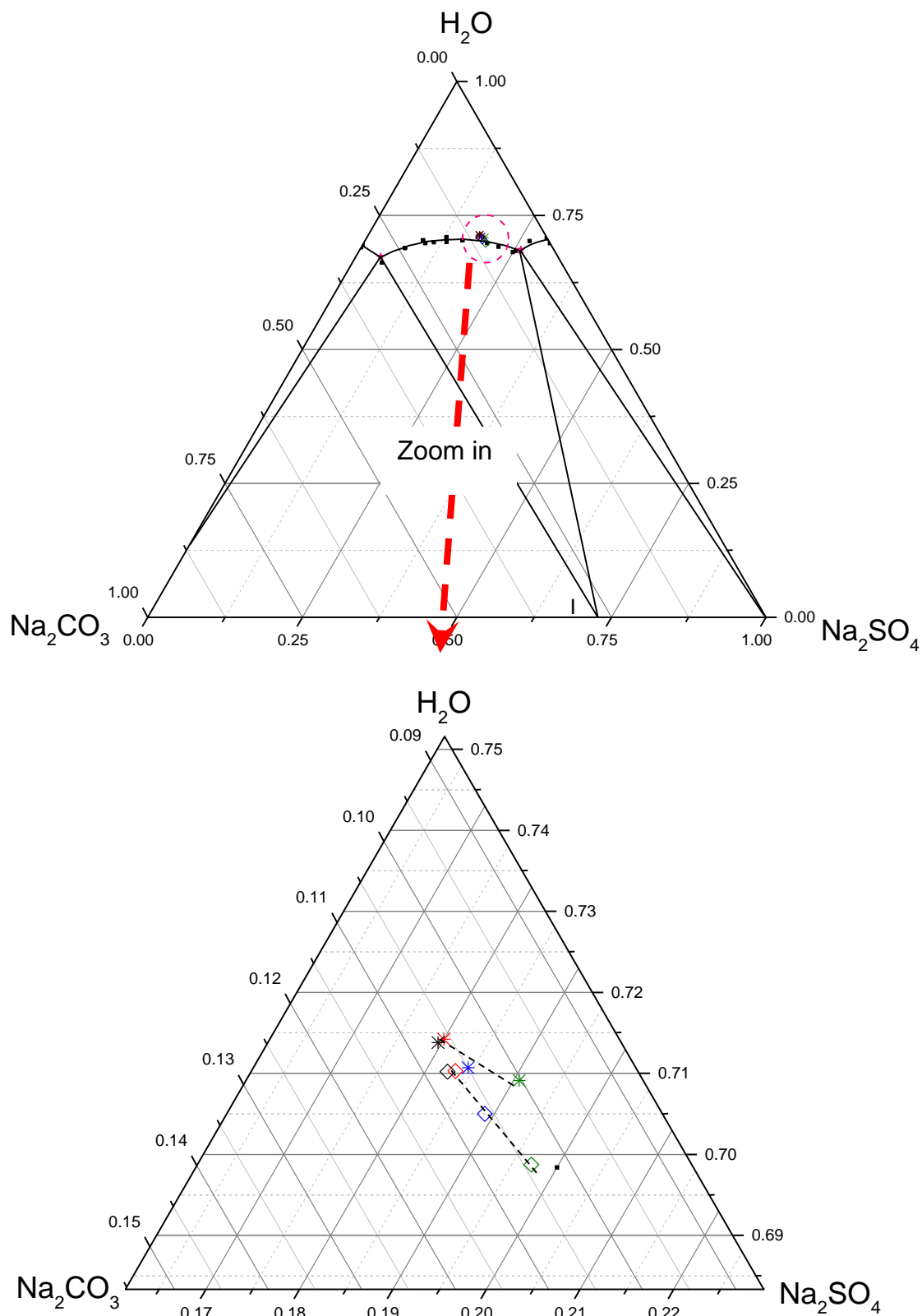
Figure 5.13: Burkeite MSZW determination by controlling the raw material Na₂SO₄ dissolution rate (dissolving different sizes was applied) into the prepared Na₂CO₃ solutions.
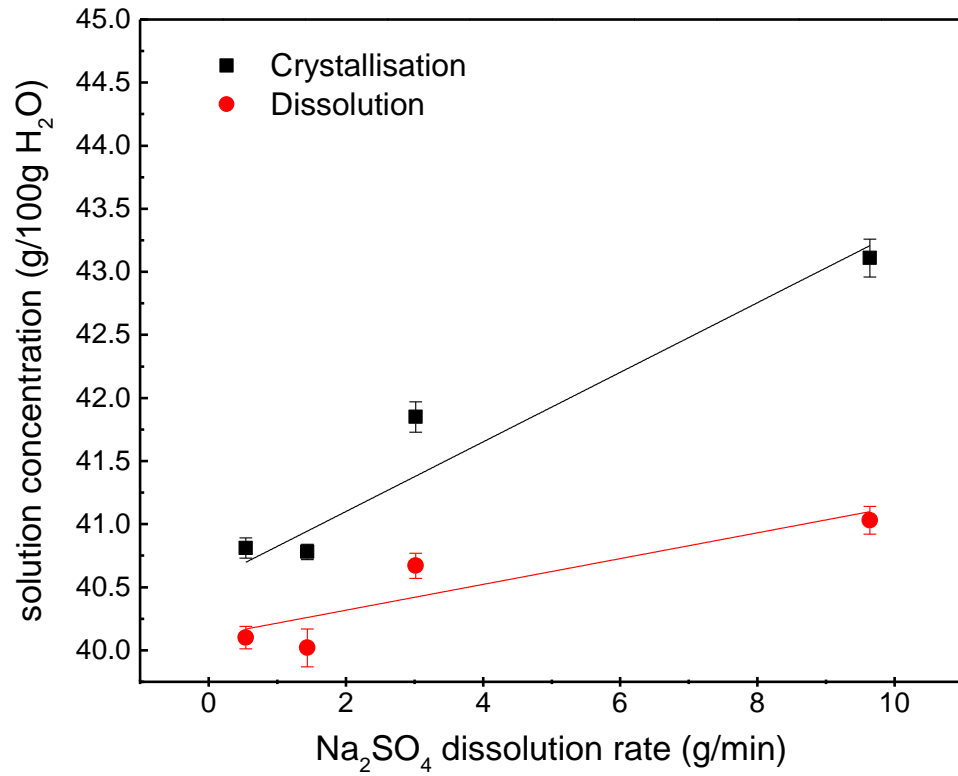
Figure 5.14: The best linear fit of dissolution and crystallisation lines of a Na_2CO_3 (13 wt%) and Na_2SO_4 solution mixture as a function of Na_2SO_4 dissolution rate (also could be seen as a function of Na_2SO_4 particle size). The fitted parameters are given in Table 5.4.

Table 5.4: Linear fitting parameters of Figure 5.14

	Intercept		Slope		Statistics
	Value	Standard Error	Value	Standard Error	R^2
Crystallisation line	40.5480	0.20084	0.2759	0.0641	0.90264
Dissolution line	40.1132	0.1655	0.1023	0.0332	0.82613

Based on Nyvlt's approach, the dependence of MSZW on the raw material dissolution rate is described in Equation 5.1 that was derived from literature (12-14).

$$\log r = \log k_j + m \log \Delta C_{max} \qquad \text{(Eq. 5.1)}$$

where r is the dissolution rate;

m is the nucleation rate order;

k_j is the nucleation rate constant;

ΔC_{max} is the MSZW in this study.

As a result of plotting $\log r$ against $\log \Delta C_{max}$ acquired a linear relationship with the slope equivalent of the order of nucleation rate, see Figure 5.15. Also, the nucleation rate constant was calculated from the intercept. For instance, for solution mixtures of Na_2CO_3 and Na_2SO_4 (with an initial 13 t% of Na_2CO_3), the relationship between the logarithm of raw material particle size (in this case is Na_2SO_4 particle size) and the metastable zone width was illustrated in Figure 5.15, from which the order of nucleation was obtained 2.7248. In addition, the nucleation constant was equal to the intercept of the linear fitting, 0.2017. A low value of nucleation order was indicated under this experimental condition, a heterogeneous nucleation event occurred. In Figure 5.14 , the black and red fitting indicated the crystallisation and dissolution line of Burkeite respectively. In general, the dissolution line of a metastable zone would present a decreasing trend, however in this case it was going up slightly, which was probably because some of the large undissolved Na_2SO_4 particles acted as a template that accelerated Burkeite formation. Therefore, the measured solubility was actually lower than the inherent solubility of the substance.
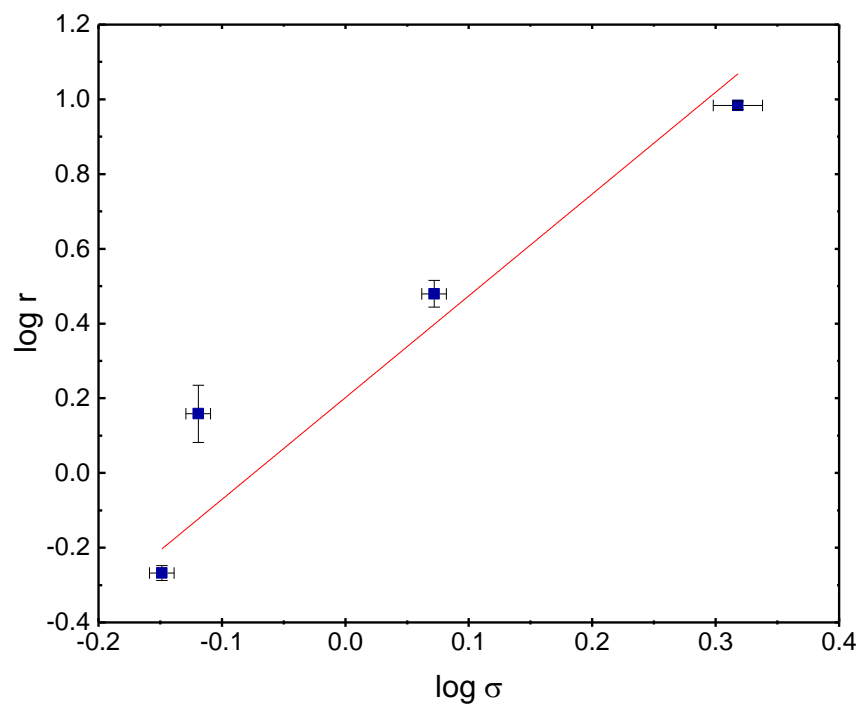
Figure 5.15: Logarithm of raw material Na$_2$SO$_4$ dissolution rate at the solution solubility limit against the logarithm of the MSZW ($\sigma = \Delta C_{max}$) for a Na$_2$CO$_3$ (13 wt%) and Na$_2$SO$_4$ solution mixture at a temperature of 75°C. The linear fitting results are listed in Table 5.5

Table 5.5: The linear fitting results of Figure 5.15

Linear fitting of log r vs. log σ	Intercept		Slope		Statistics
	Value	Standard Error	Value	Standard Error	R^2
	0.2017	0.0763	2.7248	0.4392	0.9205
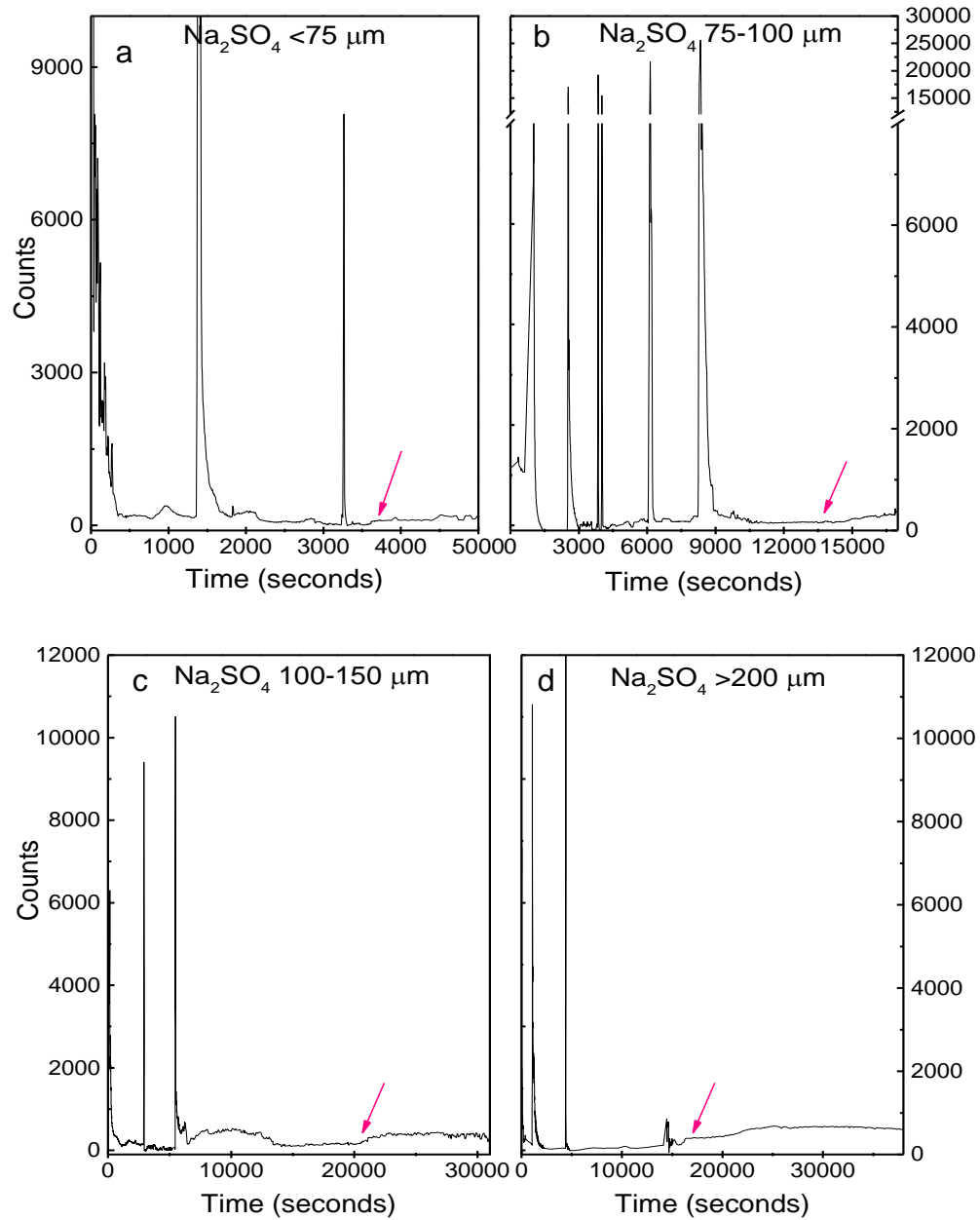
Figure 5.16: FBRM monitoring of the impact of raw material (Na₂SO₄) particle size on Burkeite formation. (Na₂SO₄ size range are indicated in the figure, the spikes denote the addition of Na₂SO₄, experiments were carried out at 75°C with 100 rpm)

FBRM was also applied for monitoring Na_2SO_4 dissolution and detecting the Burkeite precipitation process. The aim was to determine whether a mono-distribution or poly-distribution would be obtained in crystal sizes from this particular Burkeite crystallisation process. The experiments were conducted at 75°C by adding different particle size ranges of Na_2SO_4 in a 13 wt% Na_2CO_3 unsaturated solution. At the end of each experiment, the suspended particles were filtered through a pre-heated vacuum system, and dried in an oven at 80°C. Then SEM images were taken for each sample.

Equation 3.7 was applied to calculate the total number of particles observed per volume, and the outcome is presented in Figure 5.16. Each spike represents the addition of Na_2SO_4. The precipitation point of Burkeite was indicated on each interpreted data, after this point the solution becoming turbid. In the case of particle size less than $75\mu m$, some fluctuations in the count number can be seen from the profile even before the precipitation point, which was caused by air bubble effects. However, this phenomenon was hindered with the additional particles becoming larger, such as Figure 5.16(c) and (d). In Figure 5.16, after the last Na_2SO_4 addition, initially all profiles showed a decreasing tendency in the total particle numbers that reflected the dissolution process of Na_2SO_4. A period of time after that, the gradual increasing trend was illustrated in Burkeite formation.

A further interpretation of the data was implemented based on Equations 3.7 and 3.5 in Chapter 3, thereby the total volume of particles per channel was achieved. (Each channel stands for a certain range of chord length distribution; there were 90 channels across 1-1000 μm). The data was summed into four ranges, which are 1-30 μm, 30-50 μm, 50-100 μm and 100-200 μm, and presented in Figure 5.17.

Figure 5.17(a), approximately 500 seconds after the last addition of Na_2SO_4, the volume percentage of 1-30 μm particles started declining, in the meantime particles in the range 100-200 μm increased but insignificantly. Particles around 30-50 μm appeared to show a declining tendency for the initial 1000 seconds, then the number began to grow extremely slowly. The crystallisation of Burkeite must occur within the first 500 seconds, aggregation and growth occurred afterwards. This was also proved by the later SEM images, see Figure 5.18 and Figure 5.19.

Figure 5.17(b) has a clearer trend, volume percentage of Na_2SO_4 particles in all ranges dissolved in water at the beginning. The vol % of 1-30 μm particles was the first starting to increase at (900-1200 seconds), which was followed by the 100-200 μm particles around 10500 seconds. The former increase might illustrate Burkeite crystallisation occurring, and the later one should attribute to the aggregation.

Figure 5.17(c) demonstrates that after a long time at steady state, small crystals started precipitating (possibly Burkeite) which acted as a driving force leading larger particles (Na_2SO_4) to dissolve.

Figure 5.17(d) describes a short period after the last addition, the percentage of particles in all ranges (below 100 μm) began to increase but not simultaneously. The increase in the range 50-100 μm may be attributed to both aggregation and growth. All these existing crystals might act as the template that induced the smaller ones to form (i.e. particles in 10-30 μm).

There were some inconsistent outcomes from the FBRM measurements, probably because of the formation of very irregular small Burkeite crystals, which had extensively aggregating behaviour, and a high porosity structure that would give inaccuracy to the count length measurement.
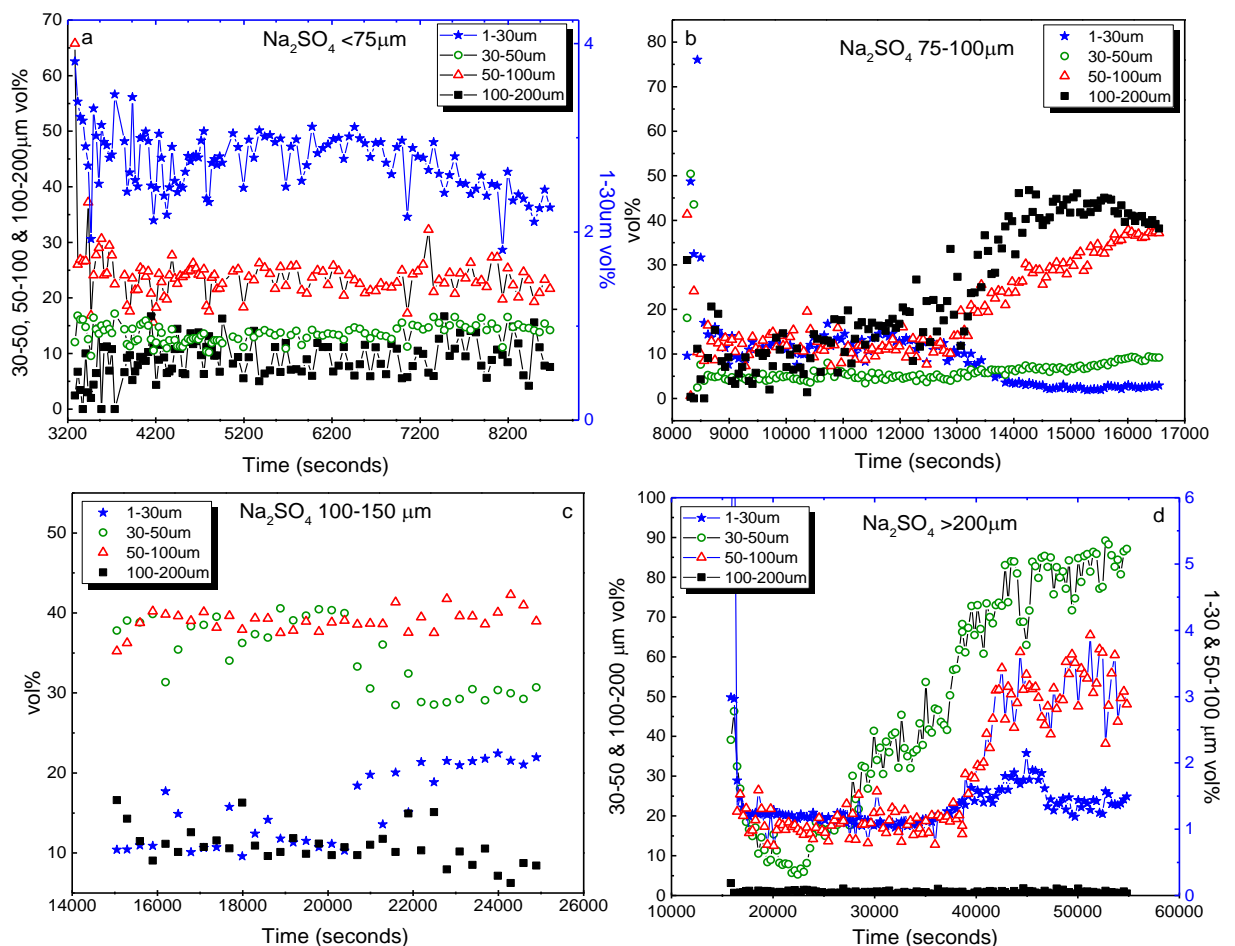
Figure 5.17: The interpretation of FBRM measurements. Particles were classified in four size ranges 1-30μm, 30-50 μm,50-100 μm and 100-200 μm (Figures a and d have a double y-axis)

LEMAS 2.0kV 3.1mm x3.50k SE(U)   10.0μm

LEMAS 2.0kV 3.1mm x35.1k SE(U)   1.00μm
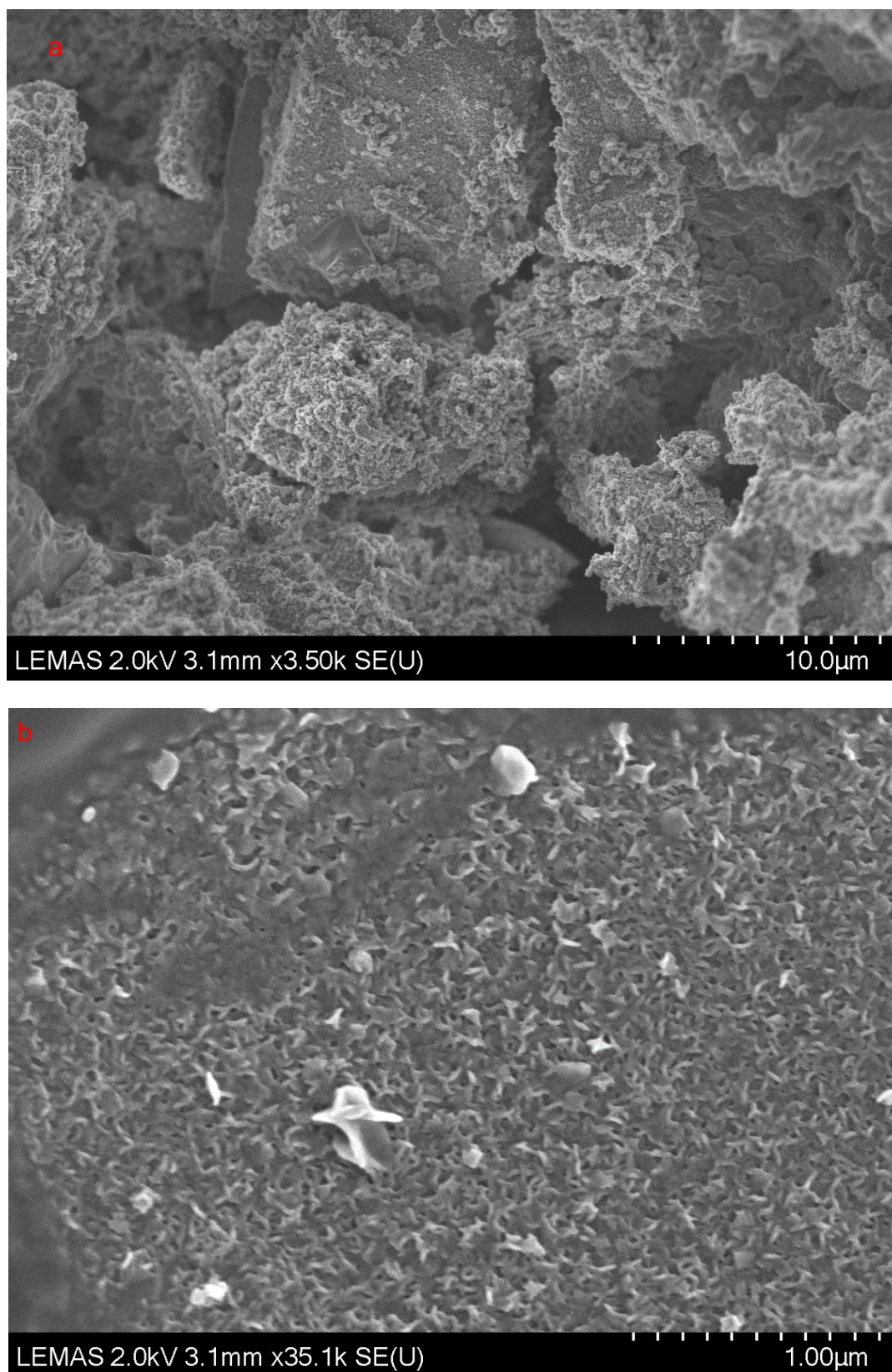
Figure 5.18: Burkeite crystals obtained from the Na_2SO_4 <75 μm FBRM experiment. (At 75ºC, 100 rpm, gradually added Na_2SO_4 (<75 μm) in a Na_2CO_3 (13wt%) solution until the count numbers constantly increased, and the solution become turbid. The suspension was then filtered through a pre-heated vacuum system, and dried in a 80ºC oven.)

LEMAS 2.0kV 2.7mm x5.00k SE(U)   10.0μm

LEMAS 2.0kV 2.7mm x8.00k SE(U)   5.00μm
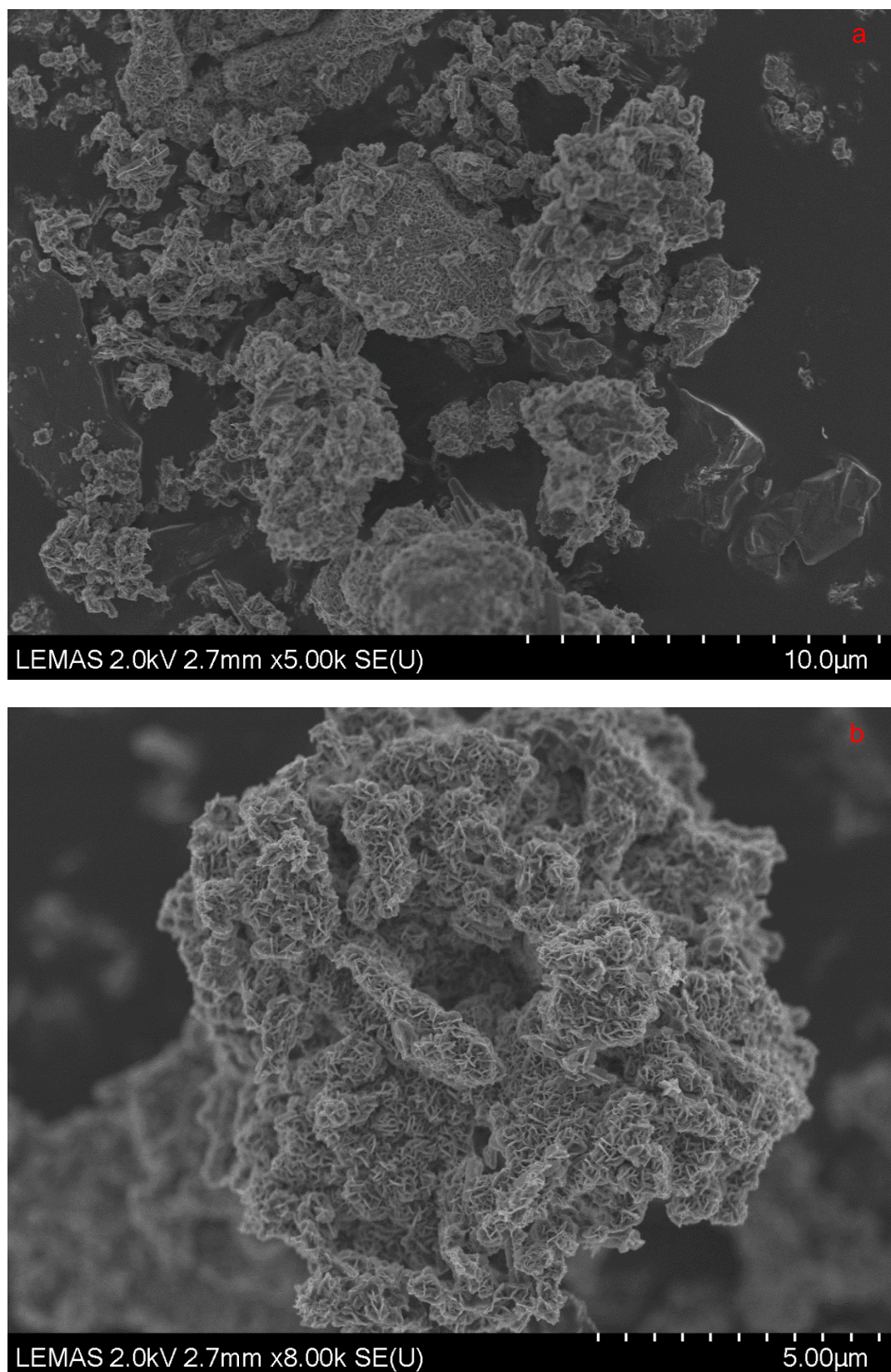
Figure 5.19: Burkeite crystals obtained from Na₂SO₄ >200 μm FBRM experiment. (At 75°C, 100 rpm, gradually added Na₂SO₄ (>200 μm) in a Na₂CO₃ (13wt%) solution until the count numbers constantly increased, and the solution become turbid. The suspension was then filtered through a pre-heated vacuum system, and dried in an 80°C oven.)

Particles achieved from FBRM Burkeite precipitation experiments were observed using SEM (Figure 5.18 and Figure 5.19). Samples from all experiments contained a high degree of aggregation and porosity. Two examples were given in Figure 5.18 and Figure 5.19, X shape dendrite Burkeite crystals were obtained. Figure 5.18 demonstrates the case of Na_2SO_4 <75 μm, small particles had a faster dissolution rate, so a higher degree of supersaturation should be obtained (Figure 5.14), where nucleation ought to dominate crystal growth and result in small crystals. For instance, as shown in Figure 5.18 most of the crystals were around 500 nm, when they aggregated and presented as larger particles. This backed up the assumption in Figure 5.17 that the increasing trend in the vol% of particles around 100-200 μm was caused by aggregation. On the contrary, Figure 5.19 exhibits the crystals obtained from the Na_2SO_4 >200 μm experiment, as indicated in Figure 5.14, a lower supersaturation level was achieved, so crystal growth was faster than nucleation and controlled the whole process, a larger particle size distribution ought to be obtained (see Figure 5.19, especially Figure (a)).

The SEM images demonstrated that the FBRM method may not be the best way of studying crystal size distribution (i.e. mono- or poly-distribution) due to the irregular Burkeite crystal shapes and high tendency of aggregation. However, through this study high porosity Burkeite was achieved, which was the desired morphology for the dry laundry industry, this could because of the high level of water content.

5.3.2 KBHR approach

The novel nucleation kinetics approach (KBHR) was reviewed in Chapter 2. Through Nyvlt's equation the nucleation order and constant would be attained. However, by applying the new kinetic approach (KBRH method) it was possible to derive more detailed nucleation information, such as nucleation mechanisms (either progressive nucleation or instantaneous nucleation), interfacial tension, critical radius of the nucleus and so on (12, 16).

Following the initial idea presented in Figure 5.10, instead of using different cooling rates to achieve the MSZW, here, as described in the Nyvlt's approach section (5.3.1) the metastability was obtained by applying different sizes of raw materials via a controlled dissolution rate to meet the solubility and super-

solubility points. A scheme was demonstrated in Figure 5.20 to help understand the changing concepts. The dissolution rate (r) of the raw material (Na₂SO₄) at the saturation point and the solution concentration difference (ΔC_{max}) between the saturation and supersaturation states were substituted for system cooling rates and temperature difference between the dissolution and crystallisation points from the KBHR method.
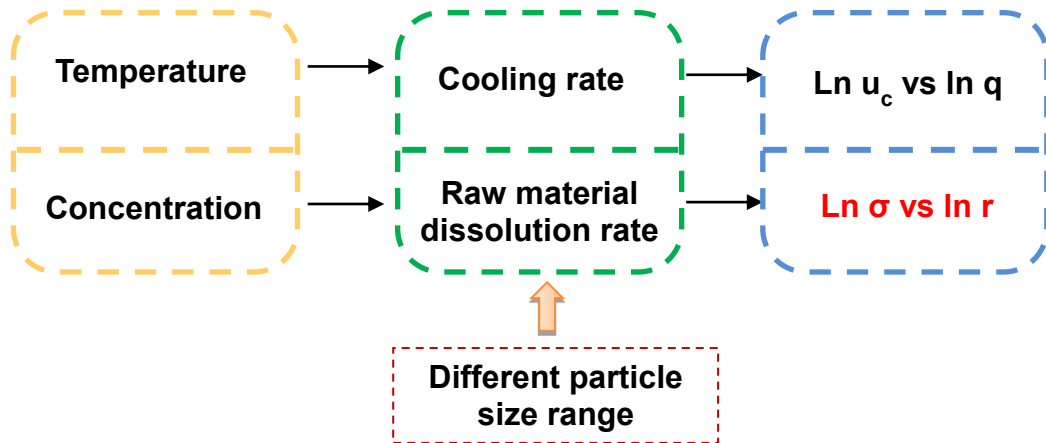
Figure 5.20: Adapting the parameters to the ones applied in the KBHR method (solution concentration difference replaced the temperature change; raw material dissolution rate replaced the cooling rate; the final plot changed to $ln\ \sigma$ vs. $ln\ r$, where $\sigma = \Delta C_{max}$ is the solution concentration difference between the saturation and supersaturation states; r is the dissolution rate of Na₂SO₄ at the saturation point).

Figure 5.21: Modification of the KBHR method for the Burkeite nucleation study of the current process.

Based on the KBHR approach (13), the calculation procedure was modified as in Figure 5.21. The resulting MSZW was shown in Figure 5.14. The relationship of $ln\,\sigma$ vs. $ln\,r$ was presented in Figure 5.22 and Table 5.6.

A linear relationship was attained that was in agreement with that obtained from Nyvlt's approach. If we follow "the Rule of Three" that was introduced in the KBHR method (15), then the Burkeite nucleation would be determined as an instantaneous nucleation by following the method studied by Kashchiev, D and Corzo, D.M.C (12, 16), the concentration of instantaneously nucleated crystallites could be calculated.

However, the question as to whether the rule of three was meaningful for this study arises. The value "3" was concluded from comparing all the derivation equations for both progressive and instantaneous nucleation events. However, the derivations of all these equations were all based on the Van't Hoff's equation, which has temperature factors involved. Therefore, the determination of the "rule of slope" for this study needs further systematic derivation and calculation.

Nevertheless, in Figure 5.22, the linear relationship obtained between $ln\,\sigma$ and $ln\,r$ implies the feasibility of solving kinetic issues through the controlling of raw material dissolution to generate different supersaturation levels.
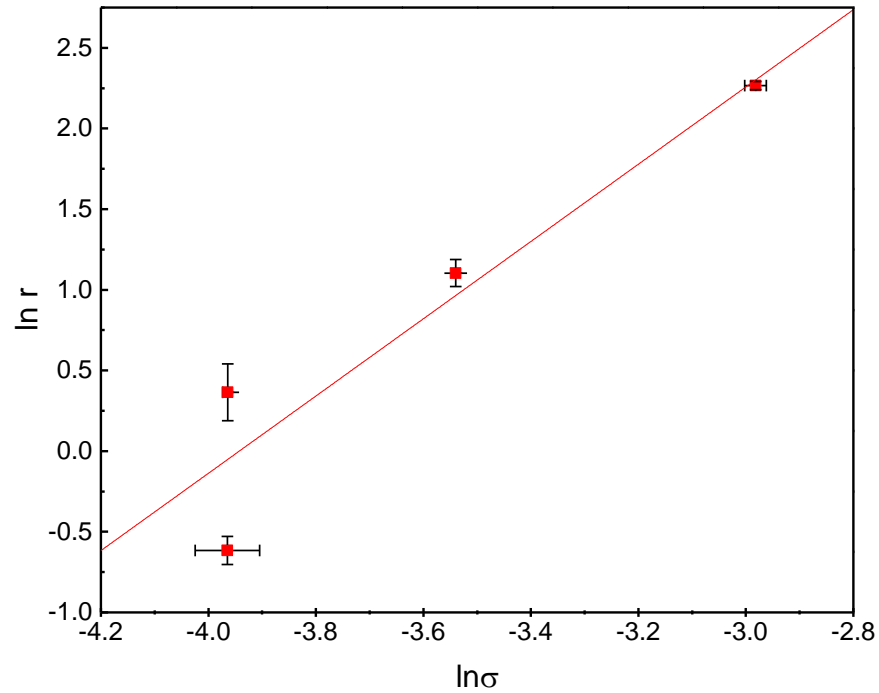
Figure 5.22: Natural logarithm of raw material Na₂SO₄ dissolution rate around the solution solubility limit against the natural logarithm of the MSZW ($\sigma = \Delta C_{max}$) for a Na₂CO₃ (13wt%) and Na₂SO₄ solution mixture at temperature 75°C. The linear fitting results are listed in Table 5.6

Table 5.6: The linear fitting results of Figure 5.22

Linear fitting of $\ln r$ vs. $\ln \sigma$	Intercept		Slope		Statistics
	Value	Standard Error	Value	Standard Error	R^2
	9.4440	1.1770	2.39538	0.3585	0.9410

5.4 Conclusion

The slurry model that was created from the previous chapter was applied to fast determining a ternary phase diagram of Na₂CO₃-H₂O-Na₂SO₄ at a fixed temperature (75°C) in this part of the study. In comparison with the conventional approach on the phase diagram determination, the in-situ Raman technique, with the aid of calibration models, would speed up and simplify the process.

Subsequent studies were able to be more focused on the region of interest of the completed phase diagram, such as in this Chapter where the Burkeite region was chosen. In addition, the phase diagram can also contribute to

kinetic studies or the final slurry composition prediction for both research and process purposes.

The FBRM technique was used in attempting to achieve the particle size distribution of newly formed double salt crystals. However, due to the Burkeite formation being highly dependent on the supersaturation of the sodium solution mixture system and its irregular growth shape and behaviour, this particle size analytical technique was not sufficient to fulfil the research aim. Using an in-process video microscope (PVM) in parallel with FBRM and Raman spectroscopy might help for a further investigation into Burkeite crystal growth or even aggregation.

The SEM images displayed that the Burkeite crystals achieved were in small thin flakes like an "X" shape, and its aggregates had a high degree of porosity. The hypothesis proposed here is that the high-water content of the system induced the development of these desirable crystals. The verification experiment of this hypothesis is going to be discussed in the following chapter.

The application of the modified KBHR approach demonstrated the possibility and potential for using this method to solve nucleation kinetics, of which MSZW were obtained by controlling the dissolution rate of raw materials. However, more detailed mathematical deviations need to be developed in order to use this approach.

Reference List

1. Harvie, C.E., Møller, N. and Weare, J.H. The prediction of mineral solubilities in natural waters: The Na-K-Mg-Ca-H-Cl-SO4-OH-HCO3-CO3-CO2-H2O system to high ionic strengths at 25 C. *Geochimica et Cosmochimica Acta.* 1984, **48**(4), pp.723-751.

2. Green, S.J. and Frattali, F.J. The System Sodium Carbonate-Sodium Sulfate-Sodium Hydroxide-Water at 100° 1. *Journal of the American Chemical Society.* 1946, **68**(9), pp.1789-1794.

3. Caspari, W.A. CCCXXIV.—The system sodium carbonate–sodium sulphate–water. *Journal of the Chemical Society, Transactions.* 1924, **125**, pp.2381-2387.

4. Teeple, J.E. The industrial development of Searles Lake brines with equilibrium data. 1929.

5. Kobe, K.A. and Sheehy, T.M. Thermochemistry of sodium carbonate and its solutions. *Industrial & Engineering Chemistry.* 1948, **40**(1), pp.99-102.

6. Mahmoudkhani, M. and Keith, D.W. Low-energy sodium hydroxide recovery for CO 2 capture from atmospheric air—Thermodynamic analysis. *International Journal of Greenhouse Gas Control.* 2009, **3**(4), pp.376-384.

7. Edward W. Washburn, e.a. *International Critical Tables of Numberical Data, Physics, Chemistry and Technology.* McGraw-Hill Book Company, New York, 1926.

8. Washburn, E.W. and West, C.J. *International critical tables of numerical data, physics, chemistry and technology.* National Academies, 1928.

9. Shi, B., Frederick, W.J. and Rousseau, R.W. Effects of calcium and other ionic impurities on the primary nucleation of burkeite. *Industrial & Engineering Chemistry Research.* 2003, **42**(12), pp.2861-2869.

10. Franklin, N.M., Rogers, N.J., Apte, S.C., Batley, G.E., Gadd, G.E. and Casey, P.S. Comparative toxicity of nanoparticulate ZnO, bulk ZnO, and ZnCl2 to a freshwater microalga (Pseudokirchneriella subcapitata): the importance of particle solubility. *Environmental Science & Technology.* 2007, **41**(24), pp.8484-8490.

11. Sun, J., Wang, F., Sui, Y., She, Z., Zhai, W., Wang, C. and Deng, Y. Effect of particle size on solubility, dissolution rate, and oral bioavailability: evaluation

using coenzyme Q10 as naked nanocrystals. *International journal of nanomedicine.* 2012, **7**, p.5733.

12.   Camacho Corzo, D.M. *Crystallisation in Diesel and Biodiesel Fuel in Relation to their Solution Composition.* thesis, University of Leeds, 2015.

13.   Kashchiev, D., Borissova, A., Hammond, R.B. and Roberts, K.J. Dependence of the critical undercooling for crystallization on the cooling rate. *The Journal of Physical Chemistry B.* 2010, **114**(16), pp.5441-5446.

Chapter 6 The Impact of Solution Conditions on the Phase Transition of Inorganic Materials

6.1 Introduction

The order of addition of raw materials has a significant influence on Burkeite crystallisation. Meenan (1) found adding Na_2SO_4 first led to the most production of Burkeite. He believed that in this case, there would be enough SO_4^{2-} ready to use to form the sulphate rich double salt (Burkeite). However, in this research an opposite phenomenon was observed. Meenan's research (1) also mentioned that the degree of porosity of Burkeite agglomerates increased as a function of crystals residence time in the mother liquid. However, in the current research the assumption of water level having an impact on the porosity of Burkeite was considered. Therefore, an investigation on the impact of solution condition on Burkeite crystallisation was implemented. Factors of water contents, solution pH and the addition of other chemicals (e.g. sodium silicate) were considered.

Burkeite crystals were generally smaller with a narrow particle size distribution compared with Na_2SO_4 and Na_2CO_3. Its normal behaviour was as an agglomeration nucleator binding particles together. (1) Generally, crystals with charge rich surfaces cannot easily agglomerate for the reason of repulsion effect. However, Burkeite is known as an intricate irregularity crystal structure (2), which probably contributed to the formation of a homogeneous crystal surface rather than charged rich layers. Without the strong repulsion force, Burkeite crystals can agglomerate more freely than either of the mother salts (i.e. Na_2CO_3 and Na_2SO_4).

As displayed on the accomplished phase diagram, Burkeite crystallisation can occur across a wide region (Figure 5.9), which reflected the ratio variation between raw materials was not the only factor in Burkeite formation. The composition of water could also play a role in the double salt formation. Currently, the water content for manufacturing the dry detergent powders varies from 35 to 50 in weight percentage. (3, 4) Therefore, a study on whether

water content had an impact on Burkeite crystallisation was carried out in this chapter.

In addition, in Chapter 4, the summarised conclusion from the order of addition experiments was that at the mass ratio of Na_2CO_3 to Na_2SO_4 =1:3 introduced Na_2SO_4 after Na_2CO_3 into solution would lead to more Burkeite precipitating out. The proposed hypothesis was that the addition of carbonate salt changed the properties of aqueous solutions, which accelerated the crystallisation process of Burkeite. Hence, a pH trial was designed for proving the assumption. The outcome would be compared with the order of addition (OOA) experiments that were carried out in normal water solutions on both the composition and kinetics of Burkeite formation.

Furthermore, if the solution pH influenced Burkeite crystallisation, then possibly adding other alkaline materials could also achieve the same effect. In the dry detergent industry a variety of chemicals are required for a preliminary mixing before the addition of inorganic phases. Therefore, the impact of these chemicals on inorganic salts should be considered. Here, sodium silicate was chosen to be studied because it is one the key ingredients to provide structural support in the spray-dried detergent granules. Additionally, its high pH attributes probably can be used as an alkaline agent to improve the Burkeite precipitation.

However, an opposite phenomenon (in section 4.4) was observed through the study. In seeking the root causes, the interaction between inorganic phases and sodium silicates were also investigated. Furthermore, factors that would affect properties and speciation of sodium silicate were considered.

6.1.1 Solution Conditions Impact on the Percentage of Burkeite Formation

Currently, two levels of water content are applied in industrial processes and were reported as 34% and 50% to achieve the high production of Burkeite (4), which has been indicated on the completed phase diagram Figure 5.9. So, an investigation on the impact of water content combined with the order of

addition of raw inorganic materials on Burkeite crystallisation (i.e. production) have been conducted, and the results are discussed below.

The order of addition experiment (mass ratio 1:3) was repeated in a larger reactor (2L) with an anchor impeller (Figure 3.16). Instead of using the raw material (i.e. adding Na_2CO_3 to the solution first) to change the pH, here caustic soda was applied before Na_2SO_4 was added, then Na_2CO_3 was introduced at the end. Two water levels were chosen, 48 wt% (high water level) and 25 wt% (low water level).
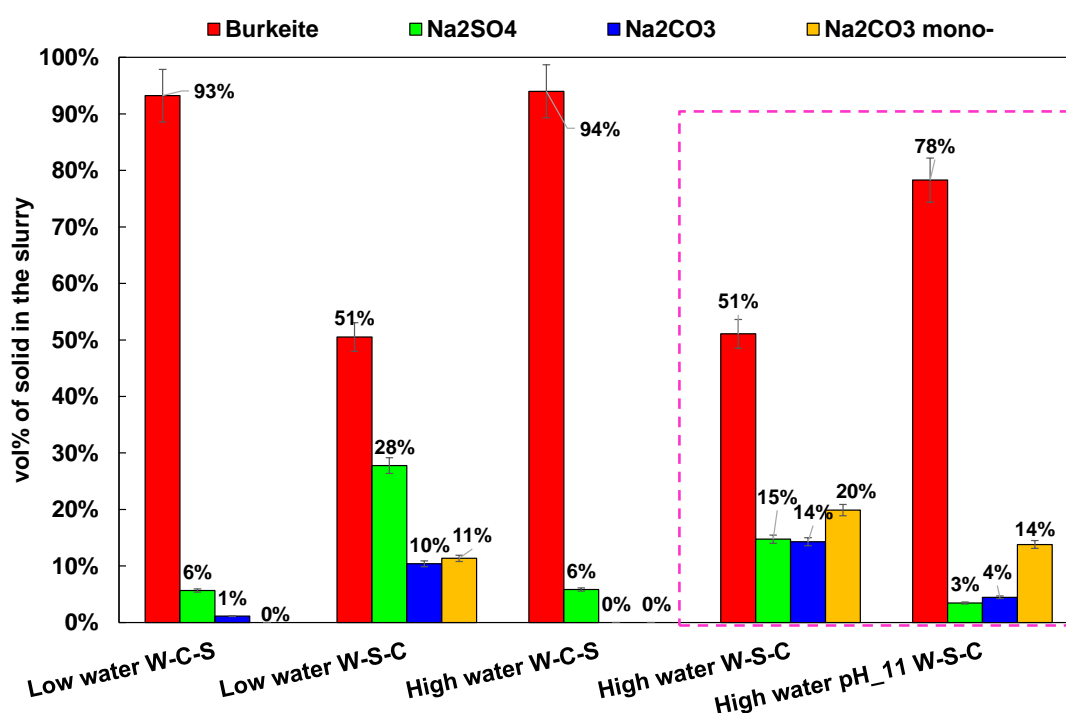
Figure 6.1: The impact of the order of addition of raw inorganic materials and the water content on the precipitation of Burkeite. (Note: the data was achieved by applying the in-situ Raman slurry models. Low water: 25% of water content; High water: 48% of water; W-S-C: the order of addition as water-Na_2SO_4-Na_2CO_3, W-C-S: water-Na_2CO_3-Na_2SO_4).

The data in Figure 6.1 shows that the level of water content used in this work does not have a significant impact on the percentage of Burkeite precipitation for both orders of addition. However, changing the order of addition caused a massive difference on Burkeite formation. When Na_2CO_3 was added before Na_2SO_4, the volume fraction of precipitated Burkeite in the solid phase was higher than 90%, and for the opposite additional sequence, the yield of

Burkeite only reached around 50%, see Figure 6.1. Apart from the low percentage of precipitation, for the latter case (W-S-C), there was around 50% of other salts involved in the final slurry (i.e. Na_2SO_4, Na_2CO_3 and $Na_2CO_3 \cdot H_2O$), which was almost nine times higher than was presented in the former case (W-C-S). This phenomenon perfectly aligned with the result in Chapter 4 that was achieved from small scale experiments. Therefore, with no influence of reactor size, the preferred order of addition of inorganics to obtain a Burkeite rich slurry was for Na_2CO_3 to be added before Na_2SO_4. This is because the pre-dissolved Na_2CO_3 created a high pH solution that might be a more desirable environment for Burkeite crystallisation to occur. Moreover, Burkeite has been mostly found and reported in the alkaline solution conditions (5, 6), which was consistent with the hypothesis here.

To further prove the concept, caustic soda was firstly introduced into the deionized water as an alkaline agent to adjust the pH to approximately 11 and then followed by the Na_2SO_4 and Na_2CO_3. As shown in Figure 6.1, the percentage of Burkeite increased almost 50% compared with non-pH modified deionised water. The amount of solid residue of Na_2CO_3 and Na_2SO_4 decreased significantly in the slurry. However, there was still a considerably high level of $Na_2CO_3 \cdot H_2O$ remaining, which was probably due to Na_2CO_3 being added into the system with a large excessive amount of Na_2SO_4 that was already presented, which limited Na_2CO_3 dissolution and led to its monohydrate forming. According to the Na_2CO_3-H_2O phase diagram (Figure 2.6), under this experimental condition undissolved Na_2CO_3 would convert and stay in its monohydrate form. The $Na_2CO_3 \cdot H_2O$ has slightly lower solubility and is more stable as compared with other inorganics in this system, so once this crystal formed it would be more preferable to stay in solid in this slurry system (7).

6.1.2 The Impact of Solution Conditions on the Kinetics of Burkeite Formation

Figure 6.2 illustrates real time quantitative analysis profiles of the in-situ measurement of monitoring the influence of solution pH on the composition of sodium salt slurry systems.
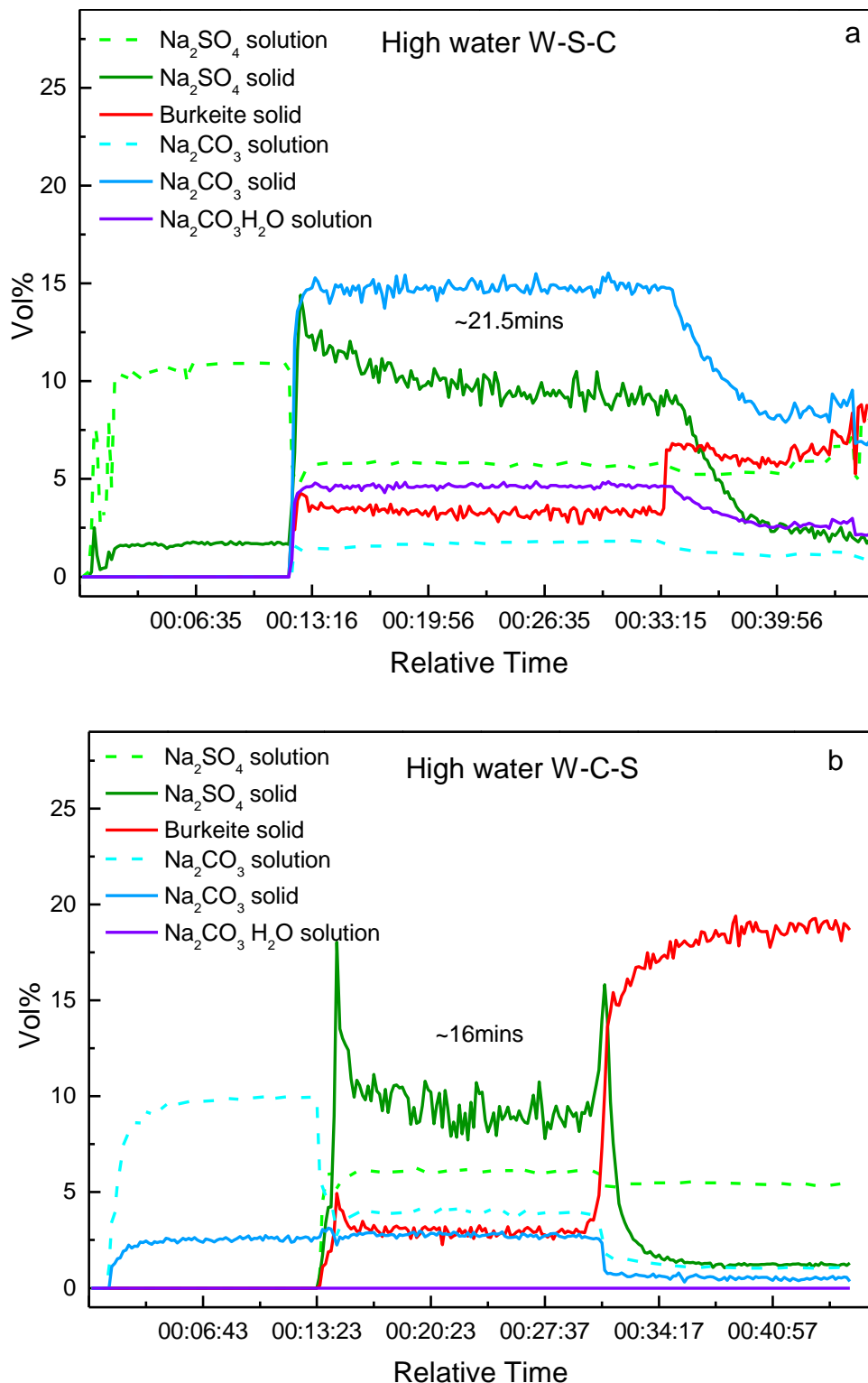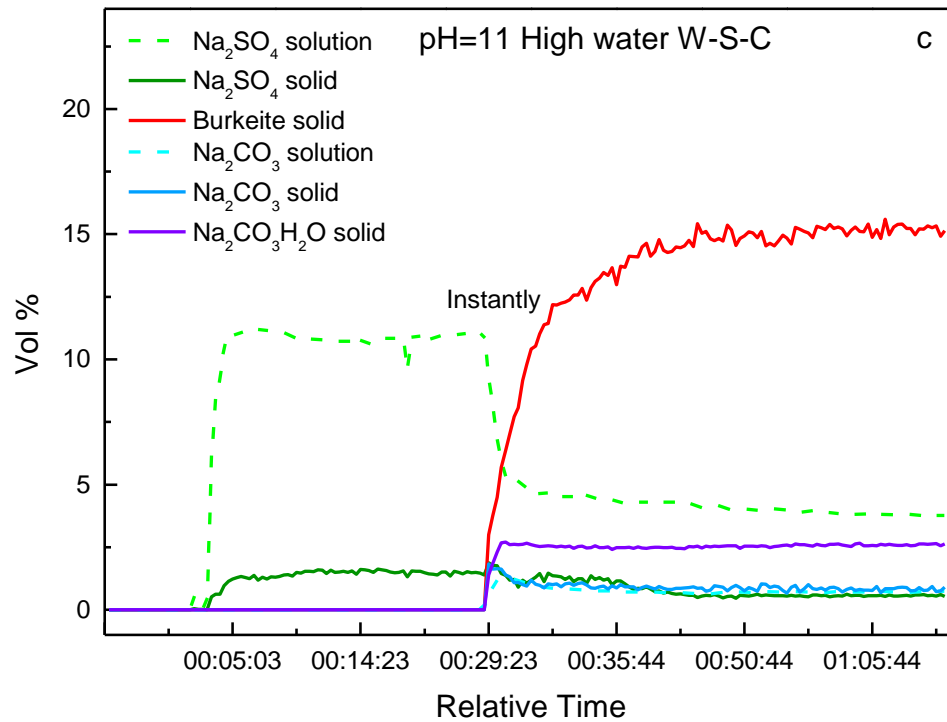
Figure 6.2: Impact of the order of addition and pH of deionized water on Burkeite formation.

Two steps of crystallisation occurred in Figure 6.2 a and b, which was a different phenomenon in contrast with the profiles obtained from OOA experiments in section 4.4.1. In consideration of reactor set-ups, different impeller utilisation might cause this discrepancy. The pitch blade turbine impeller was used for the half litre reactor; this kind of impeller was excellent for dispersion operation. It provided great radial flow pattern and was efficient for mixing liquid suspensions with less than 15-20 Ns/m^2 viscosity (8). In contrast, the anchor impeller provided sufficient mixing under the laminar flow pattern which prevented sedimentation occurring in the high viscosity slurry system. So, at the beginning of experiments the mixing effect of the anchor impeller was not as adequate as the pitch blade turbine impeller, thus profiles of the dissolution and crystallisation were different, slower for the anchor mixer, a plateau obtained in Figure 6.2 a and b.

In Figure 6.2 (a), the solution pH after the addition of Na_2SO_4 was 7.12, some Burkeite and $Na_2CO_3 \cdot H_2O$ crystals precipitated simultaneously and rapidly after Na_2CO_3 was added. Around 21.5 minutes later more Burkeite crystallised out, at that instant, the volume fraction of both Na_2CO_3 and Na_2SO_4 was decreasing dramatically. Moreover, in between these two crystallisation

events, the vol% of the Na_2SO_4 solid was decreasing slowly, this may be as a result of the solid arrangement or packing density changing in the slurry, in order to be prepared for the growth of the already formed Burkeite or the precipitation of the new Burkeite.

Changing the additional sequence of inorganics W-C-S like in Figure 6.2 (b), the pH of the solution was 10.84 after adding Na_2CO_3 in. The yield of the final Burkeite increased more than 50% compared with that achieved from the previous case. Moreover, there was no evidence of the existence of $Na_2CO_3 \cdot H_2O$ solids at the end of the experiment, so the purity of the slurry has been improved. Furthermore, the time interval required for the second crystallisation to occur was shortened to 16 minutes.

Last but not least, using an alkaline solution to accelerate the kinetics of Burkeite formation. As shown in Figure 6.2(c), when the pH of water increased to 11 the water level was kept the same and followed the sequence of addition as W-S-C, the crystallisation of Burkeite only happened once which started instantly after the addition of the second salt (Na_2CO_3).

This set of experiments produced evidence of the hypothesis that high pH solution condition could accelerate and enhance the purity of Burkeite crystallisation.

6.1.3 The impact of solution conditions on the crystal properties of Burkeite

The high pH environment not only accelerated the kinetics of Burkeite crystallisation but also had an influence on its crystal morphology and the packing density of aggregates.

SEM images were taken for Burkeite that were achieved from the different order of addition experiments are illustrated in Figure 6.3. Crystals achieved from High water W-S-C formula contained relatively large primary particles; the average value was around 50 µm, besides the purity of Burkeite crystals was quite low. Alternating the adding sequence to W-C-S, the particle size of final Burkeite reduced to approximately 20 µm. If vary the solution pH first then

add salts to react afterwards, the achieved Burkeite particle size decreased to 10μm or even smaller.

High water W-S-C   L x200 500 um

High water W-S-C   L x1.0k 100 um

High water W-C-S   L x200 500 um

High water High pH   L x200 500 um
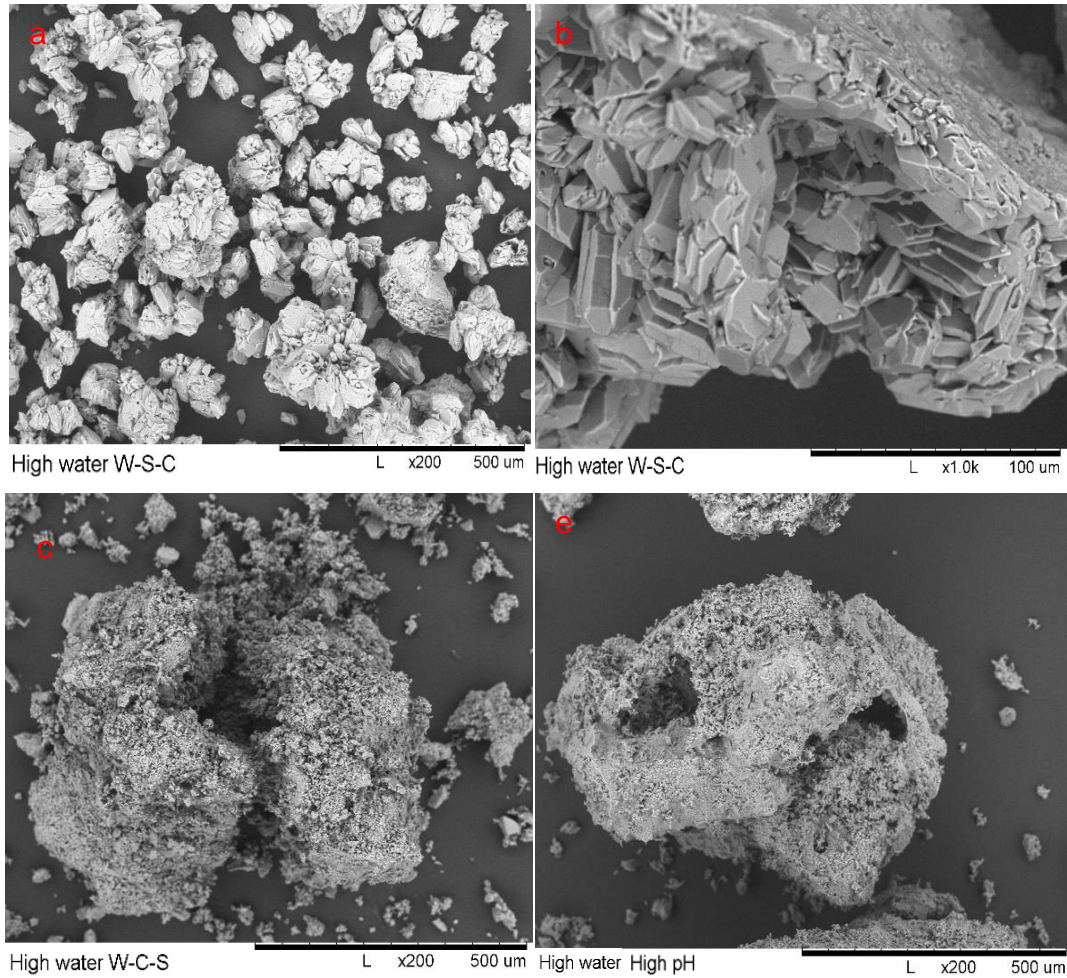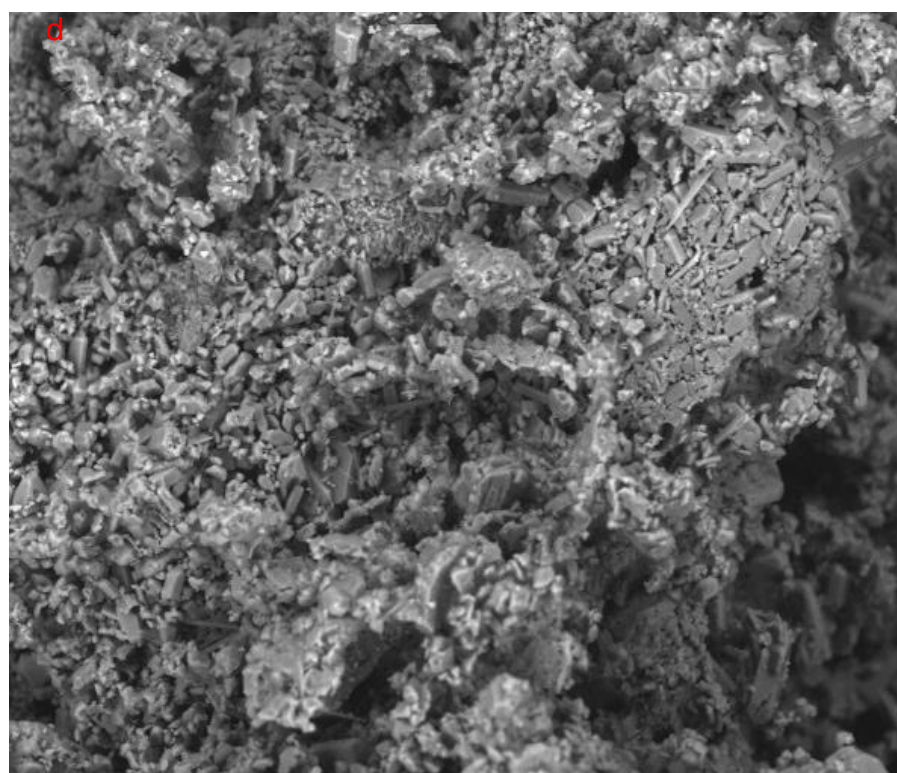
High water W-C-S   L   x1.0k   100 um
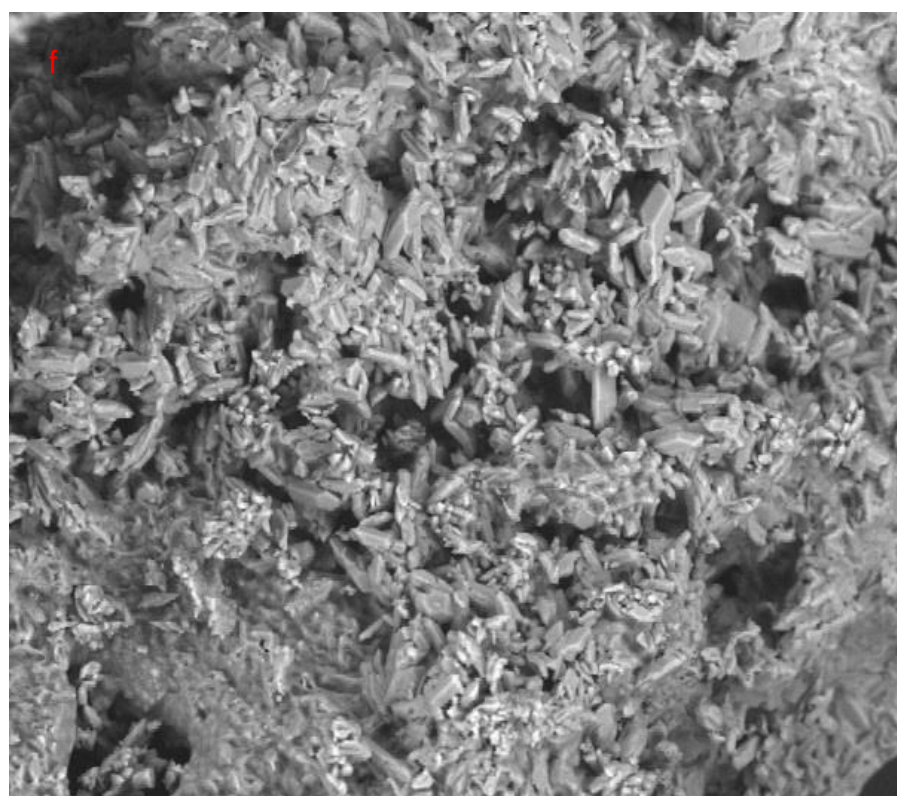
High water High pH   L   x1.0k   100 um

**Figure 6.3: SEM images of burkeite formed under different conditions
(a and b: W-S-C; c and d: W-C-S; e and f: High pH W-S-C)**

Moreover, Burkeite achieved through the tuning pH method had less aggregation degree and higher porosity. In general, small particles contain relatively large surface area that will benefit from the dissolution process. To further verify small crystals, larger surface areas were generated, two kinds of Burkeite were taken for the BET test. The detailed BET, external surface area, average pore size and total pore volume for both samples were concluded in Table 6.1. In this table, Burkeite crystallised through W-C-S and W-alkaline-S-C was presented as normal Burkeite and High pH Burkeite, respectively. The data showed that high pH Burkeite had almost double the surface area compared with the normal Burkeite. In addition, the average pore size of the high pH crystals was larger, which proved a lower level of aggregation of the Burkeite crystals.   This was probably because the induced caustic soda increased the charge on the surface of particles, developed a larger repulsion force, therefore limited the agglomeration occurring. More experiments need to be designed to explore the real mechanism for this phenomenon.

Table 6.1: Summary the property of two different Burkeite particles

Sample	name	Surface Area, m^2 / g			Pore Volume, cm^3/g	Pore Size (4V/A), Å
		BET	t-Plot External	BJH (Abs) 17 - 1000Å	BJH (Abs) 17 - 1000Å	BJH (Abs) 17 - 1000Å
Normal Burkeite	**1st Run**	0.3206	0.1318	0.2159	*0.00044*	82.0000
	2nd Run	0.4649	0.1951	0.3000	*0.00059*	79.1590
	Average	**0.3928**	**0.1635**	**0.2580**	*0.00052*	**80.5795**
High pH Burkeite	**1st Run**	0.8228	0.6133	0.6009	*0.00203*	113.76
	2nd Run	0.6841	0.4873	0.5704	*0.00153*	106.953
	Average	**0.7535**	**0.5503**	**0.5857**	*0.00178*	**110.3565**
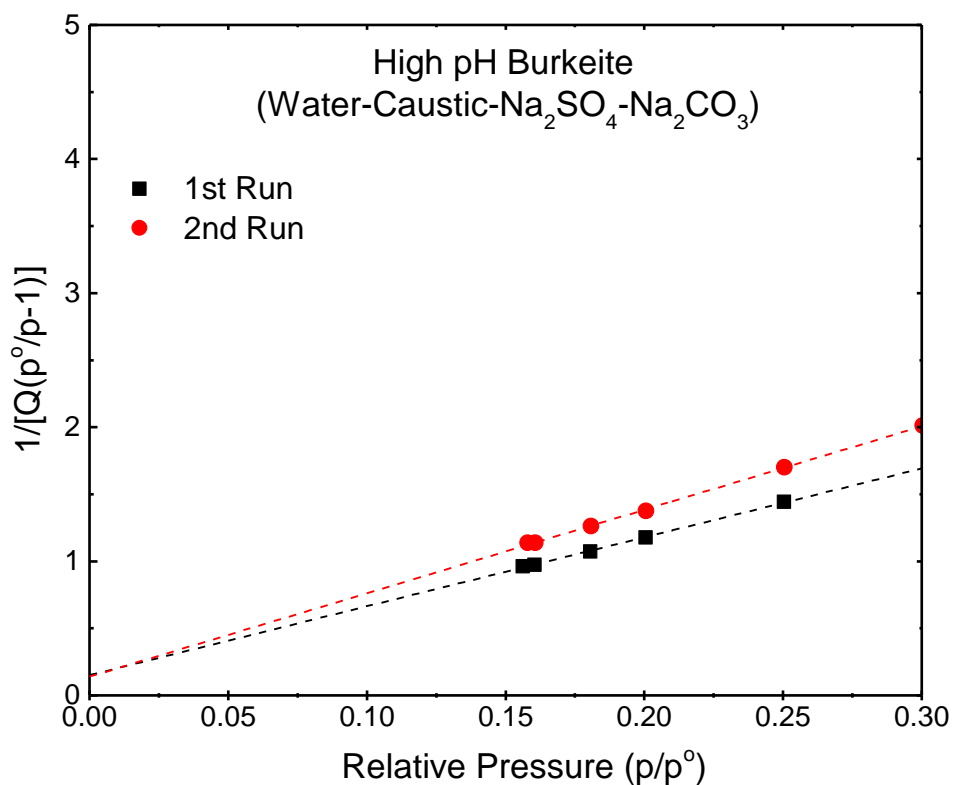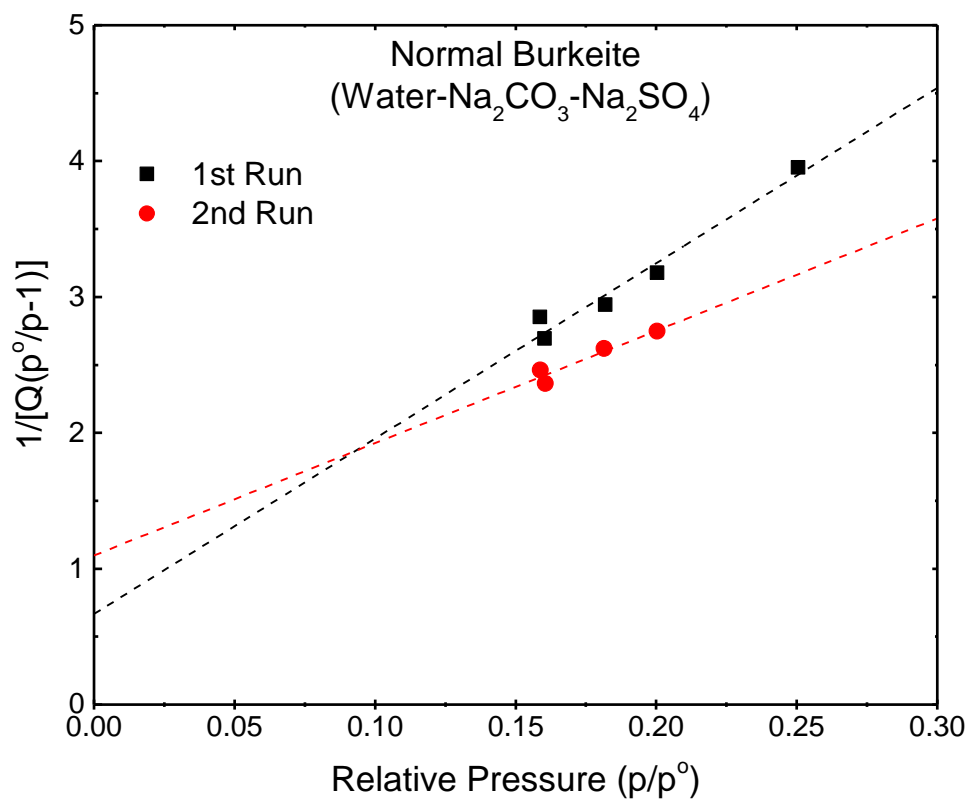
Figure 6.4: The BET surface area plot of normal and high pH Burkeite particles.

Overall, changing the solution environment with the addition of alkaline agent would modify the kinetics, yield, size and morphology of Burkeite crystal formation.

6.2 Sodium Silicate and Its Interaction with the Inorganic Phase

Burkeite with small particle size and a high degree of porosity would give benefit to the powder detergent, for instance, improve the stability (no hydrate phase will form) and fast dissolution (larger surface area). However, apart from inorganic phases, the impact of other chemicals on detergent powders should also be considered. In this section, the influence of sodium silicate was investigated that was due to silicate being one of the ingredients typically added to spray-dried detergent granules. In addition to that, according to the result from the previous section, the high pH property of it probably will also provide benefits on Burkeite crystallisation as an alkaline agent.

Therefore, the order of addition experiment was repeated once more with the presence of 10 wt% sodium silicate in the solution. As a result of this experiment, it can be seen whether using sodium silicate would attain the desirable benefits on Burkeite crystallisation can be revealed directly.

Figure 6.5 shows the quantitative analysis result, which was achieved by implementing in-situ PLS models, of the order of addition experiment with sodium silicate presenting in the solution. Table 6.2 denoted the composition analysis of the final slurry system for each experiment. In Table 6.3, the total amount of sodium salt that was dissolved in two different solution condition, water and sodium silicate, is compared. The results presented in Figure 6.5 & Table 6.2 did not turn out as expected, that a high pH solution environment would benefit Burkeite formation (i.e. higher and faster Burkeite crystallisation).
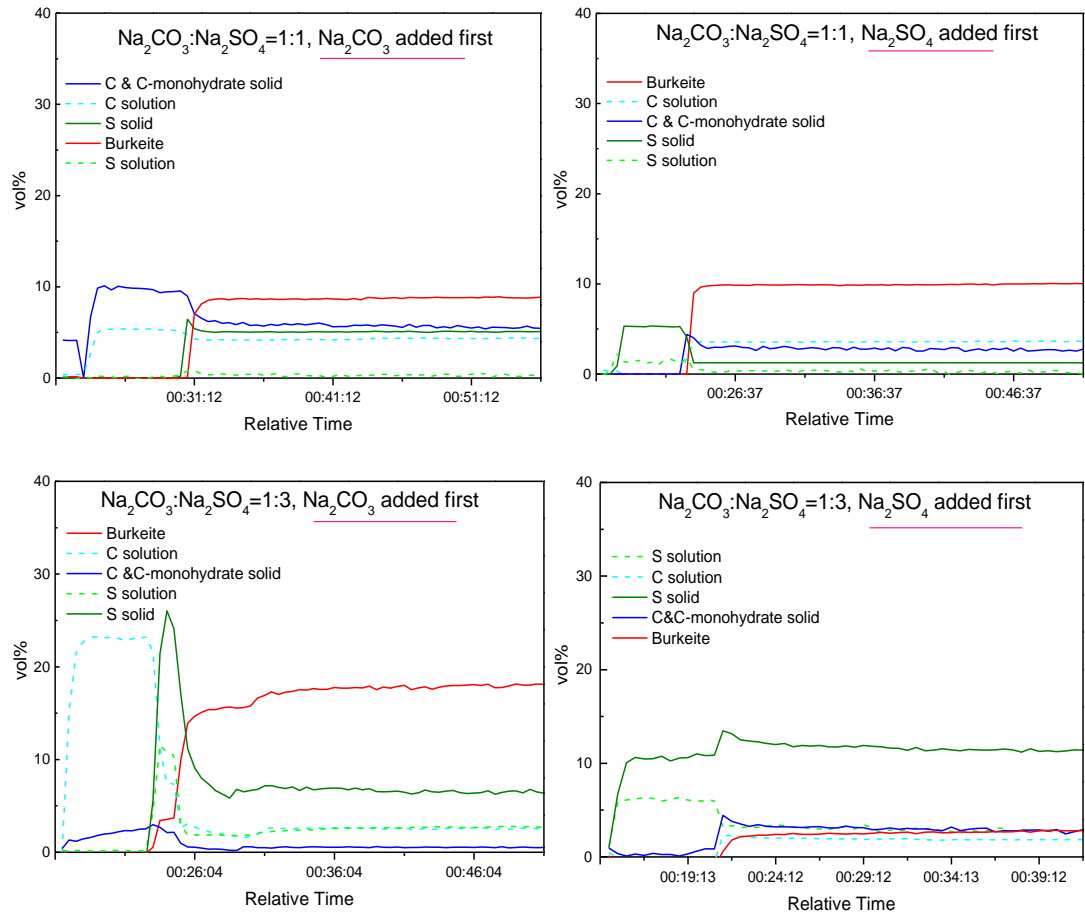
Figure 6.5: The impact of inorganic adding sequence on the Burkeite crystallisation in sodium silicate solution (1.6R, 45wt%). (Experimental variables: Na₂CO₃ to Na₂SO₄ mass ratio and the additional sequence; Fixed condition: 75°C and 100 rpm).

Table 6.2: Mass Balance of OOA in 10 wt% sodium silicate solutions (the total water content was 35.5 wt%)

OOA	Addition (wt%)		PLS (wt%)					Predicted (wt%)	
	S	C	B Solid	C & C·H2O solid	C soln.	S solid	S soln.	S	C
C:S 1:1	30.0	30.0	19.27	16.74	10.72	12.43	0.84	27.79	32.21
S:C 1:1	30.0	30.0	29.99	11.21	12.71	5.09	1.00	28.68	31.32
C:S 1:3	45.0	15.0	35.23	1.04	5.02	12.79	5.92	45.25	14.75
S:C 3:1	45.0	15.0	10.39	8.12	5.36	30.11	6.01	43.95	16.05

Table 6.3: The solubility of materials in two different solutions of the OOA experiment. (the total water content in both cases was ~34wt%)

OOA	Solution with 10 wt% sodium silicate		Water	
	Dissolved salts (wt%)	std.	Dissolved salts (wt%)	std.
C:S 1:1	11.56	1.31%	14.89	0.37%
S:C 1:1	13.71	1.21%	14.49	0.47%
C:S 1:3	10.94	1.05%	13.46	0.37%
S:C 3:1	11.37	1.25%	14.66	0.21%

In all cases, without regarding the adding sequence, a smaller amount of Burkeite was formed as compared to Table 4.6. The consistency outcome was that the most Burkeite (~35 wt%) was still achieved from the mass ratio of 1:3 with firstly introducing Na_2CO_3, but it was nearly 20% less than was obtained from the solution with no sodium silicate involved. Also, the amount of salt dissolved in the solution was around 3% less than the pure water condition in Table 6.3, correspondingly more undissolved raw materials remained in the system. Over time, a small amount of Burkeite was still precipitating while more of the raw materials were dissolving, especially in the case of 1:3 ratios, however the kinetics were rather slow. Hence, sodium silicate decreases the solubility of raw materials, possibly even Burkeite.

According to the assumption above, the solubility of raw materials in different concentrations of sodium silicate (1.6 R) solutions was tested by following the same method as that for determing the solubility of sodium salt in water (see section 4.2.2. The results are given in Table 6.4, and the solubility of both salts decreased with the increasing silicate concentration.

Table 6.4: Solubility of Na_2CO_3 and Na_2SO_4 in 1.6R silicate solutions

Sil. 1.6R conc. (wt%)	Na_2CO_3 solubility (g/100g H2O)	Na_2SO_4 solubility (g/100g H2O)
10	38	33.5
15	34	30
25	27	21
35	19	16.5
45	11	7.5

There were two possible ways for sodium silicate to prevent sodium salt dissolution, the common ion effect and/or insufficient water in the sodium silicate solution to dissolve the inorganic salts.

$$Na_2SO_4 \rightleftharpoons Na^+ + SO_4{}^{2-} \qquad \text{Eq. (6.1)}$$

$$K_{sp} = [Na^+]^2 * [SO_4{}^{2-}] \qquad \text{Eq. (6.2)}$$

For example, Equation (6.1) was showing the ionized equation of Na_2SO_4 dissolving in water. If a second material (i.e. sodium silicate) that has an ion in common with Na_2SO_4, then according to Le Chatelier's principle, the position of equilibrium in Equation (6.1) would shift to counter the exceeded common ion (i.e. Na+). Because the degree of sodium silicate polymerization would increase with the presence of foreign ions and its own solution concentration, (which will be discussed in the following sections) therefore more free Na+ would exist in the solution (see section 2.4.3) inhibiting the dissolution of Na_2CO_3 and Na_2SO_4.

As reviewed in Chapter 2 (section 2.4), the composition of different species of silicates can be easily altered by internal and external factors. In the current situation, the internal factor would be sodium silicate concentration, and the external factor was inorganic salt intervention. Both factors could cause sodium silicate polymerisation to occur, or more higher degree of polymers to be achieved. Therefore, another hypothesis was purposed as the newly formed higher degree of polymers would decrease the amount of free water that was used to dissolve sodium salts. Some of the water was trapped inside the silicate structures (i.e. ring structures), thus less free water would be used for the salt dissolution (9), so a less amount of Burkeite can be generated with the lack of Na^+, $CO_3{}^{2-}$ and $SO_4{}^{2-}$ ions present in the solution. A simple calculation was applied to find the correlation between the amount of trapped water and sodium silicate solution condition, such as solution concentration and the dissolved sodium salt content. An example was given in Table 6.5, which displays a decreasing tendency of the available water with the increasing silicate concentration.

In Table 6.5, the second column denotes the solubility of Na_2CO_3 in sodium silicate solutions. Column three indicates the amount of water which will be required to dissolve the corresponding quantity of Na_2CO_3 in a pure water system. The last column represents the amount of water which may be

trapped in silicate structures. The calculation of the last two columns is demonstrated in Equations 6.3 and 6.4, respectively:

$$column\ 3 = (column\ 2) * 100/41 \qquad \text{(Eq. 6.3)}$$

$$column\ 4 = 100 - column\ 3 \qquad \text{(Eq. 6.4)}$$

Table 6.5: The amount of water which may be trapped by silicate structures (the total water content in each system was 100g, and Na_2CO_3 solubility in water is 41g/100g H_2O at 75°C)

Sil 1.6R_wt%	Na_2CO_3_g /100g water content	Available water_g	Water trapped by Ring structures_g
15	34	82.9	17.1
25	27	65.9	34.1
35	19	46.3	53.7
45	11	26.8	73.2

Another possibility for the decreasing solubility behaviour could be the excess Na^+ substituted the hydrogen ions (H^+) from sodium silicate structures, due to the fact that Si-O ions can stay more stable and have more interactions with Na^+, therefore not enough efficient Na^+ to form Burkeite.

In order to prove the last two hypotheses we needed to find the real mechanism for the decreasing solubility behaviour of the sodium salts in silicate solutions. The impact of solution concentration and inorganic salts on sodium silicate speciation were investigated in the following two sections.

6.2.1 Speciation of sodium silicate solutions

The speciation information of sodium silicate solutions, which can be interpreted from Raman spectra, is summarised in Table 6.6. The spectra were focused on the region of 400-1200cm^{-1} for the interest of silicate solutions. The sharp peaks around 450, 577 and 750 cm^{-1} are probably due to the interference from light sources during the experiments; they do not represent any information on silicate structures. Peak separation information was specified in Figure 6.7, which delivers a better indication of the peak position of different species.

Table 6.6: Q^n assignment of Raman peak positions (10-19) (δ: bending mode; v: stretching mode; as: asymmetry and s: symmetry details)

Raman peak position (cm^{-1})	Speciation	Vibrational mode	
~464	6 ring structure T^6	δ_s O-Si-O	Symmetric or asymmetric bending of bridging oxygens (see Figure 6.6) or Si-O-Si linkages.
~523	5 ring structure T^5	Linkages between $\equiv$SiO	
~540	4 ring structure T^4		
~606	3 ring structure T^3	δ_{as} (Na)O-Si-O(Na)	
~778 & 800~850	Q^0	δ_{as} (H)O-Si-O(H) & v_s SiO$_4$	Symmetric stretching of Si and non-bridging O (see Figure 6.6) in the SiO$_4$ tetrahedral units.
~870$\pm$20	Q^1	v_s $-$SiO$_3$	
~965-1030	Q^2	v_s $=$SiO$_2$	
~925$\pm$25 & ~1075$\pm$25	Q^3	v_s $\equiv$SiO	
~1150	Q^4	v_{as} $=$Si$=$	

Figure 6.6: The indication of the non-bridging and bridging structure in silicate systems (reproduced from (10))
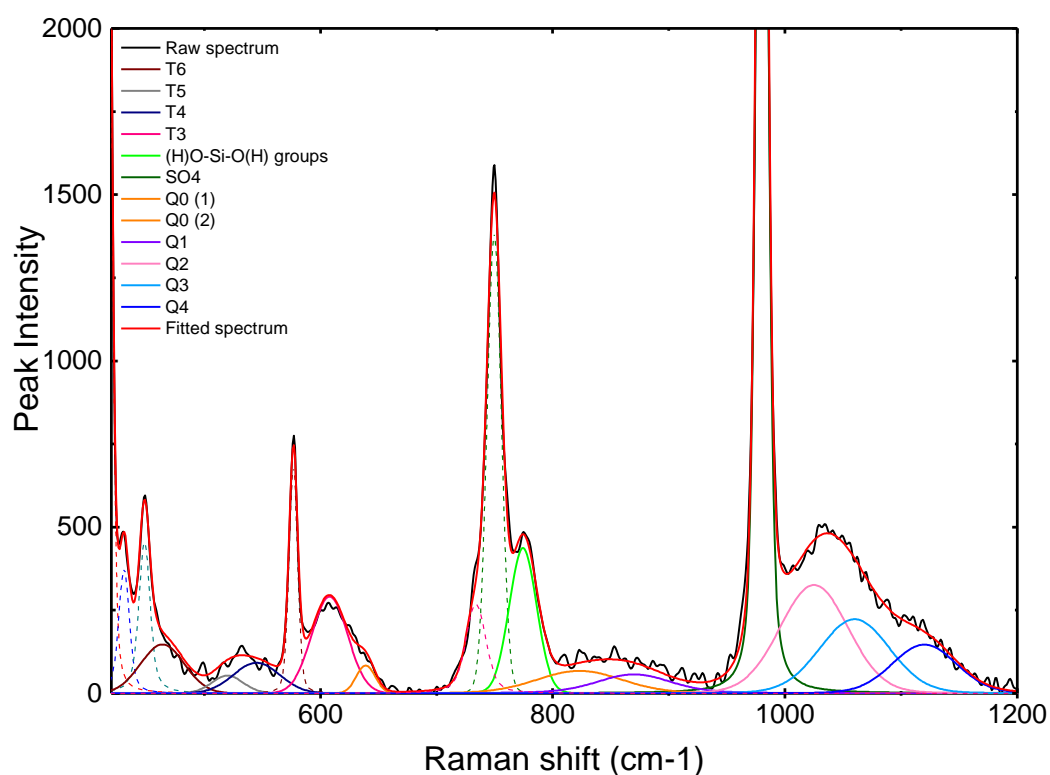
Figure 6.7: An example of the decomposition of a Raman spectrum of sodium silicate solution in the presence of H₂SO₄. The peak separation method contributed to the sodium silicate speciation studies. The peak separation was processed by using Fityk software, a Voigt function was applied for peak fitting (see the Appendix).

The speciation of two weight ratios (1.6 and 3.2 SiO_2/Na_2O) of sodium silicate with different concentrations was studied in this part.

Figure 6.8 illustrates changes in the Raman spectrum with sodium silicate solution concentrations.
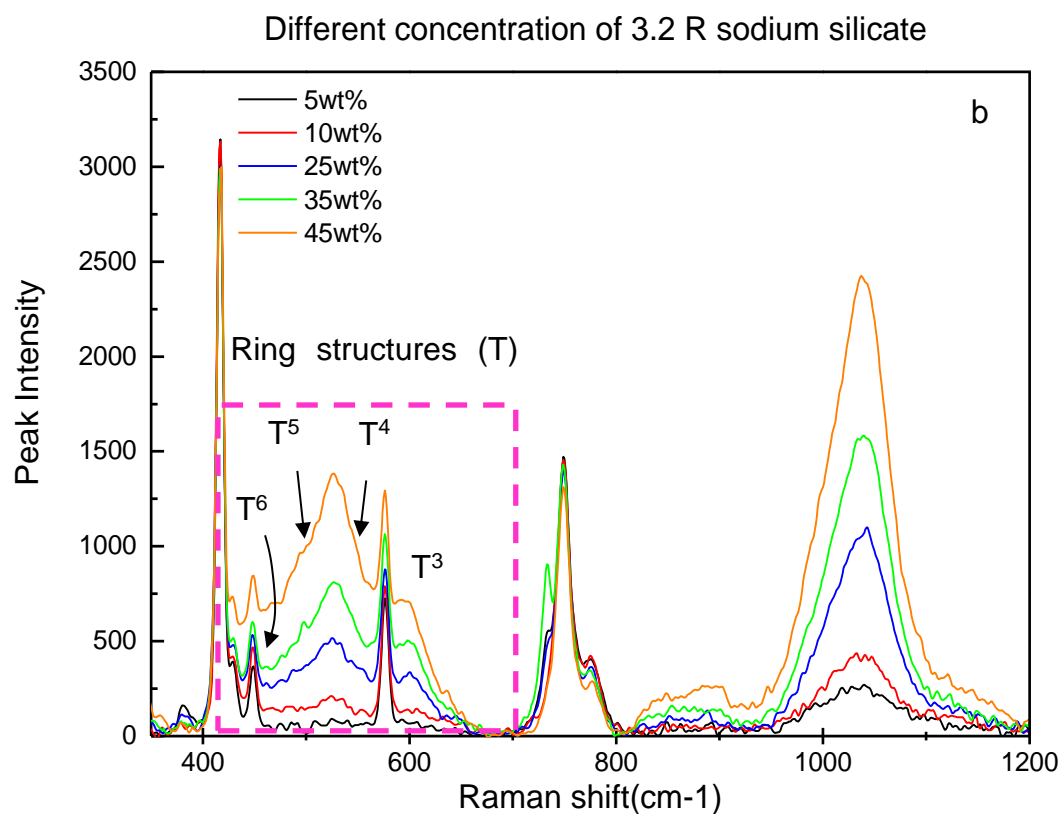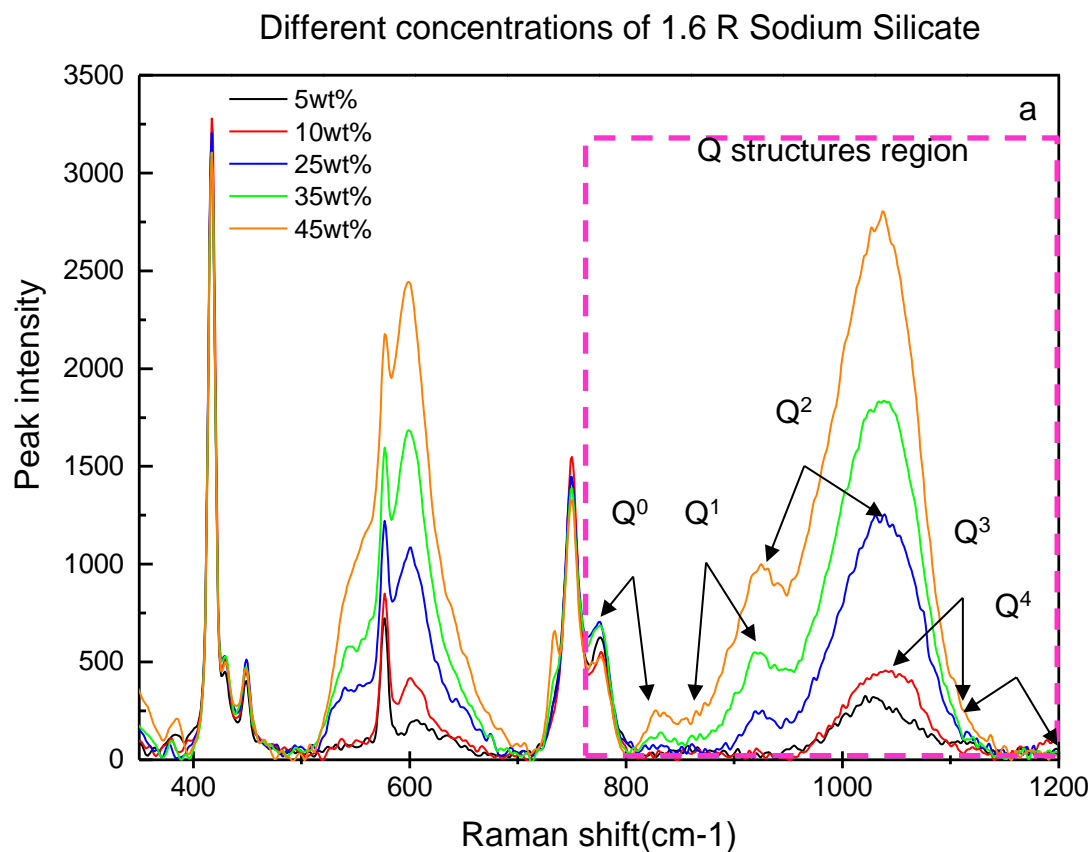
Figure 6.8: Changes in the Raman spectrum of sodium silicate with different solution concentrations. a: 1.6 ratio sodium silicate; b: 3.2 ratio sodium silicate

As shown in Figure 6.8, the higher ratio of sodium silicate solutions contains more complex polymers. For instance, 3.2 R solutions possess more T^5 and T^6 ring structures (~450cm^{-1}) and also Q^4 cross-linked structure (1050-1200cm^{-1}). On the contrary, in 1.6 R solutions there was a lower level of Si units T^3, T^4 and Q^1 structure than in the higher composition. Another dominant structure Q^2 in the 1.6 R solution also had a significantly high level. This structure covered a wide region of Raman spectra which overlapped with the area of both Q^1 and Q^3. Therefore, with this structure present, the background of the spectra that crossed area 850-1050cm^{-1} has risen. Additionally, the big band around 1000 cm^{-1} became broader. For solutions with a concentration of 45 wt% (Figure 6.8), more high polymerised structures existed in the 3.2 ratio, such as Q^4, T^5 and T^6, as the ratio decreased (1.6R) the more a lower degree of polymers appeared. Because low ratio solutions possess more alkaline properties, thereby the alkali metals will behave as a Si-O bond breaker promoting the disintegration to occur.
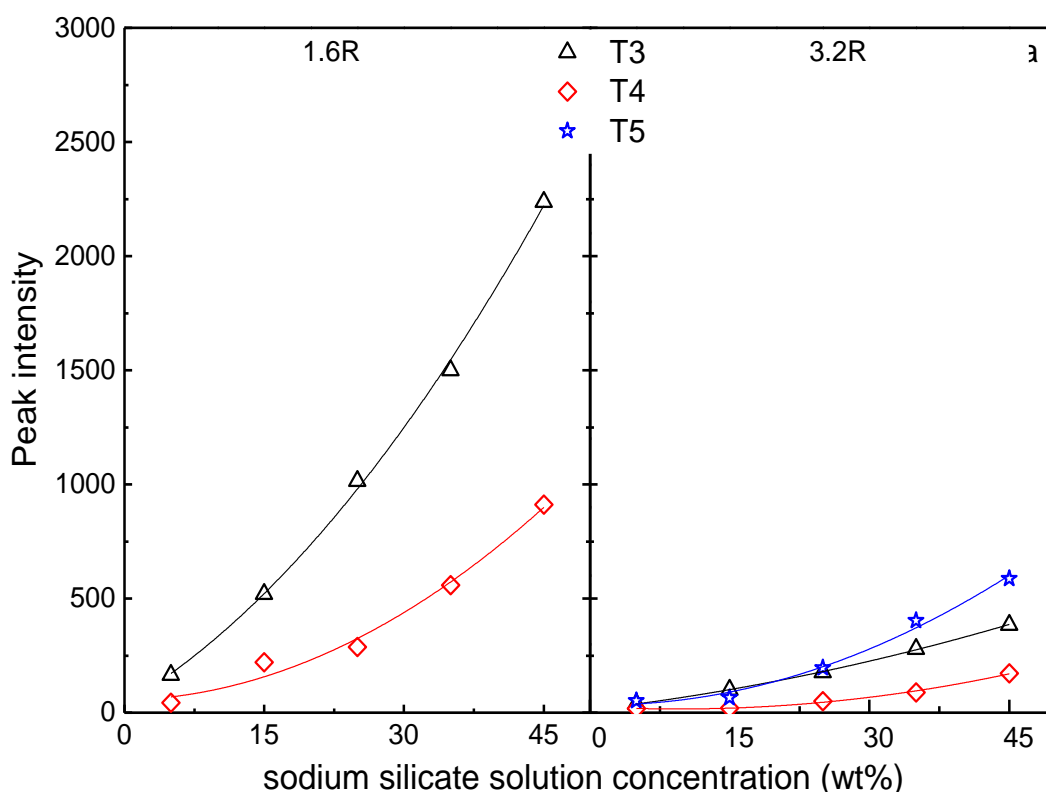
Figure 6.9: Speciation of ring structures in different concentrations of sodium silicate solutions (analysis based on the Raman spectra Figure 6.8, peak separation was processed by applying Fityk software)

By directly looking at the spectra in Figure 6.8 one would assume that the peak intensities of all structures increase proportionally with the silicate concentration. However, the real situation is after processing the peak separation to each spectrum, only ring structures displayed a polynomial increasing trend with sodium silicate solution concentration, see Figure 6.9, the changing trend of other species can be found in Figure 6.11. If the increasing tendency of ring structures is linked with the amount of water trapped in silicate structures in Table 6.5, then we achieve Figure 6.10 and Table 6.7.

Figure 6.10 indicates the quantity of the trapped water increasing with the composition (intensity) of ring structure presence in the solution. Assuming each ring structure could trap a fixed amount of water, for instance here T^3 and T^4 will bond 3 and 4 water respectively was assumed. Therefore, a constant value should be obtained as the product of ring structure peak intensity divided by the total amount of trapped water, see Table 6.7 column 4 & 5. The result values were quite consistent, which supports the hypothesis that the low solubility behaviour of sodium salt in silicate was affected by lower amount of free water in the system.
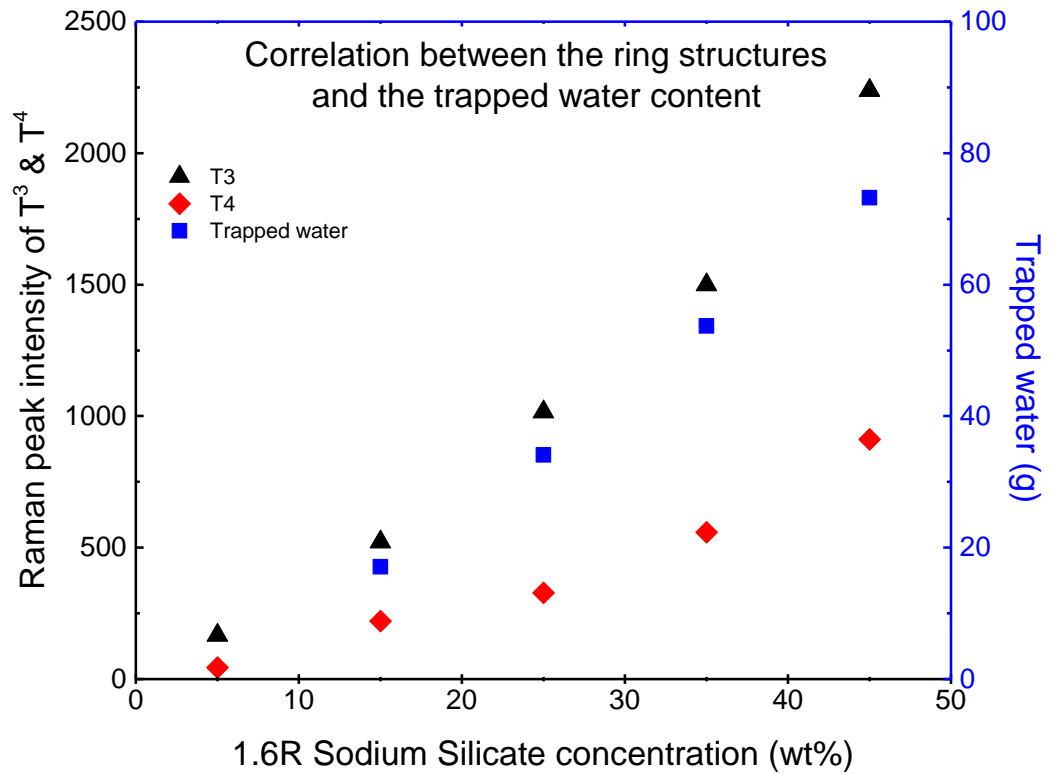
Figure 6.10: The relationship between sodium silicate (1.6R) ring structures and the non-free water (The intensity of T3 and T4 corresponds to the left y axis, the amount of trapped water corresponds to the right y axis)

Table 6.7: Correlating the Raman peak intensity of the ring structures with the amount water that may be trapped (Assuming T^3 and T^4 will bond 3 and 4 water respectively. So if the assumption was true, a constant value would be obtained as the product of (peak intensity/the amount of non-free water (Table 6.5).)

| Sil 1.6R_wt%	T^3_Intensity	T^4_Intensity	T^3_Intensity /trapped water	T^4_Intensity /trapped water
15	520.78	220.06	31	12
25	1015.50	328.31	30	10
35	1599.67	558.45	30	10
45	2238.00	911.98	31	12
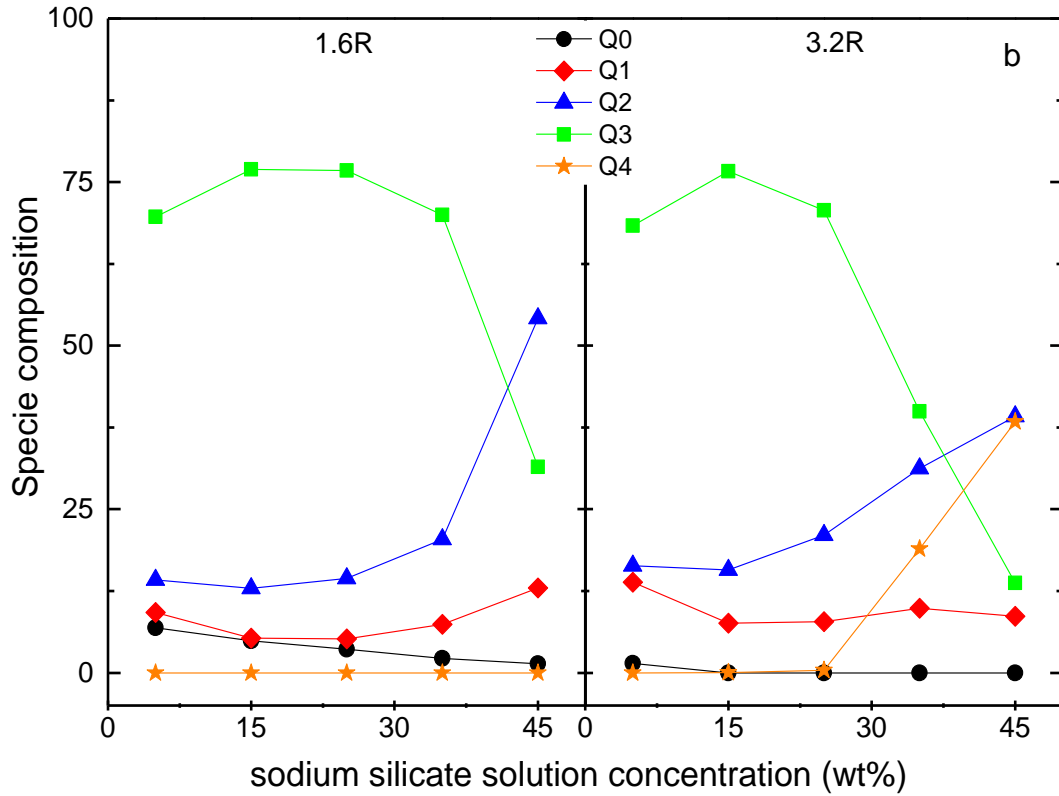
Figure 6.11: Speciation of Q structures in the different concentration of sodium silicate solutions (analysed based on the Raman spectra Figure 6.8, peak separation was processed by applying Fityk software) The composition of each structure was determined by correlation the peak intensity each species with a mathematic model (20)

In Figure 6.11, the calibration curves were obtained after processing the peak separation to each spectrum, and the composition was calculated for the individual structures. The method of determining the composition for different solution concentrations was done by correlating the peak intensity of each species at 5 wt% with the determined composition at the same weight percentage which was resolved by Svensson in 1986 (20) through a mathematic model. Then, the Raman peak intensity of 1% of the individual species would be obtained. Next, the compositions for other solutions (i.e. 10 wt%, 25 wt%, 35 wt% and 45 wt%) can be determined following the equation below (Equation 6.5). The mathematical model was completed based upon previous NMR studies for the purpose of predicting the composition variation of different structures as the function of the changing pH and the SiO_2/Na_2O ratio, the detailed derivation process was given in (17, 20).

$$x = \frac{I_m^i}{I_{1\%}^i}$$

Eq. 6.5

where x is the composition of the species i;

$I_{1\%}^i$ is the peak intensity of 1% of the species i at 5 wt% of sodium silicate solution;

I_m^i is the measured intensity of species i at current solution concentration;

In Figure 6.11, the data suggests that both 1.6 R and 3.2 R silicate solutions contained a relatively high level of Q^3 structure even in the case of diluted solutions. Below 25 wt%, the composition of Q^3 slightly increased above 70% with the solution concentration. Above 25 wt% Q^3 began decreasing especially in 3.2 R silicate solutions, at the same time the composition of Q^2 went up rapidly. Moreover, in 3.2 R solutions, the percentage of structure Q^4 increased dramatically as soon as the concentration went beyond 25 wt%. Hence, for solutions with the same SiO_2/Na_2O ratio, the polymerisation degree is slightly higher in the low concentration solutions.

The composition analysis of other sodium silicate concentrations from Raman has also been compared with the NMR studies; the outcomes are displayed in Figure 6.12. Most of the analyses exhibited a good agreement apart from 1.6 R 45 wt% solution. According to Raman analysis, there was less Q^2 structure, instead more Q^0 and Q^1 were achieved. From mass balance, the exceeded amount of Q^0 and Q^1 is equivalent to the amount of reduced Q^2.
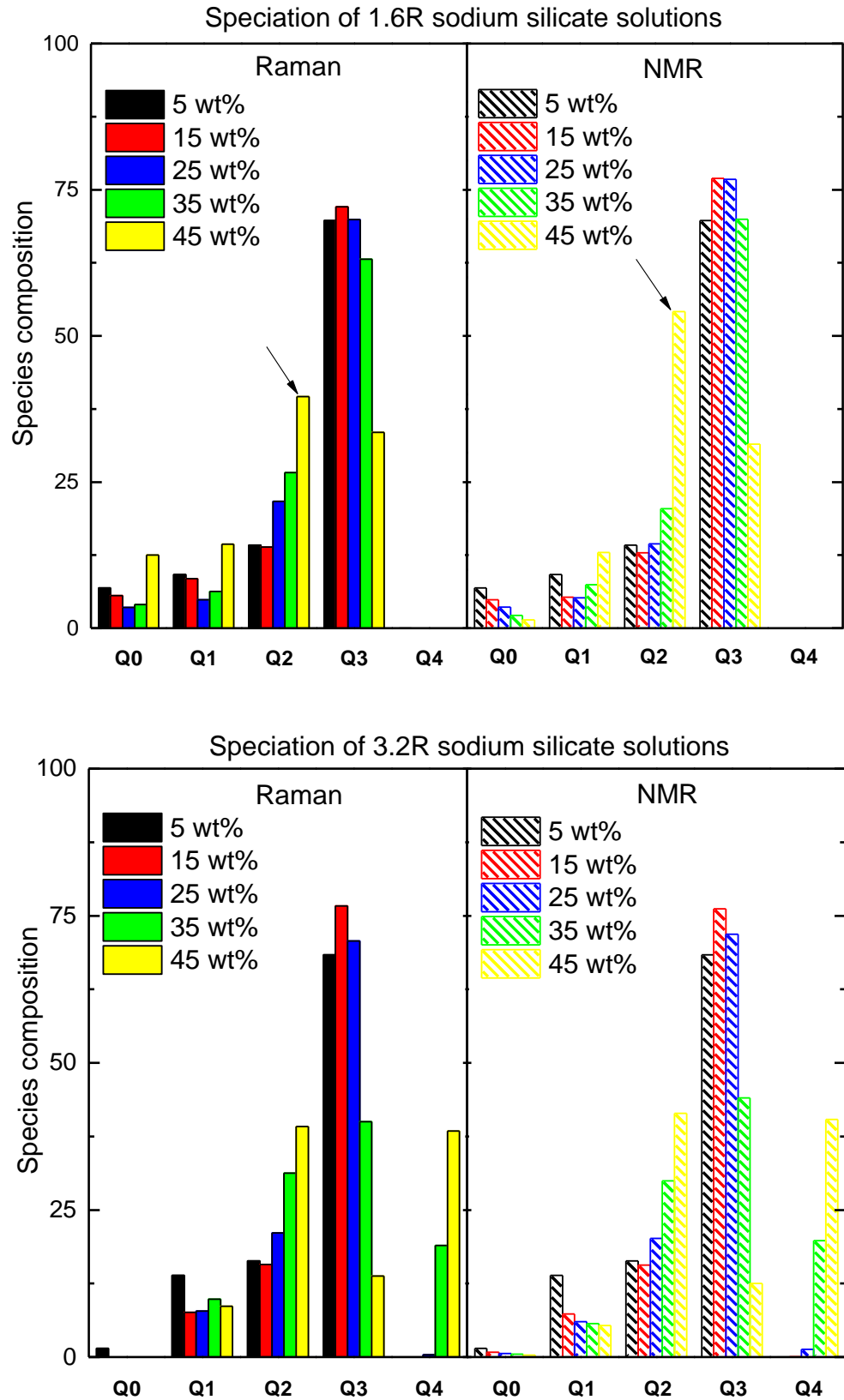
Figure 6.12: Comparison the Raman and NMR results of the speciation of sodium silicate solutions (the NMR result was achieved by implementing the model which was given in (20). The Q^2 and Q^3 here equivalent to the symbol of Q^2_y and Q^3_y in (20))

Following a similar methodology, the impact of inorganic phase on sodium silicates can be conducted with the basic understanding of the speciation variation in sodium silicate systems.

6.2.2 Inorganic salts in sodium silicate systems

Na_2CO_3 and Na_2SO_4 were introduced to different concentrations of sodium silicate solutions individually. Salt was added to each solution as it reached its saturated state and no excessive undissolved particles remained. The solubility of each salt in the individual solution has already been shown in Table 6.4.

The experiment was initially designed for studying the impact of sodium silicate on the solubility of sodium salts as shown at the beginning of section 6.2. However, due to the fact that cations and anions can influence the speciation of silicate, therefore, by considering this issue from another angle, the impact of sodium salts on silicate polymerisation was considered.
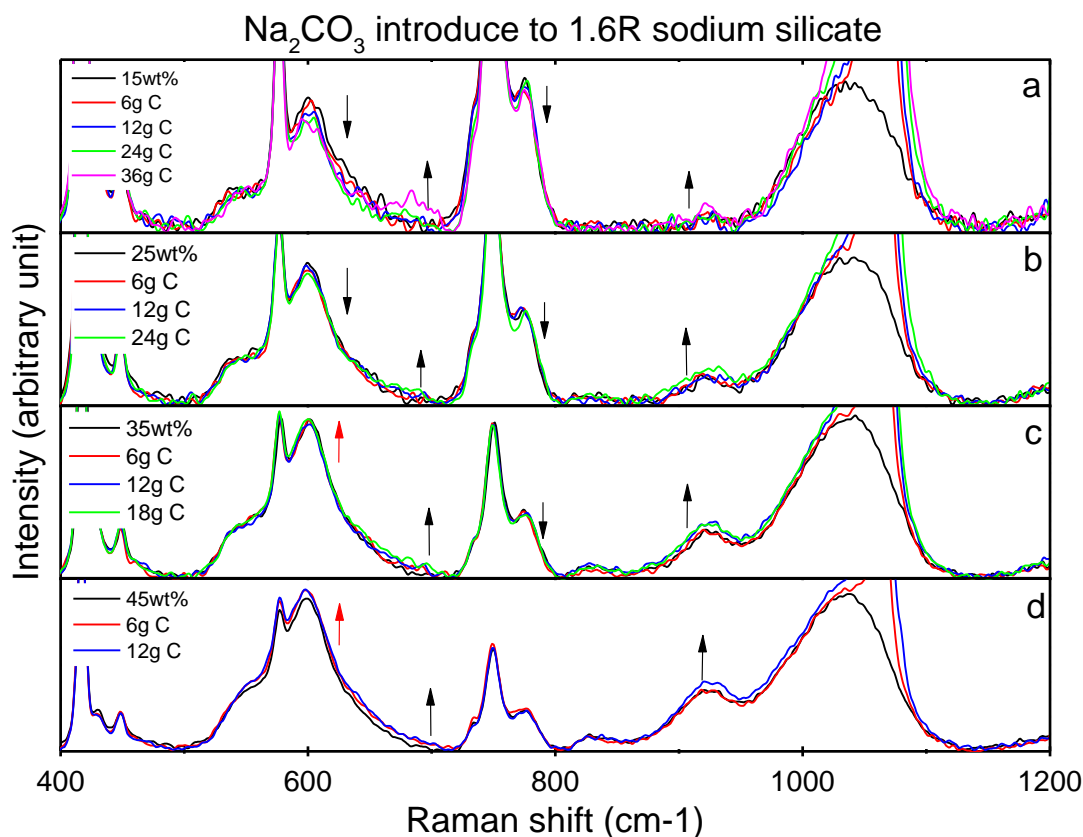
Figure 6.13: The impact of Na_2CO_3 on 1.6 R sodium silicate solution polymerisation. Spectra were taken after system reached equilibrium. (The enlarge figures are given in appendix to show the significance in peak intensity change)

An obvious variation on the Raman spectra can be observed after the addition of Na_2CO_3, especially in the low concentration sodium silicate solutions (Figure 6.13a). The band around 606 and 778cm^{-1} decreased with the addition of Na_2CO_3. Q^2, T^3 and δ_{as} NaO-Si-ONa they might all contribute to the former peak intensity (19, 21). If 606 cm^{-1} represented structure (δ_{as} NaO-Si-ONa), then the peak intensity should increase or at least remain constant with the additional input of Na$^+$. However, in both cases in Figure 6.13a and b, 606cm^{-1} retained the declining trend, which suggests it possesses the information from Q^2 and/or T^3. Thus, the decrease in the intensity was possibly due to the breakage of T^3 structures that were interfered by the cation ion Na$^+$. The broken structures rearranged to form high degree of polymers, such as Q^3. Band ~930cm^{-1} attributed to the vibration of v_a NaO-Si-OH and Q^3 (v Si-O-Si) (19, 21), both of the structures could result from the rupture and restructuring of the small size polymers. A marginal increase can also be found around 630 cm^{-1}, which denotes the v Si-O in monomers (17), hence there must be a small amount of monomer generated simultaneously when the polymerisation occurred.

The peak 778cm^{-1} is an asymmetry bending vibration of polarisable HO-Si-OH which usually decreases with the increasing solution concentration, which indicates more SiO_4 units connected together, the HO-Si-OH bonds became less, so the overall diminished vibration reflected a reduction in the peak intensity. Therefore, the decrease of 778cm^{-1} in this case also indicates that the polymerisation event is happening.

In Figure 6.13 (c and d), an opposite phenomenon was detected around ~600 cm^{-1} when the solution concentration was above 25 wt%. The peak intensity increased with the amount of Na_2CO_3 added. Because over 25 wt% the composition of Q^2 increased sharply and it gradually became the dominant phase (Figure 6.12). Therefore the contribution from Q^2 to the spectra would eventually overtake the effect of the disintegration of T^3 on spectra, leading to an increasing trend to the band around 600 cm^{-1}.

A similar conclusion can be drawn in the case of Na_2SO_4 influence on sodium silicates (Figure 6.14). However, the peak information of sodium silicate overlapped with Na_2SO_4 solution signals at the region of 400-700 cm^{-1} and

1050-1200 cm^{-1} (Figure 4.7). Therefore, the polymerisation taking place can only be judged from the increase of 778cm^{-1} and ~930 cm^{-1}.
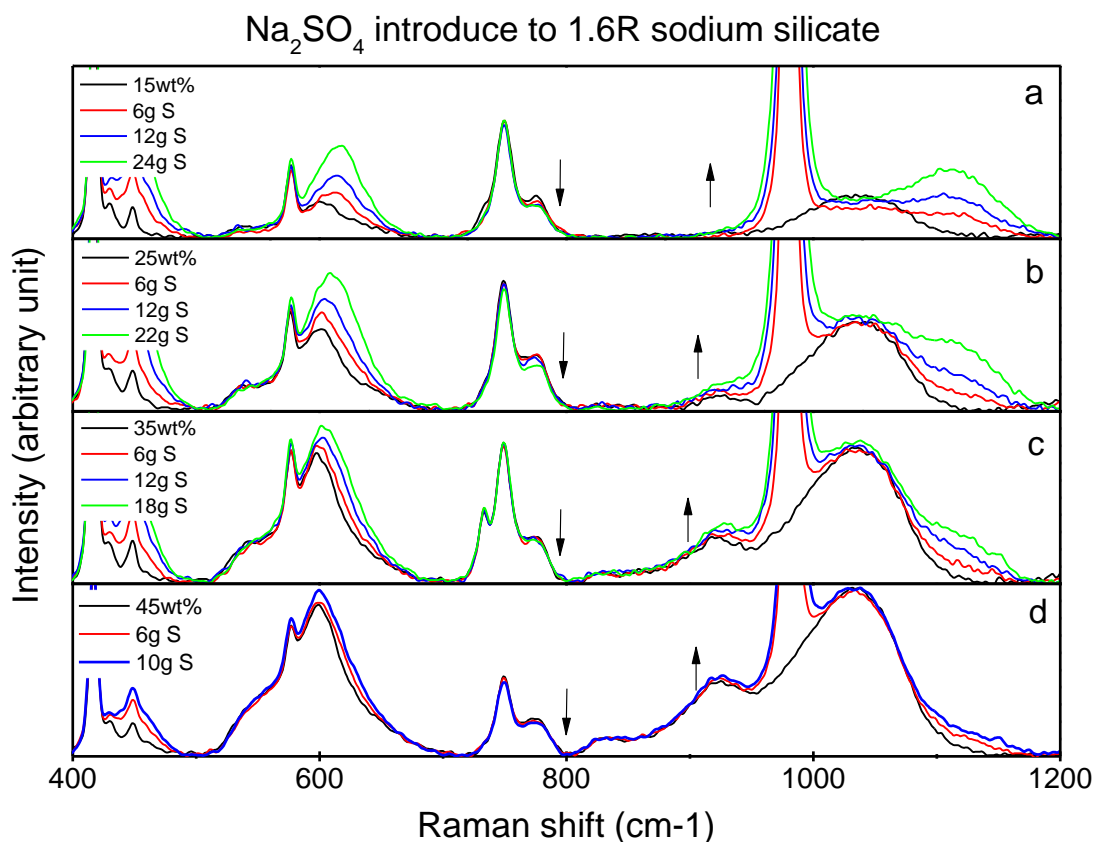
Figure 6.14: Polymerisation study of Na$_2$SO$_4$ impact on 1.6 R sodium silicate solutions. Spectra were taken after system reached equilibrium. (The enlarge figures are given in appendix to show the significance in peak intensity change)

Another evidence of the inorganic salts influencing sodium silicate is showing in Figure 6.15. A reduction in trend on solution pH was monitored along with the salt accumulation, which denotes the polymerisation is occurring.
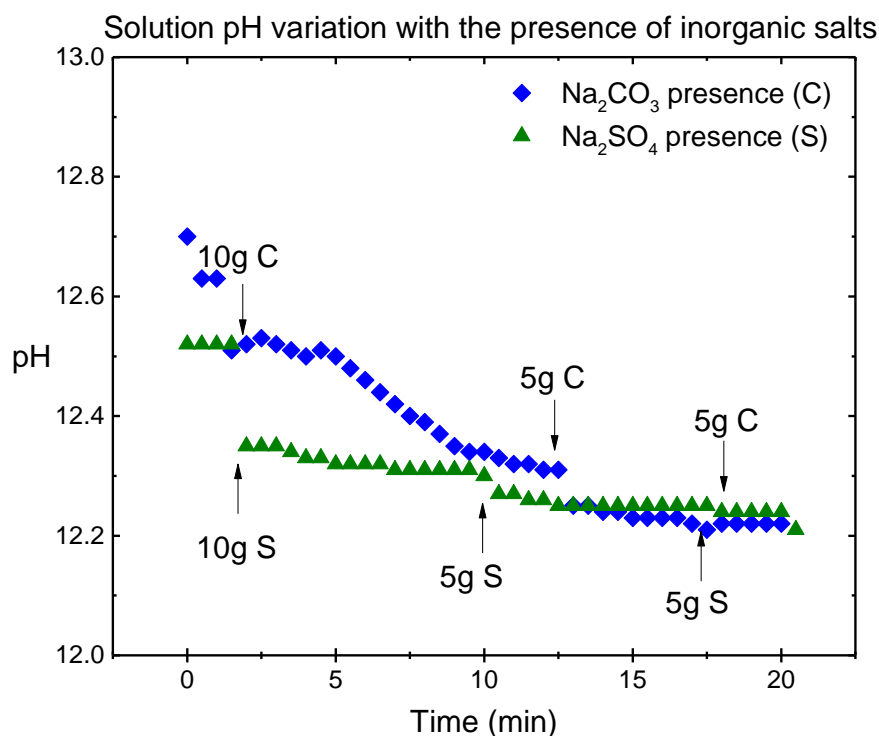
Figure 6.15: Impact of the inorganic salts on 10 wt% of 1.6 R sodium silicate, the pH recording (at 75°C).

To sum up, sodium silicate and sodium salt have mutual restraints. The composition of ring structures increases with the sodium silicate solution concentration. More water will be trapped in the growing ring structures, therefore reducing the amount of free water for dissolving the sodium salts.

On the contrary, for example in Figure 6.5, as more Burkeite precipitated, more of the sodium salt gradually dissolved in the system. It facilitated the polymerisation of sodium silicates, as a consequence more water may be trapped in a high degree of polymers. Thus, the dissolution of sodium salts declined further. Therefore, a sluggish process of Burkeite formation observed after the first crystallisation event occurred in Figure 6.5, as compared with OAA figure the kinetics are rather slow.

6.2.3 Temperature sensitivity of sodium silicate solutions

As an extended study, additional factors which impact on silicate studies have also been explored, such as temperature and pH effects (see section 6.2.4).

Figure 6.16 displays Raman spectra of the same weight percentage of two sodium silicate solutions under different temperatures. The aim was to

understand the significance of process temperature variation on the speciation of current sodium silicates. Two different temperatures (55 and 75°C) and ratios (1.6 R and 3.2 R) of sodium silicate were studied in this part.
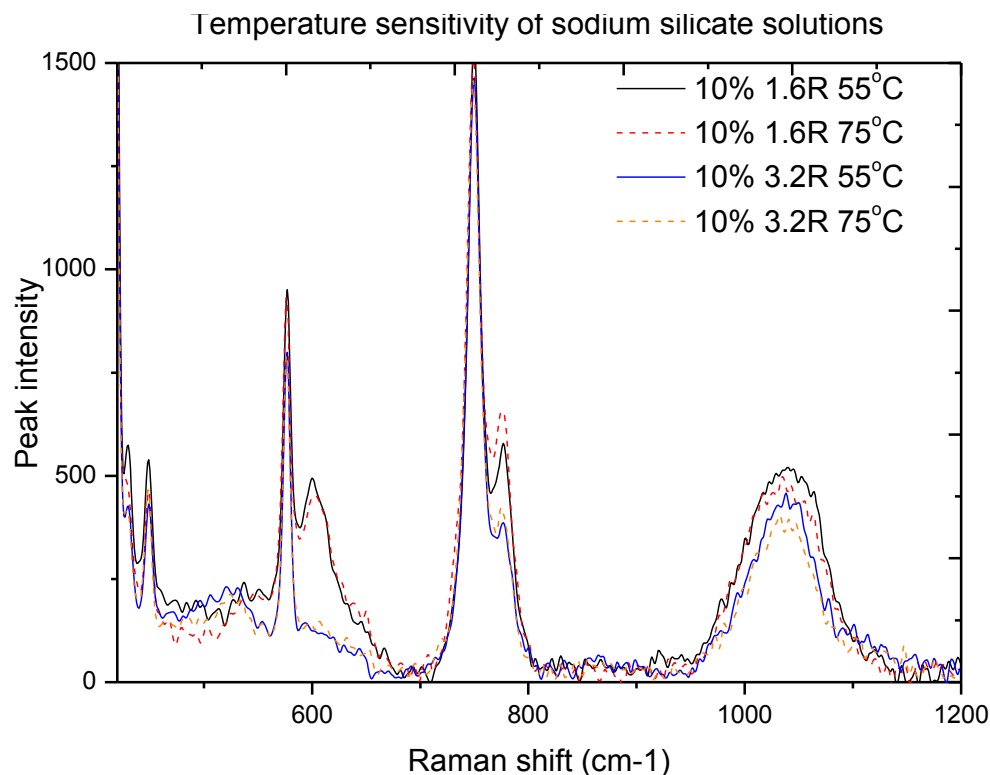
Figure 6.16: The impact of changing temperatures on the composition variation of sodium silicate solutions.

As expected, increasing the temperature led to de-polymerisation of large polymers (22), which can be observed from Q^2 - Q^4 (~950-1200 cm^{-1}) peak regions in Figure 6.16. For sodium silicate solution, the composition among all the species is under a dynamic equilibrium state. Therefore, the amount of smaller Si units (i.e. monomer Q^0 ~778cm^{-1}) with the lower polymerisation degree was achieved through the decomposition of large polymers. The results were consistent with the literature (22), therefore keeping the experimental temperature under good control was necessary for all silicate studies in this research.

6.2.4 pH impact on the de-polymerisation and polymerisation of sodium silicates

As previously reviewed, pH has a great influence on the (de-polymerisation) process of silicate systems (22). Hence, in this section the impact of pH on the speciation of sodium silicates was investigated, which helped understanding of the changing trend in the composition of each silicate structure.

Firstly, solutions with 10 wt% of 1.6 R and 3.2 R sodium silicate were prepared individually. Raman spectra were taken for these two solutions as references for following studies, see Figure 6.17.
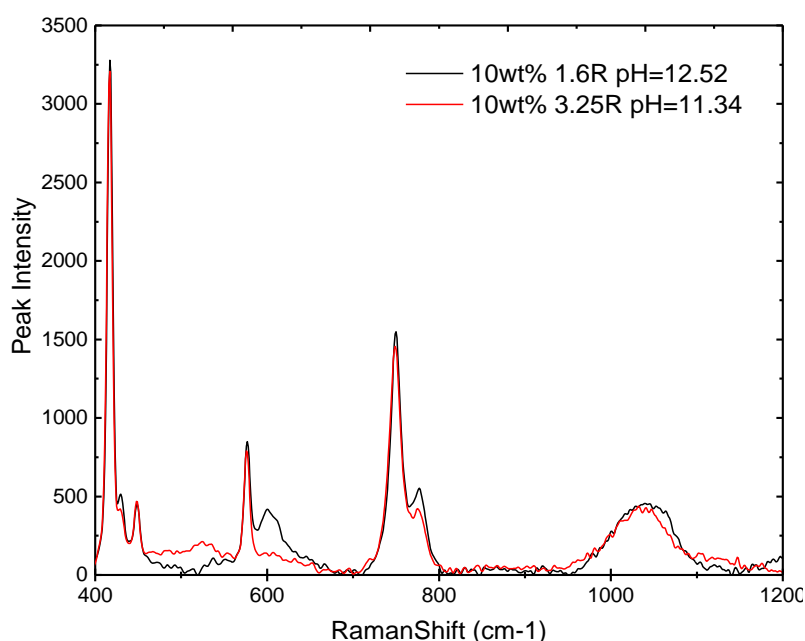
Figure 6.17: Raman spectra of 10 wt% of 1.6 R & 3.2 R sodium silicate solutions at 75ºC.

These two solutions can be distinguished by comparing the existence of Raman bands around 545, 606, 778 and 1050cm^{-1}.

The peaks 545 and 606 were assigned to the deformation vibration of 4 and 3 [SiO$_4$]$^-$ ring structures, respectively (19, 23). The Raman shift near 778 cm^{-1} was assigned to the asymmetric bending of polarisable (H)O-Si-O(H) groups, which existed on the surface of both monomer and polymer structures (21). The Raman band around 1050 cm^{-1} was the indication of the present of Q^2 and Q^3 species. Additionally, they may be a certain level of T^6 (463cm^{-1}) in the 10 wt% 3.2R solution.

6.2.4.1   De-polymerisation of 3.2 R sodium silicate solutions

4M NaOH solution was gradually added to increase the pH of 3.2 R sodium silicate, and the in-situ Raman was applied for tracking the composition variation of different species along the pH changing process. A background offset was applied for all collected spectra that are displayed in Figure 6.18.

NaOH induced de-polymerisation of
3.2R sodium silicate
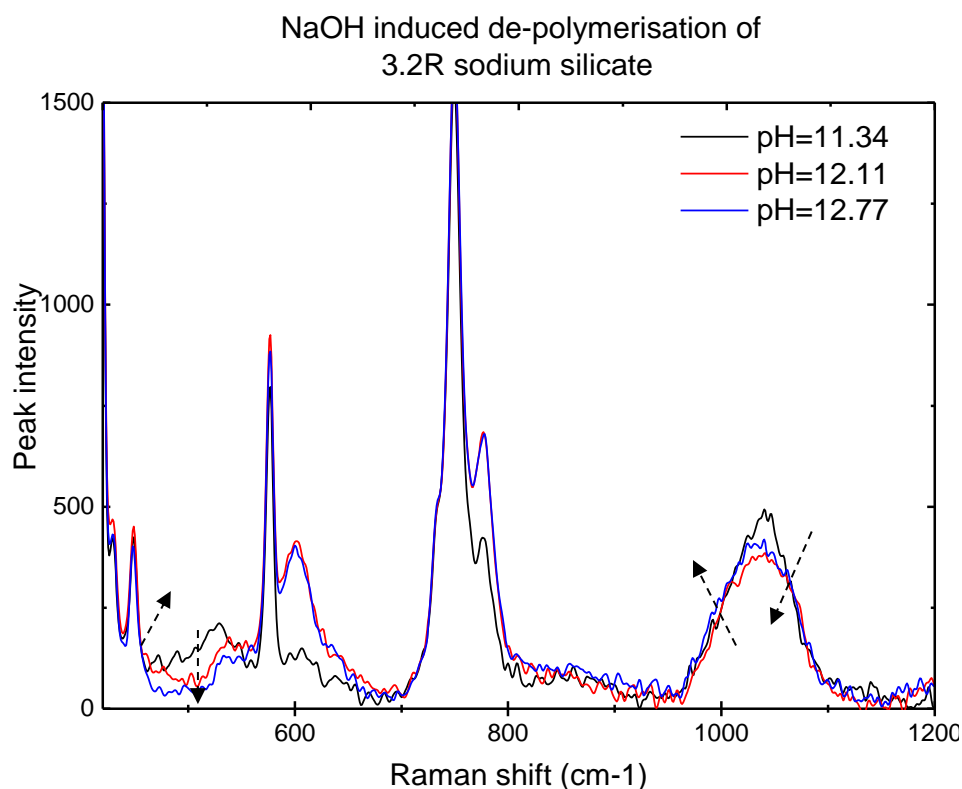
Figure 6.18: NaOH was introduced in a 10 wt% 3.2 R sodium silicate solution to trigger a de-polymerisation of the solution to occur. The process was mornitored with an in-situ Raman spectroscope.

From an overview of the spectra in Figure 6.18, a variation in the species can be observed clearly. There was no high level of cross-linked polymers in the original solution (pH=11.34), such as Q^4, possibly due to the low solution concentration. The peak shoulder ~1050cm^{-1} (Q^3) and T^5 band (~520cm^{-1}) decreased with the addition of alkaline solution that illustrates that de-polymerisation occurred. At the same time the intensity of T^4 (~545cm^{-1}) and T^6 (~463cm^{-1}) peak bands increased. However, after the initial increase T^4 peak had a drop down, meanwhile T^6 was more sensitive to the changing pH and kept the increasing trend. The 778cm^{-1} peak also had an apparent jump, which was probably because of the decomposition of the complex structures

and the hydrolysis of the broken Si-O bonds. More H-O-Si-O-H structures were exposed therefore enhancing the vibration mode of this specific bond.

So, NaOH caused de-polymerisation of sodium silicate which could be easily traced from interpreting the Raman spectra. The appearing and disappearing of specific structures was determined by simply comparing the characterisation peaks individually. Different lower degree structures were obtained from the disintegration of high degree polymers, especially ring structures. Additionally, with more OH⁻ introduced, more Si-OH bonds were formed instead of Na-Si bonds during the process.

More detailed information has been achieved from the composition analysis after deconvolution of spectra. An initial fraction of each species was predicted, their subsequent composition variation along with the changing pH value was also calculated in a similar way, which was described in section 6.2.1 (Figure 6.19). The result was compared with the outcome obtained by employing the NMR model.
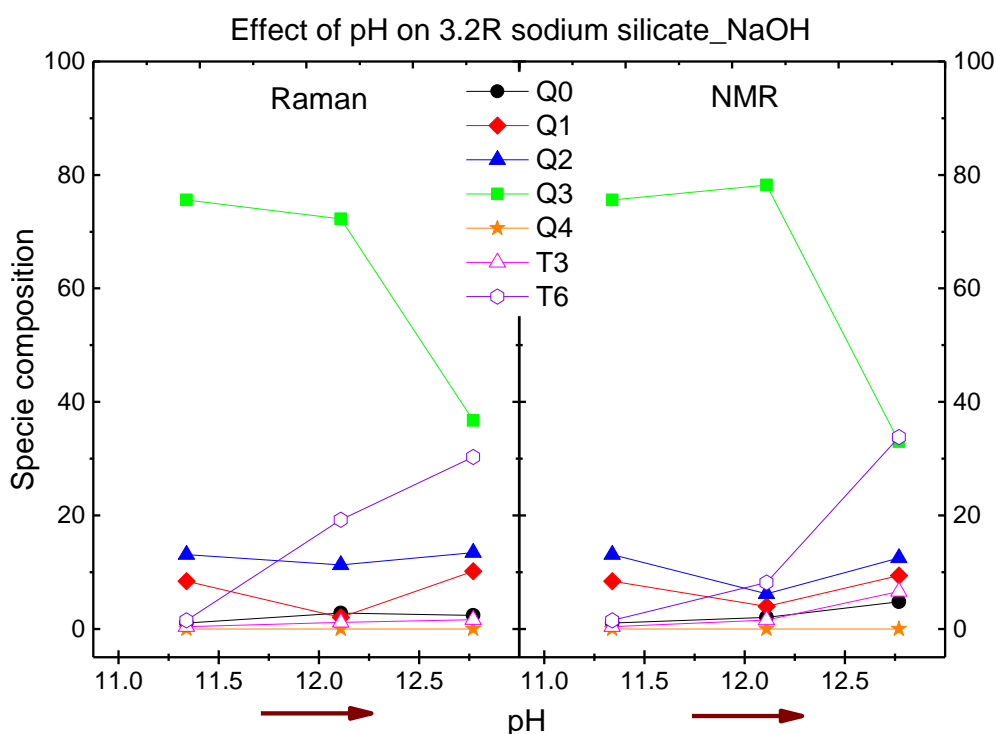

Figure 6.19: The pH impact on the speciation of 10 wt% 3.2 R sodium silicate solutions. (Note the NMR result was achieved by implementing the model which were given in (20). The Q^2 and Q^3 here equivalent to the symbol of Q^2_y and Q^3_y in (20)).

Initially, the presence of NaOH must help to break down the siloxane bonds in the chain Q^3 and/or the T^5 ring structures (according to Figure 6.18 and Figure 6.19 Raman data), so these structures disintegrated and converted to one or several short chain oligomers. Then, with more and more NaOH being introduced, the excessive amount of base would speed up the de-polymerisation, thereby accelerating the protonation process and achieving more $Si(OH)_4$, monomeric ions or low level of oligomer ions. All these structures could be reconnected with each other to form new polymers in different orders. Therefore, in Figure 6.19 an increasing trend was attained for T^6 and all other lower degrees of Q structures after pH's over 12. The Q^3 decreased significantly after this pH value, which suggests that the short chain structure requires a higher pH to depolymerise. The formation of ring structures in high alkaline solutions has also been discussed in (24).

There was a small disagreement between the Raman and NMR results, which is probably due to the Raman spectra being taken before solutions reached their equilibrium. The variation can also be caused by the differentiation of the initial raw materials.

6.2.4.2   Polymerisation of 1.6 R sodium silicate solutions

As discussed above, the de-polymerisation of the higher ratio silicates can be measured; the addition of H_2SO_4 into 1.6 R silicate solution was applied to acidify silicates to obtain polymeric species (i.e. long chain and/or cross-linked network of $[SiO_4]$ tetrahedral), which is an opposite process to depolymerisation.
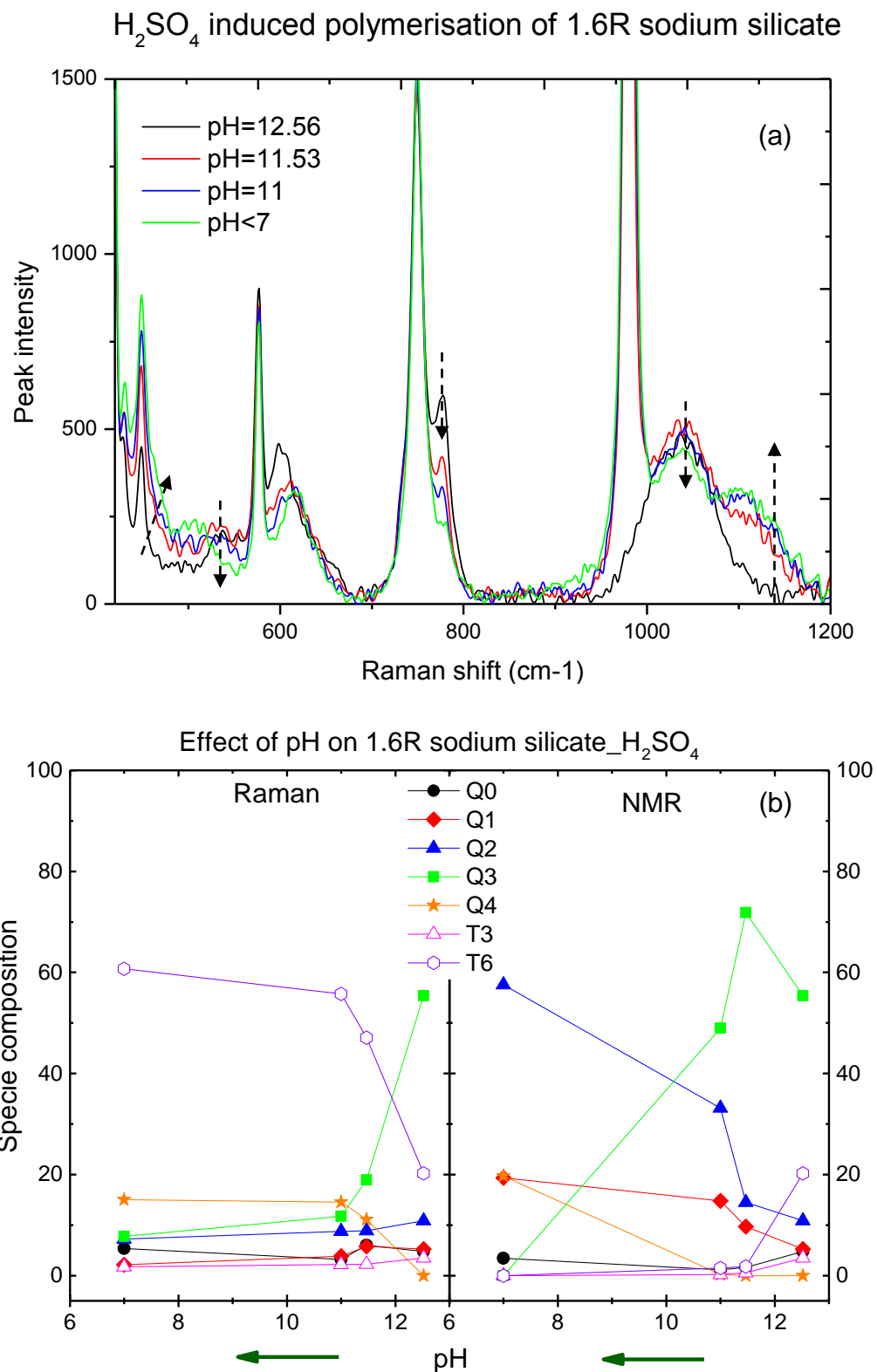
Figure 6.20: Effect of pH reduction by adding H₂SO₄ on the polymerisation of 1.6 R sodium silicate solution (10 wt%). (a) Raman spectra (b) variation of the composition of structures.

As shown in Figure 6.20, the initial pH of 10 wt% 1.6 R silicate is around 12.5 at 75°C, the pH started to decrease after the addition of H₂SO₄; at pH 11.5, a

dramatic decrease of Q^3 structure from ~55% to ~19% has been observed. In the meantime, an increase in the percentage of more complex structured Q^4 and T^6 were detected. Also, there was some minor decline in the composition of other simple structures, such as Q^2 & Q^3. Moreover, the decreasing in peak 778 cm^{-1} indicated a deprotonation process, through which the H-O bonds were broken down, then oligomer ions re-linked together to form longer or more complicated networks. Furthermore, due to the instability of T^3 in acid solutions, a decreasing trend can also be traced along this polymerisation process (24). Monomer almost remained at the same level in the comparison of the initial solution composition with the final state.

All the phenomena suggested that a low degree of polymers have begun to polymerise to the complex structures when pH decreased. A great amount of Q^4 was polymerised out when pH reached 11. Gelation occurred rapidly from further reducing the pH below 10.5; actually the Raman probe was not measuring a homogametic solution, but only the composition of the clear solution, which was surrounding the probe in Figure 6.21. Not changing pH showed no sign of decreasing the amount of gel formation, which indicates the system had reached equilibrium.
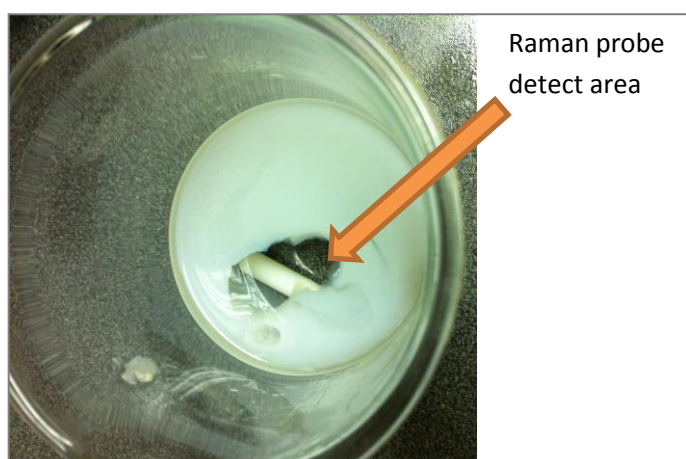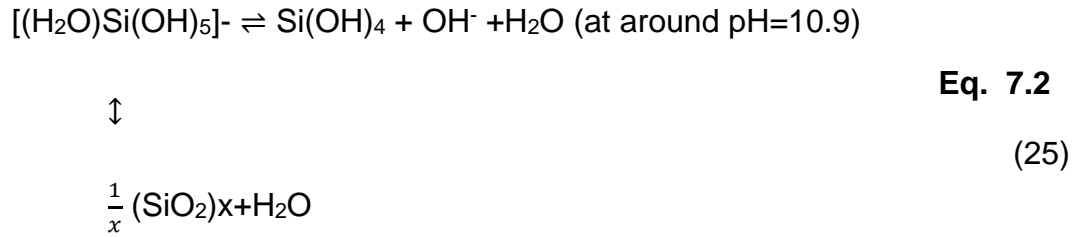

Figure 6.21: Polymerization of 1.6R sodium silicate solution (10wt%) after lower the pH below 10.5.

The neutralisation of soluble silicate solutions can be expressed as:

$$[(H_2O)Si(OH)_5]^- \rightleftharpoons Si(OH)_4 + OH^- + H_2O \text{ (at around pH=10.9)}$$

Eq. 7.2

(25)

$$\updownarrow$$

$$\frac{1}{x}(SiO_2)x + H_2O$$

The pH under which determined polymerisation occurs changes with the solution concentration (26). The polymerisation would occur very rapidly when the solution pH went below this critical value. This explains why the polymerisation was not able to catch step by step during the neutralisation of 10 wt% 1.6 R sodium silicate solution. Theoretically, the higher the solution concentration, the larger the critical pH would be achieved.

In Figure 6.20(b), there is a quite discrepancy between the Raman and NMR prediction. It must because the relative fast acid addition led to rapid polymerisation taking place, which gave no time for the solution to reach equilibrium in the short period. In the NMR prediction, a lower degree of polymer Q^1 and Q^2 appeared instead of the formation of T^6. However, in both cases a significant amount of Q^4 was generated at the end, which is the evidence that polymerisation occurred.

6.3 Conclusion

Investigation of the impact of solution conditions on Burkeite crystallisation was carried out. Three factors were considered in this section of the study, which were system water content, solution pH and (de-)polymerisation sodium silicates as well as the influence of silicate properties on the inorganic phase.

The water content had no significant impact on the percentage of Burkeite formation. However, a low water level was determined for the purpose of process feasibility of Burkeite formation. This finding would reduce the water usage significantly for producing slurries in the dry laundry industry, moreover, if needed by following the suggested optimal production method in this research, the solution can be recycled without limit for the following batch,

subsequently less energy would be required in the drying process. Ultimately, decreasing the capital of production.

The OOA was repeated, the outcome was consistent with the conclusion that was drawn in Chapter 4. Adding Na_2CO_3 first created an alkaline solution environment that accelerated the Burkeite crystallisation. Apart from using Na_2CO_3, the same result was also achieved by applying caustic soda to tune the solution pH before any inorganic addition. Smaller Burkeite crystals (<10 μm) were obtained from the high pH solutions, their aggregates possessed a high porosity and larger surface area. This product may be beneficial to the downstream processes in the dry laundry industry, such as high level of perfume or other additives pick up, or providing fast dissolution.

Furthermore, sodium silicate was chosen for study because of its high pH property and wide application in a variety of industries, especially in laundry production. First of all, the speciation of sodium silicate was explored by using the Raman spectroscopy technique. Moreover, the mutual influence between sodium silicate and inorganic salt were discussed. The solubility of sodium salt decreased dramatically with the increasing concentration of sodium silicate solutions because of the common ion effects and a relatively less amount of free water can be used for inorganic dissolution. On the other hand, sodium salt can induce sodium silicate polymerisation to occur, which may lead to more water associating with the high degree polymers, so having further adverse effects on both dissolution and crystallisation of sodium salts. Finally, in the interest of knowing more about the polymerisation and de-polymerisation of sodium silicates, temperature and pH effects were also studied.

The speciation study of sodium silicates would guide the selection of a suitable concentration and optimal process operation conditions for slurry mixing, in order to minimize the amount of unwanted high degree of polymers, accordingly reduction in the amount of residue, enhancing the dissolution of the final detergent powder.

Reference List

1.   Meenan, P. *Experimental and theoretical studies on the nucleation, growth and habit modification of some inorganic carbonates, phosphates and sulphates*. thesis, University of Strathclyde, 1992.

2.   Goldstein, J., Newbury, D.E., Echlin, P., Joy, D.C., Romig Jr, A.D., Lyman, C.E., Fiori, C. and Lifshin, E. *Scanning electron microscopy and X-ray microanalysis: a text for biologists, materials scientists, and geologists.* Springer Science & Business Media, 2012.

3.   Evans, E.H. and Knight, P.C. *Process for the preparation of a granular detergent composition*. Google Patents. 1989.

4.   Atkinson, C., Heybourne, M.J., Iley, W.J., Knight, P.C., Russell, P.J., Taylor, T. and Jones, D.P. *Process for preparing needle-shaped crystal growth modified burkeite detergent additive*. Google Patents. 1990. Available from: https://www.google.be/patents/US4900466

5.   Grace, T.M. Solubility limits in black liquors. 1975.

6.   Tran, H. and Earl, P.F. Chloride and potassium removal processes for kraft pulp mills: a technical review. In: *International Chemical Recovery Conference, TAPPI/PACTAC, Charleston, SC*, 2004.

7.   Shaikh, A.A., Salman, A.D., Mcnamara, S., Littlewood, G., Ramsay, F. and Hounslow, M.J. In situ observation of the conversion of sodium carbonate to sodium carbonate monohydrate in aqueous suspension. *Industrial & Engineering Chemistry Research.* 2005, **44**(26), pp.9921-9930.

8.   *Types of Agitators.* [Online]. [Accessed].

9.   Uchino, T., Sakka, T. and Iwasaki, M. Interpretation of hydrated states of sodium silicate glasses by infrared and Raman analysis. *Journal of the American Ceramic Society.* 1991, **74**(2), pp.306-313.

10.   Brawer, S. Theory of the vibrational spectra of some network and molecular glasses. *Physical Review B.* 1975, **11**(8), p.3173.

11.   Brawer, S.A. and White, W.B. Raman spectroscopic investigation of the structure of silicate glasses. I. The binary alkali silicates. *The Journal of Chemical Physics.* 1975, **63**(6), pp.2421-2432.

12.   Furukawa, T., Fox, K.E. and White, W.B. Raman spectroscopic investigation of the structure of silicate glasses. III. Raman intensities and structural units

in sodium silicate glasses. *The Journal of Chemical Physics.* 1981, **75**(7), pp.3226-3237.

13. Malfait, W.J. Quantitative Raman spectroscopy: speciation of cesium silicate glasses. *Journal of Raman Spectroscopy.* 2009, **40**(12), pp.1895-1901.

14. McMillan, P. Structural studies of silicate glasses and melts—applications and limitations of Raman spectroscopy. *American Mineralogist.* 1984, **69**(7-8), pp.622-644.

15. Mysen, B.O. and Frantz, J.D. Raman spectroscopy of silicate melts at magmatic temperatures: Na2O☐ 1bSiO2, K2O☐ 1bSiO2 and Li2O☐ 1bSiO2 binary compositions in the temperature range 25–1475° C. *Chemical Geology.* 1992, **96**(3-4), pp.321-332.

16. Mysen, B.O., Virgo, D. and Scarfe, C.M. Relations between the anionic structure and viscosity of silicate melts—a Raman spectroscopic study. *Am. Mineral.* 1980, **65**(7-8), pp.690-710.

17. Vidal, L., Joussein, E., Colas, M., Cornette, J., Sanz, J., Sobrados, I., Gelet, J., Absi, J. and Rossignol, S. Controlling the reactivity of silicate solutions: A FTIR, Raman and NMR study. *Colloids and Surfaces A: Physicochemical and Engineering Aspects.* 2016, **503**, pp.101-109.

18. Neuville, D. and Cormier, L. Structure of Na2O-CaO-Al2O3-SiO2 glasses using Raman spectroscopy.

19. Halasz, I., Agarwal, M., Li, R. and Miller, N. Vibrational spectra and dissociation of aqueous Na2SiO3 solutions. *Catalysis Letters.* 2007, **117**(1-2), pp.34-42.

20. Svensson, I.L., Sjöberg, S. and Öhman, L.-O. Polysilicate equilibria in concentrated sodium silicate solutions. *Journal of the Chemical Society, Faraday Transactions 1: Physical Chemistry in Condensed Phases.* 1986, **82**(12), pp.3635-3646.

21. Halasz, I., Agarwal, M., Li, R. and Miller, N. Monitoring the structure of water soluble silicates. *Catalysis Today.* 2007, **126**(1), pp.196-202.

22. Bass, J.L. and Turner, G.L. Anion distributions in sodium silicate solutions. Characterization by 29Si NMR and infrared spectroscopies, and vapor phase osmometry. *The Journal of Physical Chemistry B.* 1997, **101**(50), pp.10638-10644.

23. Pasquarello, A. and Car, R. Identification of Raman Defect Lines as Signatures of Ring Structures in Vitreous Silica. *Physical Review Letters.* 1998, **80**(23), pp.5145-5147.

24. Andersson, K.R., Dent Glasser, L.S. and Smith, D.N. Polymerization and colloid formation in silicate solutions. In, 1982.

25. Iler, R.K. The colloid chemistry of silica and silicates. *Soil Science.* 1955, **80**(1), p.86.

26. Halasz, I., Agarwal, M., Li, R. and Miller, N. What can vibrational spectroscopy tell about the structure of dissolved sodium silicates? *Microporous and Mesoporous Materials.* 2010, **135**(1–3), pp.74-81.

Chapter 7 Conclusions and Suggestions for Future Work

This chapter summarises the outcomes of this work, confronts the results with initial scopes, also how these findings will benefit the process production and improve the quality of final products. At the end of this chapter, some possible work that can be delivered in the future is outlined.

7.1 Conclusion

This work has investigated the feasibility of an in-situ Raman spectroscopy technique for simultaneously determining the concentration of multiple components presented in their different phases. Na_2CO_3 and Na_2SO_4 solution and slurry system were chosen to study, because of their wide application in the detergent industries. Additionally, based on the in-situ technique, the impact of process and solution conditions on the properties (such as composition and phase transformation) of Na_2CO_3-solution-Na_2SO_4 was investigated.

7.1.1 Raman Calibration Model Establishment

The solution and slurry concentration of sodium carbonate (Na_2CO_3), sodium sulphate (Na_2SO_4) and one of their double salts, Burkeite were detected in aqueous solutions using an in-situ Raman spectroscopy technique. Calibration models were developed for the five species, which were Na_2SO_4 solution and solid phase, Na_2CO_3 solution and solid phase and Burkeite solid phase. Sodium carbonate monohydrate ($Na_2CO_3 \cdot H_2O$) was applied for the solid model development of Na_2CO_3 due to Na_2CO_3 being anhydrous and very unstable when in contact with water (Figure 2.6). The subsequent validation experiment demonstrated how Raman spectroscopy could be utilised to detect the compositions and phases of Na_2CO_3 and Na_2SO_4 in a complex multi-component mixture, in both slurry phases and dry powder form.

An X-ray diffraction approach was applied for verifying the reliability of Raman calibration models. A potting method and Rietveld refinement were firstly developed and applied for reducing or eliminating the artificial effects caused

by particular geometric crystals (i.e. needle-like, plate-like) orientation preference in XRD measurements. Then, the verification of Raman calibration models was carried out by comparing the PLS monitoring outcomes of the final slurry composition with the quantitative analysis results from XRD Rietveld refinement on the dried filtrated product from each experiment. A good agreement was obtained from these two methods with a deviation smaller than 5 wt% on each substance, which indicated the reliability of the PLS models.

Additionally, the calibration model developed was then applied to study the impact of raw material mass ratio and their sequence of addition on the final composition of Na_2CO_3-H_2O-Na_2SO_4 slurry systems. The result was that introducing Na_2CO_3 before Na_2SO_4 to the system at the mass ratio of Na_2CO_3: Na_2SO_4=1:3 would lead to the least amount of raw materials remaining in the system. Instead, their double salt Burkeite became the dominant solid phase in the mixture. The formation of Burkeite may increase the final product stability because Burkeite has no hydrate form, the inorganic phase in the final product will not absorb water from ambient, therefore fewer lumps of agglomerates would occur during storage, furthermore improving product life time.

A calibration model for solid mixture systems was also developed. An example was given in Chapter 4 showing the high feasibility of applying this model to analysing the composition of solid mixtures. However, a density correction factor was required to determine between the calibration sample and the mixture that needs to be analysed. The application of this solid mixture model can also be extended to amorphous composition estimation.

Overall, applying the in-situ quantitative analysis model provided an access to gaining an insight to all variations in the slurry during process operation, which overcame the downside of previous research. Product formulation and process operation procedures, such as the input pattern of raw materials, mixing time or efficiency, can therefore be optimised in accordance with the profile from real-time monitoring. The method of offline accessing the composition of solid mixtures had great potential for tracking the impact of storage conditions on product performance, such as stability or flowability.

Both in-line and off-line modelling techniques can also be applied to other industries, such as pharmaceutical or food science, on polymorphism phase transition or amorphous to crystalline transition.

7.1.2 Isothermal Ternary Phase Diagram of Na_2CO_3-H_2O-Na_2SO_4 Determination and Kinetic Studies on Burkeite Crystallisation

Chapter 5 demonstrated a novel method to establish a ternary phase diagram by using in-situ Raman spectroscopy with the aid of the PLS calibration technique. The phase diagram accomplished offered a fast access to evaluate the constituent of any Na_2CO_3-Na_2SO_4-water mixture at 75^oC. With the understanding of the phase diagram, it was easy to achieve a high-quality product by just simply manipulating the process conditions, such as the ratio between raw materials. This method greatly reduced the time that is required for establishing a multiple component phase diagram, providing a better opportunity to reveal and understand how the process operation conditions impact on the final production composition. In addition, this new methodology provides the fundamental information for further studies, such as by controlling the kinetics to manipulate the Burkeite morphology and growth. The expanding application of the analytical technique could also give more benefit for the process industries.

FBRM was not a favourable method for detecting crystallisation and particle size distribution of irregular and/or a high degree of aggregation crystals, for instance Burkeite crystals in this research. An in-process video microscopy device was suggested.

Industrial process precipitate crystals (Burkeite) isothermally form the solution system while raw materials are dissolving, which makes the kinetic study using the conventional measurement of induction time unfeasible, because of the co-existence of multiple component particles in the system and the varying degree of supersaturation prior to the precipitation of desired crystals. The modified KBHR method was attempted to apply to this isothermal crystallisation system. The kinetic studies on Burkeite crystallisation suggested that an instantaneous nucleation may be obtained from these particular experiments. The plot of experimental results indicated the feasibility of applying this modified KBHR approach. However, more derivation

needs to carried out to achieve the right parameters for determining the nucleation mechanism. By completing the deviation, it will become a novel method for studying nucleation kinetics of systems in the same manner (i.e. isothermal, crystallisation of the new phase depending on the supersaturation degree and composition of the mother liquid).

7.1.3 The Impact of Solution Conditions on the Phase Transition of the Sodium Silicate Involved Inorganic System

The level of water content had no significant impact on the composition of the Na_2CO_3 and Na_2SO_4 slurry system. A low water level was determined for the purpose of process feasibility for Burkeite formation. This achievement would reduce the overall amount of water requirement in dry detergent production. If the raw material applied followed a mass ratio of Na_2CO_3 to Na_2SO_4 equal to 1:3, besides introducing Na_2CO_3 prior to Na_2SO_4 salt, then the mother liquid could be recycled for the next batch of reaction continuously. This action would dramatically reduce energy usage and waste, as well as decreasing the overall cost of the production.

The high pH solution condition can accelerate Burkeite precipitation from slurry systems, particles achieved from this condition were small in size (less than $10\,\mu m$) and presented a low degree of aggregation and high level of porosity. This morphology was the desirable for picking up other solvents or additives in next step of production, such as perfume or bleach.

However, high pH sodium silicate solutions demonstrated an opposite influence on Burkeite formation, which is attributed to high sensitivity of sodium silicate speciation. It varied with solution concentration, pH, temperature and the concentration or classes of cations and anions. The high degree of polymers formed would trap water from the system to a certain extent, therefore leaving less free water to participate in dissolving or crystallising inorganic salts. Also, the sodium salt present caused the polymerisation of silicate solutions, through which process more sodium ions became free, therefore inhibiting the dissolution of sodium salt.

A speciation study was also conducted on the sodium silicate system using a Raman spectroscopy technique combined with the peak decomposition

method. The result presented a high consistency with the NMR study from previous researchers (1). Hence, using Raman spectroscopy to analyse the speciation of sodium silicates can potentially substitute the NMR method with the advantage of being less time consuming.

7.2 Review of Aims and Objectives

Considering the original aims and objectives of the project, this study has proved the in-situ Raman technique was a feasible and reliable technique for simultaneous quantitative analysis of the composition of each species in a multi-component system. The models developed have contributed to phase diagram determination, Burkeite kinetics studies, the process operation and solution conditions effect on the inorganic slurry system.

Some objectives have not been met or reached the desirable depth. For instance, on the Burkeite nucleation study, the experiments could be designed more comprehensively and equations should be derived for the current experimental conditions.

However, some additional discoveries were made during the research. A significant potential for the application of Raman spectroscopy can be seen. Furthermore, outcomes from this research provided marked contributions for the current dry laundry industry from different aspects.

7.3 Suggestion for Future Work

Some work involved in this research is worthy of more extensive exploration.

❑ The Application of the Solid Mixture Calibration Model

The calibration model of the solid mixture can be applied to investigating the impact of experimental, process or storage conditions on the solid phase transition, such as polymorphic phase transition, amorphous to crystalline phase transition, anhydrous to hydrate phase transition or vice versa. The kinetics of phase transformation can be determined through this approach. Additionally, the experimental process can be optimised accordingly.

❑ **Raman Spectroscopy on the Organic Phase Phases**

Many organic materials have also been intensively applied to the detergent industry. The Raman technique may also be applied to the phase transition behaviour of organic phases. An example is given below showing the feasibility of Raman on the Linear Alkylbenzene Sulphonate (LAS).
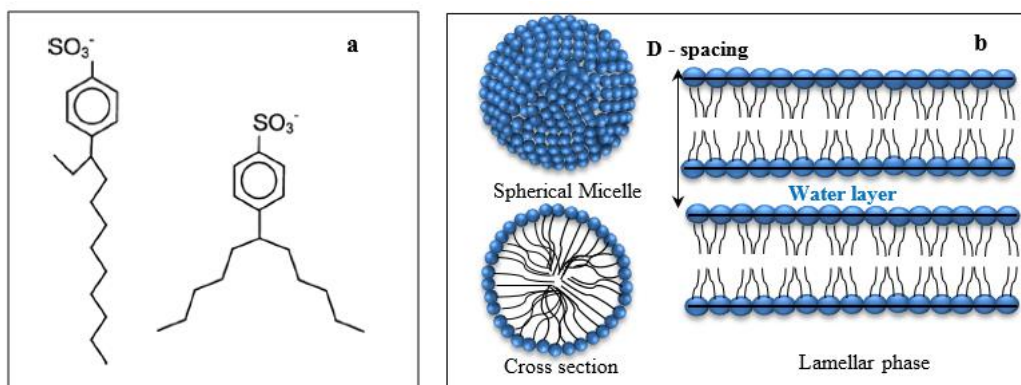

Figure 7.1: LAS in 3 and 6 positional isomers (2); b: L_1 (micelle phase) and Lα (lamellar phase, liquid crystal) structure

In aqueous solution, LAS usually presents in a mixture of L_1 (micelle phase) and Lα (lamellar phase, liquid crystal) over of wide range of compositions, Figure 7.1. The effect that LAS solution concentration and temperature have on phase composition and transition were considered.

Figure 7.2 illustrates a Raman spectrum of LAS at 20% concentration. Peak 1600cm^{-1} and 2854cm^{-1} both represent the existence of the L_1 phase.
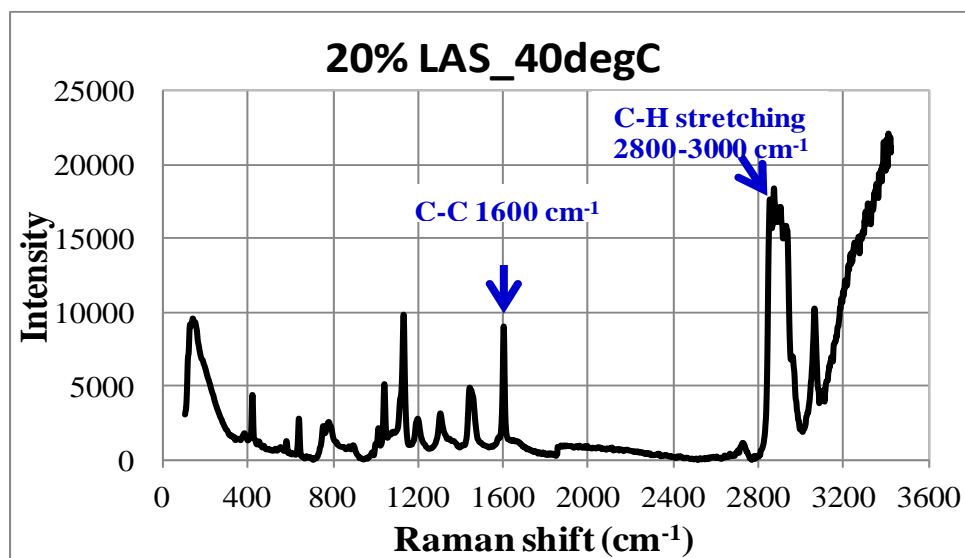
Figure 7.2: Raman spectrum of 20% LAS at 40°C.

Firstly, the impact of LAS solution concentration on the composition of L_1 and $L\alpha$ phases was studied. Figure 7.3 (right) shows the composition of L_1 increased linearly with the solution concentration when the solution concentration was below 30 wt%. Above 30 wt% the intensity of both peaks displayed a decreasing tendency, which illustrates more $L\alpha$ presence in the system. Therefore, ~30 wt% would be the transition point for L_1 converting to $L\alpha$, which is consistent with the information that was obtained by Stewart Figure 7.3 (left).
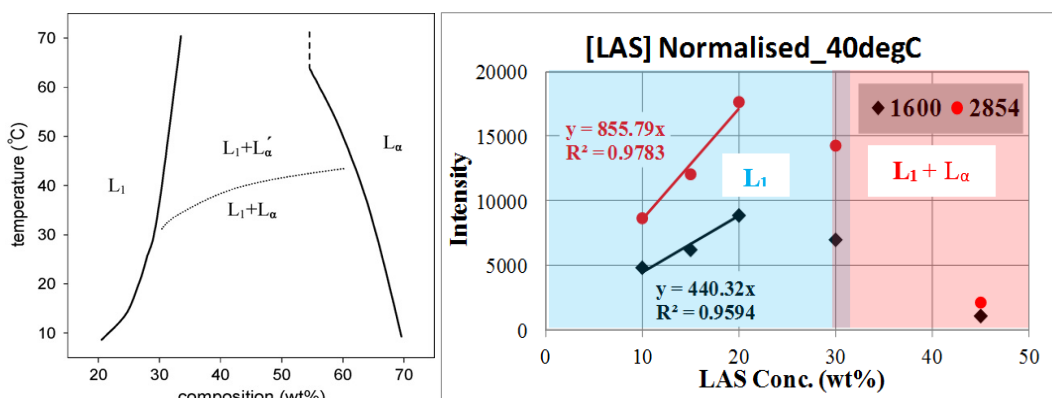
Figure 7.3: Phase diagram of LAS of using DSC (left) (2), and the intensity vs. LAS concentration of peak 1600 and 2845cm^{-1}.

The reference diagram also demonstrates that the transition LAS concentration increased with temperature. In Figure 7.4, for 10-20 wt% the data for both temperatures almost overlapped each other. Therefore the phase composition in this region is independent of the temperature. For the

higher concentration cases, the intensity of both peaks is significantly higher at 75ºC than 40ºC. In addition, the intensity of 30 wt% LAS can be fitted into the linear relationship with other lower concentrations. This suggests that 30 wt% is the L_1 phase at 75ºC that agrees well with the reference diagram.
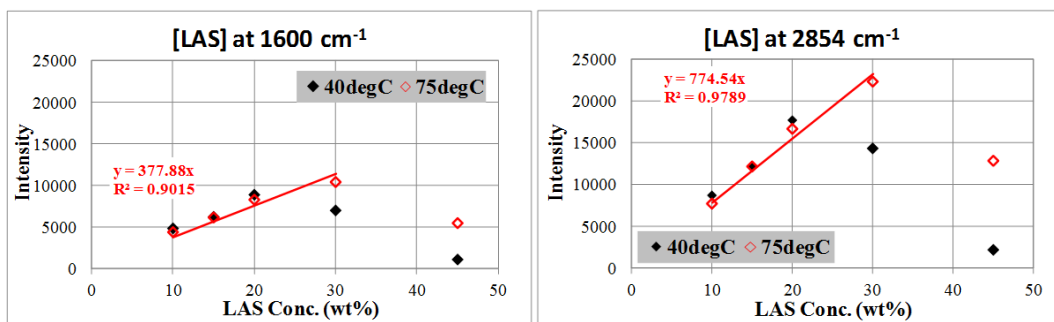
Figure 7.4: Effect of temperature (i.e. 40ºC and 75ºC) and LAS concentration on the intensity at 1600 cm^{-1} and 2584 cm^{-1}.

The two examples given above demonstrate the feasibility of using the Raman technique for the organic study. Further studies can focus on quantitatively predicting the composition of L_1 and $L\alpha$ phases, or the impact of other factors on the phase trasition in LAS solutions.

Reference List

1. Halasz, I., Agarwal, M., Li, R. and Miller, N. Vibrational spectra and dissociation of aqueous Na2SiO3 solutions. *Catalysis Letters.* 2007, **117**(1-2), pp.34-42.

2. Stewart, J., Saiani, A., Bayly, A. and Tiddy, G. Phase Behavior of Lyotropic Liquid Crystals in Linear Alkylbenzene Sulphonate (LAS) Systems in the Presence of Dilute and Concentrated Electrolyte. *Journal of Dispersion Science and Technology.* 2011, **32**(12), pp.1700-1710.

Appendix

1. Peak Separation by Fityk

The peak separation was completed by using Fityk software, the operation procedure of this action is given down below. The deconvolution of the spectrum of 43g Na_2CO_3 in 100g water is chosen as an example.

Frist of all, the baseline offset is applied to the subject spectrum, the original spectrum is indicated in green. Then, zoom to the area/peak of interest.

Secondly, peak(s) can be added by releasing the mouse under the target peak band.

Thirdly, select a peak fitting profile (i.e. Voigt, Gaussian or Lorentzian) and click "run" to process the peak fitting. The parameters of each peak fitted are given at the right corner of the operating window, which includes peak position, height, width, shape and the area under each peak.
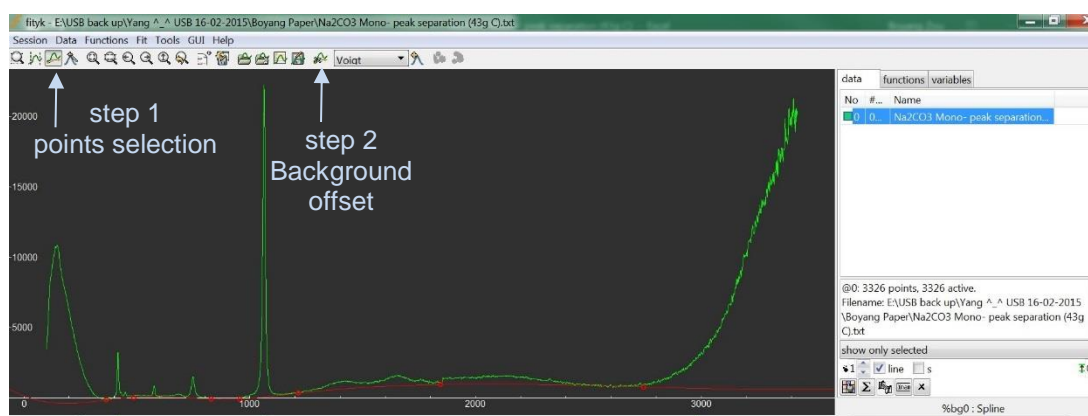
Figure 0.1: Spectrum baseline offset by Fityk software
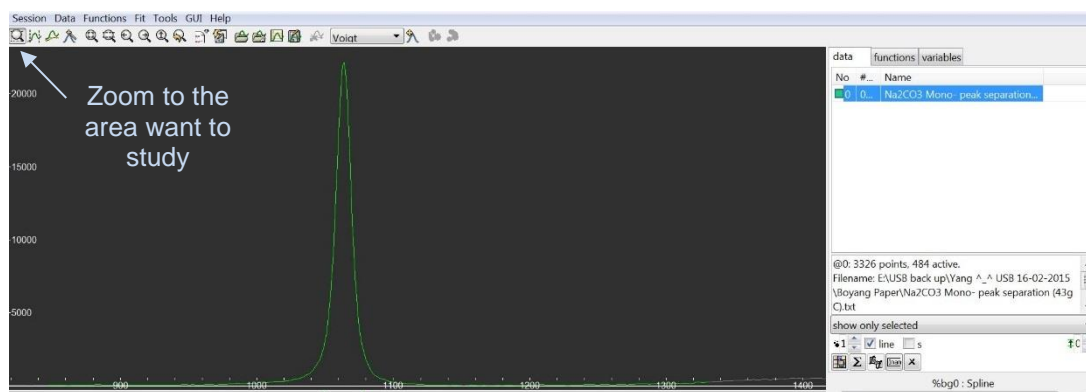
Figure 0.2: Peak area zoom in (Fityk software)
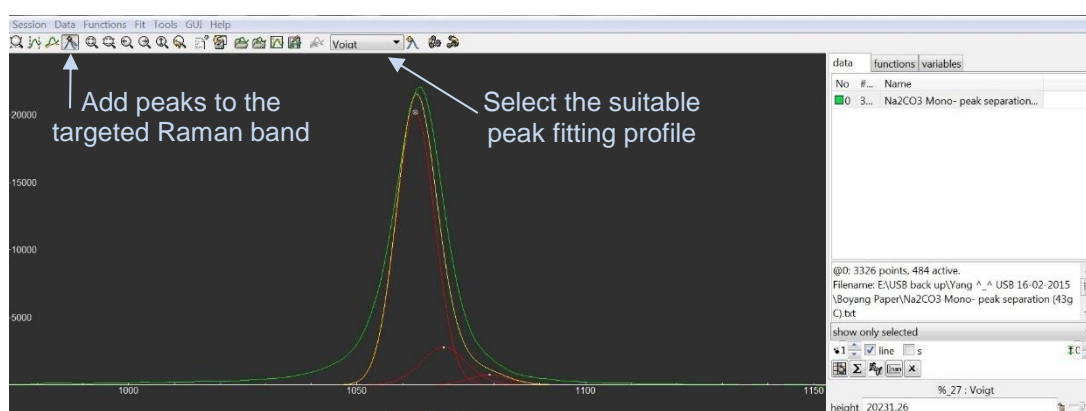
Figure 0.3: Choosing a peak fitting profile and adding peaks to the selected peak band
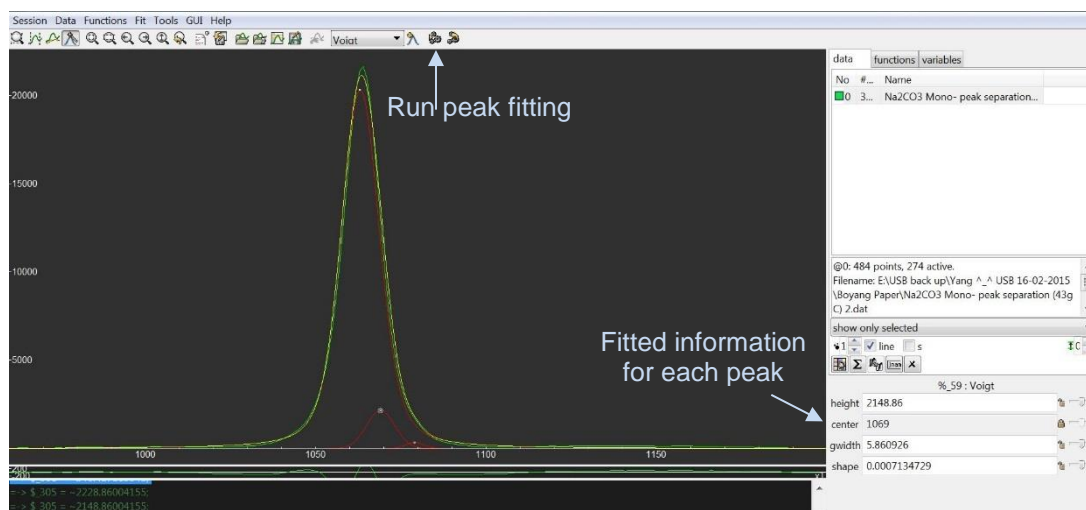
Figure 0.4: Run program to complete the peak deconvolution process

2. Validation of PLS models for Na_2CO_3 solution and slurry systems

The dissolution and adding of solid in the slurry experiments was repeated, and the PLS model was applied for on-line monitoring of the solution and slurry composition change for each addition. The result for Na_2CO_3 system is displayed in the figure below. The material was added at the beginning of each step and each plateau stands for the waiting time before the next addition. Beyond the solution saturated state, keep adding Na_2CO_3 will lead the of precipitation $Na_2CO_3 \cdot H_2O$, meanwhile, the volume percentage of Na_2CO_3 solution phase decreased. The predicted concentration was aligned with the actual amount of added materials; this consistency indicated the predictive accuracy of the Na_2CO_3 PLS models.
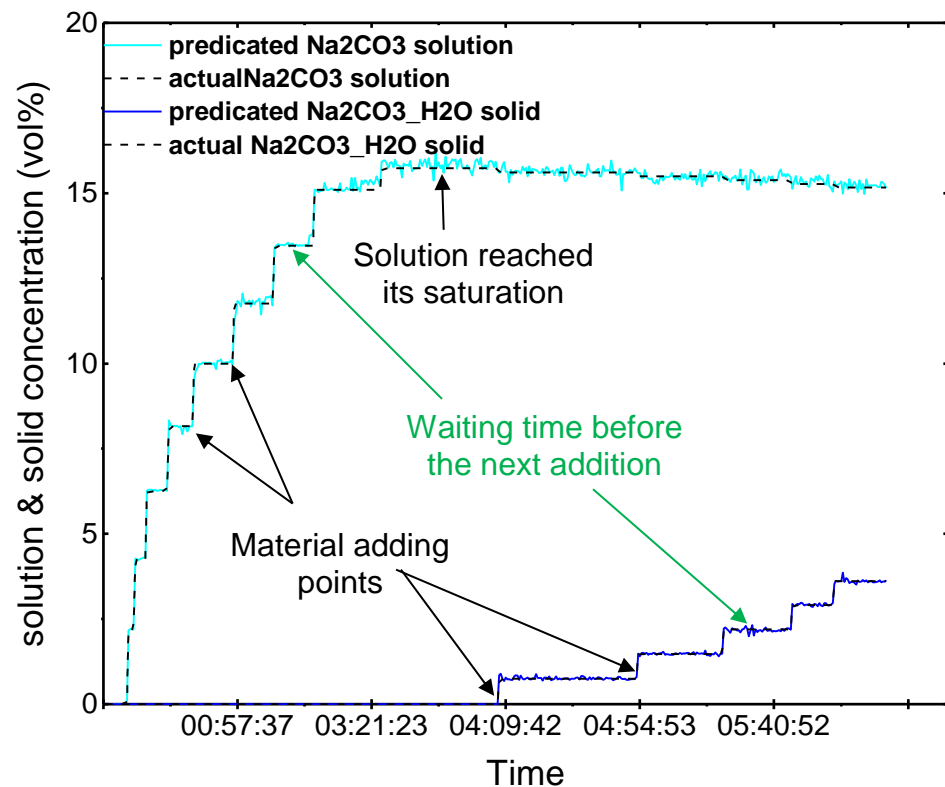
Figure 0.5: Validation of the PLS model by on-line detecting Na_2CO_3 dissolution and precipitation process. Blue solid lines illustrate predicted concentration from PLS model. The black dashed lines stand for the actual amount of Na_2CO_3 introduced in each addition

3. **Experiments for boundary lines determination of the Na_2CO_3-H_2O-Na_2SO_4 ternary phase diagram at 75°C**
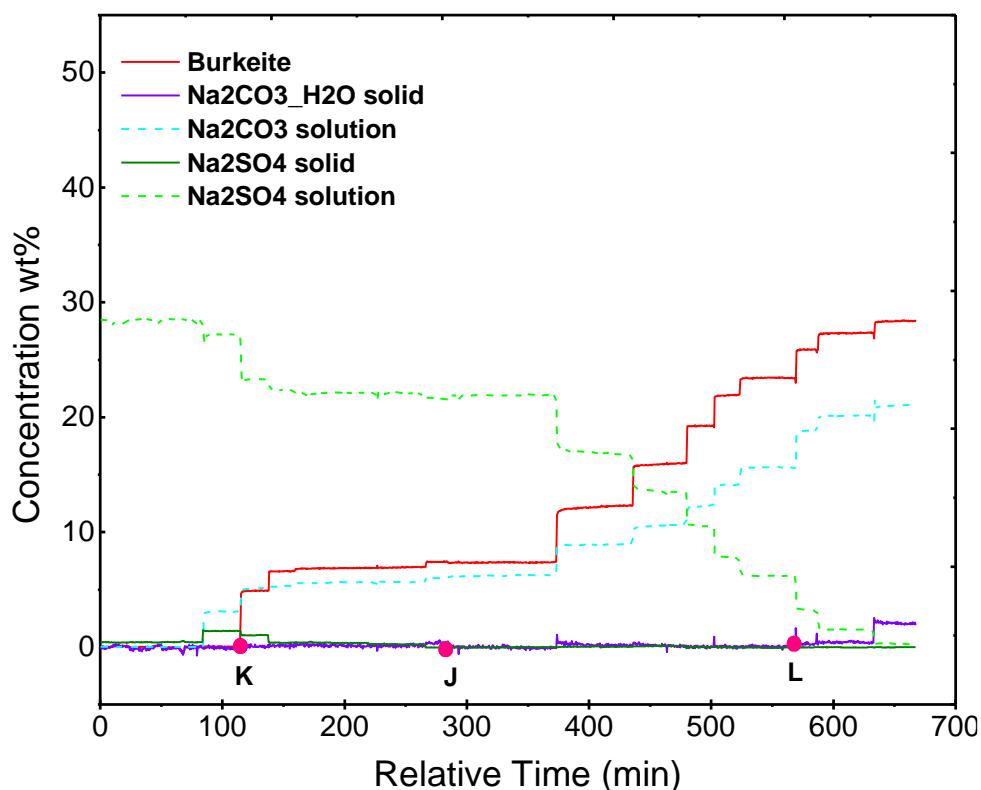
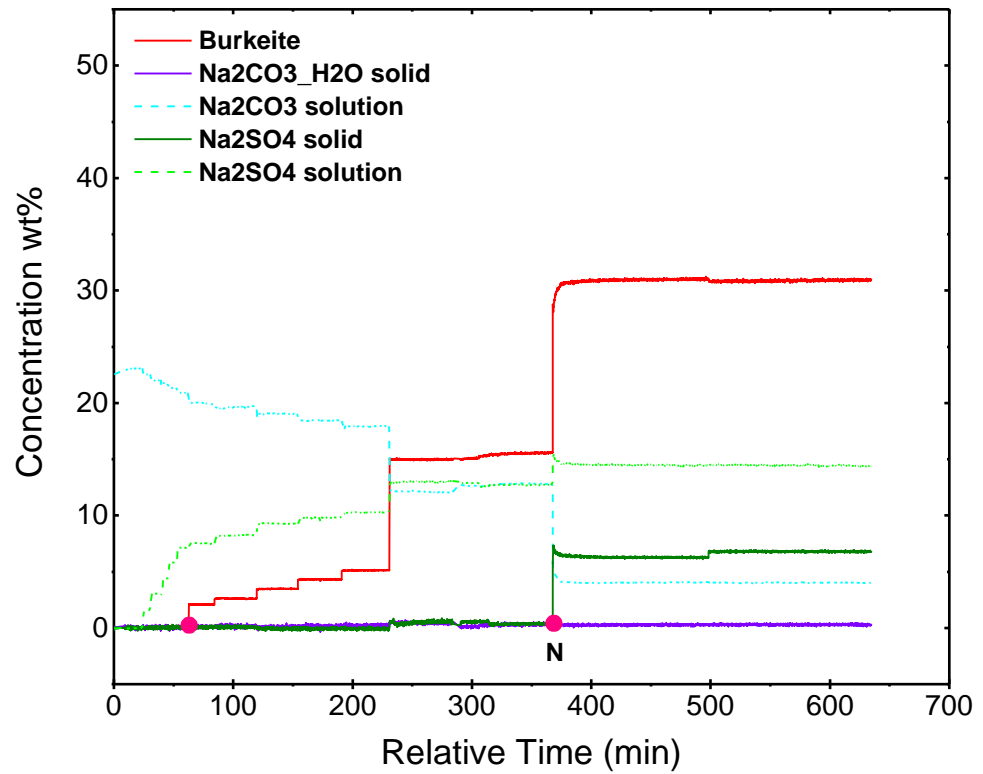**Figure 0.6: Ternary phase diagram boundary determination experiment. Real-time PLS analysis of the changing composition, while incrementally adding Na_2CO_3 into an aqueous solution system that originally contained 29.58wt% of Na_2SO_4 (corresponding to the green line in Figure 5.7). Each plateau represents the waiting time for the system to reach equilibrium; Na_2CO_3 was introduced to the system at the end of each plateau. K, J & L are the phase transition points, the phase composition of the system are different before and after this point (addition of Na_2CO_3), such as a new phase appearing or the present phase disappearing (see Figure 5.7). The change in spectra is displayed in Figure 0.7.**
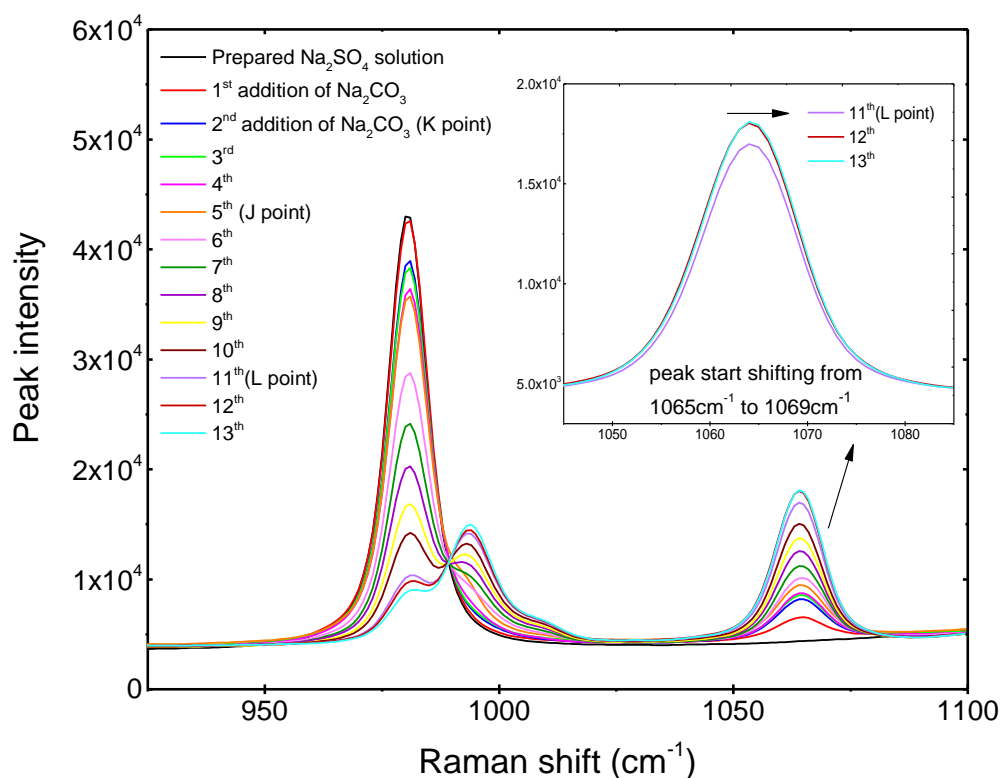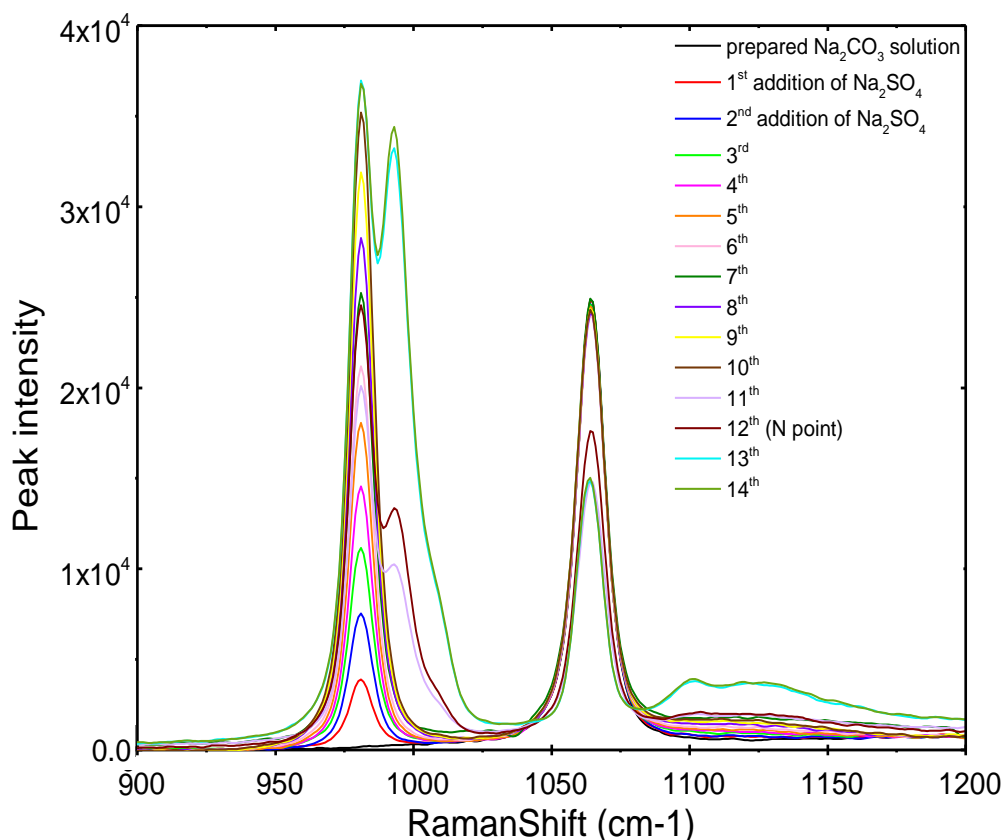
Figure 0.7: Raman spectra of incrementally adding Na_2CO_3 into an aqueous solution system that originally contained 29.58 wt% of Na_2SO_4. Each spectrum indicates the equilibrium state after the corresponding addition of Na_2CO_3. The phase transition points K, J & L can correlate with Figure 0.7 and Figure 5.7. After the 11th addition of Na_2CO_3, peak $1065 cm^{-1}$ starts shifting toward $1069 cm^{-1}$, which illustrates the precipitation of $Na_2CO_3 \cdot H_2O$.
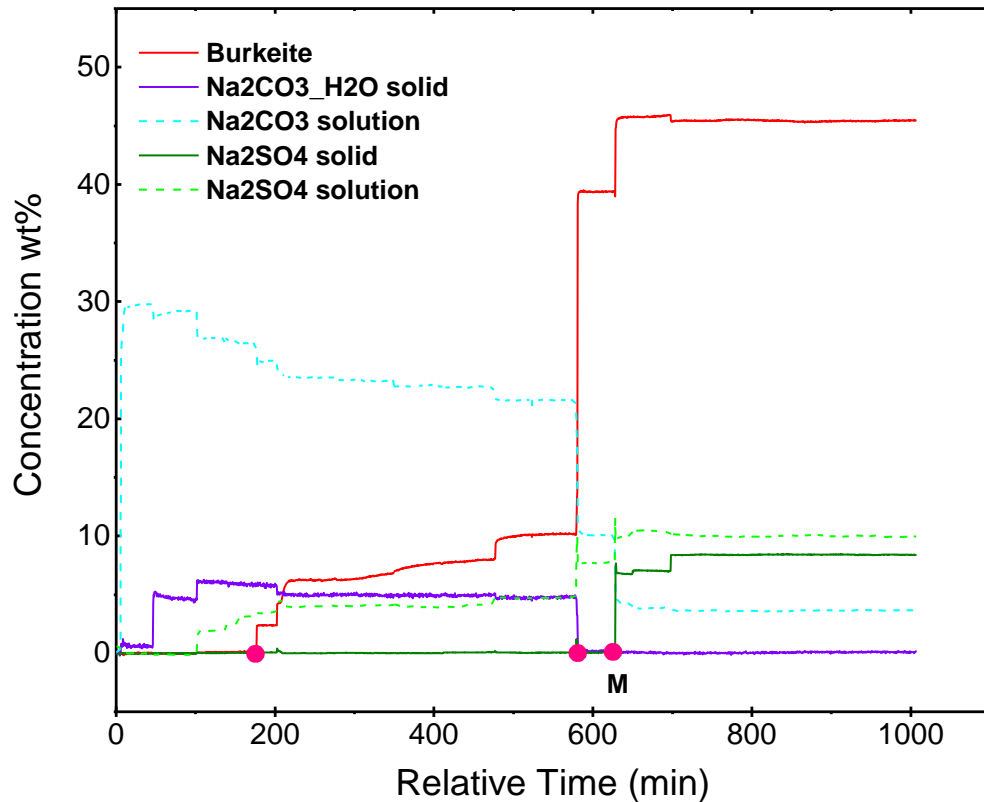
Figure 0.8: Ternary phase diagram boundary determination experiment.
Real-time PLS analysis of the changing composition, while
incrementally adding Na₂SO₄ into an aqueous solution system that
originally contained 23.08wt% of Na₂CO₃ (corresponding to the
orange line in Figure 5.7). Each plateau represents the waiting time
for the system to reach equilibrium; Na₂SO₄ was introduced to the
system at the end of each plateau. The pink points (i.e. N) are the
phase transition points, the phase composition of the system are
different before and after this point (addition of Na₂SO₄), such as a
new phase appearing or the present phase disappearing (see
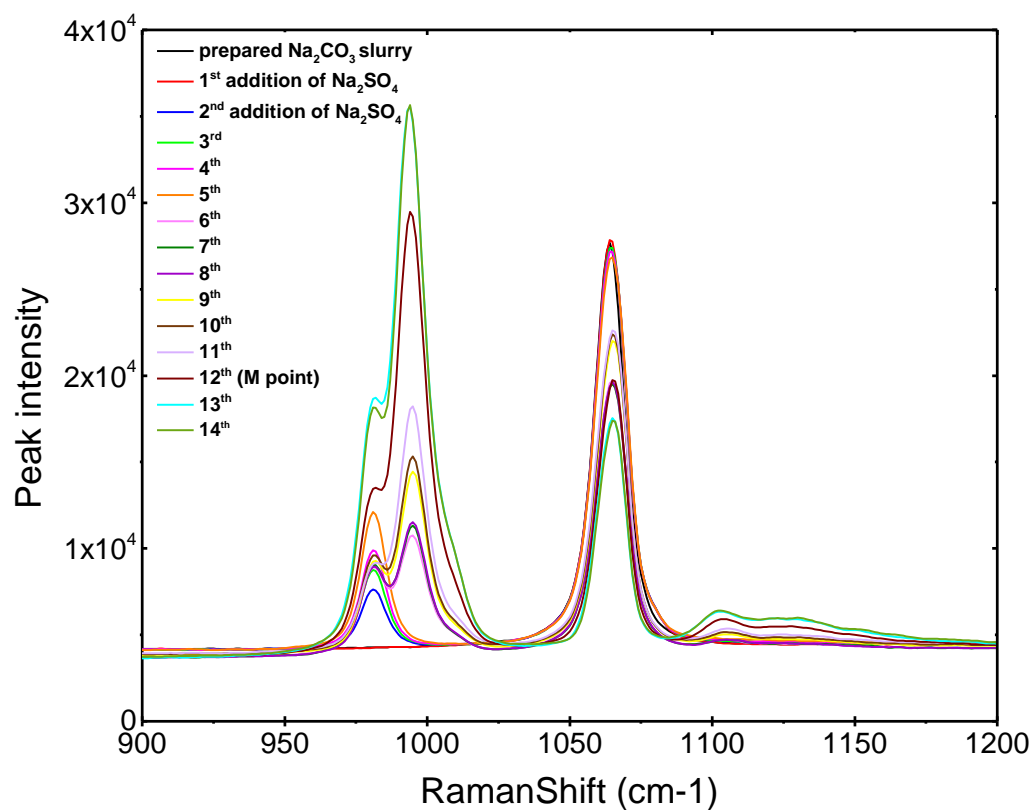**Figure 5.7). The change in spectra is displayed in Figure 0.9.**

Figure 0.9: Raman spectra of incrementally adding Na₂SO₄ into an aqueous solution system that originally contained 23.08 wt% of Na₂CO₃. Each spectrum indicates the equilibrium state after the corresponding addition of Na₂SO₄. The phase transition point N can correlate with Figure 0.8 and Figure 5.7. After the 12th addition of Na₂SO₄, a significant increase in the peak intensity around 993 cm⁻¹ indicates a great amount of Na₂SO₄ presenting in the solution.

Figure 0.10: Ternary phase diagram boundary determination experiment.
Real-time PLS analysis of the changing composition, while
incrementally adding Na$_2$SO$_4$ into an aqueous solution system that
originally contained 33.33wt% of Na$_2$CO$_3$ (corresponding to the blue
line in Figure 5.7). Each plateau represents the waiting time for the
system to reach equilibrium; Na$_2$SO$_4$ was introduced to the system
at the end of each plateau. The pink points (i.e. N) are the phase
transition points, the phase composition of the system are different
before and after this point (addition of Na$_2$SO$_4$), such as a new
phase appearing or the present phase disappearing (see Figure 5.7).
The change in spectra is displayed in Figure 0.11.

Figure 0.11: Raman spectra of incrementally adding Na₂SO₄ into an aqueous solution system that originally contained 33.33 wt% of Na₂CO₃. Each spectrum indicates the equilibrium state after the corresponding addition of Na₂SO₄. The phase transition point M can correlate with Figure 0.10 and Figure 5.7**. After the 11ᵗʰ addition of Na₂SO₄, a significant increase in the peak intensity around 993 cm⁻¹ indicates a great amount of Na₂SO₄ presenting in the solution.**

4. Inorganic salts in sodium silicate systems

The enlarge figures of Figure 6.13 and Figure 6.14 are given here to show the significance in peak intensity changes with the addition of different amount of sodium salts.
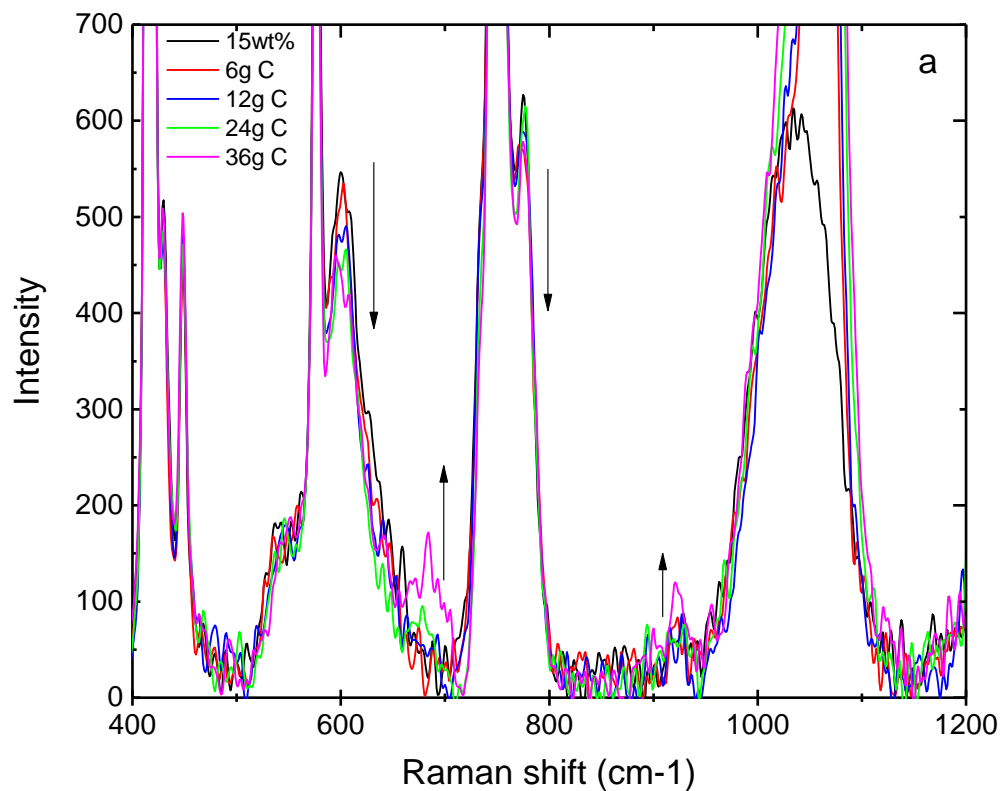
Figure 0.12: The impact of 15wt% of Na₂CO₃ on 1.6R sodium silicate solution polymerisation.
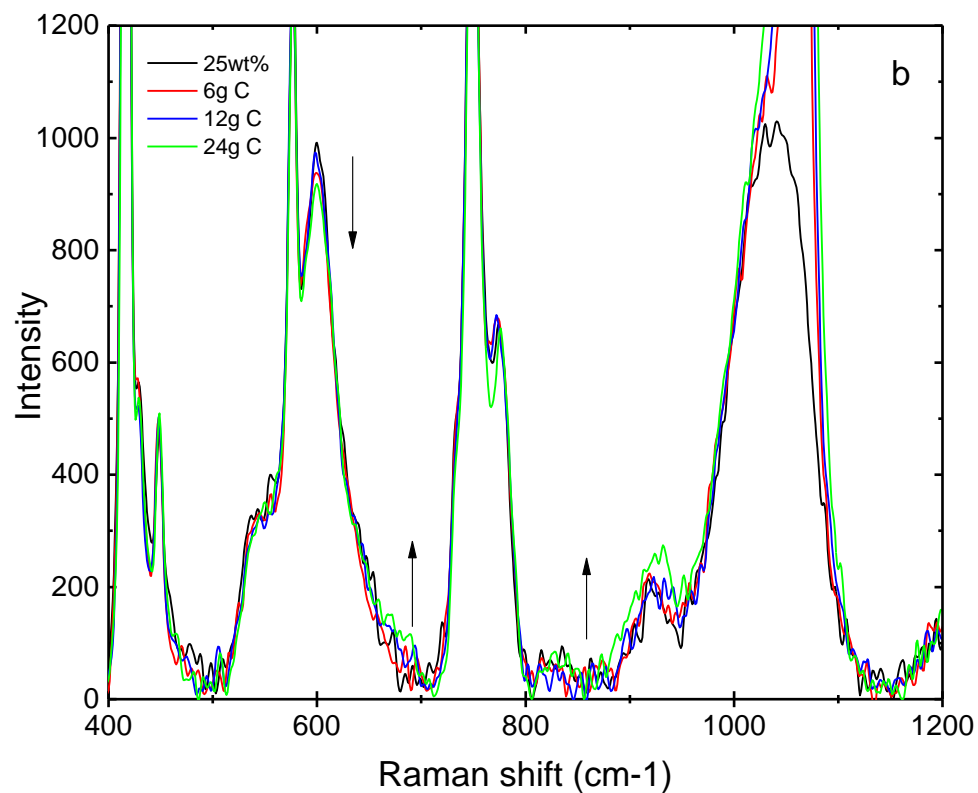
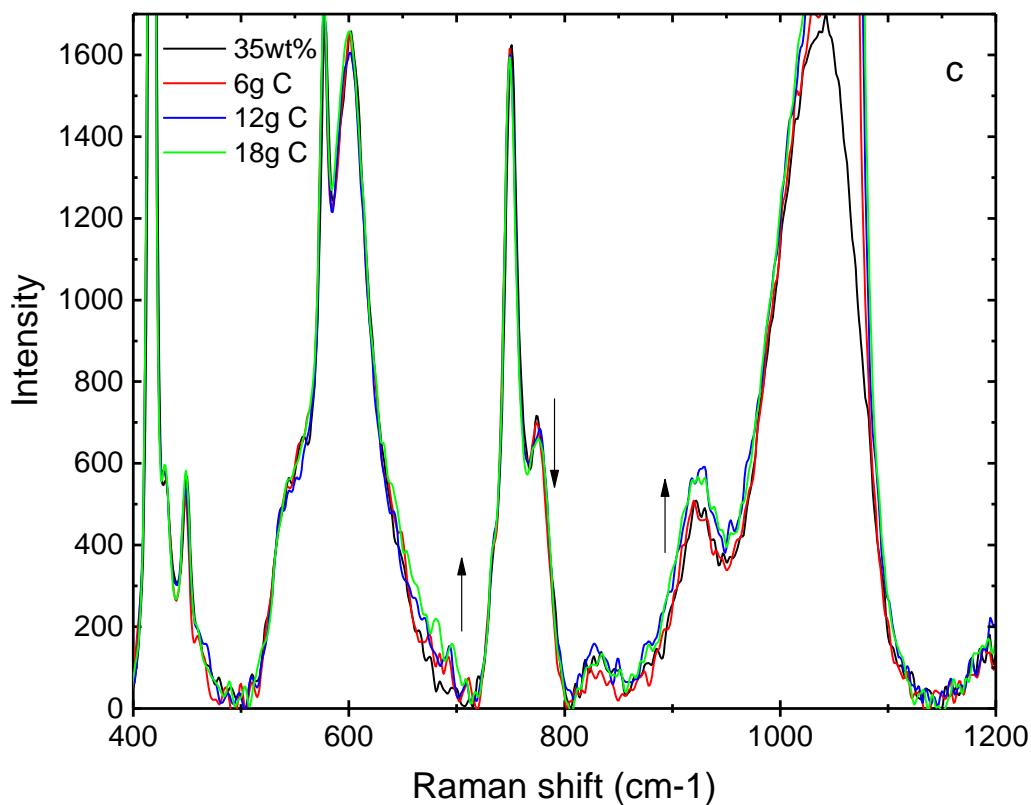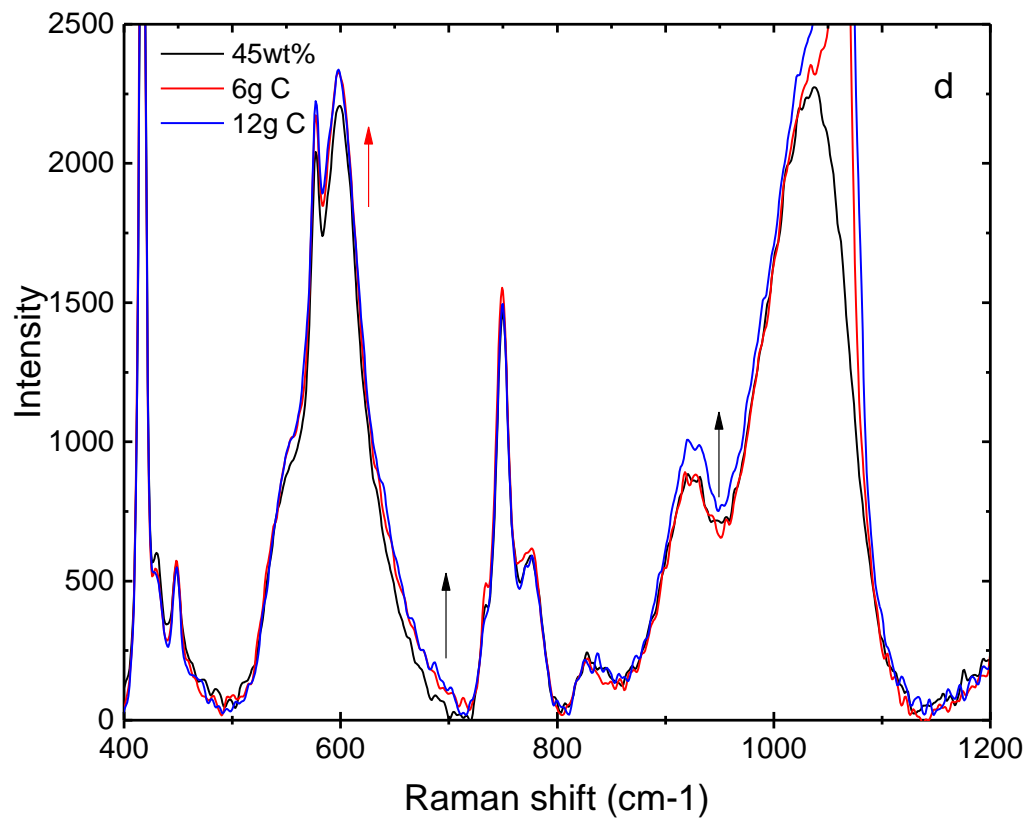**Figure 0.13: The impact of 25wt% of Na2CO3 on 1.6R sodium silicate solution polymerisation.**
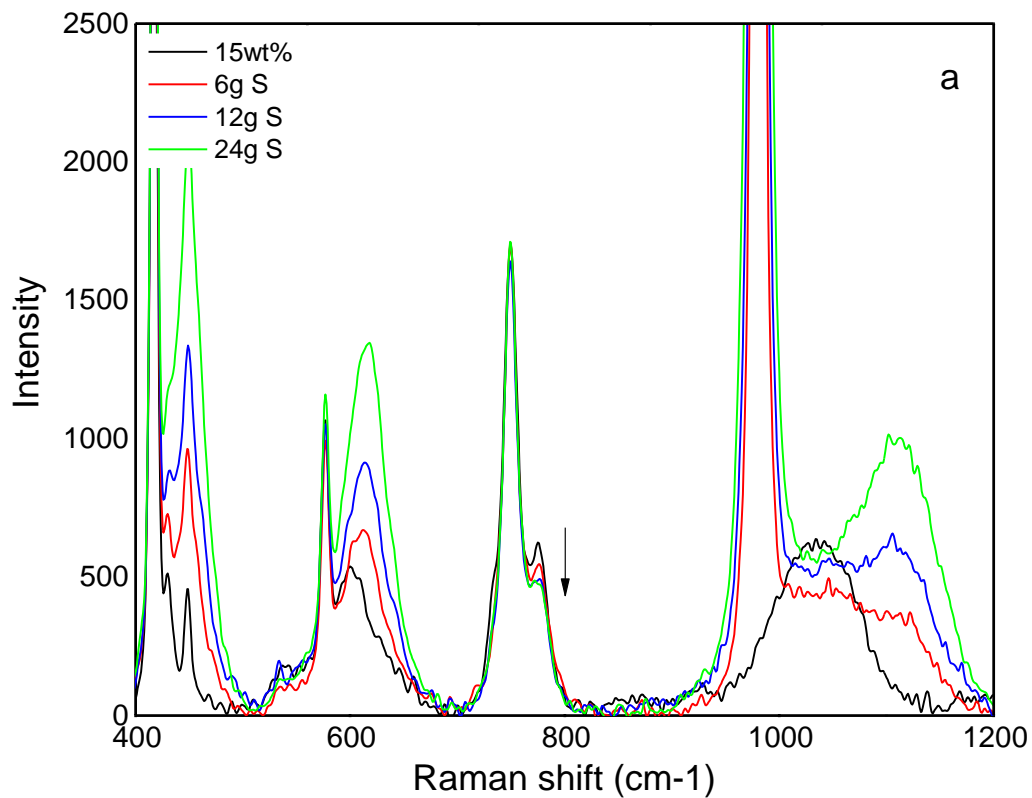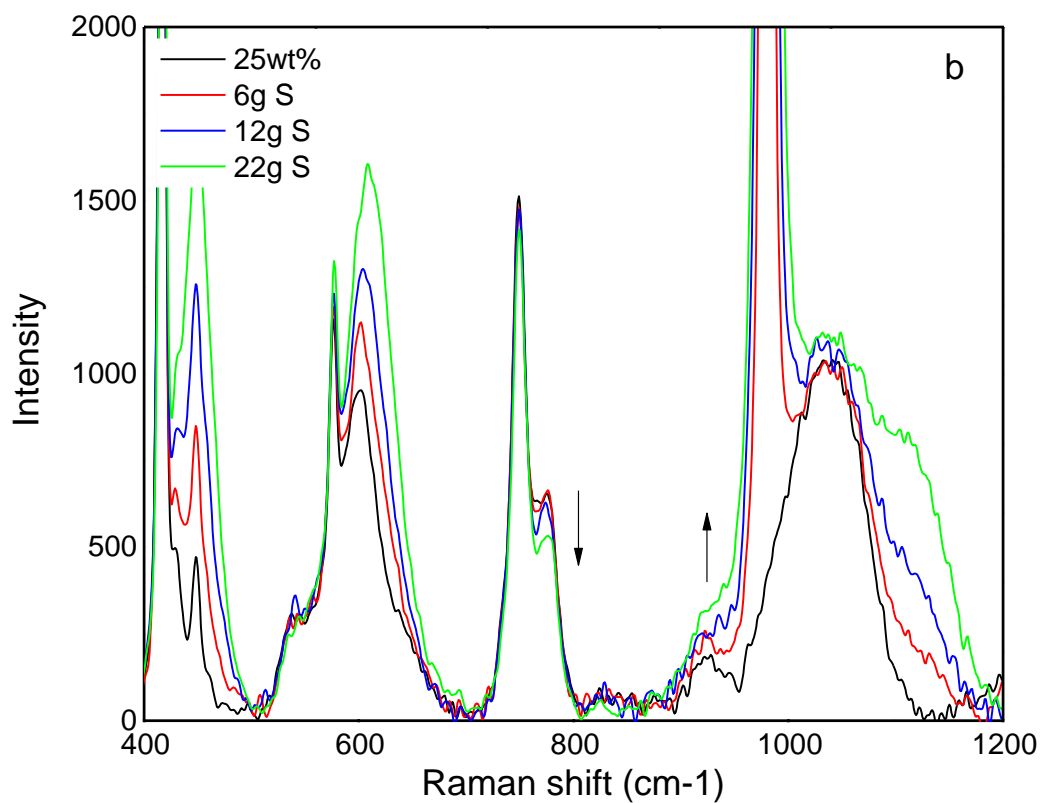

Figure 0.14: The impact of 35wt% of Na₂CO₃ on 1.6R sodium silicate solution polymerisation.

Figure 0.15: The impact of 45wt% of Na_2CO_3 on 1.6R sodium silicate solution polymerisation.

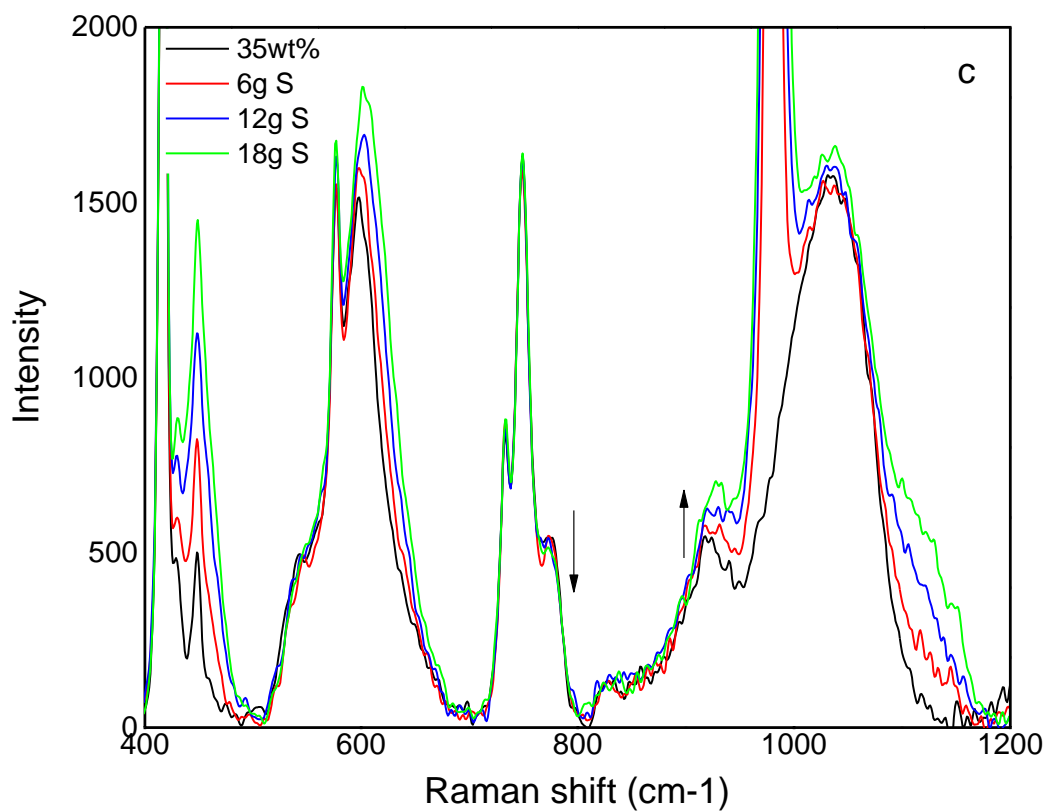**Figure 0.16: The impact of 15wt% of Na_2SO_4 on 1.6R sodium silicate solution polymerisation.**

Figure 0.17: The impact of 25wt% of Na₂SO₄ on 1.6R sodium silicate solution polymerisation.

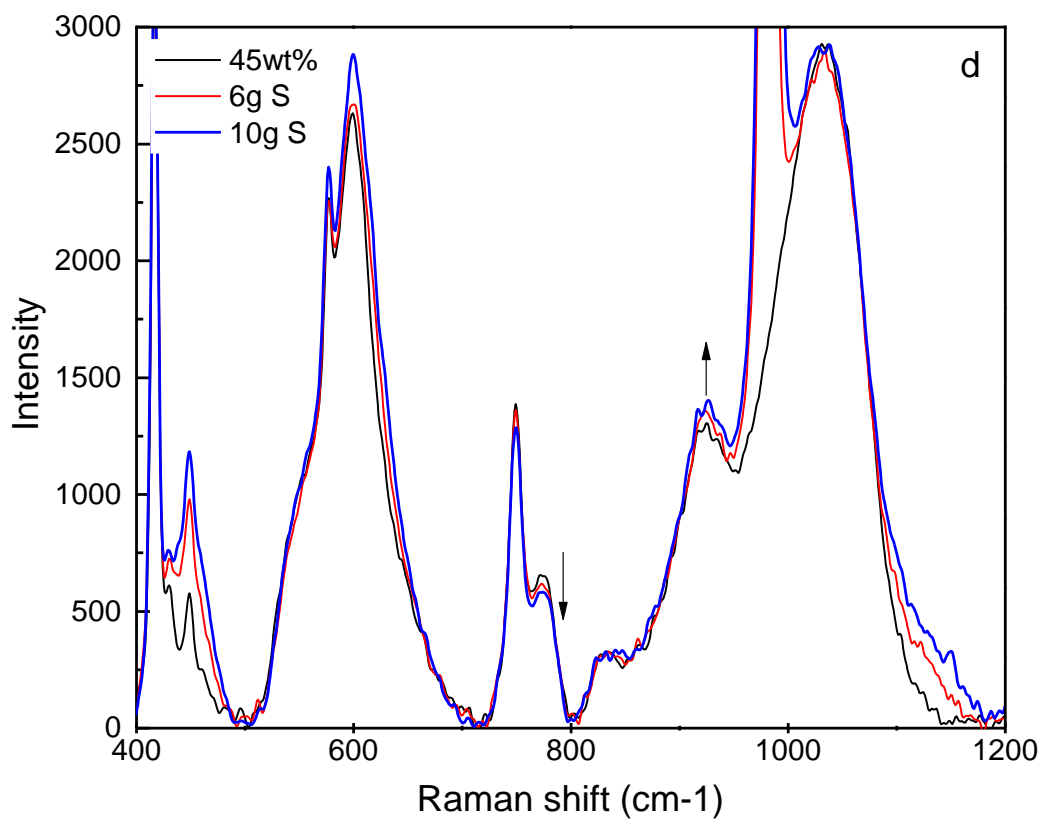**Figure 0.18: The impact of 35wt% of Na₂SO₄ on 1.6R sodium silicate solution polymerisation.**

Figure 0.19: The impact of 45wt% of Na₂SO₄ on 1.6R sodium silicate solution polymerisation.